Metal oxide heterostructured films with controlled architecture for enhanced photocatalytic properties

Periyannan, Shanmugapriya

(2020)

Joint Thesis (European Joint Doctorate - Functional Materials [EJD-FUNMAT])

Approved by:

The Doctoral School of Chemistry of the University of Liege in Fulfillment of the Requirements for the Degree of Doctor

The Department of Material and Geosciences of the Technical University of Darmstadt in Fulfillment of the Requirements for the Degree of Doctor Rerum Naturalium (Dr. Rer. Nat.)

Metal oxide heterostructured films with controlled architecture for enhanced photocatalytic properties

Academic year 2015-2019

Shanmugapriya PERIYANNAN

Born in Tamil Nadu, India

Thesis jury composed of:

PhD Supervisor	**Prof. Dr. Rudi CLOOTS**	(ULiège)
PhD Supervisor	**Prof. Dr. Wolfram JAEGERMANN**	(TU Darmstadt)
Examiner	**Prof. Dr. Ralf RIEDEL**	(TU Darmstadt)
Examiner	**Asst. Prof. Dr. Oliver CLEMENS**	(TU Darmstadt)
President	**Prof. Dr. Ngoc Duy NGUYEN**	(ULiège)
Secretary	**Dr. Catherine HENRIST**	(ULiège)
Reviewer	**Dr. Laura MANCERIU**	(ULiège)
Reviewer	**Dr. Frèdèric LUIZI**	(Aquatic Science)

“கேடில் விழுச்செல்வம் கல்வி யொருவற்கு
மாடல்ல மற்றை யவை”

“Learning is wealth that none could destroy
nothing else gives genuine joy”

- Thiruvalluvar

"I would like to dedicate this dissertation to my beloved son, husband and parents."

Declaration

I declare that this doctorate dissertation is the result of my own investigations and any material used as it is or adapted from other sources are duly acknowledged in accordance with the standard referencing practices. I also confirm that, to the best of my knowledge and belief, it contains no material that was previously published or produced by another party, for the award of any degree or for any other purpose.

Date:

Place: Liege, Belgium.

(Shanmugapriya PERIYANNAN)

Acknowledgements

This dissertation work was carried out in cooperation between the academic institutions, **University of Liege, Belgium** and **Technical University of Darmstadt, Germany**, along with the industrial partner, **Aquatic Science, Liege, Belgium**. Throughout this rigorous academic programme, a number of people extended their support and encouragement without whom this work would not have reached its present form.

First of all, I would like to thank **"European Joint Doctorate in Functional Materials - EJD-FUNMAT"** PhD programme, which provided financial support through **Horizon 2020 - Marie Sklodowska Curie Actions' Innovative Training Network** organisation. I would like to express my deepest gratitude to my PhD supervisors **Prof. Dr. Rudi Cloots** and **Prof. Dr. Wolfram Jaegermann**, for giving me this great opportunity of working in their research groups, **GREENMAT** at Liege and **Surface Science** at Darmstadt, respectively. I am thankful for their continuous support and insightful guidance throughout my doctoral studies.

I am extremely grateful to **Prof. Jaegermann, Prof. Dr. Andreas Klein and Dr. Laura Manceriu**, for their time, extensive scientific discussions and unconditional sharing of knowledge and expertise. Their contributions inspired and motivated me to gain deeper insights of research and made me an independent researcher. I feel fortunate and privileged to have the opportunity to work with them and also grateful forever.

I would like to express my gratitude and appreciation to **Prof. Dr. Ngoc Duy Nguyen**, for his time and valuable suggestions on Photoluminescence analysis. I am also grateful to **Dr. Catherine Henrist**, for her profound guidance in microstructural analysis and the support throughout the course of my PhD studies. I would also like to thank **Dr. Frèdèric Luizi**, for providing me the opportunity to do internship at his industry.

And thanks to **Dr. Pierre Colson** for his assistance to help me in keeping track of this research project and Dr. **Audrey Schrijnemakers** for providing the material needed for industrial work. I would also like to acknowledge the generosity of **Electronic materials**

research group in TU Darmstadt, for providing access to Fluorescence Spectrometer.

My special thanks to colleague **Andreas Hubmann** from the **Oxide group** in Surface Science laboratory, for his time and patience in teaching me the expertise of handling the DAISY-MAT system. I sincerely thank all my colleagues from both Surface science and GREENMAT laboratories, especially those from Oxide group, for providing the opportunity to integrate and maintaining a friendly atmosphere.

I am also thankful to all my **fellow EJD-FUNMAT researchers**, for creating unforgetful memories, listening to each other at hard times and extending their support during the course of this doctoral studies. I would also like to extend my gratitude to my **old friends in India and new friends here in Europe** who were constantly encouraging me in every possible way. A special thanks to my friend **Prasanna Ponnusamy** in Cologne for visiting me often, listening to me, providing valuable suggestions and my cousin **Saravanan Rengasamy and his family** in Bad Hambourg for providing consistent support and making me feel at home.

Last but not the least, I am forever grateful to my extended **family members Thiyagarajan, Rekha, Shanmugavalli, Manikkavalli, Gayathri, Vijayalakshmi, and Gowtham**, my **siblings Abirami and Nagarajan**, my **parents Nithyakalyani and Periyasamy** and **grandparents**, for providing support, encouragement and most importantly for taking good care of my son, while I was away here in another country, for this PhD studies. Without their help, I would not have been able to concentrate on my studies with a peace of mind. And I am deeply grateful and indebted to my **husband, Periyannan and son, Saisivaram** for their understanding, patience, unconditional love, support and encouragement, throughout the course of my PhD studies.

Zusammenfassung in Deutsch

Photokatalytische Prozesse sind interessant, um verschiedene Probleme im Zusammenhang mit der Umweltverschmutzung angehen zu können. Unter diesen Themen werden die Behandlung von verschmutztem Wasser und die Wasserspaltung zur Erzeugung von erneuerbarem Wasserstoff eingehend untersucht. Diese Verfahren sind jedoch immer noch mit Einschränkungen konfrontiert, wie beispielsweise geringen photokatalytischen Wirkungsgraden, die ihre Kommerzialisierung einschränken. Untersuchungen zu Pulvermaterialien für den Schadstoffabbau und die Wasseraufbereitung wurden in großem Umfang durchgeführt. Es bestehen jedoch Schwierigkeiten bei der Wiederverwendbarkeit des Materials. Darüber hinaus besteht die Notwendigkeit, einen geeigneten heterostrukturierten Photokatalysator zu finden, der eine bessere Ladungstransfer-Kinetik liefern könnte, ein Endziel beim Design von Photokatalysatoren. Daher haben wir in dieser Arbeit Dünnschicht-Heterostruktur-Photokatalysatoren untersucht, um die photokatalytische Aktivität, insbesondere gegenüber dem Schadstoffabbau, zu verbessern. Zu diesem Zweck haben wir die Oberflächen- und Grenzflächeneigenschaften von Halbleiter/Halbleiter- (pn-Typ, NiO/ZnO) und Metall/Halbleiter- (Metall/n-Typ, RuO_2/ZnO) Heterostrukturen mithilfe systematischen (schrittweisen) Grenzflächenexperimenten untersucht, um Kenntnisse über den Einfluss der ZnO-Oberflächenreinigung auf die Grenzflächenbandbiegung zu gewinnen und dabei die Möglichkeiten ihrer Verwendung als Photokatalysatoren zu analysieren.

Darüber hinaus haben wir die elektrischen, optischen und Grenzflächeneigenschaften von ZnO-Nanostäben (n-Typ) mit NiO-Beschichtung (p-Typ) durch Variation der NiO-Abscheidungsparameter untersucht, um eine optimierte Heterostruktur zu identifizieren. Wir untersuchten die photokatalytische Leistung dieser Filme für den Abbau von Schadstoffen (Rhodamin B). Parallel dazu untersuchten wir die Wechselwirkung von Wasser mit heterostrukturierten (NiO/ZnO) Photokatalysatoren, um die Oberflächenreaktionen und ihren Einfluss auf die Bandverbiegung an den Grenzflächen zu interpretieren.

Schließlich haben wir den ZnO-Nanostabfilm in einem industriellen Forschungskontext auf Rhodamin B-Abbau getestet, um die Hochskalierung der in diesem Projekt entwickelten Materialien zu untersuchen.

Schlüsselwörter: Dünnschicht-basierte Photokatalysatoren, eindimensionale Nanostrukturen, Heterostrukturen, ZnO, Oberflächenreinigung, NiO/ZnO, RuO_2/ZnO, Grenzflächenexperimente, Wasserkontaktstudien, Bandverbiegung, Schadstoffabbau.

Abstract

Photocatalytic processes possess favourable features that could address the various issues concerning environmental pollution. Among these issues, treatment of polluted water and water splitting for renewable hydrogen production are extensively studied but are still confronted to limitations for achieving high photocatalytic efficiencies that could be successfully commercialized. Investigations on powder materials have been widely reported for pollutant degradation/water treatment, but difficulties are prevailing in the re-usability of the material. Moreover, there is the need for finding a suitable heterostructured photocatalyst that could provide better charge kinetics, an ultimate goal in photocatalyst design. Therefore, in this work, we have investigated thin-film based heterostructure photocatalysts, for improving the photocatalytic activity, especially towards pollutant degradation.

For this purpose, we have investigated the surface and interfacial properties of semiconductor/semiconductor (p-n type, NiO/ZnO) and metal/semiconductor (metal/n-type, RuO_2/ZnO) heterostructures using systematic (step-by-step) interface studies, in order to gain knowledge regarding the influence of ZnO surface cleaning in the interfacial band bending, thereby analyzing the possibilities of their use as photocatalysts.

Furthermore, we have explored the electrical, optical and interfacial properties of ZnO nanorods (n-type) with NiO coating (p-type) by varying the NiO deposition parameters, to identify an optimized heterostructure. We examined the photocatalytic performance of these films for pollutant (Rhodamine B) degradation. In parallel, we explored the interaction of water with heterostructured (NiO/ZnO) photocatalysts, to interpret the surface reactions and their influence on interfacial band bending, a strategy for understanding the heterostructured photocatalysts, which was not explored before.

Finally, we tested the ZnO nanorod film in an industrial research context for Rhodamine B degradation, to investigate the upscaling perspectives of the materials developed in this project.

Keywords: Thin film-based photocatalysts, one dimensional nanostructures, heterostructures, ZnO, surface cleaning, NiO/ZnO, RuO_2/ZnO, interface studies, water exposure studies, band bending, pollutant degradation.

Contents

List of Figures

List of Tables

Chapter 1

State of the art

1.1. Introduction

Human need is an exponential factor, with which the industrial revolution surfaced in the 18th century and brought incredible developments and urbanisation around the world. However, the industrial growth or evolution was(is) attained by the humankind, at the expense of natural environment, by leading to severe and consequential environmental issues. The persistent release of toxic wastes into the water, air and soil has resulted into devastating environmental pollution. This in turn had affected the marine life, wildlife and also the human health. In addition to the stringent environmental laws introduced by most of the countries, research measures like water treatment, air purification, clean energy production were also initiated decades earlier, to mitigate the consequences. Though some milestones were achieved through research, no definite solutions has been identified yet. Therefore, proposing new alternatives for water treatment and energy production that are based on renewable energy sources (light energy from sun) is of paramount importance.

Photocatalysis is a century-old technology that allows the acceleration of chemical reactions, in the presence of light (ultra-violet, visible or infrared) and a specific material called 'photocatalyst'. The photocatalyst is a substance that is capable of absorbing light to induce chemical reactions at its surface. The compelling and beneficial feature lies in the fact that photocatalyst and photocatalysis could be used to address most of the environmental pollution related issues, without any further harm to the environment. Given that the natural light irradiation is used, the major efforts are directed towards identifying a suitable photocatalytic material. Though photocatalysis processes were studied since 1911, the photocatalytic era began after the successful demonstration of water splitting process by

Fujishima and Honda, in 1972. Since then, extensive research has been done by scientists from chemistry, materials science and semiconductor physics disciplines, providing a deep understanding into the phenomena of the photocatalytic process. However, there are challenges with respect to the design of an efficient photocatalytic material, that would enable faster charge transfer, efficient charge separation and consumption.

Moreover, the recent years have seen a major shift from powders to thin film materials for photocatalytic applications, owing to some serious drawbacks that lie in utilization of powder materials (high cost involved in its retrieval after the process, risk of nano toxicity). In case of thin films, reconditioning/recovery is much easier and the problem of nano toxicity is avoided. However, due to its immobilization, they suffer from a reduced surface to volume ratio and mass charge transfer. Because of which, the time taken for complete degradation of the pollutant using thin films is higher than when using powder materials. Therefore, in regard to thin film photocatalytic materials, the major challenges for researchers lie in designing new photocatalyst with enhanced charge separation capabilities, along with improved surface to volume ratio and charge transfer properties.

1.2. Methods used for water treatment

Dyes are one of the main pollutants that can be found in water. There are over 100,000 commercially available dyes that are being used in textile, paper and plastic industries and the resultant waste water which contains a mixture of various dyes is released (many times) directly / indirectly into the fresh water-bodies [35 37]. In order to increase the lifetime of colouring, industries use dyes that are more stable under sunlight exposure and resistant to chemical (soap/detergent) agents and thus more toxic, often carcinogenic. [38 39] This makes the task of removing them from water more difficult. However, from the past four decades and a half, a hand full of physical, chemical and biological methods have been developed and used, for pollutant degradation or decolorization. The conventional waste water treatment methods (Table 1.1) include coagulation, flocculation, bio-degradation, adsorption, membrane separation, ion-exchange etc [35].

Table 1.1: Existing and emerging processes for dye removal and their advantages/disadvantages. Adapted from ref. [35]

Technology used		Advantages	Disadvantages
Conventional treatment	Coagulation and flocculation	Simple, economically feasible	High sludge production and thereby the disposal problems
	Biodegradation	Economically attractive	Slow process; dependability on optimal and favourable environment; maintenance and nutrition requirements
	Adsorption on activated carbon	most effective, produce a high quality treated effluent	Ineffective against disperse and insoluble dyes; loss of the adsorbent and hence regeneration is expensive
Established or Commercialized recovery processes	Membrane separations	Removes all type of dyes; produce high quality treated effluent	Large volumes cannot be treated; requires high pressure operation and expensive
	Ion-Exchange	Regeneration is possible, effective	Not effective for disperse dyes; economic constraints
	Oxidation	Rapid and efficient process	Chemicals required, high energy costs
Emerging removal processes	Advanced Oxidation Processes (AOP)	No sludge remains; little/no consumption of chemicals; can treat recalcitrant dyes	Technical constraints; economically unfeasible
	Selective adsorbents	high selectivity; economical; regeneration is not necessary, as adsorbent is very cheap	Requires extra chemicals
	Biomass	Good efficiency and selectivity; no toxic effects; low operation costs	Slow process; mandatory optimization for external factors like pH, salts

Though each method has its own advantages, these conventional methods were found to be inefficient either due to the failure in realizing complete degradation of the pollutants or leaving behind large amount of sludge (secondary pollution) that are harmful and create further disposal problems [40–42]. The comparison of various treatment processes with

emerging processes are made, by listing out their advantages and disadvantages as shown in the Table 1.1.

The major and common issue with most of the conventional methods (coagulation, flocculation, biodegradation) were the resultant sludge that is produced after treatment and the required disposal, which usually again accumulate in the soil leading to soil pollution. Moreover, membrane based, ion exchange and oxidation processes were expensive due to higher energy consumption or operational costs. Therefore, it was(is) of great importance to develop an efficient, sustainable and green technology that will make use of natural energy source (like sunlight) and do not leave traces of secondary pollution. Moreover, with time, dyes that have complex structure and are difficult to destroy/remove are being used in industries, which also made the conventional methodologies less efficient. The Advanced Oxidation Processes (AOP) are considered as an efficient and environment-friendly technologies, for pollutant removal [38, 39].

1.2.1. Advanced oxidation processes (AOP)

Advanced oxidation processes (AOP) are used for the removal of heavy metals, sludge treatment and removal or degradation of pollutants/contaminants from water, air and soil [39]. The pollutant removal involves the generation and utilization of oxidizing agents like hydroxyl or sulfate radicals to target the organic or inorganic contaminants and is studied since 1980s. Hydroxyl radicals are powerful oxidizing agents that could sufficiently destruct even dyes with complex structure, because they are highly reactive and non selective (meaning, hydroxyl radicals can destruct any contaminant) [39, 43, 44]. Generally, AOPs are classified into photochemical and non-photochemical processes, as shown in Table 1.2. Since the ultimate goal is to alleviate environmental problems by utilizing less energy sources, photochemical processes that involves less energy consumption and less chemicals are preferred for large scale implementation. Hence, photochemical AOPs were widely used. Among them, the direct water photolysis and zerovalent iron processes are not attractive because, the former requires vacuum condition and the latter is a very slow process, making them expensive to implement. The other photochemical AOPs like UV/O_3, UV/H_2O_2, Photo-Fenton (UV/H_2O_2+Fe^{2+}/Fe^{3+}) and heterogeneous photocatalysis are promising methodologies.

Table 1.2: Types of adavnced oxidation processes (AOPs). Adapted from ref.[36]

Non-Photochemical processes	Photochemical processes	
	Types of processes	Irradiation wavelength range (λ/nm)
Alkaline ozonation (O_3/HO)	Water photolysis in vacuum ultraviolet (VUV)	< 190
Ozonation with hydrogen peroxide (O_3/H_2O_2)	Water photolysis in vacuum ultraviolet (VUV)	< 190
Ozonation with hydrogen peroxide (O_3/H_2O_2)	UV/hydrogen peroxide (UV/H_2O_2)	< 280
Fenton and related processes (Fe^{2+}/H_2O_2)	UV/ozone (UV/O_3)	280 - 315
Electrochemical oxidation	Photo-Fenton (PF) and related processes	UV-Vis upto 450
γ - Radiolysis and electron-beam treatment	Zerovalent iron plus UV light	UV range
Non-thermal plasma (surface corona discharge)	Heterogeneous Photocatalysis (HP) using TiO_2	UV up to 380 - 400
Electrohydraulic discharge-ultrasound (US, cavitation)		
Wet air oxidation		
Supercritical water oxidation		
Zerovalent iron (ZVI)		
Ferrate		

UV/O_3

In the late 1980s, use of ozone to treat drinking water was reported, where ozonation process was used to generate hydroxyl radicals (equation 1.1):

$$O_3 + H_2O \rightarrow 2HO^{\bullet} + O_2 \tag{1.1}$$

Ozone alone is already a strong oxidant, but with the presence of ultra violet (UV) light or hydrogen peroxide (H_2O_2) the AOP efficiency is significantly improved. However, there was two major concerns regarding the ozone based AOPs, the short lifetime of the hydroxyl

radicals and the high cost of the ozonation process [43,45].

UV/H_2O_2

UV/H_2O_2 is one among the old AOP technologies which can successfully lead to removal of pollutants. When the photons of energy (< 280 nm) get in contact with the H_2O_2 molecules, $^{\bullet}$OH radicals are formed by the O-O cleavage, as shown in equation 1.2:

$$H_2O_2 + h\nu \rightarrow 2HO^{\bullet} \tag{1.2}$$

UV/H_2O_2 system is capable of improving the degradation rate. But its restriction lies in two factors: (i) nearly half of the energy consumed (from light) result into heat loss and (ii) optimization of H_2O_2 dose is mandatory, because excess H_2O_2 will lead to adverse effects (H_2O_2 will become competitor to $^{\bullet}$OH, forming hydroxyperoxyl radicals [$^{\bullet}O_2H$], which are less reactive than $^{\bullet}$OH). These factors make them economically unfavourable [36].

Photo-Fenton Processes

This process is carried out with the combination of H_2O_2 and Fe^{2+}, that can perform the following reaction in dark conditions:

$$H_2O_2 + Fe^{2+} \rightarrow Fe^{3+} + HO^{-} + HO^{\bullet} \tag{1.3}$$

In case of acidic solution, photo-Fenton reaction will become autocatalytic, where Fe^{3+} will allow the decomposition of H_2O_2 into H_2O and O_2 (equation 1.4).

$$H_2O_2 + Fe^{3+} \rightarrow Fe^{2+} + H^{+} + HO^{\bullet} + \frac{1}{2} O_2 \tag{1.4}$$

These photo-Fenton reactions are usually efficient, as they can realise complete mineralisation of the pollutant. But, as mentioned for the UV/H_2O_2 system, here as well, the need for optimization is necessary, making them expensive. In addition, the requirement to maintain acidic pH (to avoid iron compounds' precipitation) of the solution, restricts its wide usage [36]. In conclusion, while ozonation or UV/H_2O_2 systems are not economical, photo-Fenton processes can be beneficial but only when used as a supplement to other AOP processes. In principle, due to the high reactivity and non-selectivity, the chemical reaction between hydroxyl radicals and the targeted chemical species occur extremely fast and non-specific. This would mean that AOP reactions are greatly governed by the mass transfer

of produced hydroxyl radicals to the chemical species. This also explains why powder photocatalysts are performing better than the thin film based photocatalysts in pollutant degradation, as the former exhibits excellent mass charge transfer abilities.

The photocatalytic degradation processes (photochemical AOP) are usually performed in the presence of target pollutant, photocatalyst, air, water and light source. Therefore, the performance of AOPs are affected by several operational parameters like light intensity, nature of the photocatalyst, photocatalyst concentration, pH and reaction temperature. These parameters and their dependence are listed in Table 1.3:

Table 1.3: List of parameters involved and their characteristic influence in the photocatalytic activity.

Parameter	Characteristic relation to photocatalytic activity
Light Intensity	Depends on the photo absorption capabilities of the photocatalyst
Nature of photocatalyst	Surface morphology and surface area affect the reaction rate
Photocatalyst concentration	Catalyst loading is proportional to the reaction rate, but when the catalyst is in excess, light scattering occurs. Therefore, the catalyst loading has to be optimized
pH	Controls surface charge properties. Usually chosen based on point of zero charge (pzc) of the photocatalyst and whether the pollutant is cationic or anionic. For ex: pzc for TiO_2, ZnO and NiO are 6.9, 8.0 and 9.0 respectively.
Reaction temperature	Increase in temperature leads to increase in charge recombination rate, thereby less photocatalytic activity.

In addition to attaining control over the above listed parameters, efforts have also been made to increase the photocatalytic activity by employing a hybrid process. Thus, electron scavengers like O_3, H_2O_2, Fe^{2+}/Fe^{3+} + H_2O_2, $S_2O_8^-$ or $Br_2O_3^-$ could be added to the pollutant mixed water, in order to trap electrons and enhance the $^{\bullet}OH$ generation. Though these electron scavengers can improve the overall efficiencies, their usage (as an additional chemical) and requirements for strict optimization, makes them less attractive.

Heterogeneous photocatalysis (where hydroxyl radicals are generated and utilized) is also a type of advanced oxidation process [38, 46] that involves the usage of light source and is cost effective as compared to other AOP related processes. It is even more interesting

because complete mineralization can be achieved even without the electron scavengers. But the challenge lies in upscaling the process for real time applications.

1.2.2. Heterogeneous photocatalysis

Heterogeneous photocatalysis is a multi-process technology[47] that involves various disciplines including semiconductor physics, chemistry, materials and surface science. Heterogeneous photocatalysis was first reported in late 1930s[48], when photo-bleaching of dyes was done with the help of titanium dioxide (TiO_2) under UV light source. But the photocatalytic era started after the successful demonstration of water splitting using TiO_2 electrodes, in 1972[49]. Following this, in 1977, Frank and Bard A.J[50], first reported the use of TiO_2 suspension for pollutant removal. Since then, during the past four decades, research investigations (both theoretical and experimental) on photocatalysis had led to deep understanding towards the fundamentals involved and strategies were developed to improve the photocatalytic efficiency by improving the design of photocatalytic materials. As a multi-process technology it involves diverse processes like light absorption, adsorption of chemical species to photocatalyst, generation of photo-induced charge carriers and active species, oxidation-reduction (redox) reactions and finally the resultant action (degradation of pollutant or splitting of water into hydrogen). In case of pollutant degradation, active species formation will lead to the mineralisation of pollutants into products like CO_2 and H_2O that is non-toxic. Given that the light absorption is the first and foremost step in heterogeneous photocatalysis, the electronic structure of semiconductor materials make them the most desirable. As shown in Figure 1.1, the semiconductors (SC) have the electronic states arrangement (filled valence band (VB) and empty conduction band (CB)) such that, the electrons in valence band will be excited when irradiated with a light source.

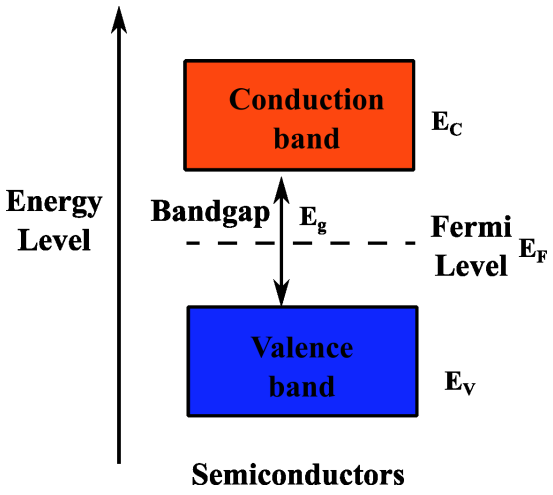

Figure 1.1: Energy band gap in Semiconductors.

When a semiconductor is irradiated with a photon of energy ($h\nu$) equal-to or higher than its bandgap (E_g) [$h\nu \geq E_g$], the electrons will be excited to the CB, leaving behind holes in VB and the following subsequent reactions will take place and the photocatalytic process (pollutant degradation for a semiconductor photocatalyst) consists of the following steps and the charge kinetics:

1. light absorption
2. generation of electron-hole pair

$$SC + h\nu\ (\geq E_g\ of\ SC) \rightarrow e^-_{CB} + h^+_{VB}\ (Photoexcitation\ and\ charge\ carrier\ generation, fs\ [very\ fast]) \tag{1.5}$$

3. migration and transfer of charge carriers, leading to red-ox reactions*
4. formation of reactive species (hydroxyl radicals, superoxide anions)

$$O_2 + e^-_{CB} \rightarrow O_2^{\bullet -} \qquad (\ Reduction\ reaction\ ) \tag{1.6}$$

$$H_2O + h^+_{VB} \rightarrow HO^\bullet + H^+ \qquad (\ Oxidation\ reaction\ ) \tag{1.7}$$

5. mineralization of targeted pollutants

$$Pollutant + {}^\bullet OH \rightarrow oxidized\ molecule \qquad (\ mineralized\ product\ 100\ ns\ [slow]) \tag{1.8}$$

$$Pollutant + O_2^{\bullet -} \rightarrow reduced\ molecule \qquad (\ mineralized\ product\ ms\ [very\ slow]) \tag{1.9}$$

*When the migration and charge transfer are not effective, recombination will occur, which is detrimental for the photocatalytic reaction; fs - femtoseconds, ps - picoseconds and ns - nanoseconds.

Above shown reactions are the elementary processes that take place during the exposure of photocatalyst to the light source. Charge dynamics studies using femto and picosecond absorption spectroscopies could help in identifying the characteristic time for each of those elementary processes. The values shown in relation to the charge dynamics, in above reactions are adapted from the representation regarding primary processes and their

time domains for TiO_2 based mineralisation of organic pollutants.[51].

Moreover, the time domain involved in charge dynamics indicates that the time taken to form superoxide anion is higher than for hydroxyl radical formation. This would mean that hole transfer (100 ns) can compete with the recombination process (100 ns)[51]. It also shows that, the excited charge carriers (e^- and h^+) are prone to recombine either at the bulk or surface of the material, in a matter of nanoseconds, as shown in the equations below:

$$e^-_{CB} \rightarrow e^-_{TR} \qquad (\ electron\ trapping\ ;10\ ns\ [deep\ traps,\ fast]\ or\ 100\ ps\ [shallow\ traps]\ ) \tag{1.10}$$

$$h^+_{VB} \rightarrow h^+_{TR} \qquad (\ hole\ trapping\ ;10\ ns\ ) \tag{1.11}$$

$$e^-_{TR} + h^+_{VB}\ (\ h^+_{TR}\ ) \rightarrow e^-_{VB} + heat \qquad (\ charge\ carrier\ recombination\ 100\ ns\ [slow]\ ) \tag{1.12}$$

where, TR - trapping.

This recombination rate can be reduced by employing surface modification techniques that are specific to semiconductor materials. They include doping, metal deposition or coupling of semiconductors and these concept will be explained in detail in the subsequent sections.

Irrespective of the type of applications in which heterogeneous photocatalysis is used (water/air purification, water splitting for H_2 production), the energy loss incurred during the process and operational costs are greatly minimized (as opposed conventional methods) due to the direct utilization of solar energy[52,53]. Especially, for pollutant degradation processes, photocatalysis allows gradual breakdown of the pollutant molecules and avoids sludge remains and thereby the necessity for their removal[53].

For effective performance of a photocatalyst in pollutant degradation, the CB electrons and VB holes are expected to be sufficiently negative (to produce superoxide anions, $E_0(O_2/O_2^{\bullet-})$ = -0.28 V vs. NHE) and positive (to produce hydroxyl radicals, $E_0(H_2O/^{\bullet}OH)$ = 2.8 V vs. NHE), respectively[1]. When this condition is fulfilled, the gradual breakdown of pollutants will take place as shown in Figure 1.2.

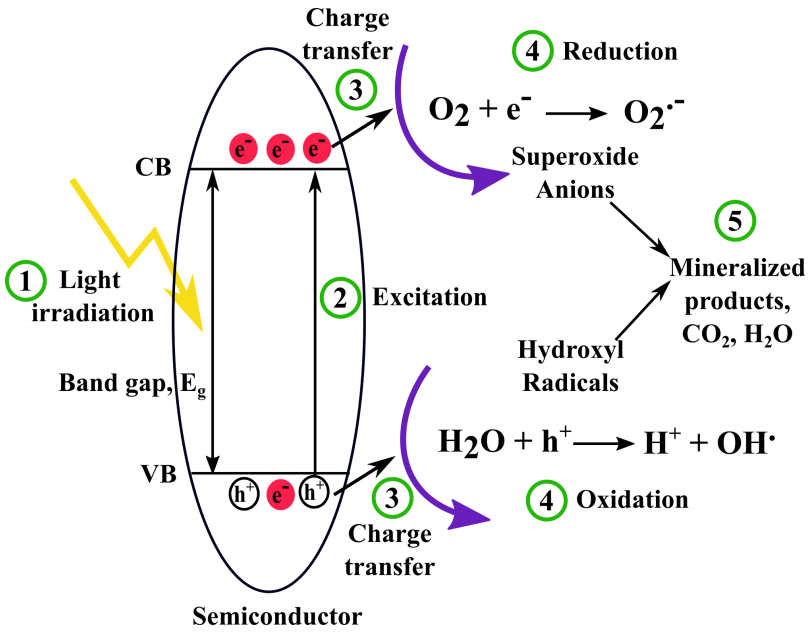

Figure 1.2: Pollutant degradation mechanism for a semiconductor, with the resultant reactions in presence of light source.

1.3. Photodegradation vs. water splitting

Pollutant degradation (PD) and water splitting(WS) are two major topics related to chemistry and materials science that are based on the concept of photocatalysis [54–56]. The similarities and differences between them needs to be understood, when designing the photocatalyst. They both rely on the absorption of photons to generate the charge carriers (electrons and holes). Differences appear once these photo induced charge carriers reach the surface and participate to the redox reactions [57]. Both PD and WS processes follow three steps:

1. carrier generation - occurs on irradiation by light source; a step that does not pose any difference

2. carrier separation - realizable by avoiding bulk and/or surface recombination; there is difference in the way it influence the specific process

3. carrier consumption - will take place effectively on effective occurrence of previous steps; difference occur in the charge consumption mechanism and number of charge carriers or energy required to perform the process

The ability to achieve an efficient photocatalyst lies on the ability to acquire good control

over all the three aforementioned steps[58,59]. PD is a thermodynamically favourable or a chemically downhill process, $\triangle G<0$ whereas, WS is a thermodynamically unfavourable process or a chemically uphill process, $\triangle G>0$[54]. The PD is a hole dependent process (one hole could result into formation of active species that are capable of degrading the pollutants), whereas, the WS is a complex process involving four electrons that should react with protons to form hydrogen, in addition to the oxygen evolution reaction. Therefore, PD is more dependent on the surface-to-volume ratio (should be higher, to allow more adsorption of pollutants) and the amount of active species that could be generated through the redox reactions, whereas WS is more dependent on efficient charge transfer, its separation and prevention of bulk recombination (Figure 1.3).

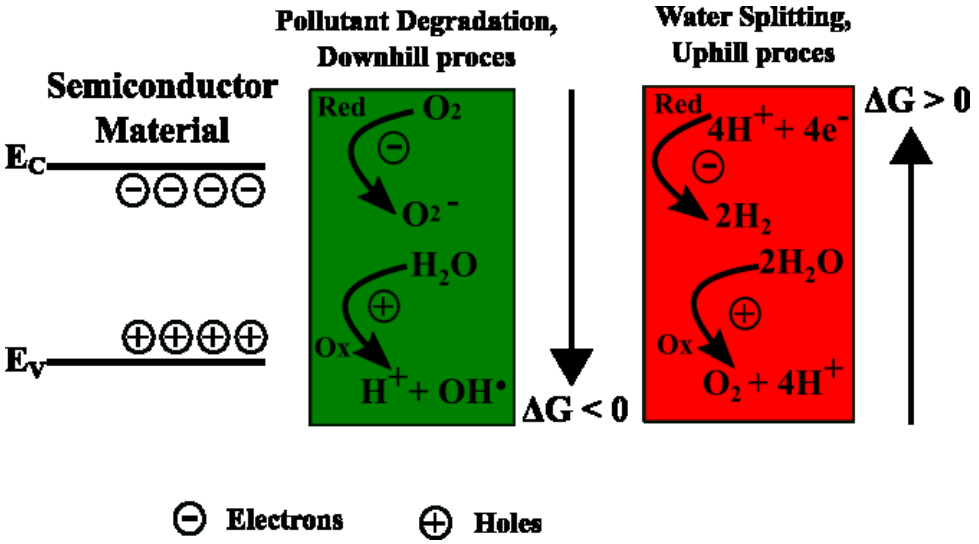

Figure 1.3: Role played by charge carriers in pollutant degradation and water splitting process

In addition to differences in the amount of electrons need to be transferred, in both PD and WS, the ability of photogenerated charge carriers to perform the redox reactions is significantly dependent on the position of the CB and VB of the semiconductor, which should be aligned in a way that minimum energy is required to induce the (reduction/oxidation) process. The alignment of VB and CB levels for some commonly investigated semiconductors in relation to the PD and WS mechanisms is shown in Figure 1.4.

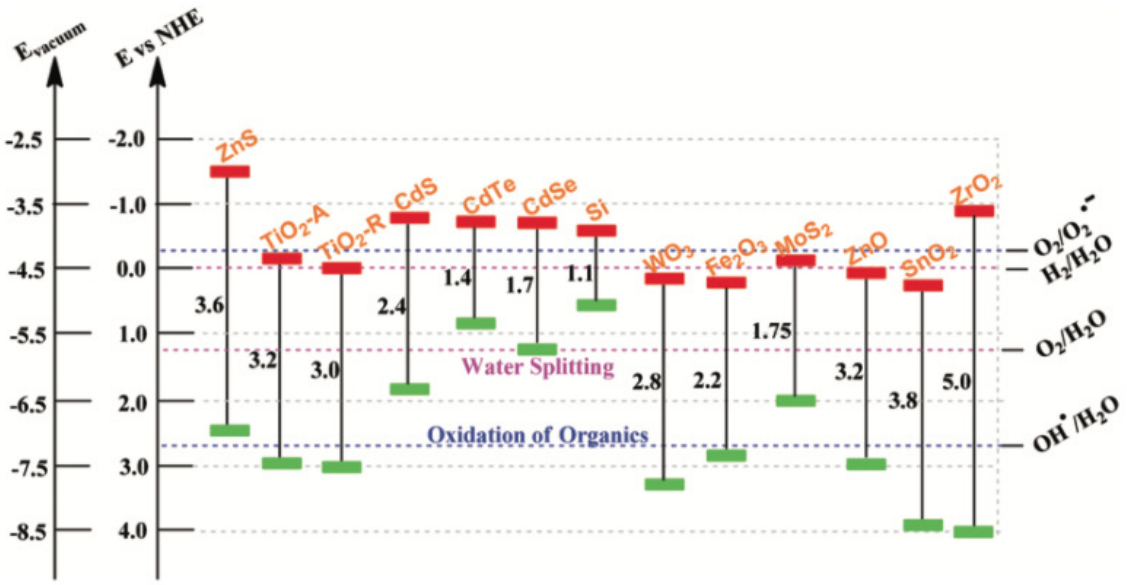

Figure 1.4: Band gap energy, VB and CB energy levels for a range of semiconductors on a potential scale (V) versus the normal hydrogen electrode (NHE). Reproduced from ref.[1].

Given the different charge transfer mechanisms involved, a photocatalyst that performs better in PD, not necessarily performs good in WS.[60]

1.3.1. Model pollutant used - RhodamineB

RhodamineB (RhB) is one of the main xanthene (characterized by the presence of xanthene as core, exhibiting fluorescent yellow to pinkish colour), synthetic dye which has wide usage in textiles, paper or plastic and even food industry. Its molecular structure is shown in Figure 8.2 which indicates its cationic nature.

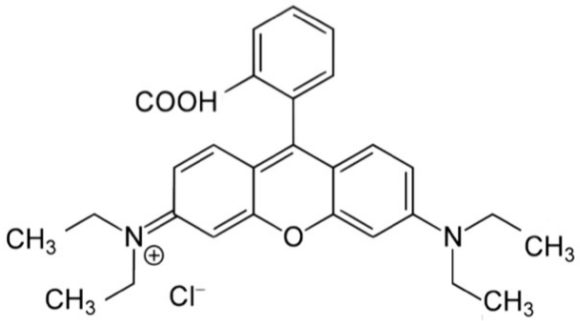

Figure 1.5: Molecular structure of RhodamineB.[2]

RhB is particularly famous for its good stability and is often found as traces in water [2,61–63] and food [64,65]. It causes serious environmental problems and is also proven to be harmful for humans and animals (carcinogenic, irritation to skin, eyes and respiratory tract). As with many other dyes, conventional methods like adsorption and ozonation are not effective for RhB degradation as well and hence, heterogeneous photocatalysis is considered to be a promising method.

In this thesis, RhB is used as the model pollutant and its degradation process is monitored by using thin film based scaffold and heterostructured photocatalysts. Dye degradation processes are usually initiated by the photo-induced reactions (producing e^-/h^+ pairs) that will accelerate the catalytic process resulting into formation of the active species (superoxide anions [$O_2^{\bullet-}$] or hydroxyl radical [$^\bullet$OH]). This will further form the intermediates and eventually the mineralization products like CO_2 and H_2O. Therefore, it is necessary to understand the reaction pathways/mechanisms and the intermediates formed during the dye degradation, in order to analyse the performance results.

Previous reports have shown that RhB degradation involves two different pathways called chromophoric cleavage and successive deethylation (as shown in Figure 1.6), that could occur independently and simultaneously. Chromophore cleavage takes place with the support of photo generated e^-/h^+ pairs and hence associated with direct photocatalysis [66]. Whereas, deethylation is a step-wise process where the intermediates include N,N,N′ - triethyl rhodamine (TER, 539 nm), N,N′ - diethyl rhodamine (DER, 522 nm), N - ethyl rhodamine (MER, 510 nm) and rhodamine (498 nm). This process is generally related to indirect photocatalysis, where light irradiation results into dye excitation (producing the $RhB^{+\bullet}$ radical cation) and repetitive e^- injection paves the way for the completion of subsequent deethylation steps [3,66]. This indicates that deethylation steps could occur even when a photocatalyst is not available.

When deethylation process dominates, the reduction in absorbance peak will be identified with a hypsochromic shift (shift towards lower wavelength), revealing the occurrence of intermediates formation. The presence or absence of such hypsochromic shifts were studied in detail by Zhuang et al. [67] by employing varying TiO_2 bilayer surfaces (normal surface, interface defective and surface defective) and each of their influence on inducing such shifts. Their studies suggest that complete RhB degradation, i.e, mineralization occurs only when both deethylation and chromophore cleavage processes are taking place. However, their explanation regarding the improvement in degradation efficiency (75% after 5 h of illumination) in the presence of interface defects is in contrary to the fact that interface defects deteriorate the charge kinetics of the photocatalytic process [11]. In addition, their studies have not reported about the choice of pH which is an important parameter in

controlling the pollutant adsorption at the catalyst surface.

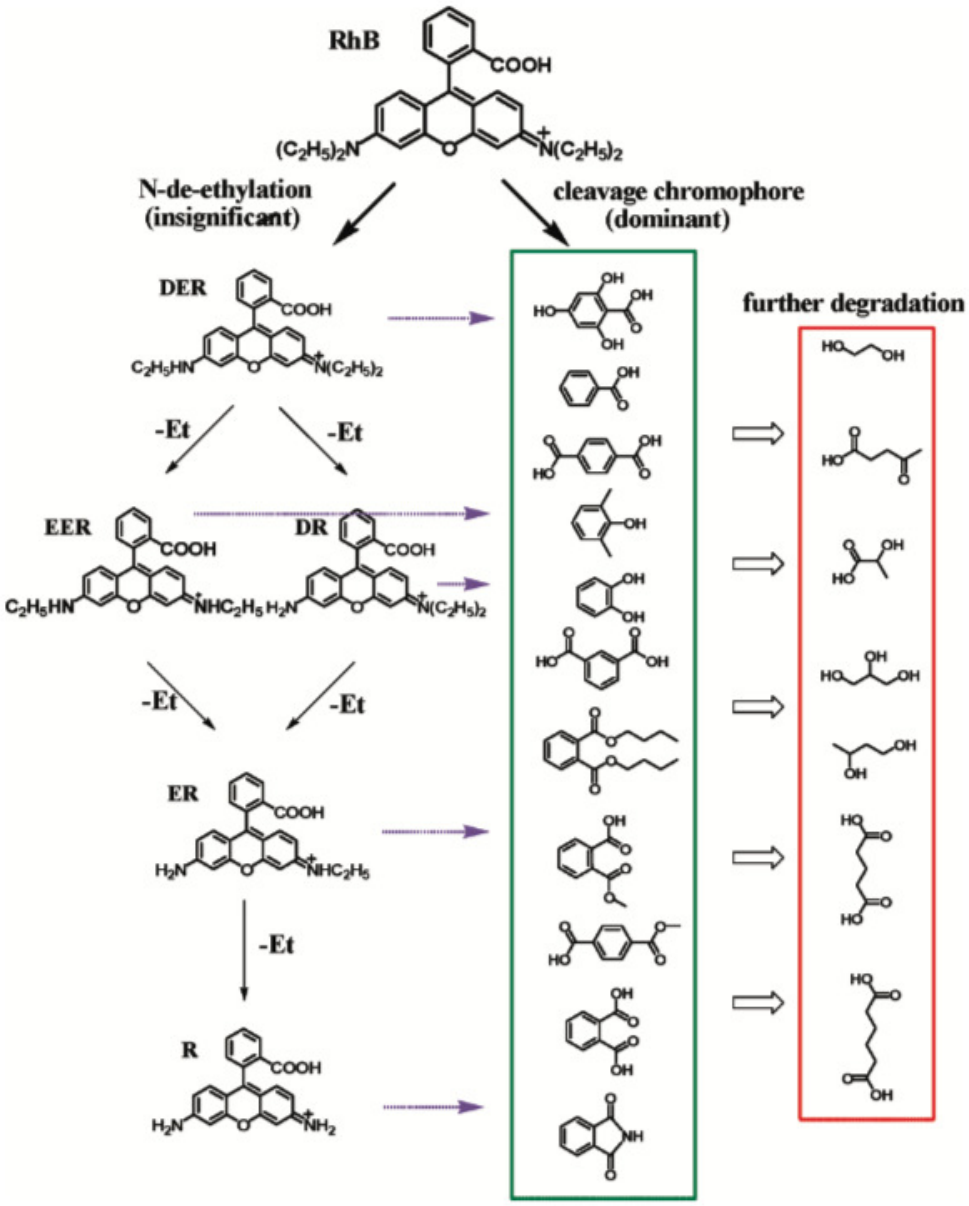

Figure 1.6: Proposed pathway of RhB in suspension, irradiated by light source. [3]

In addition, studies by Zhao et al., [67,68] have shown that hydroxyl radicals formed at the catalyst surface ($^{\bullet}OH_{surf}$) will enhance the deethylation process while that in the bulk solution ($^{\bullet}OH_{sol}$) will induce chromophore cleavage. This indicates that there is an advantage of using radicals present both in the surface and bulk solution to improve RhB degradation efficiency. This could be further related to the type of photocatalyst (powder or thin films) used. Therefore, chromophore cleavage might be a dominating process when powder materials are used, since they are known to perform the photocatalytic degradation in the bulk solution. Concurrently, deethylation, a surface related process, (for which pH

might not matter) could be the dominating process when thin films are used, as the reaction occurs on the catalyst surface[69]. Hence, in order to achieve mineralization, i.e, to induce chromophore cleavage as well, one would need to adjust the pH and find an optimized one.

In terms of pH influence on RhB degradation using ZnO nanorod based films, Wang et al.[70] have shown that, when ZnO alone is used, both acidic and alkaline pH (3 and 11, respectively) have led to photo corrosion. Surprisingly, when iodine doped ZnO nanorod was coated with TiO_2 layer, the photo corrosion was avoided and both the acidic and alkaline pH was observed to be performing better, by achieving efficiency of up to 97%, after 6 h of illumination.

Choosing the pH - In general, when a material (like metal oxide) is immersed into the liquid, ion exchange is induced, which is influenced by the net surface charge of the photocatalyst material used. Moreover, the surface of the material could be positively or negatively charged as a function of pH and the value of pH at which zero net surface charge is attained is called as point of zero charge (pzc)[71]. Therefore, the surface electric charge of the photocatalysts could be controlled by adjusting the solution pH, such that it can favour the adsorption of the pollutants and thereby its degradation[72]. When the pH $>$ pzc, the photocatalyst's surface will be negatively charged, allowing the adsorption of positive charged pollutants (as shown in Figure 1.7) and the contrary holds true for pH $<$ pzc.

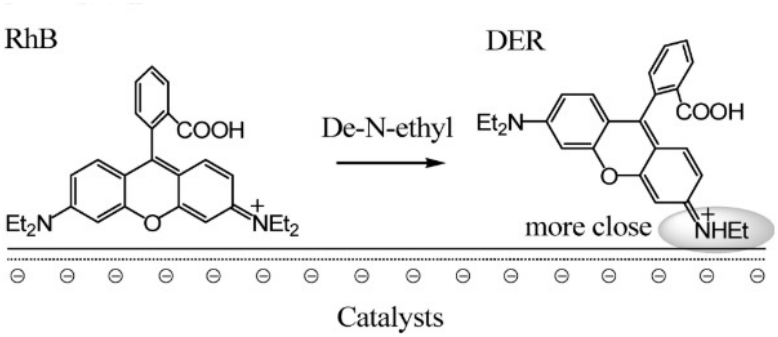

Figure 1.7: Schematic representation of the specific adsorption mode of positively charged RhB and DER on the surface of the negatively charged catalyst in aqueous dispersion.[3]

The pzc of ZnO lies in the range of 8.4 - 9.48[73–75] and that of NiO lies in the range of 8.3 - 10.5[76]. However, depending on the hypothesis that surface electric charge of combined materials or heterostructures (as studied in this thesis) will vary in relation to the involved materials[71], it has been demonstrated that, pzc of ZnO in combination with other materials (metals or metal oxides) will reduce and occur in the range of 7.3 - 7.6[75,77,78]. Therefore, RhB being a cationic dye (which becomes positively charged pollutants on dissolution in

water) that is examined for the performance of heterostructured films, the pH of the RhB solution should be above the pzc value 7.3 - 7.6. This is, in order to ensure the adsorption of positively charged RhB molecules on the negatively charged heterostructures' surface. Hence, the pH of RhB solution was adjusted to 8 before test, for all the samples examined for RhB degradation in this thesis.

1.4. Powder vs. thin films

Ever since the photocatalytic era started (about 5 decades now), the investigations regarding photocatalytic applications were performed mostly with powder materials. In case of water splitting, the photocatalyst is either deposited directly on a suitable substrate or the powder material is made into a slurry which is then cast on the substrate. Whereas, in case of pollutant degradation, the powder is usually suspended in the water mixed with pollutant(s). Such a suspension needs a retrieval process after the treatment, which is both time consuming and expensive. This may not be a serious issue in lab-scale investigations, but has a major impact on the operational costs, for commercial / industrial-scale implementation. Even when nanomaterials (10 - 100 nm) are used, which are expected to form 0.5 μm agglomerates after the treatment, complete retrieval of the material is strenuous and very costly [4]. Therefore, strategies have been developed for the immobilization of the photocatalyst [79] on suitable substrates like quartz, soda-lime glass, Indium doped Tin oxide (ITO), Fluorine doped Tin oxide (FTO), Silicon (Si), stainless steel and porous or microfibrous substrates. With respect to the the major goal of reducing post treatment retrieval or regeneration of photocatalysts, substrates like FTO / ITO / Si are mostly preferred [4].

Nevertheless, this alternative path come with a compromise in the photodegradation performance. Powder materials (as single or heterostructured materials), in the form of suspended particles are so far the better performing, owing to their higher surface to volume ratio and the efficient mass transfer (some examples are given in Table 1.4).

Table 1.4: ZnO powder materials examined for pollutant degradation, from literature review. ⊙ - nanorod; degradation time - in minute [min] or hour [h]; TPA - terephthalic acid, AO7 - acid orange 7 and RhB - rhodamineB; • - (after H_2O_2 and pH optimization)

Samples discussed	Performance (in %)	Catalyst loading / (particle size)	Pollutant used, Molarity details	Degradation time	Light source	Reference
TiO_2 nanoparticles (P-25)	42	2.5 g (21 nm)	TPA, 20 mg/L	30 min	UV	[80] [2010]
ZnO nanoparticles	63	2.5 g (100 nm)	TPA, 20 mg/L	30 min	UV	[80] [2010]
ZnO nanoparticles	≃99•	160 mg (33 nm)	AO7, 20 mg/L	60 min	UV	[81] [2007]
ZnO/TiO_2 nanocomposites	≃99	10 mg (14 nm)	4-Chlorophenol, ≃6.5 mg/L	480 min	UV	[82] [2013]
ZnO/CeO_2 nanocomposites	≃99	20 mg (≃5 nm)	RhB, 5 mg/L	120 min	UV	[83] [2010]
ZnO (nanorod)/Au (nanoparticles) powder	≃97	not clear (ZnO[50 nm]/Au[6-12 nm])	RhB, 20 mg/L	90 min	UV	[84] [2014]

As seen in the table above, ZnO has the capacity to outperform TiO_2, which is considered the model photocatalyst and also a well-established and commercialized material. This is due to ZnO's enhanced ability (compared to TiO_2) for light absorption and rapid charge transfer (discussed in detail, in next section). However, the fact that ZnO as a single material, is highly prone to photocorrosion, makes it less developed as a photocatalyst material. And hence, decades long research regarding ZnO as a photocatalyst are devoted to developing strategies for enhancing its photo stability and reducing the recombination rates.

Through immobilization, the surface area is reduced and hence the mass transfer is greatly limited [47 85]. As an example, lower degradation rates are obtained for the TiO_2 films with report to powder [as illustrated in Figure 1.8 [4]].

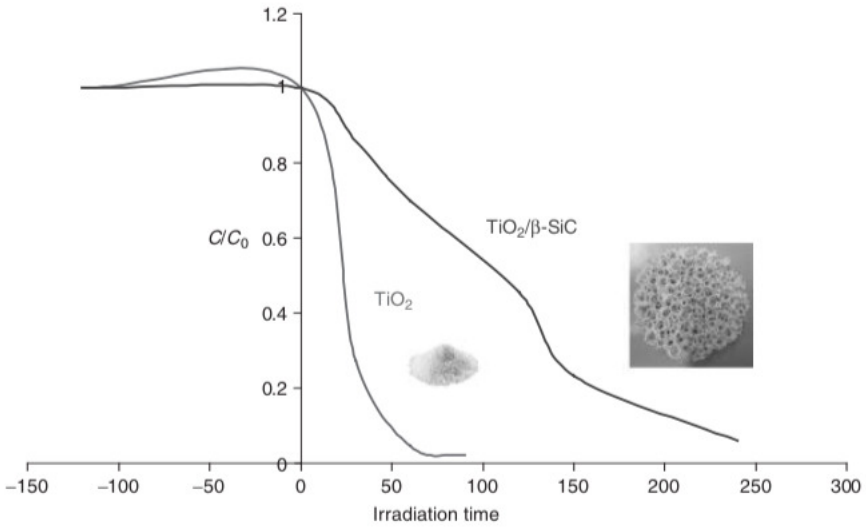

Figure 1.8: Comparison of TiO_2 sol-gel powder suspensions and TiO_2 supported on β-SiC foam as photocatalytic systems (with same loading in TiO_2) for the elimination of Diuron in water. Reproduced from the book photocatalysis and water purification by Pierre Pichat[4].

Likewise, ZnO thin films also have lower performance ($\simeq$25%[86]), compared to ZnO powders (in Table 1.4). This implies that the interaction mechanism between the semiconductor and pollutant is different in each case, as shown by Gumy et al, where the average half-distance between the semiconductor and the targeted pollutant was demonstrated to be increasing, as a result of immobilization (because reactions occur only near the semiconductor surface and not in the solution as in case of powder materials). A way to overcome the above problem is to increase the surface area of the immobilized photocatalysts, which could be done by adopting the nanostructured approach towards the material growth.

1.5. Planar vs. nanostructured thin films

Nanostructured materials are highly desired, irrespective of whether in the form of powder or thin films, owing to their superior electrical, optical and catalytic properties, as compared to the bulk counterparts. There are several types of nanostructures (particles, cones, sheets, flower-like, rods/tubes, dendrites) which benefit from the increase in surface area[87–89]. There are several advantages of using 1D nanostructured film over the planar films and it is illustrated in the Figure 1.9.

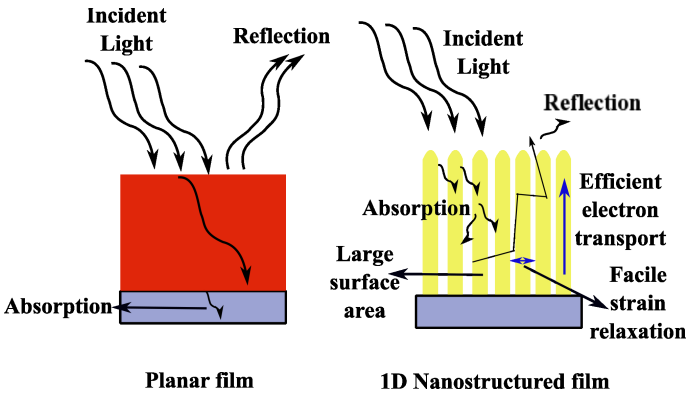

Figure 1.9: Illustration of planar and 1D nanostructured film, their properties.

The planar films usually suffer from lower surface area, reflection (less light absorption) and the photo generated charge carriers that must move through inter-particles (or grain boundaries) resulting in high amount of recombination [89–91]. Whereas, 1D nanomaterials (nanorods) have some striking advantages that include larger surface area, increased light absorption or trapping capabilities and direct electron pathway allowing efficient charge transport [92–94]. 1D nanomaterials also have an increased diffusion length that enables efficient charge separation and thus reduced charge carrier recombination. Moreover, it has facile strain relaxation (due to the gap between each nanorod) that will allow facile preparation of heterostructures, without any damage to the nanorod. This will also enhance the synergetic integration of properties from the second material, rather than a separate effect, as in case of bilayered planar films. In addition, 1D nanomaterials require significantly less quantity of the material, thus, reducing the overall material preparation costs. Therefore, 1D based thin films are expected to perform better than planar films.

This concept was observed by Wu et al. [95], where vapour deposited ZnO (planar) film and ZnO nanorods were examined for pollutant degradation (MO). The efficiency of the film was $<$10%, while that of nanorods was $\simeq$60%, thus a 5-6 times improvement in the performance.

1.6. Semiconducting transition metal oxide as photocatalysts

In general, conventional semiconductor systems have the origin of bandgap from octet rule, where the closed shell configuration is composed of the s and p atomic orbitals [96,97]. This makes them defect intolerant and unstable or metastable [97]. But, semiconducting transition metal oxide (STMO) materials usually have the presence of additional d orbitals

(from transition metals), making them relatively stable and defect tolerant. From a material design point of view for photocatalysis or any other applications, it is important to be able to control and optimize the material properties (optical, electrical, catalytic etc). This along with the necessity for choosing abundant, non-toxic, chemically stable, easy and low-cost processable materials (also governed by the ability to control the properties) in terms of large-area applications, make the STMOs interesting candidates. A photocatalyst is considered ideal, if it meets the following requirements:

a) suitable band gap, for light absorption abilities

b) large surface to volume ratio

c) desirable band edge positions with respect to the required red-ox potentials

d) high lifetime of photogenerated charge carriers or reduced charge carrier recombination

e) good photochemical stability and re-usability

Semiconductor or heterogeneous photocatalysis is often called Titanium dioxide photocatalysis, due to its huge popularity after the pioneering study of Fujishima and Honda in 1972 [49]. An extensive research has been carried out in TiO_2 photocatalysis, leading to its application in water treatment, air purification, water splitting, CO_2 reduction etc.,

Nevertheless, ZnO (especailly nanorods) has greater potential for photocatalytic reactions, as a result of its ability for rapid carrier transport, as compared to TiO_2. More precisely, ZnO possess a direct bandgap with a very high electron mobility of $\simeq 100$ cm^2 V^{-1} s^{-1}, whereas TiO_2 has an indirect bandgap with < 1 cm^2 V^{-1} s^{-1} electron mobility [98,99]. Therefore, ZnO allows easier migration of photogenerated charge carriers (electrons/holes) towards the surface, a crucial step in the photocatalytic process.

ZnO's capability to encourage anisotropic growth [98], and hence easier synthesis of 1D ZnO nanostructures makes it highly desirable for thin film oriented photocatalytic applications. However, the drawback of ZnO (in relation to TiO_2) lies in its lower chemical stability and higher (charge carrier) recombination rate but also the poor visible light absorption. Still, all these drawbacks could be eliminated or reduced by adopting the heterostructure formation strategy.

The materials that have been employed in this thesis and its basic properties are discussed briefly as follows:

1.6.1. Zinc oxide - photocatalyst

ZnO is a n-type semiconducting transition metal oxide material, that has a wide (direct) band gap of $\simeq$ 3.37 eV and a high exciton binding energy of 60 meV[100,101]. In general, ZnO crystallizes in the wurtzite structure (as shown in Figure 1.10) which has a hexagonal unit cell and in which every O atom is tetragonally coordinated to four Zn atoms. This along with the anisotropic growth, facilitates the formation of ZnO nanorods (ZNR), compared to other nanostructures.

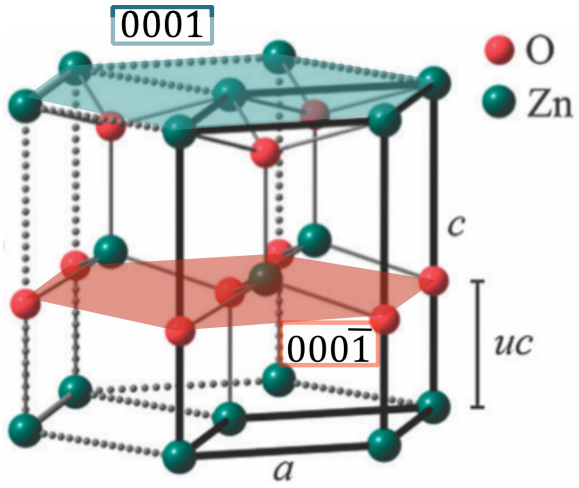

Figure 1.10: Unit cell of the wurtzite structure of ZnO. Adapted from ref.[5]

Nanorods are grown along the c-axis by alternating positively charged Zn (0001) and negatively charged O (000$\bar{1}$) atom planes, making this structure polar. The polarity of a material impacts the electrical, optical, the chemical stability and the reactivity. This being said, it is important to note that the polarity dependent properties of the ZnO single crystals are extensively investigated, but the ZnO nanostructures are less studied.

With the increase of studies on thin film based photocatalysts, ZnO nanorods have gained attention owing to their unique electrical, optical and growth characteristics (as mentioned earlier in this section). ZnO nanorods were often reported to be prepared by adopting hydrothermal method [2 step process involving: seed layer - by spin coating/lithography/ sputtering and nanorod growth - hydrothermal], growing them on FTO/ITO substrates[70,100,102–104]. Other preparation methods include electrochemical deposition[18,105], dip coating[9] and Chemical vapour deposition[95]. Hydrothermal method is mostly used because of its simplicity, facile control over growth[104] and budget-friendliness. As mentioned in Section 1.5, thin film based nanorods were shown to be performing better (a maximum of 60% among previous reports), compared to planar films. Therefore, in this dissertation, ZnO (1D

nanostructured) nanorods grown on FTO substrates by hydrothermal method is employed as a scaffold material.

1.6.2. Nickel oxide - photocatalyst

Nickel Oxide (NiO) is also a STMO, which has p-type character and possess a wide bandgap of 3.6-3.7 eV. NiO is known to adopt a crystal structure similar to NaCl (rock salt, face centered cubic), forming octahedral Ni^{2+} and O^{2-} sites (Figure 1.11, left side). When sputtering is adopted as the preparation protocol, NiO (111) [Figure 1.11, right side] will be formed under two circumstances: (i) deposition at lower temperature and (ii) at high temperature (under lower oxygen ratio). In both cases, collision of Ni^{2+} and O^{2-} will take place on the surface of the growing film, but each in a different manner. Under condition (i), non-stoichiometric ratio occurs, because, the collision takes place separately, without much energy for them to recombine. Whereas, under condition (ii), the collision will take place at the same time, resulting into a stoichiometric ratio [6].

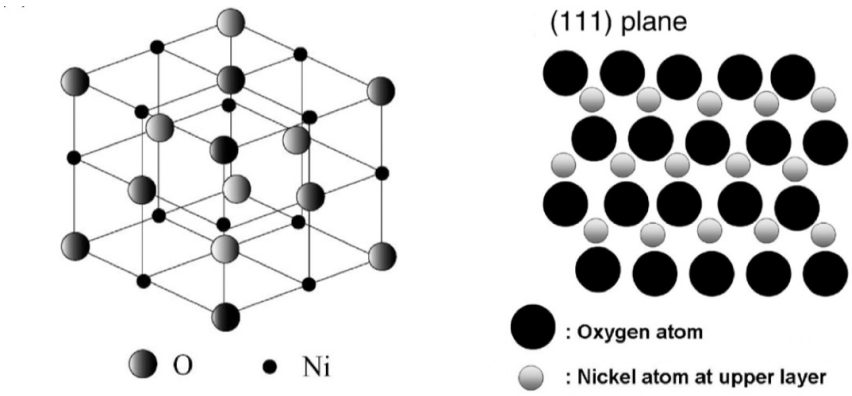

Figure 1.11: Unit cell of the NiO structure (left) and atom arrangement in the (111) plane (right). [6]

Among the possible configuration, both (100) and (111) NiO planes have been shown to adsorb hydroxyls (-OH) [whose presence is capable of inducing catalytic reactions], however the latter one is considered to be more active, due to its polarity [106,107]. NiO (111) facets usually include a positive (111) plane terminated with Ni atoms and a negative $(\bar{1}\bar{1}\bar{1})$ plane composed of O atoms (Figure 1.11) and have shown significant enhancement in photocatalytic applications [107]. The reasons behind the (111) plane reactivity were explored (but not extensively) through both theoretical [20] and experimental [106,108,109] studies. While Zhang [109] and his co-workers examined the photocatalytic performance (for RhodamineB) of (100), (110) and (111) NiO and demonstrated that (111) NiO was performing better; Cappus et al. [106] and Kitakatsu et al. [108] showed that hydroxylation occurs readily on the NiO

(111) surface, through surface studies like XPS, LEED and STM. As a proof of this, Zhao and his co-workers demonstrated the energetics (theory vs. experiment) involved in water dissociation on the NiO (111) surface, thereby providing both theoretical and experimental evidences that -OH readily adsorbs on them. Given that, surface hydroxyls/adsorbed molecular water are important intermediates in the catalytic reactions (pollutant degradation/water splitting), the above mentioned proof for -OH adsorption in a ready manner, depicts the role of NiO (111) surface in promoting catalytic reactions.

Although all these studies and material properties recommend NiO as a good photocatalyst, the wide bandgap reduces its light absorption capabilities as a single material and hence it is often used as a co-catalyst. Reports with NiO were demonstrating the increase in degradation efficiency by adopting a nanostructure, as compared to a planar film. Ding et al.[7] prepared NiO nanosheets on carbon fibre cloth (electrochemical deposition) that showed RhB degradation efficiencies of up to 33%, whereas, Zhang et al.[109] prepared planar films with poor efficiencies (<10%). In case of water splitting reactions, NiO is considered as an effective co-catalyst for hydrogen evolution and hence used widely in water splitting processes[110,111]. In addition, owing to its lower stability towards the chemical species (with respect to metal oxide catalysts like TiO_2, ZnO, CrO_2, $BiVO_4$)[112], it is widely used as co-catalysts in pollutant degradation as well.

NiO coupled to TiO_2 as powder heterostructures were shown to completely degrade MO in 25 min[113], whereas NiO and TiO_2 as single material exhibited performances of up to 25 and 60% (in 30 min), respectively[113]. Similarly, ZnO/NiO powder heterostructures completely degraded RhB after 25 min[114], whereas the efficiencies of single materials reached 15 (NiO) and 45% (ZnO). NiO as co-catalyst with other materials like Vanadium Oxide - V_2O_5 (MO degradation - 80% in 100 min), Bismuth Oxide - Bi_2O_3 (Acid Red degradation - $\simeq$60% in 120 min), Carbon Nitride - C_3N_4 (MO degradation - $\simeq$98% in 50 min), Nickel Ferrite - $NiFe_2O_4$ (RhB degradation - $\simeq$90% in 60 min) were not observed to be as effective as with TiO_2 or ZnO. Heterostructures of NiO with metal loading like Silver (Ag), showed efficiencies of $\simeq$98% in 60 min, for the degradation of sunset yellow (not relatively effective).

In all the above mentioned cases, the enhancement in degradation efficiency (compared to single material) was attributed to the charge separation capabilities by adopting a heterostructured material. As an example, the energy band alignment and the charge separation for ZnO/NiO heterostructures is shown in Figure 1.12

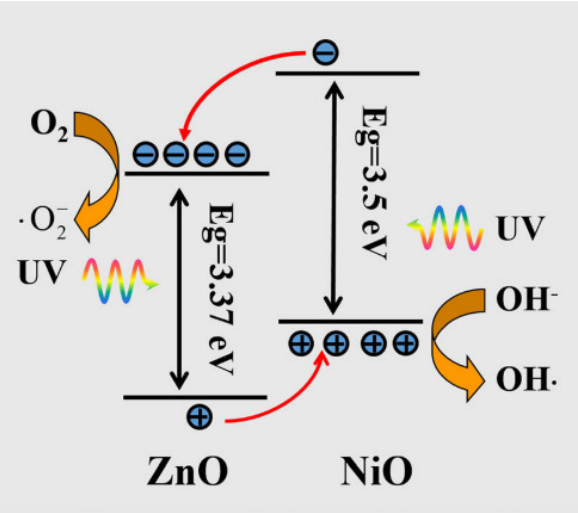

Figure 1.12: Scheme of the energy band alignment between ZnO and NiO.[7]

As per our knowledge, the pollutant degradation of NiO/ZnO thin film heterostructures have not yet been reported. In this context, thin film based, ZnO/NiO heterostructured photocatalysts are investigated in this thesis.

1.6.3. Ruthenium oxide - photocatalyst

Ruthenium Oxide (RuO_2) also belongs to the family of transition metal oxides but shows semi-metallic behaviour, owing to the overlap of the partially filled metal (d orbitals) and oxygen (p orbitals) bands[115,116]. It crystallizes in the rutile phase as shown in Figure 1.13, exhibiting higher thermal and chemical stability[117].

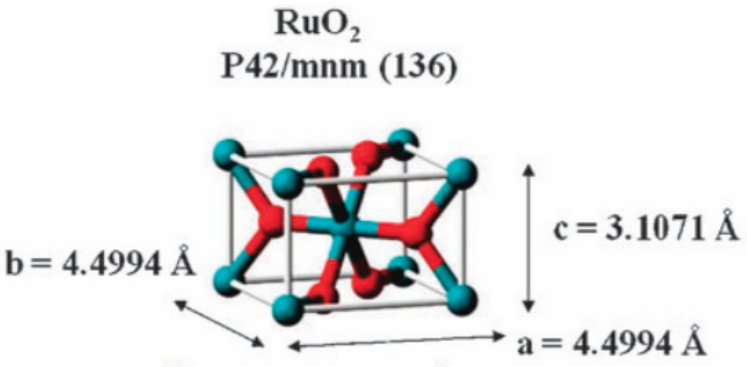

Figure 1.13: Unit cell of the RuO_2 wurtzite structure.[8]

Metal nanoparticles like Silver and Gold (Au) were widely studied for both TiO_2 and ZnO metal oxides and have shown an improvement in the photocatalytic degradation

efficiency. For example, Alshammari et al.[118] prepared Au/TiO_2 and Au/ZnO heterostructures that exhibited $\simeq$ 95% of degradation efficiency for RhB, in 40 and 80 min, respectively; while Su et al.[119] and Kim et al.[120] prepared ZnO/Ag-Ag_2O and Au/ZnO powders which reached over $\simeq$ 90% efficiency for the degradation of congo red (in 80 min) and methylene blue (in 160 min), respectively. In general, adding noble metals will increase the visible light absorption capabilities but will also support charge separation. Additionally, when metal particles like Ag or Au are used, they can behave as electron sinks (i.e, electron acceptors), encouraging charge separation (Figure 1.14a). More precisely, when Au is used, Localized surface plasmon resonance (LSPR, detailed in Section 1.7.2.3) effect (as shown in Figure 1.14b) will take place resulting into hot (highly energetic) electrons generation on continuous light irradiation, helping in the effective charge separation. Therefore, in all the above mentioned reports, better charge separation ability by using metal nanoparticles as co-catalysts, have been attributed to the increase in their performance (in relation to single material). The working mechanism of metal/n-type semiconductor heterojunctions on contact formation and in presence of light irradiation are detailed in Section 1.7.2 and 1.7.3.

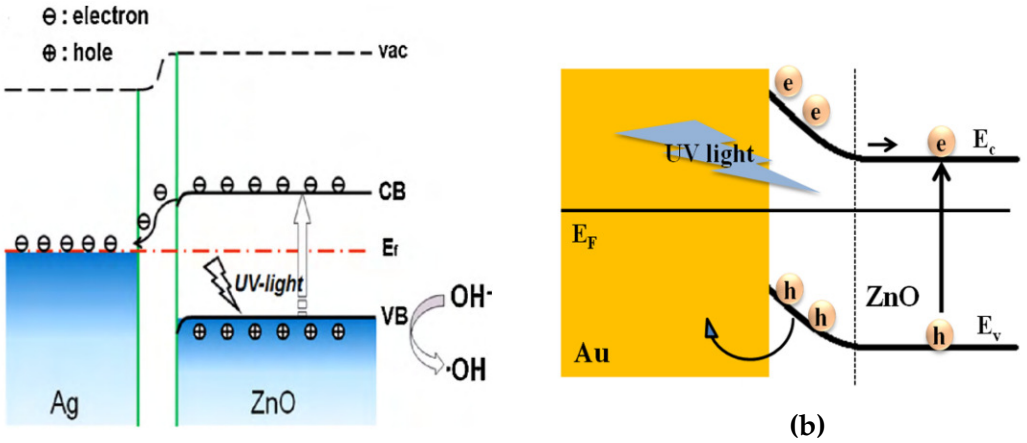

Figure 1.14: Illustration of the plasmonic effect in a metal/n-type semiconductor heterostructure and (a) illustration of charge separation in Ag/ZnO heterostructures[9] and (b) Au/ZnO heterostructures[10].

Similarly, Ag and Au nanoparticle decorated ZnO nanorods were studied by Chang et al.[105], Ren et al.[9] and Wu et al.[95], exhibiting improved performance in pollutant degradation. Ren et al.[9] prepared Ag/ZnO by photodepositing Ag on hydrothermally grown ZnO that reached $\simeq$ 50% MB degradation after 90 min of light irradiation (Single material, ZnO showed $\simeq$ 36% efficiency). Wu et al.[95] detailed the Au/ZnO heterostructures (ZnO by CVD + Au by photosynthesis) and reported $\simeq$ 80% of MO degradation after 180 min of light irradiation. Likewise, Chang et al.[105] reported efficiency of $\simeq$95%, for the degradation of

MO (in 180 mins) using Ag/ZnO heterostructures (ZnO by Photoelectrochemical-Scanning Electrochemical Microscopy [PEC-SECM] and Ag by photosynthesis). Here, special efforts were done to increase the surface area of the thin film by adopting a selective growth method for ZnO which resulted in only $\simeq 15\%$ efficiency, and the same (type of ZnO growth) was attributed to the increase in performance along with the charge separation effect after decoration with Ag nanoparticles. Furthermore, Ag/ZnO and Au/ZnO preparation by hydrothermal [ZnO] + Solution based synthesis, inducing electrostatic force [Ag/Au] was reported by Arai et al.[102]. In this report Ag/ZnO and Au/ZnO was shown to degrade MB 2 and 3 times higher than that of ZnO alone, respectively. As it can be observed, most reports refer to metal/ZnO heterostructures as efficient photocatalysts.

These reports clearly indicate that metal/semiconductor heterostructures perform better in photocatalysis, as compared to single semiconductors. Therefore, RuO_2 could be used as a co-catalyst. RuO_2 has higher chemical stability, ease of nanomaterial processing and also excellent diffusion barrier properties due to which it can perform well as hole and electron transport catalyst[121]. In general, these properties have made RuO_2, a promising candidate for photocatalytic and energy storage applications. RuO_2 Was earlier shown to be a highly efficient oxidation catalyst and hence widely investigated for oxygen evolution reactions[122]. Though there are some studies regarding RuO_2/TiO_2 (as powder materials), its combination with ZnO was reported for the first time in relation to photocatalytic degradation properties only recently (as powders)[115]. Moreover, their interfacial properties in relation to the surface of ZnO scaffold was not reported earlier. Hence, in this dissertation, ZnO/RuO_2 thin film heterostructures are examined for the tunability of interfacial band bending, which could reveal the optimized preparation, thereby the band bending that will eventually be beneficial for photocatalytic applications.

1.6.4. Effects of nanoscale

Any material which measures in the range of 1 - 100 nm, in at least one of its dimensions is usually referred to as nanomaterial and is shown to exhibit excellent properties (with respect to the bulk), being part of almost all 21st century applications. Nanostructured materials are playing a vital role in photocatalytic applications as well and are most often demonstrated to improve the efficiency of the process[101,123]. However, as mentioned earlier, the search for an effective photocatalyst that could be implemented at real-scale and that would satisfy the real-time requirements in terms of life-time and costs is still ongoing. There are handful of reviews that discuss the materials that have been already examined[46,124–126] and possible new potential candidates[127,128] and all of them specify the ultimate importance of nanoscale effects (control over optical properties, charge transfer

abilities and quantum confinement effects), especially for photocatalytic reactions, where surface reactions play a vital role.

In general, for bulk materials, there are only a small percentage of atoms present at the surface, which is why, they are considered to have less surface area and hence less reactive. Whereas, nanostructured materials, due to the smaller size, half or more of the atoms will be present at its surface, thereby increasing the surface area and hence the active sites for the catalytic reactions. One can gain fine control over the electrical conductivity, light absorption, carrier transport and quantum size confinement, properties as required, by tuning the size and shape of the nanoparticles [129–131].

Light absorption - The bandgap of a semiconductor have been shown to vary as function of the particle size and this effect is reflected in the red or blue shift of the absorption edge.

Change in electronic structure - When a material reaches below a critical size, the density of states (electrons) in the energy levels would undergo a systematic transformation (localization of electrons with varying dimensions) as shown in Figure 1.15.

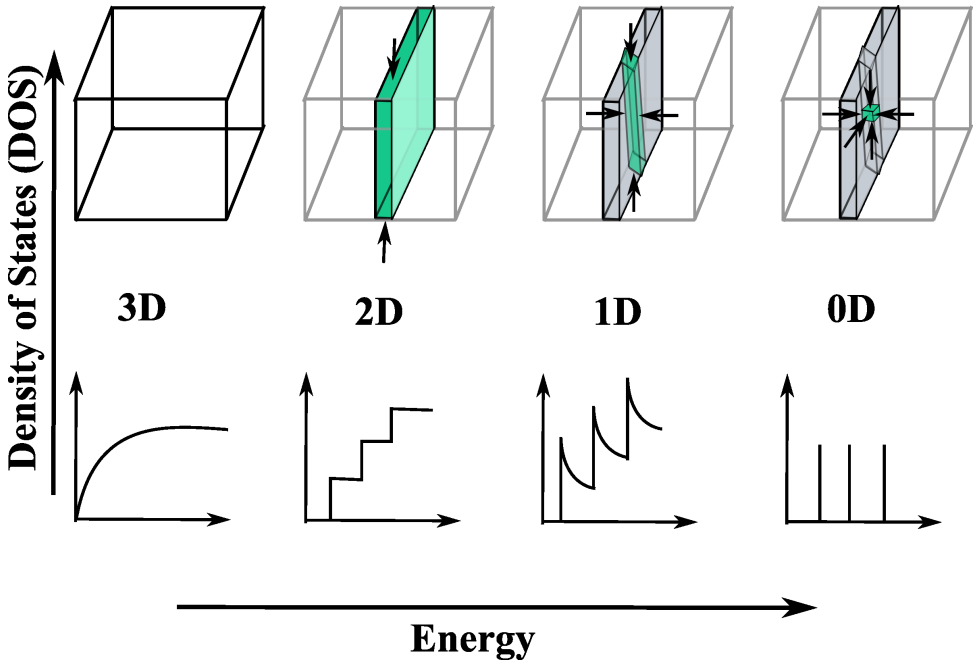

Figure 1.15: Schematic representation showing the concept of dimensionality: in top panel - 3D (bulk semiconductors), 2D (thin film or layer or quantum well, 1D (quantum wire or rod) and 0D (quantum dot) nanostructures; bottom panel - corresponding density of states [DOS] versus energy (E) levels for the corresponding structures.

With 3D structures (non-nano size or microstructure), electrons will be free to move in all the directions. But in case of 2D, 1D and 0D, as the name suggests, the movement of electrons are allowed only in two, one and zero directions, respectively. This is called quantum confinement effect and it is also observed with the wavelength shifts occurring

in the optical measurements like UV-VIS or Photoluminescence (PL). Basically, quantum confinement would mean, that the movement of electrons is confined within the shape and dimension of the material. The extent of quantum confinement regime is dependent on the crystallite size (R) of the material and its relation to the Bohr radius (a_B).

1. when $R \gg a_B$, the confinement is weaker - ex: 2D, quantum wells
2. when $R \approx a_B$, the confinement is said to be moderate - ex: 1D, quantum wires
3. when $R \ll a_B$, the confinement is very strong - ex: 0D, quantum dots

Quantum transport - The confinement of electrons further influence the movement of electrons and holes in presence of phonons or photons, which in turn affects the overall charge transport. The photo induced charge transfer of electrons and hole and eventually the mass charge transfer properties that are observed in powder photocatalyst materials are observed as a result of nanoscale size of the materials. However, charge separation becomes an issue with the use of smaller particles. Therefore, interparticle charge transfer is used by aligning the energy levels of two materials (coupling of two materials) such that electrons and holes are separated in each of them, thereby enhancing the performance in photocatalytic processes. Depending on the space charge region width at the surface or interface (of two materials), the charge transport will be influenced. If the width is smaller, tunnelling might occur, resulting in loss of available charge carriers for redox reactions, and if it is higher than a defined criteria (material size specific, explained in next section), the charge carrier separation and transport will be effective, thereby photocatalytic efficiency will be enhanced.

However, in thin films, the mass charge transfer is reduced due to immobilization. Though, 1D materials that provide efficient charge transport are capable of overcoming this hindrance, the challenge lies in controlling the recombination at the defects, which arise with higher surface area and smaller particle size. Therefore, attaining both an efficient charge separation and control over defects at the interface are key factors in achieving an efficient heterostructure that could perform better in photocatalytic applications.

1.7. Semiconducting metal oxide based heterostructures

A typical photocatalytic process involves three vital charge kinetics steps as follows: i) charge carrier generation, ii) effective charge transfer and separation and iii) effective charge consumption[58]. They are interdependent with each other and compromising

any of these steps will result in slower kinetics, thereby affecting the efficiency. Therefore, one needs to pay closer attention to the overall structure engineering (surface + interface + energy band) of the photocatalyst while designing it[11]. With the study of a plethora of standard materials like TiO_2, ZnO and WO_3 and also after the emergence of new catalytic materias (with well defined nanostructures), it is widely agreed that the single material does not possess all necessary properties to successfully conduct the photocatalytic reactions[41,55,132]. This led to the path towards involvement of more than one material, in photocatalysis applications. Several metal oxides like TiO_2, ZnO, WO_3, $BiVO_4$, Fe_2O_3, SnO_2, ZrO_2 were already studied for their photocatalytic capabilities in the form of single materials or embedded in heterostructures, either as powder or thin films[113,133,134].

There are several major reviews (by Kling et al.[135], Lee et al.[46], Hamid et al.[52], Adnan et al.[136], Qi et al.[137], Gu et al.[98], Kumar et al.[99]) dedicated in specific to the ZnO based heterostructures (powder materials) as photocatalysts, which gives insights into the understanding about material, morphology, optical and electrical properties, photocatalysis mechanism and their performance. Previous studies have established the necessity for modification to single material, to reduce recombination losses and increase photostability in case of ZnO. In the decades of research, heterostructures that can provide visible light utilization or effective charge separation or even both, have been explored widely, for reducing the recombination issues. The challenges in attainig fine control over dopant concentration and optimal bonding with co-catalysts in a budget friendly synthesis techniques, are still prevailing (even in case of powders). However, by adopting heterostructures, it has been well established (in case of powders) that efficient charge separation, reduction in charge carrier recombination, and better interfacial charge transfer could be attained, after careful optimization. In spite of achieving better performing heterostructures, there are still problems like durability, reaction selectivity, long-time performance etc, that are still need to be addressed.

However, all the above mentioned conclusions from powder materials could not be directly implemented for thin film based photocatalysts, as it holds greater complexity in degradation reaction mechanism, as compared to powder materials. Several of the recent reviews (in the last 4 or 5 years) have discussed and stressed the importance of nano-sized heterostructured photocatalysts for photocatalytic applications[14,58,124,138,139]. Their discussions lie in the need for careful design and control over the surface and interface parameters, in order to attain optimization of charge kinetics and thereby the photocatalytic performance. When two materials are coupled, an interface is a region where charge transfer occurs between the two components and the transfer efficiency is greatly governed by the interfacial properties attained. Heterostructures can take different forms as exemplified in Figure 1.16.

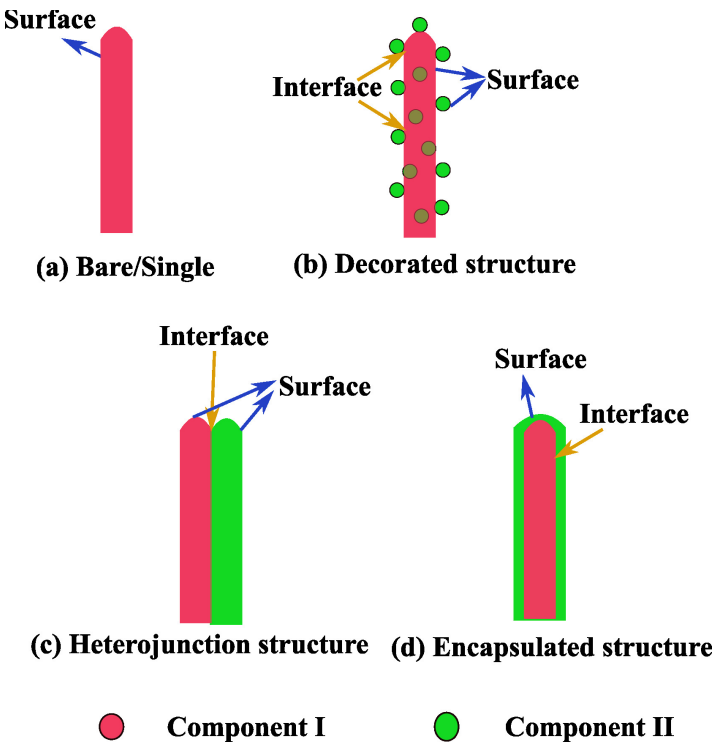

Figure 1.16: Schematic illustration of interfaces and surfaces in one dimensional architectural structures.

1. **Homogeneous** - A bare/single semiconductor ((a) in Figure 1.16), will possess a spatial charge separation at its surface

2. **Decorated structure** - Component I will be synthesized or deposited on Component II ((b) in Figure 1.16) in such a way, that it will result into an incomplete coverage leading to multiple interfaces. Thereby the surface of both the components will participate in the photocatalytic reactions; involves more than one surface or interface

3. **Heterojunction structure** - This structure is formed when the nucleation and growth of Component I takes place at a particular site (whereas in decorated structures, number of nucleation sites will be more) on Component II ((c) in Figure 1.16); involves one surface for each component and one interface at their junction

4. **Encapsulated structure** - It is difficult to attain this structure, where Component I is completely covered by Component II ((d) in Figure 1.16); involved surface and interface are same as in case of heterojunction structures; also called as core-shell structure; it is desirable, if Component I suffers from chemical or photo instability

These information clearly indicate that the attained surface and interface structures on forming a heterostructure will be dependent on the architectural structure that will be obtained from the material preparation. Furthermore, this would mean that the charge kinetics in-

volved in photocatalytic reactions will differ based on the surface and interface structures that have been attained [11]. Hence, surface and interface engineering are two important factors to be understood and explored, in order to design an effective photocatalyst.

Surface Engineering - There are several surface related parameters that govern the performance of a photocatalyst (surface on which reactions take place): surface composition, phase, facets, area, pores, vacancies, band bending and particle size. This shows that though much of emphasis is basically given for improving the surface area, it is not the sole factor that determines the performance of a photocatalyst.

1. **Surface area** (influenced by particle size [41]) and **pores** are closely related where, presence of pores can increase the area [11] and allows increase in adsorption properties

2. **Surface composition and facet** regulate the adsorption of chemical species and activation of redox reactions but also influences the light absorption and reactivity of the material [58]

3. **Surface vacancies -** The presence of vacancies results into an coordinately unsaturated surfaces that attracts impurities in the atmosphere (water, carbon dioxide) to form dangling bonds (that are prone to capture and trap charge carriers). This is known to influence the surface catalytic reactions because they can occur readily on coordinately unsaturated surfaces than on a perfect surface. Moreover, the type of vacancies (metal or oxygen, in case of metal oxides) and the region where they lie in the material (shallow/surface or deep/bulk) determine the surface reactivity in catalytic reactions. Photocatalytic activity being a surface reaction, have been shown to be enhanced, when the concentration of surface defects are higher than the bulk defects. This is because, charge carriers trapped at the surface are available for the interaction with the chemical species, whereas, charges trapped at deep levels hinders the further travel of charge carriers to the surface, thus cannot participate to the reactions [58].

4. **Surface band bending** is evident when the doping level at the surface is different from the one in the bulk, as a result of surface termination and the resultant adsorption of impurities on the surface. In the presence of impurities or defects, an n-type (p-type) material will have upward (downward) band bending, driving the holes (transferring electrons) for oxidation (reduction) reactions. For photocatalytic applications, an upward band bending is desired as it will allow the facile transfer of holes to the aqueous media and form the active hydroxyl radicals.

The detailing of the effects due to surface parameters on surface reactions display the importance of optimizing the surface or surface engineering, before the interfacial prop-

erties are optimized.

Interface Engineering - All the above mentioned parameters are need to be adjusted as well, with respect to the interface between the two materials.

1. **Interface composition** is dependent on the composition of original component (component I) for light absorption and the formed interface for charge transfer that determines the surface reactions

2. **Interfacial area -** An efficient charge transfer is attained with a large interfacial area

3. **Interface facet** Charge transfer rate is dependent on the atom arrangement (facet) at the surface of both the components

4. **Interface defects -** In contrary to the surface defects that have the probabilities for enhancing the performance of a photocatalyst, interface defects allows recombination of photo generated charge carriers, hindering the interfacial charge transfer and thereby the performance

5. **Interfacial band bending -** Its orientation (upward/downward) is dependent on the work function of the materials involved, where electrons and holes will migrate to the material with more positive CB and more negative VB level, respectively, through interfacial charge transfer and is affected by the degree of band bending attained

Among them, the interface defects are the most impinging on the efficiency of the photocatalytic process, as they promote the recombination of photogenerated charge carriers. Moreover, the parameters involved in surface and interface engineering are interlinked, because the improvement in overall efficiency is possible only when effective interfacial charge transfer is attained, which is dependent on the optimization of surface (scaffold material)[11]. The relationship between both factors are represented in Figure 1.17. For example, as a bare or scaffold material, defects might enhance the photocatalytic activity ((a) in Figure 1.17), but its presence while forming an interface with another material is detrimental, as this will result into interface defects ((b) in Figure 1.17). In addition, effective charge consumption should also happen and is dependent on the interfacial charge transfer. If it is ineffective, accumulation of charge carriers will occur on both sides ((c) in Figure 1.17), weakening the attained band bending and thereby the photocatalytic performance.

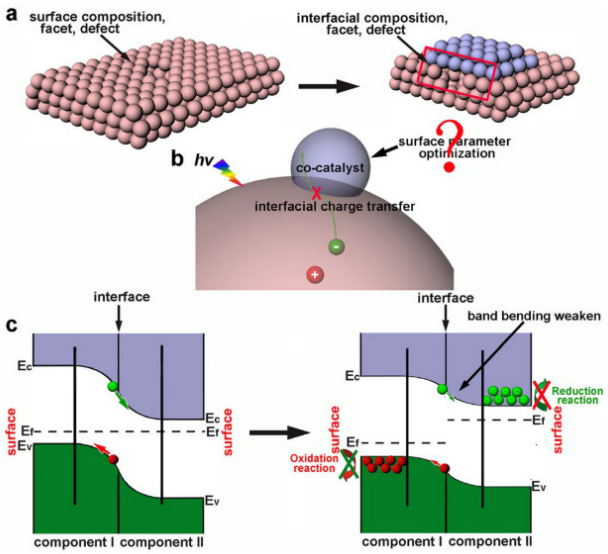

Figure 1.17: Schematic illustration of the relationship between surface and interface parameters in photocatalysis:(a) presence of defects on the surface of a single material that leads to defectious interface;(b) the inefficient interfacial charge transfer that limits the efficacy of optimizing surface parameters and (c) the inefficient surface charge transfer and consumption that weakens the degree of interfacial band bending, in presence of external factor like water/electrolyte.[11]

Theses overall observations emphasize that tailoring the surface and interfacial properties of the nanoscale heterostructures is a potential factor that needs to be explored in order to optimize the design of the photocatalyst.

1.7.1. Classification of heterostructures or heterojunctions

There are several categories of heterostructure or heterojunctions that can be formed: (i) semiconductor-semiconductor, (ii) semiconductor-metal, (iii) semiconductor-carbon and (iv) multicomponent heterojunction[132]. In general, semiconductor-semiconductor heterojunctions can be either p-n or non p-n heterojunction systems, which can lead to the development of three types of band alignment: straddling, staggerered and broken-gap[13], as shown in Figures 1.18a to 1.18c. The band alignment usually occurs based on the band energy levels of the chosen semiconductors, where straddling type results in accumulation of both the charge carriers in one semiconductor only (Figure 1.18a), staggered type is capable of separating electrons and holes in each semiconductor (Figure 1.18b) and the broken-gap does not allow charge migration and separation (Figure 1.18c). Therefore, the staggered type is capable of enhancing the charge migration and separation and consequently the photocatalytic efficiency.

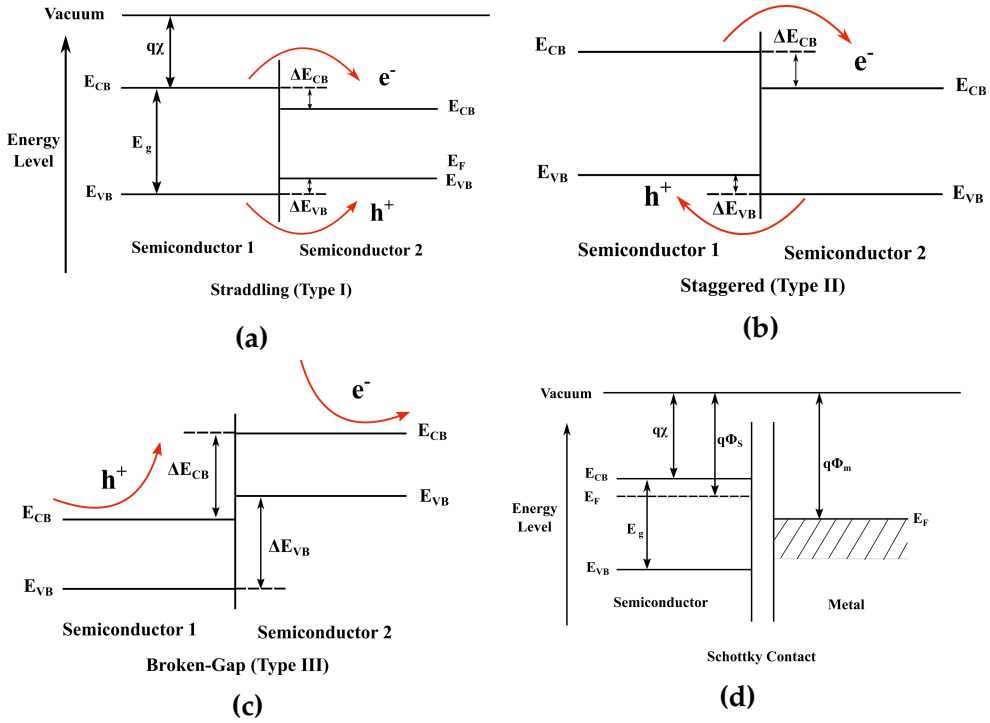

Figure 1.18: Schematic illustration of band alignment for semiconductor/semiconductor heterojunctions (a) straddling, (b) staggered and (c) broken-gap; and (d) metal/ semiconductor contact. △CB and △VB stand for the Conduction and valence band offset, qχ is the energy needed to move the charge from CB into vacuum or infinity, χ being electron affinity and qΦ is the energy needed to move electron from the Fermi level (E_F) to infinity, Φ being the workfunction. In (d), Φ_m - metal workfunction and Φ_S - semiconductor workfunction.

The semiconductor-metal heterojunctions are also known to enhance the charge separation by forming a Schottky barrier at the interface (Figure 1.18d), which can significantly reduce the charge carrier recombination. The commonly explored junction is metal/n-type semiconductor, which is capable of enhancing the light absorption and quantum efficiency. These characteristics in turn could greatly enhance the photocatalytic efficiency of such heterojunctions.

The semiconductor-carbon heterojunctions involves the coupling of semiconductors with carbon materials (most often carbon nano tubes or graphene) and are known to enhance only the charge separation capabilities[132]. At the same time, multicomponent heterojunctions involve coupling of one semiconductor with two or more visible light components, with the same advantages as in bi-component systems mentioned above, except that more than two materials are available for charge transfer and light absorption processes[132]. However, the involvement of more than two materials, raises the difficulty in understanding the underlying mechanisms and designing effective heterostructures. Overall,

Semiconductor-Semiconductor, Semiconductor-Metal and multicomponent heterostructure formations are more attractive than Semiconductor-Carbon junctions, because the coupling of semiconductors with another semiconductor or metal can enhance both light absorption and charge transfer kinetics (effective charge separation, rapid charge transfer, increased lifetime of charge carriers) of the material.

1.7.2. Band bending

The band bending concept was first introduced by Mott-Schottky[12] to describe the rectifying behaviour of the metal-semiconductor junction, which was later on applied for the association of any other types of hybrid phases that involved a difference in the Fermi level or the redox potential. Whenever a semiconductor comes into contact with any phase (i.e. liquid, gas, or metal) that exhibits a different Fermi level or redox potential, the charge carriers will be redistributed at the interface, in such a way that the chemical potential between the semiconductor and the second phase are levelled, resulting into a space charge region[12,140] and band bending at the interface.

In principle, the electric field in the space charge region that occurs at the interface, encourages the spatial separation of the photogenerated charge carriers (electrons and holes) and consequently reduces the recombination rate. But, the width of the space charge region governs the charge transport and tunnelling might occur if the space charge region is not optimum, which in turn will degrade the performance of photocatalytic activity. In case of smaller particles, the depletion width or magnitude of band bending is controlled by three parameters, namely the particle size, the donor concentration and the relative dielectric constant[12]. The band bending is directly proportional to the particle size and dopant concentration (are widely discussed) but inversely proportional to the material's dielectric constant[12].

Quintana and his co-workers[141] studied ZnO and TiO_2 of similar size and demonstrated that lifetime of photogenerated electrons are higher in ZnO (than TiO_2), attributing it to the presence of higher band bending, hence a reduced recombination rate. Furthermore, the significant band bending in ZnO was attributed to its smaller dielectric constant (≈8), as compared to that of TiO_2 (≈50 - 100)[12], thereby revealing the relation between dielectric constant and band bending. The depletion width depends on the donor concentration and it influences the photon penetration depth (as represented in Figure 1.19), in turn will affect the photocatalytic efficiency.

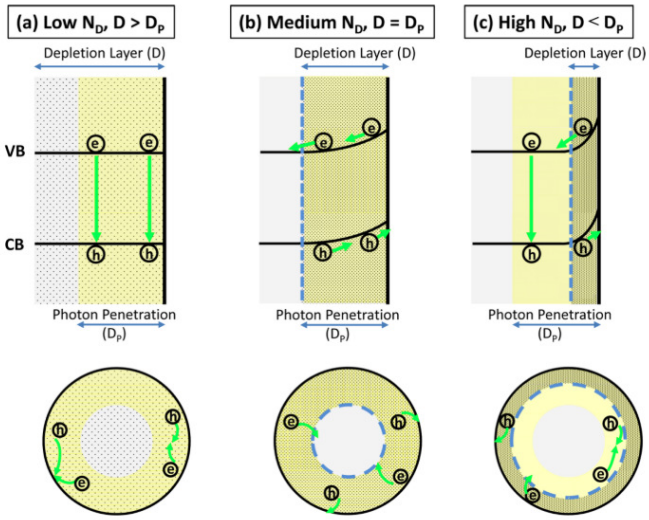

Figure 1.19: The effect of dopant concentration (N_D) on the band bending and photogenerated carrier behaviour in semiconductor nanoparticles for (a) lower donor concentration where depletion layer length (D) > photon penetration (D_P); (b) medium donor concentration where D = D_P; (c) higher donor concentration where D < D_P. In panel c, where extreme upward band bending exists because of high N_D, holes are efficiently transferred to the particle surface, thereby partial enhancing in photocatalytic process. [12]

For a lower donor concentration, the depletion width [D] becomes greater than the photon penetration depth [D_P] (D > D_P), leading to recombination of photo induced charge carriers in bulk and/or surface and thus improved photocatalytic efficiency cannot be expected (Figure 1.19a). At an optimized level of donor concentration, the photon penetration depth will equalise that of the depletion width (D = D_P), hence effective charge separation is expected, thereby a decrease in the recombination rate and maximum photocatalytic efficiency can also be expected (Figure 1.19b). Concurrently, for excess donor concentration (Figure 1.19c), the depletion width will be smaller than the photon penetration depth (D < D_P), limiting the charge separation effect only to the depletion region. In such a case, hole transfer to the surface can occur effectively, but the electron lifetime in the bulk will decrease, leading to an increase in the recombination and hence a drop in the photocatalytic efficiency.

Based on the second phase that is involved, the band bending can be classified as: (i) surface state and adsorption induced band bending, (ii) semiconductor(n-type)/ semiconductor(p-type) junction; (iii) metal/ semiconductor junction; (iv) semiconductor/ electrolyte interface and (v) field-effect-induced band bending [12]. In relation to the materials and applications involved in this thesis, the first four types of band bending are discussed further.

1.7.2.1. Surface state and adsorption induced band bending

In case of a clean or ambience exposed semiconductor, due to termination of lattice periodicity at the surface or due to contamination with impurities (and the resultant dangling bonds like hydroxyls), surface states may exist. These surface states can induce band bending as illustrated in Figure 1.20 for n-type and p-type semiconductors respectively.

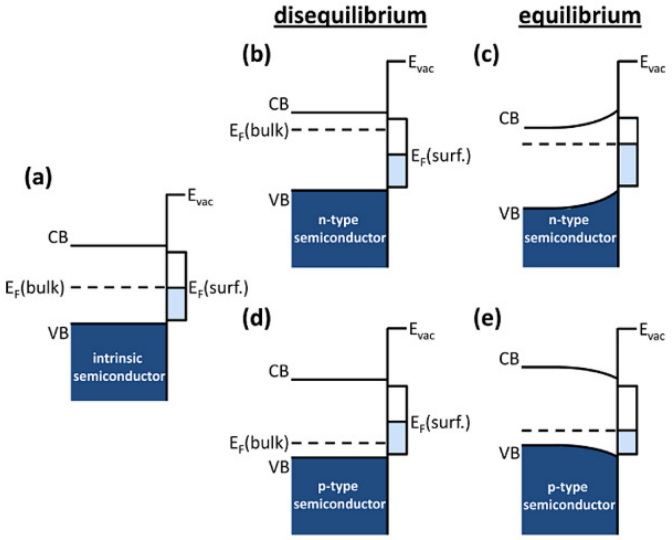

Figure 1.20: Schematic of the electron energy levels near the surface of a clean semiconductor (a) undoped (intrinsic) semiconductor; (b) disequilibrium and (c) equilibrium between n-type bulk and its surface; (d) disequilibrium and (e) equilibrium between p-type bulk and its surface.[12]

For an intrinsic semiconductor (undoped), the Fermi level of the bulk (E_F(bulk)) will be located at the midgap that occurs at the same level with the surface Fermi level (E_F(surf)),(Figure 1.20a), and hence the bands will be flat. But on disequilibrium i.e, on doping, E_F(bulk) $>$ E_F(surf) or E_F(bulk) $<$ E_F(surf) for n-type and p-type semiconductors, respectively. This will result into charge transfer from bulk to surface, until equilibrium is attained, giving rise to an upward (n-type) or downward (p-type) band bending, as shown in Figure 1.20a and 19b, respectively. Usually, the density of surface states are higher than that in the bulk and hence the Fermi level is pinned by surface states, an effect called Fermi level pinning[12].

1.7.2.2. Semiconductor/semiconductor (p-n) junction

In relation to the subject of interest in this thesis, band bending at p-n heterojunction alone is discussed here. When a p-type semiconductor is brought into contact with an n-

type semiconductor, diffusion of electrons and holes will take place resulting into the space charge layer and the development of an internal electric field, as shown in Figure 1.21. A p-n heterojunction is often the staggered type and allows the efficient spatial charge separation. In such a heterostructure, the semiconductor with high E_F (low work function) will initiate the transfer of electrons and the one with low E_F (high work function) will lose the holes, leading to Fermi level equilibration (Figure 1.21 right side)[14]. Near the interface, the n-type semiconductor will be depleted of electrons and the p-type semiconductor of holes. This charge separation leads to the formation of an internal electric field that prevents the electron hole recombination.

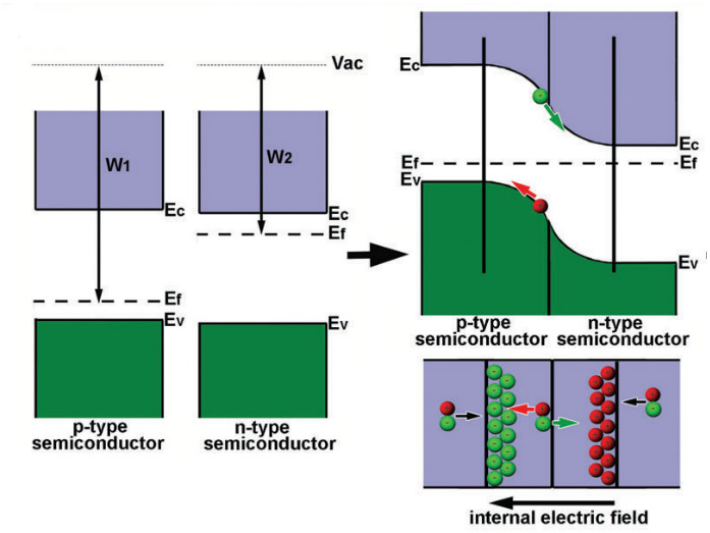

Figure 1.21: Schematic band diagram showing showing band bending at p - n junction.[13]

The stronger the internal electric field the higher the enhancement in electron-hole separation. Hence, p-n heterojunctions (among semiconductor/semiconductor heterojunctions) are widely used in photocatalytic applications.

1.7.2.3. Metal/semiconductor contact

At the interface of a metal and semiconductor materials, electrons will flow from the material with lower work function to the one with higher work function, until the equilibrium is attained (Figure 1.22a). The ideal situation is when the metal work function is higher than that of the semiconductor[14] (Figure 1.22a left side), to enable efficient charge transfer and separation. Given that most noble metals, have higher work function than the n-type semiconductors and smaller than the p-type counterparts, the metal/n-type semiconductor is the ideal combination. In this case, electrons flow from the semiconductor to the metal leading to the formation of a depletion layer on the semiconductor side.

When the semiconductor work function is higher than that of the metal (Figure 1.22a, right side), the electron flow will be inversed and an accumulation layer will be formed on the semiconductor side.

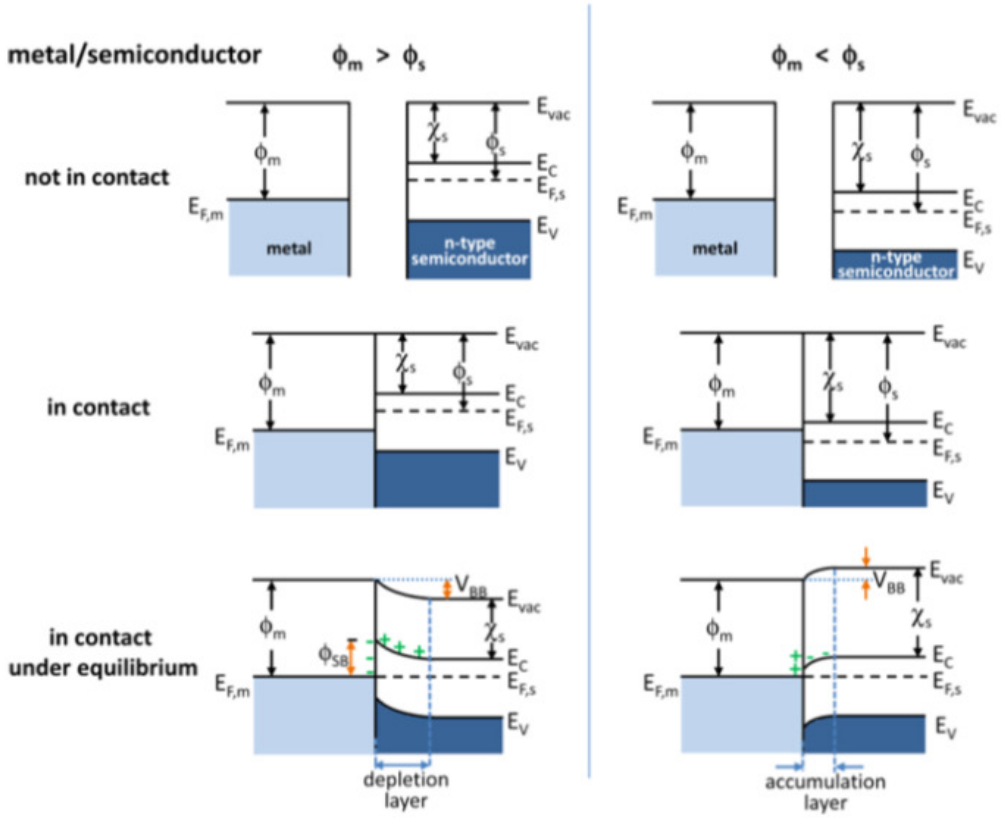

(a)

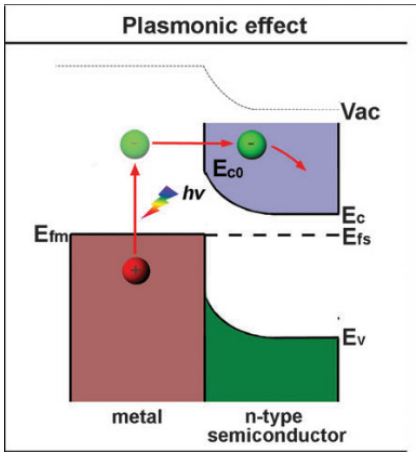

(b)

Figure 1.22: (a) Energy band diagrams of metal/n-type semiconductor junctions. E_{vac} - vacuum energy; E_c - energy of conduction band minimum; E_v - energy of valence band maximum; Φ_m - metal work function; Φ_s - semiconductor work function; χ_s - electron affinity of the semiconductor[12]; (b) Schematic band diagram illustrating the plasmonic hot carrier effect in the hybrid structures between metal and n-type semiconductor[14].

In the first case, the Schottky barrier formation will enable the metal to possess excess negative charges and the semiconductor to have excess positive charges, preventing the charge carrier recombination. Due to the high density of electrons in the metal, no further changes can occur in its E_F and only the band edges near semiconductor surface will modify with the bending due to the increase in hole density. These type of heterojunctions also benefit from the plasmonic effect (when the plasmonic material is irradiated with light, with a frequency matching that of oscillating surface free electrons, strong localized electromagnetic fields will occur due to the collective oscillation of free electrons, also called as localized surface plasmon resonance effect, (Figure 1.22b), which will significantly improve the charge kinetics [14].

Normally, when the semiconductor is irradiated with an energy higher than the bandgap, an electron is promoted to the CB (leaving behind a hole in the VB) and finally transferred to the metal. When, only the metal is irradiated, the induced surface plasmon can excite the electrons to higher energy state (from here, the name is "hot electrons"), higher than the CB minimum of the semiconductor, possibly allowing their transfer to the semiconductor. Furthermore, the backflow of electrons to the metal will be hindered with the presence of an efficient Schottky barrier. The effective charge carrier separation (Schottky contact) and improvement in charge kinetics (plasmonic effect) provides a fruitful combination, which is often required for an enhanced photocatalytic performance.

1.7.2.4. Semiconductor/electrolyte interface

When a semiconductor or photocatalyst is brought into contact with an electrolyte (for eg, water containing organic pollutants), due to the differences in the electrochemical potential levels, charge transfer will occur between them until equilibrium is achieved [140], leading to the formation of a space charge layer formation at the interface. As a result, the semiconductor will be charged positively at the surface and the negative species in the electrolyte will compensate the change. The underlying mechanism for the bending in a semiconductor/electrolyte interface is similar to that of metal/semiconductor junction. The formation of the space charge region and the resultant band bending depends on the Fermi level position of the semiconductor with respect to the electrolyte redox potential.

When the Fermi energy of the semiconductor lies in equilibrium with the redox potential of the electrolyte solution, no net charge transfer will occur and hence no space charge at the interface. This corresponds to the flat band condition (Figure 1.23, middle).

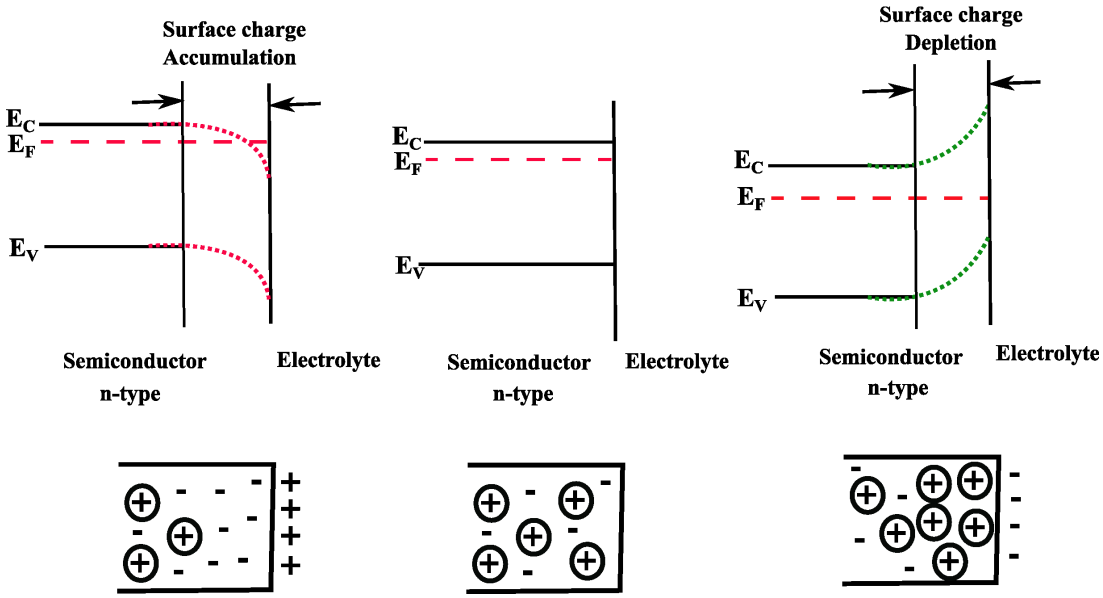

Figure 1.23: Schematic diagrams showing the energy levels (top panel) and charge carrier densities (bottom panel) for the n-type semiconductor surface/electrolyte interface; Flat band condition (middle); downward band bending (left side) and upward band bending (right side) are illustrated, for an n-type semiconductor in equilibrium with an electrolyte.

When the Fermi level of the semiconductor is lower than the electrolyte redox potential, accumulation layer occurs as shown in Figure 1.23 (left side). As a result of charge redistribution, negative charges will accumulate at the semiconductor surface and positive charges on the electrolyte side. In most of the cases, the Fermi level of an n-doped semiconductor is usually higher than the redox potential of the electrolyte, due to which the depletion of negative charges occurs in the semiconductor and hence upward band bending. Therefore, positive charges exist at the surface of semiconductor and negative charges at its interface (Figure 1.23, right side).

Among the above mentioned situations, depletion layer formation at the semiconductor/electrolyte interface plays a crucial role when charge separation occurs after the light irradiation. The built-in (or internal) electrostatic field generally drives the charge carrier kinetics and thereby will separate the photo generated charge carriers. For an n-type semiconductor, the direction of the field is such that holes migrate to the interface where they will undergo the chemical reaction (targeting the pollutants) and the electrons will move towards the bulk part of the semiconductor.

1.7.3. Charge transfer upon light irradiation

As mentioned earlier, the built-in electric field, plays a crucial role in driving the charge kinetics of the semiconductor upon light irradiation and it occurs differently for bare semiconductor and heterostructures (semiconductor/semiconductor and metal/semiconductor), owing to the differences in their surface and interface properties. The occurrence of charge transfer in bare semiconductor (n-type), semiconductor/semiconductor and semiconductor/metal type heterojunctions under light irradiation is shown in Figure 1.24. It is well known that bare semiconductors suffer from light harvesting, high probability of charge carrier recombination and inefficient charge consumption. However, with the improvement in synthesis procedures and material downscaling and with the help of facet or surface engineering, there is enhancement in bare semiconductors. As shown in Figure 1.24a, on light irradiation, the electrons will be depleted from the surface (transferred to electrolyte in case of photocatalysis reaction), resulting into the upward band bending, in case of single n-type semiconductor. As a result, the holes trapped at the semiconductor will participate in the oxidation reaction. However, spatial charge separation effects are significantly weaker in the bare semiconductors, hence heterostructures are highly desirable.

Facet engineering (presence of various crystal facets due to surface states [variation in atomic arrangement] and surface adsorbates [termination of bonding networks]) will influence the material interaction with acceptors or donors and hence the potential difference and band bending development [14]. For example, when the outer surface is polar (as in case of ZnO nanorods) the photocatalytic performance will be enhanced, due to the presence of a dipole moment and thus a built-in electric field which already enables the separation of photogenerated charge carriers (Figure 1.24b).

Among the semiconductor/semiconductor heterojunctions, the staggered type (Figure 1.24c) that consists of a p-n heterojunction is the most capable of enhancing the photocatalytic performance, on grounds of large difference in work function and potentials between the n-type and p-type semiconductors. With the formation of p-n heterojunction and diffusion of charge carriers, an internal electric field builds up at the interface. Upon light irradiation, the internal electric field will drive the electrons and holes to the conduction band of n-type and valence band of p-type semiconductors, respectively [93].

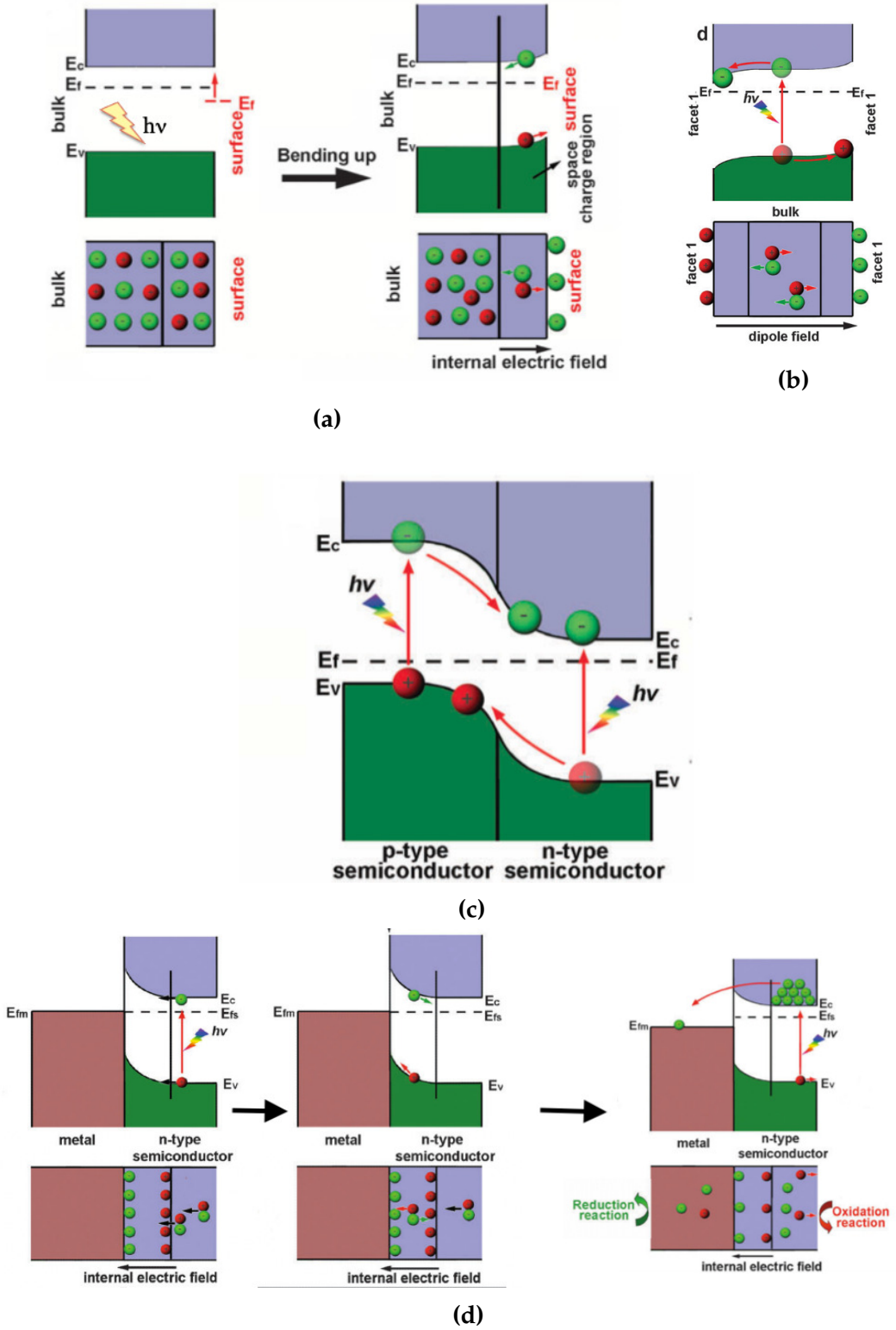

Figure 1.24: Schematic illustrating the processes of charge separation and transfer driven by (a) bare n-type semiconductor surface, (b) bare semiconductor with polar surface, (c) p-n semiconductor heterojunction and (d) metal/n-type semiconductor Schottky junction. (a) and (d) were adapted from ref.[14], (b) and (c) were reproduced from ref.[14].

In case of metal/semiconductor heterojunctions, the charge redistribution results into the formation of internal electric field at the interface (Figure 1.24d). On light irradiation, the internal electric field will cause the migration of the photo-generated electrons and holes, to the bulk of semiconductor and to the metal, respectively (Figure 1.24d, left side and in the middle). This enables the separation of photo induced charge carriers but on continuous photo-irradiation on the semiconductor, the electrons accumulated in the semiconductor will become "hot" enough to be transferred to the metal, called hot carrier generation (Figure 1.24d, right side) and can participate to reduction reactions. Furthermore, the electron drift from metal to semiconductor, i.e, the reverse flow will be prevented by the Schottky barrier. Instead, the holes will migrate to the surface and participate to the oxidation reactions. Similarly, when a metal like Au is used as a conformal coating and with its the continuous light exposure, it is no more an electron sink (as is the case at the beginning of light exposure), because with hot electron generation, the electrons accumulated in metal will be transferred to the semiconductor and the subsequent processes as detailed for continuous irradiation of semiconductor will take place here as well. Overall, the presence of a plasmonic effect (detailed in Section 1.7.2.3) will provide other advantages like extension of the light absorption range, excitation of more electron-hole pairs in the semiconductor, acceleration of the charge transfer due to the Localized surface plasmon resonance (LSPR) and the enhancement in reactant adsorption due to dipole-dipole interactions [14].

Most importantly, it is worth to mention that in both semiconductor/semiconductor and semiconductor/metal heterojunctions, the presence of an internal electric field only guarantees the charge separation capabilities of the corresponding material and that charge transfer from the interface to the bulk or inside the bulk, depends on the potential difference between the two materials. For the charge kinetics to be enhanced, it is crucial to attain a heterostructure that will have migration direction of electrons and holes for charge separation in accordance with the charge transfer direction that occurs outside the space charge region [14]. This could be effectively attained in p-n and metal/n-type semiconductor heterojunctions, whereas in case of straddling or n-n heterojunctions, the above mentioned processes take opposite directions, thereby suppressing each other.

1.8. ZnO nanorods as scaffold and their heterostructures

As described in Section 1.4, thin films are considered promising candidates for photocatalytic activities. 1D nanostructuration is an effective method for improving surface area and the charge transport. Hence, the thesis is focussed on using ZnO nanorods (ZNR) as a single (or scaffold) material or embedded in semiconductor/semiconductor and

semiconductor/metal heterostructures, for the degradation of dyes in water. Though there are a plethora of studies regarding ZnO as powder photocatalysts [46,99,101], for both single and heterostructured materials, reports on ZnO thin films for pollutant degradation are not many.

In general, many studies on ZNR films were widely focused on sensor applications and less on pollutant degradation [142–145]. One of the reasons is the issue of photocorosion of ZnO on longer exposure to light source, and the other is the lack of a driving force for the effective separation of charge carriers [146,147]. Heterostructure formation could also protect the ZNR, in addition to improving the charge separation, thereby enhancing the lifetime of the material [148]. So far, in case of powder materials, various metal oxide semiconductors including TiO_2, $BiVO_4$, Fe_2O_3, SnO_2, CdS, Cu_2O and NiO have been used as second material in heterostructure formation with ZnO either for pollutant degradation or water splitting applications [46,99]. Though these studies have given insights into optimal parameters for the preparation of stable powder heterostructures, these evidences could not be directly implemented for thin film based photocatalysts [18], owing the complex nature it possess and also to the different pollutant adsorption mechanism. Moreover, even for powder materials, there is lack of in-depth studies correlating the surface and interface parameters, with the pollutant degradation activity [14].

Therefore, design of thin film based photocatalyst (scaffold and heterostructures) with insights into the surface and interfacial properties are elusive and previous reports on single ZnO thin films and heterostructures will be discussed in this section.

1.8.1. Scaffold surface treatment

Metal oxides are generally well known for possessing defects such as oxygen vacancies which are highly reactive [149] and play a major role in photocatalysis process [14]. It is important to get rid of the vacancies in the scaffold material, before the heterostructure formation, since it greatly influence the interface quality.

ZnO being an attractive semiconductor for numerous applications, its surfaces and interfaces have been systematically studied since five decades ago by G. Heiland on ZnO surface conductivity under ultrahigh vacuum (UHV) conditions [150]. Most often studies were carried out on single crystals, in relation to the electronic or optic oriented applications [135,151,152]. Since then, there were extensive studies on them both experimentally and theoretically, that led to the basic understanding of ZnO surfaces. ZnO being an n-type semiconductor, its surface could be tuned with oxygen or hydrogen treatment to vary the

doping levels at its surface as shown in Figure 1.25.

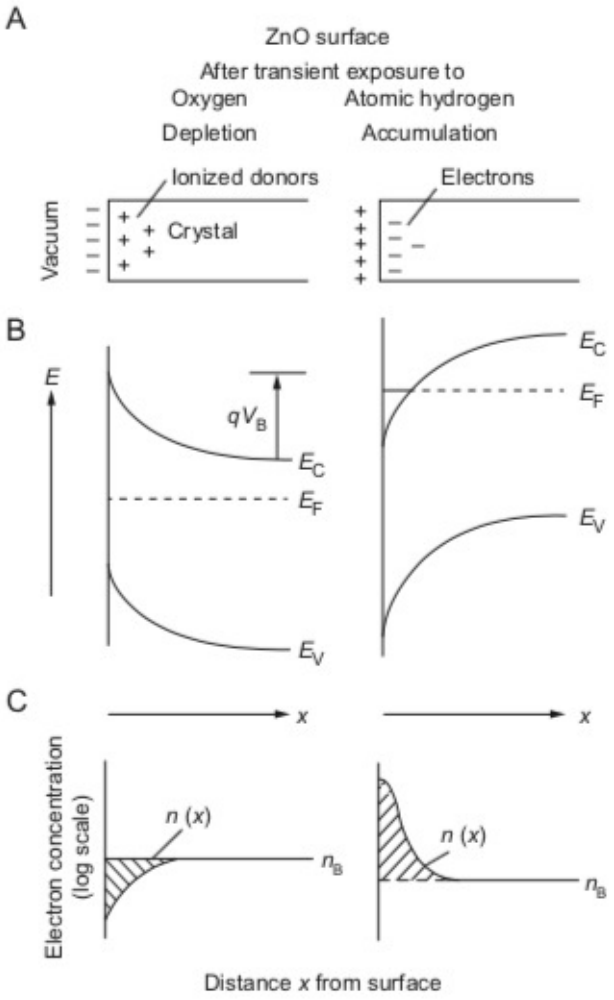

Figure 1.25: ZnO surface (A) charge distribution, (B) band bending, and (C) electron concentration before and after transient exposure to oxygen and atomic hydrogen. Oxygen depletes the surface of electrons, while atomic hydrogen induces electron accumulation.[15]

Oxygen vacancies that have lower formation energy[153,154] were often attributed to the n-type conductivity in ZnO and are believed to influence the optical, semiconducting and also catalytic properties. The formation of (through annealing in presence of hydrogen/argon/nitrogen[151,155,156]) or filling up of oxygen vacancies (through annealing in presence of oxygen[155–157]) is supposed to influence the catalytic reaction, due to the different band bending induced at the surface (Figure 1.25).

For example, Tu et al[153], had recently demonstrated that performing the annealing (under a fixed gas flow rate and temperature) step on as-grown (sol-gel method) ZnO nanorod film under different atmospheres like O_2 and N_2 have influenced the defect levels in the material. Through X-ray photoelectron spectroscopy (XPS), Photoluminescence (PL)

and Mott-Schottky (MS) analysis, they were able to show that the annealing in N_2 increased the oxygen vacancy related defects whereas the O_2 annealing had a reverse effect. Similarly, Gheisi and his co-workers[156], employed Auger Electron spectroscopy (AES) and PL to demonstrate that, upon stepwise annealing (cooling between each steps) of ZnO nanopowder, deep level traps were formed (increase in deep level emission with exhibition of yellow emission through PL and upward band bending with depletion of electrons at the surface through AES), under oxygen rich conditions. Whereas under vacuum conditions deep defects were not noticed (enhanced surface emission and decrease in deep level emission in PL, less band bending at the surface through AES). Cesar et al.[157] used hydrothermally grown ZnO nanorods (on Si substrates) in his study and followed by PL analysis, the evolution of defects. Before annealing, the deep level oxygen defects (yellow and orange-red emissions) were increased with growth time, while the oxygen interstitial content (green emission) was almost constant. At the same time, as a function of post-annealing in air, the deep defects decreased as confirmed by the reduced green emission. They concluded in their study that the orange-red emission involves, apart from hydroxides (-OH, desorption temperature is 150° C, while their annealing was done at 400° C), the interstitials. Other similar studies[155,158,159] also employed PL as the main characterization tool to analyse the defect level's presence in ZnO. All these studies relate the reduction in the green emission to the annealing in the presence of oxygen. Even more, the green emission is attributed to neutral oxygen vacancies ($V_O{}^0$) and a blue shift is expected to occur after annealing, as the vacancies are ionized (by losing one or two electrons it becomes singly ($V_O{}^+$) or doubly ionized ($V_O{}^{++}$)), as shown in equations 1.13, 1.14, 1.15[155,158,160].

$$O_0{}^x \rightarrow V_O{}^x + \frac{1}{2} O_2\,(gas) \qquad (\textit{Neutral vacancy formation}) \tag{1.13}$$

$$V_O{}^x \rightarrow V_O{}^+ + e^- \qquad (\textit{Singly ionized}) \tag{1.14}$$

$$V_O{}^x \rightarrow V_O{}^{++} + 2e^- \qquad (\textit{Doubly ionized}) \tag{1.15}$$

Drouilly et al.,[155] demonstrated their studies (Electron paramagnetic resonance (EPR) and PL techniques) on ZnO that had native oxygen defects, to show that the defect content was influenced by both the nature (O_2, N_2, vacuum and O_2 + N_2) and the pressure of the gas involved during the annealing process. Under oxygenated annealing, competition between formation and filling of vacancies occurs depending on the temperature and oxygen partial pressure employed. Mostly the filling of vacancies was observed for oxygen atmosphere, while in all other atmospheres, new oxygen vacancies were formed in addition to the native vacancies.

Furthermore, there are several studies that have correlated the enhancement in the performance of photocatalytic systems to the quenching of deep level emission or increase in surface emission of ZnO (powder and films)[7,148,161–163], and a handful of studies (in the last decade[16,164–166], powders or ZnO on polymer membranes/fibers) that demonstrated the direct correlation between the role of oxygen vacancies in ZnO and pollutant degradation efficiency. A schematic representation of various defects (Zinc interstitials [Zn_i], extended zinc interstitials [ex-Zn_i], oxygen vacancies [V_O]) present in a typical ZnO material and their position inside the bandgap, the possible role of vacancies and its relation to the type of emission observed in PL are shown in Figures 1.26a and 1.26b.

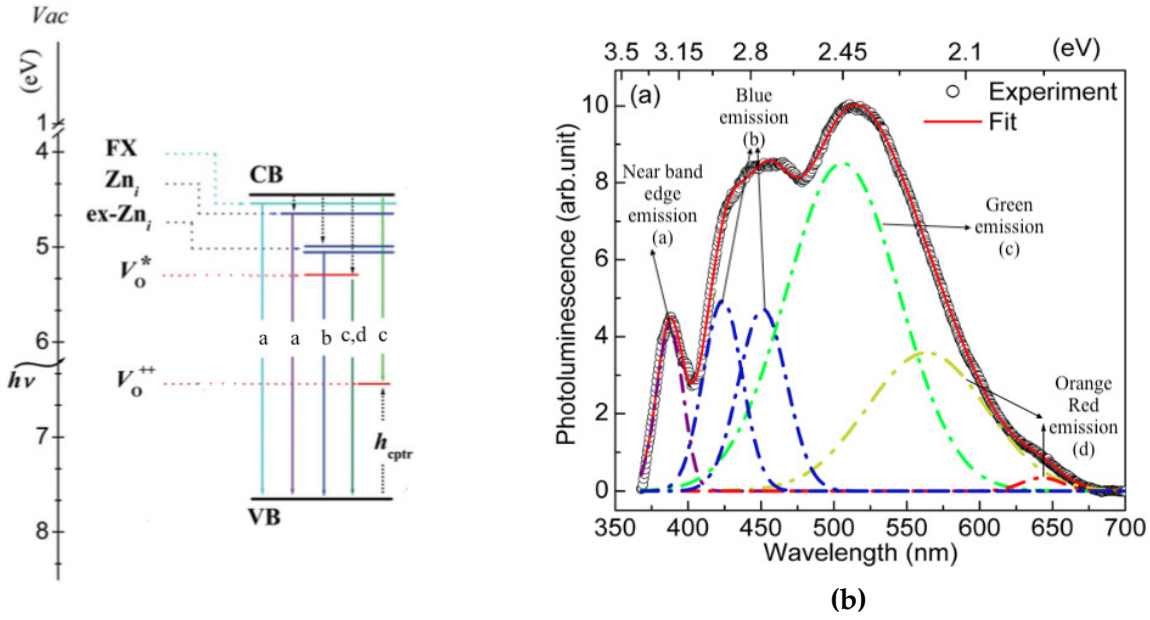

(a) (b)

Figure 1.26: (a) Schematic diagram depicting the various defects and the ascribed transitions (each denoted as a, b, c, and d). Surface excitons (FX) and Zn_i are 0.06 eV and 0.22 eV below the CB, respectively, while ex-Zn_is are 0.54 to 0.635 eV below the CB. $V_O{}^*$ is $\simeq$0.86 eV below the CB and VB is 1.16 eV above the VB, for a typical band gap of 3.36 eV; $V_O{}^{++}$ - doubly ionized oxygen vacancy and (b) PL spectrum of ZnO with deconvoluted peaks, representing the various emissions that correspond to transitions ascribed in (a) Adapted from ref.[16] and[17].

While most of these studies, correlate the improvement in photocatalytic activity to the presence of oxygen vacancies[99], some argue about the fact that a high amount of vacancies will act as recombination centers that will deteriorate the catalytic system[167], leaving the conclusions inconsistent. And also, presence of vacancies at the surface are known to negatively impact the interfacial properties (as discussed in Section 1.7), from a material science point of view. Therefore, understanding the effect of surface and interface characteristics on the photocatalytic activity is still elusive. The behaviour of heterostruc-

tured thin films formed on scaffold surfaces like ZNR with and without adsorbates (or oxygen vacancies) have never been explored in relation to pollutant degradation. Therefore, in order to have a better understanding regarding the influence of oxygen vacancies in the interface formation, ZNR scaffold was heat treated in the presence of oxygen under UHV conditions and the properties of heterostructures formed with cleaned and uncleaned scaffold have been studied in this thesis.

1.8.2. ZnO based thin films and heterostructures for pollutant degradation

So far, ZnO (planar/mesoporous/1D) thin films that have been studied as single material examined or embedded in heterostructures (semiconductor/semiconductor and semiconductor/metal) for pollutant degradation application (Table 1.5).

ZnO nanorods were prepared through hydrothermal growth [168], anodization [18] and CVD [95]; whereas planar films were prepared by atomic layer deposition [169], electro deposition [86] and spin/dip coating [170]. As mentioned earlier, the adsorption mechanism during pollutant degradation is different from powders to thin films [69], hence, one cannot compare the efficiencies attained for thin films of similar structures with that of powders. However, the following conclusions could be drawn:

1. some reports showed either lack or limited improvement after heterostrcuture formation, as opposed to the respective scaffolds, for smaller (1 - 3 h) [9 168] light exposure time

2. improved performance was only obtained for longer light exposure times (>3 h) [70 105 171]

3. improved performance was obtained (at shorter exposure time itself), mostly when using a metal as second material [metal/n-type semiconductor heterojunction] [95 172 173]

Table 1.5: Performance of planar and heterostructured ZnO thin films in pollutant degradation. • - Nanorod; Degradation time - in minute [min] or hour [h]; MB - Methylene Blue, RhB - RhodamineB, MO - Methyl Orange and MG - Malachite Green; ⋆ - Degradation was observed when light source was off, upto 25% ([1] - ZnO preparation procedure 1 - spin coating(and 50%(procedure 2 - dip coating), respectively; △ - Indium doped ZnO.

Samples discussed		Performance (in %)	Substrate/Size	Dye / Concentration	Degradation time	Light source	Reference [year]
Planar	ZnO	35	PMMA/ 1 cm^2	MB / 5 mg/L	60 min	UV	[169] [2017]
	ZnO on Si	40					
NR•	ZnO	≃37	PET/ not provided	MO / 16 mg/L	8 h	UV-Vis	[162] [2016]
	Ag/ZnO	≃37					
Planar	ZnO - 2μM	≃25	FTO/≃1 cm^2	MB / 10 mg/L	60 min	UV-Vis	[86] [2007]
	2.9μM	≃45					
Planar	ZnO^1	≃65⋆	Glass/≃20cm^2	MG / 5 mg/L	220 min	UV	[170] [2010]
	ZnO^2	≃85⋆					
NR	ZnO	≃25	Zn foil/ not provided	Phenol / 5 mg/L	250 min	UV	[18] [2018]
	Hierarchy	≃60					
NR	ZnO	≃40	FTO/1 cm^2	MB / 16 mg/L	60 min	UV	[172] [2011]
	Au/ZnO	≃ 25 - 99 (Au content)					
NR	ZnO	≃68	Si/1 cm^2	MO / 15 mg/L	180 min	UV	[95] [2006]
	Au/ZnO	≃80					
NR	ZnO	68	Glass/ 2.5cm^2	MO / 20 mg/L	2 h	UV-Vis	[173] [2014]
	TiO_2/ZnO	≃85					
NR	ZnO	≃36	Glass/ 2cm^2	MB / 2 mg/L	90 min	UV	[9] [2010]
	Ag/ZnO	≃44					
NR	ZnO	≃75	Glass/ 4 cm^2	MB / 9.6 mg/L	450 min	He lamp	[171] [2016]
	GO/ZnO	≃65					
	UV treated GO/ZnO	≃99					
NR	ZnO	≃15	ITO/ not provided	MO / 15 mg/L	230 min	UV	[105] [2013]
	Ag/ZnO	≃95					
NR	ZnO	≃50	ITO/ not provided	RhB / 2.5 mg/L	6 h	Xe lamp	[70] [2015]
	ZnO:I△	≃97					
	TiO_2/ZnO:I	≃97					
NR	ZnO	≃35	FTO/4cm^2	MO / 20 mg/L	180 m	Xe lamp	[168] [2016]
	$CuInS_2$/ZnO	≃60 - 90 (pH variation)					

Canon and his co-workers[18] prepared ZnO thin films by anodizing the Zn foil. With the variation of applied potential, morphologies with transitions from planar to nanoflake and nanowire were obtained. Phenol was tested for its degradation and even nearly featureless films (neither planar nor nanoflake) were capable of exhibiting better performance than nanowires, when the nanowire diameter was very high and nanoflakes showed the highest performance. However, owing to the benefit of higher surface area for 1D nanostructures (nanorods), further optimization was carried out in controlling the diameter of nanorods. This has showed that with reduction in the diameter, the alignment was compromised. Among the randomly oriented nanorods, those with higher interpenetration between the neighbouring nanorods were seen to be displaying poor degradation efficiency (Figure 1.27 [right side], attributed to limitation in the accessibility for light to reach the surface and induce the redox reactions), whereas the performance of those with a moderate alignment was increased. Furthermore, immersing the films in water for 24 h has led to formation of hierarchial structures on the surface of ZnO nanorods and it was exhibiting better performance by reaching upto 60% than plain ZnO nanorods. This shows that when nanorods are used, control should be attained over its diameter and the alignment, along with formation of hierarchy or heterostructures for improving the performance.

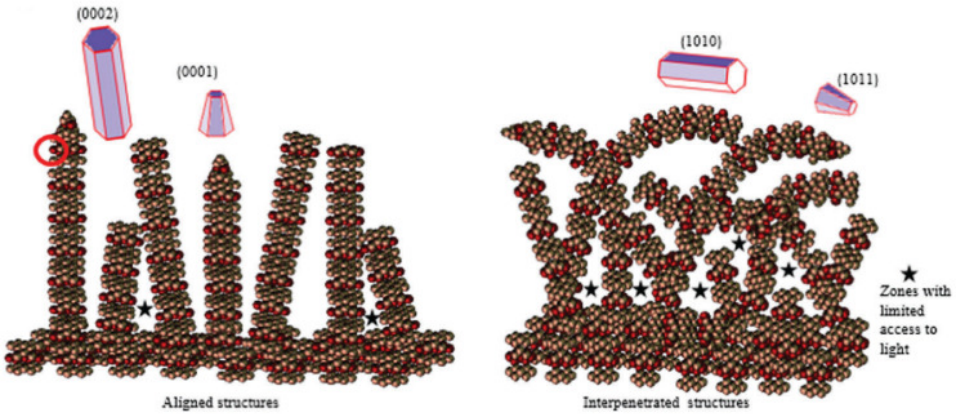

Figure 1.27: Scheme of ZnO wurtzite-type crystals and ZnO nanowires with controlled interpenetration (left side) and higher interpenetration (right side).[18].

With the reports[70,105,171] that have showed better performance at longer exposure times, it is clear that the trend explained in Section 1.4, regarding the powder vs. thin films, holds true here. Surprisingly there was also report of degradation performance (of 25 - 50 %) in dark conditions as well[170], making the results unreliable. But there are few reports[95,172,173] regarding higher performance with shorter exposure times (1 - 3 h). Among them, ref.[95] and[172], have showed Au/ZnO heterostructures, by employing CVD

[ZnO] + Photolysis [Au] and wet chemical [ZnO] + Photolysis [Au] methods respectively. Wu et al.[95] have discussed about the role of Au nanoparticle size in influencing the photocatalytic performance, where larger nanoparticles were performing worse than smaller particles. And it was attributed to the difference in charge transfer in each case, where larger nanoparticle was considered to form Schottky barriers as in case of bulk and that Au would have behaved asan electron sinks in case of smaller particles. However, the plasmonic effect of Au nanoparticles and its variation with nanorod to nanoparticle distance and its effect in charge transfer was not taken into account here. Moreover, by CVD deposition, ZnO nanorods were shown to be oxygen vacancy free and performing better in degrading MO (180 min), as both scaffold (68%) and heterostructures, (80%) compared to the planar ZnO film (5%). Whereas, Zhang et al.[172] showed chemically prepared ZnO nanorods with high amount of deep level centers that exhibited 40% efficiency in the MB degradation (60 min). For its heterostructures with Au (number of Au nanoparticles per nanorod and size of nanorods were compared), those with optimized coverage and size (9 nanoparticles of 20 nm size) were shown to perform better than those with higher coverage (about 50 - 500 nanoparticles of size 10 or 20 nm) and the scaffold itself. This is because the light and pollutant accessibility to ZnO was blocked. However, when density was not taken into account, but only the nanoparticle size, smaller Au particles ($<$ 20 nm, [10 and 5 nm]) were shown to perform better, as seen in case of Wu et al.[95]'s studies. This leaves the proposal of better performance inconclusive, because less or optimized coverage of 20nm Au nanoparticle was also shown to be exhibiting higher performance, in the same study. Moreover, in case of decorated nanoparticles, as shown in this study, optimum performance was attained for lower Au coverage, meaning that more of ZnO surface is exposed, which might in turn affect the lifetime of the material, given that ZnO suffers from photocorrosion.

Xiao et al.[173] reported the formation of ZnO nanorods by wet chemical method, which were then corroded using ammonia + cetyltrimethyl ammonium bromide (CTAB) before spin coating TiO_2 on top. No evidence was provided for confirming the removal of CTAB (before TiO_2 was coated), though high temperature calcination was said to be done. TiO_2 P-25 (commercially obtained and coated to glass for comparison studies), TiO_2/ZnO and ZnO NR were examined for MO degradation and the performance varied in the order of P-25>TiO_2/ZnO>ZnO. However, less difference (in the performance among the studied samples) was observed for MB degradation. This was ascribed to the role of photogenerated holes (as directly targeting MB molecules) in MB degradation and $^{\bullet}$OH radicals in case of MO degradation. However, there are few surprising revelations, which make this study as well inconclusive. First of all, chemically prepared ZnO is well known for excessive electrons and high conductivity and thereby the Fermi level usually occurs above the conduction band, but in this study, the Fermi level position was surprisingly low at 2.61 eV. In addition, TiO_2 which is made as planar film (even though with smaller nanoparticles)

have been shown in general to perform better only after longer exposure times (as a result of immobilization[4]), but here, the performance of planar P-25 film was higher than both the nano structured scaffold and its heterostructure, for short light exposure time. Also, the Fermi level position of ZnO after TiO_2 coating was not discussed, and thus the conclusion on charge transfer was not supported.

In conclusion, though better efficiency was attained by using TiO_2 or Au as second material with ZnO nanorods (thin films), many questions remain unanswered regarding the improvement in performance. MO and MB are often used as model pollutant whereas reports on RhB degradation are lacking. Moreover, the studies so far indicate that either the degradation rate is lower (i.e, higher light exposure times are needed to achieve higher performance) or for higher degradation rates, the reasons behind the improved performance remains unknown, as charge separation is assumed but not proven. Overall, all these reports indicate that exploration of thin films in relation to the influence of surface and interfacial properties and their influence on pollutant degradation is novel.

Therefore, in this thesis, ZnO nanorods (250-300 nm long and 50-60 nm wide) were hydrothermally grown on F:SnO2/glass substrates and covered (decorated) by a very thin layer of NiO by sputtering, for photocatalysis applications. In case of ZnO/NiO heterostructures, this way of preparation was never reported for dyes photodegradation. Yu-Ren Li et al.[174] reported the fabrication of NiO/ZnO heterostructures for UV detection applications by sputtering much more thicker NiO (150-450 nm) layers on top of chemically grown ZNR (700 nm long and 50 nm wide). No correlation with a precise application was realized. A. Echresh et al.[175] prepared ZnO /NiO heterostructures by thermally evaporating NiO (50 nm) onto hydrothermally grown ZnO nanorods. The nanorods were completely covered at the top resulting in an evident loss of specific surface which in exchange did not impact their photoresponse. They correlated the drop in the deep level emission and the constant NBE efficiency with the lower dark current. The improved photocurrent was related to the enhanced charge separation without further insight into the interface properties.

Although ZnO/NiO heterostructures with a structure similar[174–176] or different (planar ZnO-600 nm on top of planar NiO-500 nm[177], ZnO@NiO core-shell heterostructures[7], ZnO/NiO hollow nanofibers[174], flower-like ZnO decorated with cubic NiO particles[178], ZnO/NiO composite (um range/nm range) powders[114]) than ours were prepared by entirely chemical[7,114,176,178], entirely physical[177] or combined processes[175], most of the time the improvement in the photocatalytic response is more readily related to an enhancement in specific surface. All the previously cited reports fail to simultaneously and comprehensively correlate the photodegradation results with the surface (presence/absence of adsorbates and defects) and interface (Fermi level position, band bending) properties.

For example, Meng Ding et al.[7] have prepared ZnO-NiO core-shell hetero structures with high photocatalytic efficiency and reusability via electrochemical deposition on carbon fibre cloth substrates. In this case the variation of the photocatalytic activity with the NiO layer thickness is directly correlated with the specific surface. The reduction in the PL intensity (the deep level emission is not shown) is attributed to the decreased band to band recombination however a measure of the attained band bending is not given. In another example, ZnO/NiO hollow nanofibers with improved photocatalytic activity[174] were fabricated by impregnating electrospun polyethersulfone (PES) nanofiber webs in nickel and zinc acetate solutions and subsequent thermal treatment. The improved photocatalytic efficiency was attributed to the efficient separation of photogenerated electron-hole pairs without a measure of the attained band bending. Moreover, the difference in specific surface between the composite and the single material fibres is not shown.

Both the heterostructure, surface and interface parameters of ZnO/NiO were not previously explored for pollutant degradation purposes and thus constitute thus one of the novelty points of this thesis.

As shown in the Table 1.5, only Silver (Ag) and Gold (Au) have been investigated so far in case of semiconductor/metal heterojunctions in relation to the thin films based on ZnO nanorods, for photocatalytic applications[9,105,162,172]. RuO_2/ZnO heterostructures have been explored only recently[115,161], in the form of powders for photocatalytic applications and showed promising results. Therefore, it is interesting to understand the interfacial properties of RuO_2 with ZnO. Even more, elucidating the influence of ZnO surface as with and without cleaning in the interfacial band bending was not explored before. Hence, in this thesis, a systematic interface study was investigated for RuO_2/ZnO heterostructures, to analyse the possibilities of tuning the interfacial band bending, which is an important feature in charge separation and eventually in photocatalytic processes.

1.8.3. Single and heterostructured metal oxide in contact with water

Metal oxides are part of many applications like batteries, sensors, energy storage, catalysis/ photocatalysis, memory storage etc[149,179,180]. Despite the opportunities posed by these materials, the difficulties lie in the ability to control morphology or dimension, impurities or defects that occur during the growth. These characteristics along with the surface properties highly influence the functioning of devices or application in use[149]. The high reactivity of the surface or near-surface region of metal oxides, play a major role in processes like catalysis. Therefore, a deep understanding of the electronic structure, of the influence that defects or impurities have on interface formation and of the surface reaction

with incoming/adsorbed materials is necessary for designing an efficient structure.

Surface and interface properties of these materials have been approched by either experimental or theoretical (DFT calculations) methods and they were both found very challenging since they involve interactions at the atomic or molecular level. The experimental techniques used so far to study the interaction of water with solid surfaces include photoemission (X-ray photoelectron spectroscopy - XPS), scanning probe techniques (scanning tunneling microscopy - STM and atomic force microscopy - AFM), thermal desorption spectroscopy (TPD), vibrational spectroscopies (High resolution electron energy loss spectroscopy - HREELS and infrared reflection absorption spectroscopy - IRAS) and so on[149,152,181,182]. Among them, desorption related techniques are capable of identifying the decomposition products and whether reversible or irreversible desorption has taken place at the surface. HREELS and IRAS are capable of recognizing the vibrational modes related to OH and H_2O. However, the desorption methods have issues in correlating water coverage with the amount desorbed, whereas vibrational methods have issues in differentiating between dissociated and molecularly adsorbed water. In exchange, with STM and AFM imaging techniques, it is now possible to directly image the adsorption, dissociation and diffusion of water molecules or atoms at the surface[183]. However, difficulties lie in investigating water exposed samples because the H-bonds (much weaker than covalent or ionic bonds) could be disturbed by the STM/AFM tip during the imaging. XPS is capable of identifying not only the elemental composition, but also precise information on the molecule dissociation/bonding on the surface and their influence on heterostructure interface properties. For example, after water vapour exposure, traces of hydroxyl group (-OH) and molecular water can be identified in the oxygen peak (O1s). However, careful investigation of the O1s peak is recommended, due to the overlap of several components (lattice oxygen, -OH and H_2O). The ability to discriminate betweeen dissociated and molecular water[181], along with the possibility to study the interface between two different materials (in our case semiconductors), holds a unique way to understand the change in surface chemistry on heterostructure interface properties with water interaction. These studies find their utility in single or heterostructure based materials when optimising processes occurring in water media.

Major advancements were made in investigating the water interaction with solid surfaces, since the review of Thiel and Madey published in 1987[184]. Almost a decade and half later, the developments in comprehending the fundamentals about water interactions were rediscussed by Michael A. Henderson[181]. While Thiel's review discussed in detail about the water adsorption pathways (associative [molecular] or dissociative), the thermodynamic and kinetic factors involved in water interaction, the adsorption studies on clean metals, well characterized oxides and some non-metals; Henderson's review details the

various techniques available for surface investigations, their advantages and disadvantages, the interplay between the water-water and water-surface interactions in influencing the adsorption pathways on surfaces, the role of co-adsorbates (alkalis, oxygen, carbon monoxide) as passive or active participant in surface chemistry and water interaction with surfaces under non-UHV conditions.

Some of the major conclusions from their reviews are summarized here:

1. Behaviour of water on most of the metals and noble metals are well understood but the exploration of reactive metals and oxides are missing.

2. The interaction of water with metal surfaces is weak, in most cases, and is attributed to the fact the atoms are perfectly arranged. This is because, dissociation of water tends to occur more readily at atomically rough areas than on smooth areas.

3. Investigations on (metal) oxides have revealed that chemisorbed oxygen is more active for water dissociation, compared to oxidic oxygen, i.e, O_2^-. This is attributed to the ability of non-lattice oxygen to encourage the abstraction of hydrogen from H_2O, which in turn mean water is dissociated.

4. When water is weakly adsorbed to the surface, water-water interaction will dominate and clustering takes place, leading to diffusion of water molecules on the surface but the situation is not clear for surfaces on which water is strongly adsorbed to.

5. Clustering of water takes place when water-surface interaction is weaker, whereas strong water-surface interaction will discourage the water-water hydrogen bonding interaction, therefore promoting strong bonding between water and surface.

6. Very little is know about the diffusion mechanism or how the surface structure can influence the diffusion.

7. The presence of electronic defects does not necessarily guarantee the dissociation of water but the other key factors that will induce water dissociation on an oxide surface includes, the geometric arrangement of cations and anions (the configuration/polarity of the outer plane) and the inherent ability to bind with water and receive protons.

8. Though TiO_2 is one of the extensively studied metal oxide, experimental understanding of water dissociation on its surface is lacking.

9. Whether and under what conditions water dissociates and the possible influence of defect sites on dissociation, on the surface of ZnO are questions that remain unanswered

10. The conclusion of Carley et al. regarding the role played by chemisorbed oxygen in water dissociation was not adopted in the recent studies reviewed by Henderson (or most probably even after his review).

These reviews along with the subsequent reviews by A. Verdaguer et al[21] , A. Michaelides[185] , A. Hodgson et al[186] , Hendrik Bluhm[182] and Olle BjoÌĹrneholm et al[187] highlight that the major part of investigations (both experimentally and theoretically) were done on the interface of water with metals or metal oxides or other non-metallic surfaces as single crystalline materials. This is due to the fact that having defects or impurities at the surface, adds to the already prevailing complexity in such molecular scale investigations. However, the real time applications are involved with polycrystalline materials (at nanoscale level), which makes it complex to correlate the findings from those fundamental studies[182]. Also, the complexity increases when considering polycrystalline nanostructured heterostructures.

Moreover, studies regarding the molecular-level role of water in catalysis or photocatalysis, non-thermal activation of water or heteroatomic materials is scarcely reported. With the emerge of nanoscale materials and heterostructures based on them, the understanding about the interaction of molecular water with polycrystalline, defective and heterojunction surfaces is a key factor in improving the design of efficient photocatalytic materials.

Herein, we have studied for the first time the interaction of the Zinc Oxide (ZnO) scaffold films and their heterostructures with Nickel Oxide (NiO) (nano and planar based) films, with water vapour under ultra high vacuum (UHV) conditions, by using XPS, along with room temperature (RT) photo luminescence (PL).

Many of the previous reports discuss either the XPS or other surface science techniques individually or they correlate experimental results with theoretical calculations[19,152,181,182,188-
These studies shed light on several factors that should be considered while surface investigation is done, as opposed to laboratory prepared single crystalline materials: samples used in technological applications are both structurally and chemically more complex being rich in contaminants/defects; a strong water-surface interaction or the presence of oxygen vacancies encourages the water dissociation process and even more in case of oxides; heterostructure interface properties, polar surfaces or surfaces rich in adsorbates are ambient sensitive and are need to be examined under UHV conditions. As mentioned earlier, the interaction of water with metal oxides is more complex than with metals, because both the metal cations and oxygen anions can bind with water, where the latter is usually known to facilitate water dissociation. Among metal oxides or non metallic surfaces, the interaction of water and the corresponding surface reactions were investigated on TiO_2, ZnO, MgO, NiO and Silicon surfaces[181,184], with however, no direct correlation to photocatalysis.

In particular, the surface interaction of ZnO with CO_2, CO, H_2O and H-atoms was only studied for single crystalline, non-polar surfaces. The reports of Stephane et al[19], John et al[193] and others[15,152] have revealed that water can either be molecularly adsorbed (Figure 1.28a) or dissociated (Figure 1.28b) depending on the strength of water-water or water-surface interactions and the availability of dangling -OH groups. Water dissociation occurs through hydrogen extraction, which will be transferred to bond with oxygen and hydroxyl gets adsorbed to the metal ion, leving a dissociated structures as shown in Figure 1.28b. However, studies also show that both forms can co-exist on the surface of ZnO, especially under UHV conditions[193].

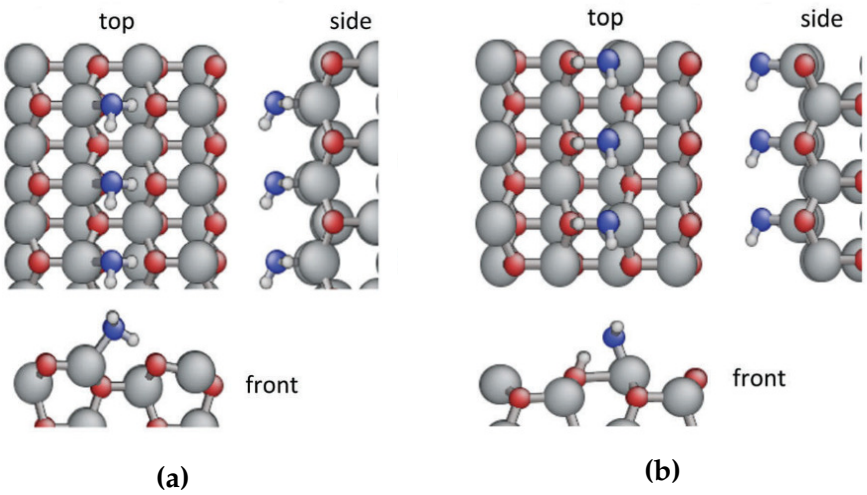

Figure 1.28: Top, front and side views of molecularly adsorbed water on the ZnO($10\bar{1}0$) surface; In the figure, Zinc atoms are grey, the oxygen atoms of ZnO are red, the oxygen atoms of water molecules are blue and hydrogen atoms are white.[19]

In-depth studies on polar ZnO surfaces are lacking. Zinc oxide nanorods (ZNR) are considered by definition a polar[154,194,195] surface owing to the ability of Zn atoms and O atoms to grow alternatively along the c-axis[196], resulting in the stacking of opposite charged planes which generate a dipole moment perpendicular to the (0001) plane. The ZNR prepared by a chemical route, is prone to have vacancies or impurities. In general, it is agreed that vacancies play a major role in the process of water dissociation[188,197,198]. Heat treatment in presence of oxygen, of an as prepared ZNR surface is capable of removing the impurities/adsorbates, forming layer(s) of oxygen adatoms (oxygen atoms adsorbed to the surface by treating with oxygen gas flow). This chemisorbed oxygen is considered to be more reactive in promoting water dissociation[184,199], but not widely studied. Hu et al[188] demonstrated theoretically (in parallel to experimental studies of Huang et al.[198] and Sun et al.[197]), that in the presence of oxygen vacancies (V_O) water dissociation is promoted. ZNR scaffold is known to have good charge separation effects, due to its one dimensional

structure[93,200]. In this study, in order to reduce surface charge recombination[55,201] and to enhance the charge transfer characteristics[58,93,202–206], the ZNR scaffold was coated with a thin layer of NiO, targeting photocatalysis and water splitting applications.

In case of Nickel Oxide (NiO), water interaction with (100) and (111) surfaces are widely studied in earlier reviews[181,184]. The major revelations were that, water does not dissociate on the (100) surface, especially under UHV conditions and that NiO (111) is capable of readily dissociating water. It was expected that -OH terminated NiO(100) obtained through growth, could facilitate water dissociation, however that is not the case. The energy required for dissociative adsorption for water molecules on NiO (111) was recently reported (through theoretical and experimental analysis [single crystal adsorption calorimetry] by Zhao et al. by employing varying water coverage. Figure 1.29a shows the water dissociation on NiO(111) and the energy involved[20]). The obtained dissociation energy was seen to be matching the previous results (through temperature programmed XPS), with the formation of characteristic -OH and O + H adsorption near the metallic centers, as shown in Figure 1.29a.

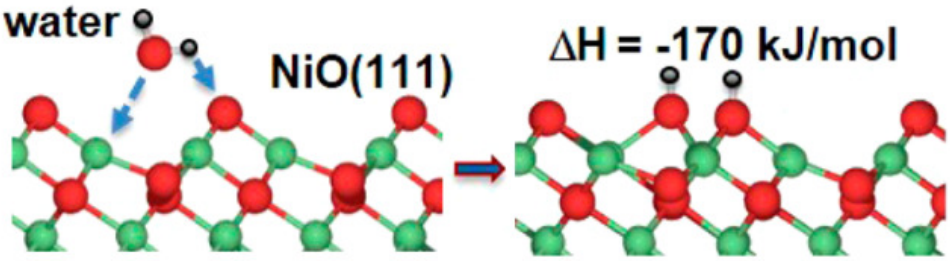

(a)

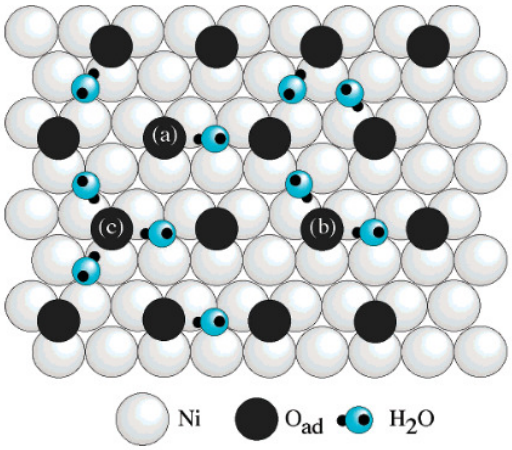

(b)

Figure 1.29: (a) The dissociative adsorption of water on NiO (111) plane) and the energy required[20]; (b) Schematic model of the H_2O adsorption on a Ni(111) surface showing that each O in the 2×2 structure can bind one (a), two (b), or three (c) water molecules[21]

Moreover, Nakamura et al.[21] have shown that at room temperature, NiO (111) plane is capable of allowing stronger water-surface interaction (H_2O-O[from NiO]) and hence preventing the molecular adsorption of water. Moreover, their model structure have shown that each oxygen atom in NiO(111) is capable of accommodating one, two or three water molecules, as shown in Figure 1.29b. Probably, this is why, water dissociation occurs readily on NiO(111).

In this dissertation, the influence of the presence or absence of adsorbates on the bare ZnO and on the ZnO/NiO heterostructure formation, but also the junction interface properties modification with water exposure were studied by step-by-step in-situ XPS. The heterostructure with planar ZnO/NiO films and planar NiO films, were also studied for comparison purposes. In addition, photoluminescence investigations were carried out on ZnO scaffold and their heterostructures to elucidate the role of oxygen vacancies in band bending.

The interaction of water with semiconductor metal oxide polar surfaces and in particular with polycrystalline nano structured ZnO and its heterostructures with NiO is first time reported here. The investigation was done by XPS under UHV conditions. Such a study finds a direct application in the design and optimization of materials for processes occurring in aqueous media such as photocatalysis or water splitting. We provide experimental evidences that surface with less vacancies promote water dissociation.

Optical studies like photoluminescence will enable deep understanding about surface plasmon interactions and interface fluctuations at the interface of metal/semiconductor heterostructures. Therefore, all the heterostructures were thoroughly examined under PL and the relative charge transfer mechanisms were elucidated, along with the revelations from XPS investigations. Their correlation to photocatalytic activity showed the interdependence of several factors (band bending, surface plasmon interactions, NBE emission, deep level centers etc) of the material properties that had strong influence in the pollutant degradation performance.

1.9. Conclusion

The review of the state of the art allowed emphasizing the advantages of the advanced oxidation process like heterogeneous photocatalysis over the conventional methods used for water treatment and the advances made so far in the semiconductor based photocatalytic systems and also the level of comprehension on the underlying mechanism. Furthermore, the advantages of using nanostructured thin films over powder materials and

of the necessity for scaffold surface treatment are summarized in this chapter. The theory and background related to band bending and charge transfer characteristics in case of heterostructured photocatalysts prioritized the need for attaining an internal electric field at the interface that would enable separation of photo induced charge carriers. Moreover, the fact that it is important to realise either p-type/n-type or metal/n-type heterostructure, in order to enable the migration of the charge carriers in a complying manner both during charge separation and consumption process have been taken into account, therefore to enhance the overall charge kinetics. A comprehensive literature survey regarding the use of ZnO based thin films (in specific based on Zinc Oxide nanorods) as single/scaffold and in heterostructures, for pollutant degradation was realised. In most of the cases, the improvement in performance was attained with the help of utilizing modification techniques (doping, metal or semiconductor deposition forming heterostructures). The highest performance was obtained in metal/ZnO heterostructures for exposure times equal or longer than the time employed in our studies (reported in this thesis), with values comparable/lower with powder counterparts. However, systematic studies regarding the influence of the internal (band bending at the interface, ratio of shallow level defects vs. deep level defects) and external parameters (surface properties of scaffold material and deposition conditions involved with second or contact material) on the photocatalytic response are elusive. Additionally, the role of shallow vs. deep level defects in heterostructures, the possibilities to attain control over NBE efficiency and interface fluctuations and their direct correlation to the charge transfer characteristics and photocatalytic activity is not widely reported. Moreover, such correlations were never reported for NiO/ZnO heterostructures and the correlation of the above constitute one of the novelties of this thesis.

Literature study regarding water interaction on solid surfaces has highlighted that either water adsorption can take place either molecularly or dissociatively depending on whether water-water or water-surface interaction is dominating. In case of metal oxides, the dominance in dissociative adsorption of water was often attributed to the presence of vacancies and to the fact that it is more reactive. But it is also revealed that presence of vacancies on the metal oxides, do not necessarily guarantee the dissociation of water and that it could also be induced by the chemisorbed or adsorbed oxygen atoms at the surface (but attributed less, when compared to vacancies). Moreover, studies on metal oxides are always done on single crystalline materials and the surface reactions of poorly ordered or polycrystalline materials on interaction with water was greatly unexplored. In specific, the water-surface interaction in relation to photocatalysis on a polycrystalline surface (which is usually implemented in real time applications) was never explored before. The study of the complex nanostructures and delicate surface and interface properties being involved in the heterostructured systems will provide an insight into the understanding towards the performance of heterostructured photocatalysts and will help in improving the design of

photocatalytic materials.

Therefore, for the first time here, we have studied the surface-water interactions on the single material's surface properties and on the interface properties when embedded in heterostructures. Such a study finds a direct application in the design and optimization of materials for processes occurring in aqueous media such as photocatalysis or water splitting.

1.10. Dissertation approach

The major goal of this thesis was to prepare efficient ZnO-based heterostructured photocatalysts for the degradation dyes in water. A model schematic of such product is shown in Figure 1.30.

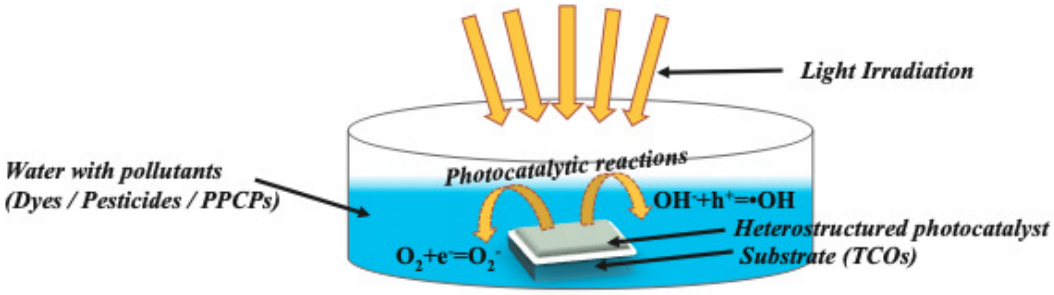

Figure 1.30: Schematic representation showing the ultimate aim of using heterostructured photocatalysts supported on substrates for pollutant degradation.

A derivate objective consisted in the fundamental exploration of such heterostructures with the purpose of elucidating the influence of external factors (type of adsorbates, water exposure, deposition conditions) on the internal parameters (Fermi level, band bending, ratio of shallow vs. deep level defect) and consequently on the photocatalytic efficiency.

The philosophy followed to achieve these goals is illustrated in the flowchart Figure 1.31.

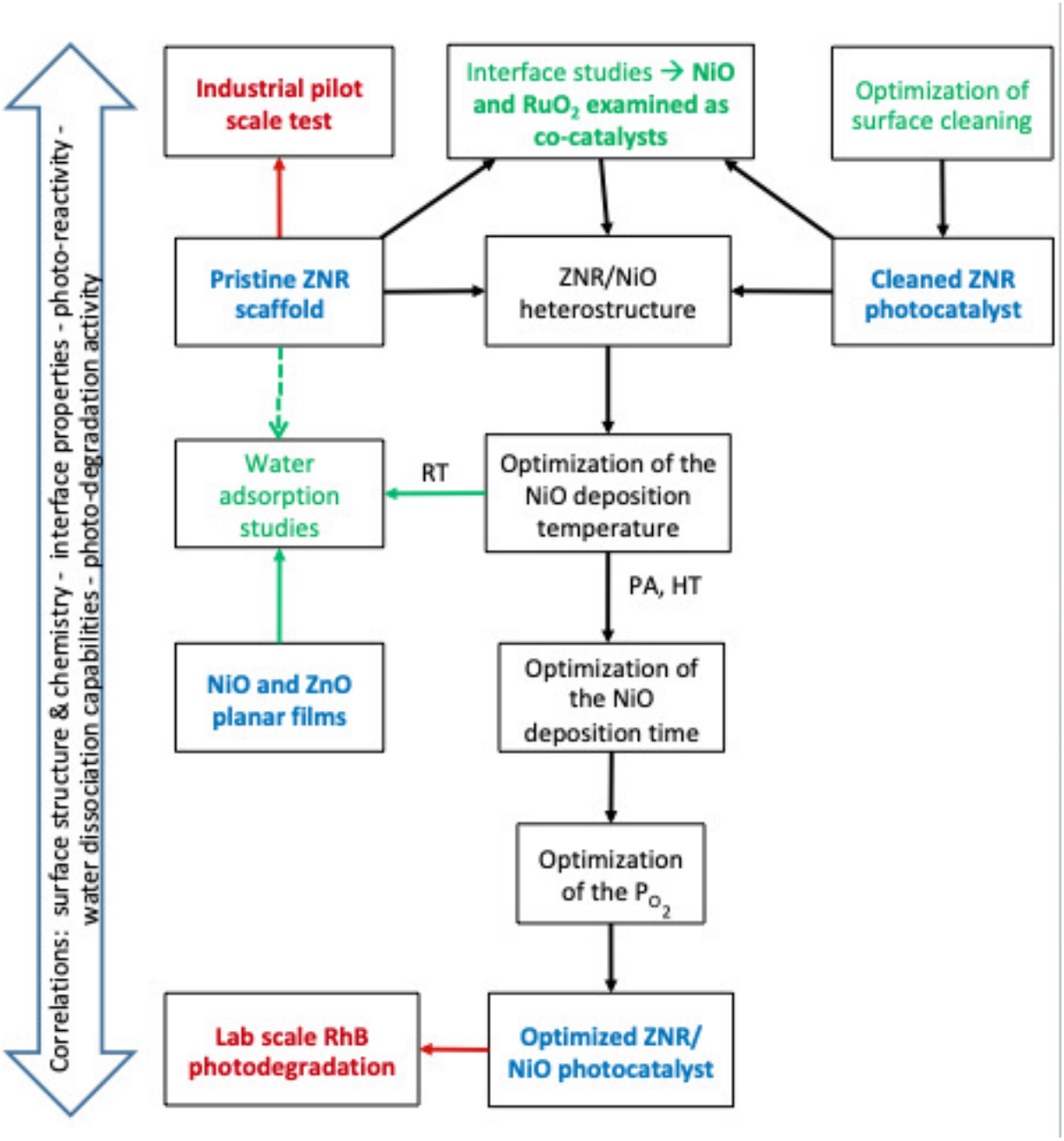

Figure 1.31: Flow chart representing the summary of work done in this dissertation. RT, PA and HT represent room temperature, post annealing and high temperature and P_{O_2} implies partial oxygen pressure.

ZnO was chosen as scaffold due to its abundance, low toxicity and especially facile one-directional growth. 1D nanostructuration was our choice due to improved charge percolation and specific surface. To begin with, a comprehensive literature review was realized on single and ZnO-based heterostructured materials (planar or nanostructured, powders or thin films) as photocatalytic materials and included in **Chapter 1**. Also, all the fundamental notions such as metal-semiconductor, n-p or semiconductor electrolyte junctions, photo-

degradation principle and mechanism, plasmonic effect, etc. are presented in **Chapter 1**.

All along the studies performed in this work, the following correlations were realized: surface structure (TEM, XRD) and chemistry (XPS) and interface properties (band bending, Fermi level position in-situ XPS) with the material photo-reactivity (PL, I-V in light) and water dissociation capabilities (in-situ water exposure and XPS analysis) and finally with the photodegradation activity (only for NiO/ZnO heterostructures). The experimental methods that were used for the heterostructure preparation and the major characterization techniques like XPS and PL (others are detailed in appendix), the interpretation methods used for thin film's analysis in this work are detailed in **Chapter 2**.

The first step consisted in verifying the suitability of p-type NiO and metal-like RuO_2 as second material in the formation of heterostructures with ZnO, which is the subject of **Chapter 3**. For this, step-by-step interface studies were realized by coating RuO_2 and NiO onto previously optimized pristine ZNR substrates but also on cleaned ones (heat treatment at 400° C in the presence of oxygen). The studies demonstrated the successful formation of the p-n and metal-n-semiconductor junctions and revealed the importance of surface cleaning prior to co-catalyst coating.

Further on, the ZnO/NiO heterostructures preparation was optimized by identifying the optimum surface cleaning conditions, followed by the optimization of the NiO deposition here including the deposition temperature, the deposition time and the oxygen partial pressure, as presented in **Chapter 4**. Finally, since these materials are used in an aqueous environment, we have studied the influence of water exposure on the interface properties and evaluated the water dissociation capabilities of single (nanostructured [pristine and cleaned] and planar) and ZnO based heterostructures and correlated them with the photo-degradation activity (**Chapter 5**).

The applicability of such 1D materials in real-life conditions was proven (as detailed in **Chapter 6**) by the successful up-scaling of the ZNR preparation and the pilot-scale implementation of ZNR substrates for the purification of water in fish tanks from Aquatic Science.

Chapter 2

Experimental and Characterization methods

2.1. Experimental techniques

Zinc Oxide nanorod (ZNR), the scaffold material preparation involved a two-step chemical technique: spin coating the seed layer and hydrothermal growth of the nanorod. The deposition of contact material (NiO and RuO_2) was carried by another major technique called magnetron sputtering, for all the heterostructures studied in this thesis. All these techniques are detailed in the following sections.

2.1.1. Spin coating

Spin coating consists in the following steps:

i) few drops of the solvent are dispensed onto the substrate

ii) he humidity and the rotation speed can be controlled in order to vary the desired outcome of coated layer

iii) with the help of the rotation, the precursor will be deposited the molecules all over the substrate's surface

iv) the above mentioned steps can be repeated depending on the desired layer thickness

v) after obtaining the desired thickness, calcination was done at 500° C, for 2 hours

These steps are illustrated in Figure 2.1.

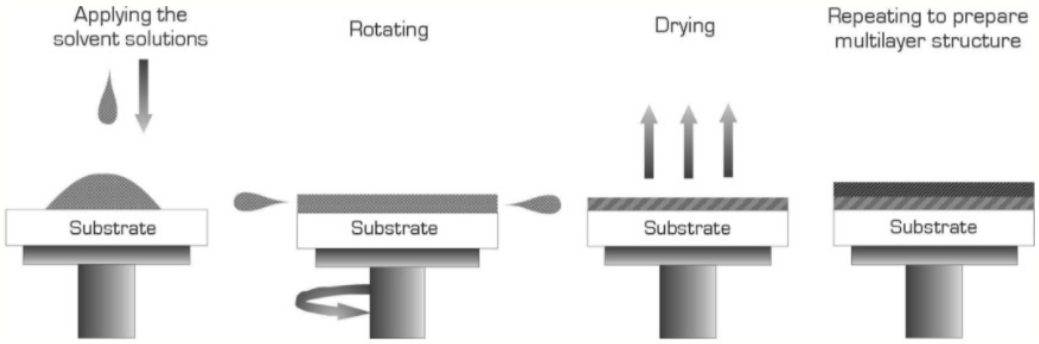

Figure 2.1: The stages of the deposition thin films by spin coating method.[22]

2.1.2. Hydrothermal growth

The substrates coated with seed layer were immersed into the solution, inside a teflon-lined autoclave. The substrate was positioned in such a way that the substrate is inclined to the walls at about 45° angle. The hydrothermal reaction was carried out in the oven at 92° C for 1 h and the resultant ZnO Nanorod grown substrates were washed with distilled water, dried in oven at 60○ C for 30 min and then calcined at 500○ C, for 2 h (at the ramp of 300○ C/h).

The detailed procedure for spin coating and hydrothermal method, the materials used and the optimization of ZnO nanorod preparation are all described in Section 3.2.

2.1.3. Sputtering

The grown and calcined ZNR were further used as substrates to deposit the second material for heterostructure formation. A physical deposition method, called magnetron sputtering, which involves ions from desired target material that are derived from a plasma that occurs due to low-pressure gas between two electrodes, is used here. The important advantages of sputtering over other vacuum coating techniques are the high deposition rates, ease of sputtering any material, high-purity films, significant adhesion and homogeneity of films, excellent coverage, ability to do coating on heat-sensitive substrates etc. Therefore, this technique is also easy to do upscaling and thereby to be implemented in commercial applications.

Magnetron sputtering is a vacuum coating technique, that allows deposition of metals, alloys and wide range of other materials for thicknesses of up to 5 μm. Its working principle involves creation of ions with sufficient energy that could be directed towards the surface of target. This will allow ejection of atoms from the material and with the help of low pressure, these ejected atoms will travel the distance to reach the substrate. The reachability of atoms without atom-gas collisions is ensured by the employed pressure in the system. The average distance the atoms can move without colliding with gas atoms is called mean free path and for this unimpeded travel, operating pressure should be at least 1Pa. Moreover, this is closely related to the deposition rate, i.e the fewer the collisions, the higher will be the deposition rate and vice versa. In addition, temperature conditions will influence the surface diffusion and crystallinity of the sample being deposited, where high temperature allows obtaining highly crystalline materials due to the higher surface diffusion rate.

In order to create the positively charged ionic species and accelerate them towards the substrate to which deposition should be done, a plasma and an electric field are required. An electric field could be created by direct current (DC), alternating current (AC) or pulsed DC signals and DC is used for the all the contact material depositions done and discussed in this dissertation. Moreover, for the creation of ionic species, many gases are available for use, however, argon is widely used due to its inertness even in non-ionized state and as it holds a desirable mass that can provide the ability to sputter variety of elements. In addition to argon gas, oxygen gas needs to be used in combination, for the deposition of oxide materials, as in case of the contact materials deposited here.

A typical magnetron sputtering setup (as shown in Figure 2.2) consists of two major parts called anode and cathode, between which the electric field is applied, for the creation of ionic species. For the deposition of a conductive material, DC is often used with the help of a DC generator where a constant current is applied.

However, it is not preferable for the deposition of less conductive materials, since a steady bombardment of the target by cations needs an alternating current supply, to stabilize the system. Hence, an AC signal at a standard frequency of 13.56 MHz (since no impedance is created at the targets, at this frequency) is chosen for the current supply. This technique is often referred as radio frequency (RF) sputtering, as the chosen frequency lies under the radio frequency regime. This method was used for the deposition of planar ZnO (Section 5.2), which was used in water exposure experiments.

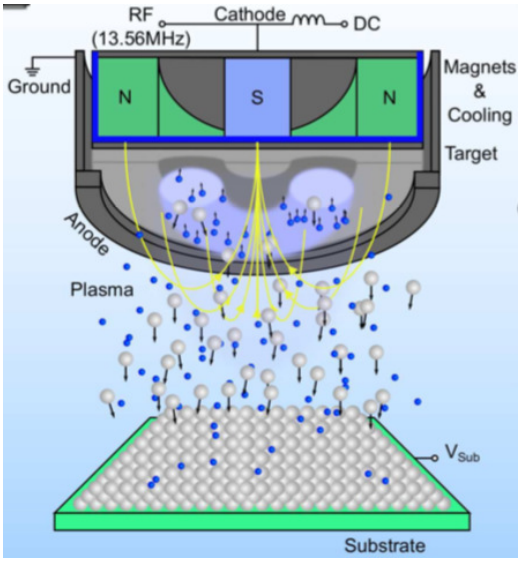

Figure 2.2: Schematic representation of the magnetron sputtering setup. The sputtered target atoms or ionice species and the sputter gas atoms are represented as grey and blue spheres, respectively.[23]

The DC and RF magnetrons used in this study, in DAISY-MAT system, were equipped by Thin Film Consulting and HüĬLttinger PFG 300RF RF generator was used for the RF signal generation. The preparation strategy and parameters involved in the deposition of NiO and RuO_2, the contact materials that were investigated in this dissertation are described in Chapters 3 to 5, in their respective 'Sample Description' section.

2.2. Characterization techniques

2.2.1. X-Ray photoelectron spectroscopy (XPS)

XPS is a non-destructive and quantitative spectroscopic technique which measures the elemental composition, and provides information about the chemical and electronic states of the elements that exists in a material.

Principle and working

Photoelectron spectroscopy (often simply referred to as photoemission), works with the concept of photoelectric effect, where illumination of a sample with photons of defined energy larger than the ionization energy causes electrons to be emitted from the sample, Figure 2.3) [24]. These excited electrons are called a photoelectrons.

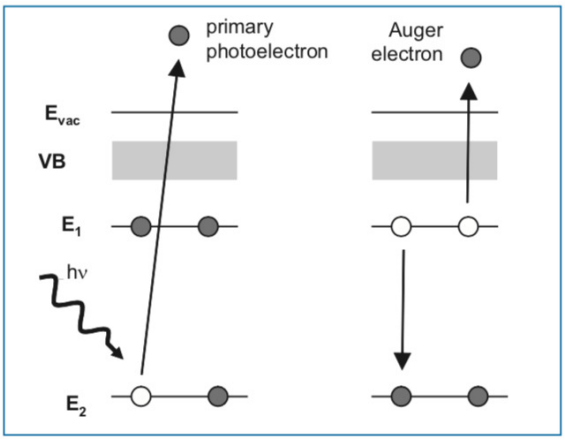

Figure 2.3: Primary photoemission and Auger process .[24]

The energy required to excite the electrons from the energy levels of the atoms, increases from the outer shell (valence electrons) to the inner shell (core level electrons). This is because, the more closer an electron is to the nucleus of the atom, the stronger will be the binding energy. And the minimum energy required to excite an electron from the solid's surface into vacuum is called as the work function (ϕ) of the material. Usually, core level electrons have a very high binding energy that requires photons from the X-ray spectral region (as in case of XPS technique) for the excitation to take place, while the valence electrons that have a relatively lower binding energy require photons from ultraviolet spectral region for their liberation (used in a technique called ultraviolet photoelectron spectroscopy [UPS]).

A typical photoelectron spectrometer uses monochromatic X-ray source (Al Kα [photon energy - 1486.6 eV and energy width - 0.85 eV] or Mg Kα [photon energy - 1253.6 eV and energy width - 0.70 eV] X-rays) to excite the electrons from core levels of the atoms near the surface ($\simeq$ 1-10 nm, Sampling Depth (SD) = 3λ, where λ represents the inelastic mean free path of an electron in a solid. Hence, SD is the depth from which $\simeq$95% of all photoelectrons are ejected from the surface) of a material into vacuum. These excited photoelectrons will pass through a set of electrostatic lenses, where they are decelerated and focused into the entrance slit of hemispherical analyzer. The hemispherical electron energy analyzer then collects only the ejected electrons that are of specific kinetic energy or pass energy, which is received in the detector channel. This complete process needs to be carried out under UHV conditions, in order to avoid photoelectron inelastic scattering.

The specific kinetic energy used to collect the photoelectrons is used to determine the binding energy (BE) of the electron from the following equation:

$$E_{\mathrm{BE}} = h\nu - E_{\mathrm{Kin}} - \phi_{\mathrm{sp}} \tag{2.1}$$

Where h is Planck's constant, ν is the frequency of the exciting energy source, and ϕ_{sp} is the work function of the spectrometer [24].

In general, a photoelectron spectra is recorded through the sweeping mode, in which the pass energy and sweeping voltage is fixed and the chosen energy region could be swept once or multiple times, such that the photoelectrons are counted by the detector channels for the given amount of time. The obtained XPS spectra is considered as a finger print of the material being studied, because each ejected electron from an element correspond to a characteristic binding energy and the position of this binding energy is used for identifying the element. The core level of the electron for a corresponding material can be identified by consulting the binding energy tables. In addition to element identification, quantification can be done using the peak intensities, while the peak positions can be correlated to the oxidation state of the element that is being studied.

Moreover, photoemission process usually involves two effects called initial and final state (state of the 'photohole' [that occurs on electron excitation] and possible loss of screening effect of the core level electron) effects, both of which are known to impact the binding energy that is being recorded. The common final state effects that account for any changes observed in the photoelectrons spectra are spin orbit coupling, shake-up/shake-off, plasmon and phonon interactions. Spin orbit coupling process will occur, when an unpaired core electron of the atom, on photoemission results into coupling of the spin and angular momentum of the orbital and this process is more recognizable for the electrons that are present in the p,d,f orbitals. For example, a core level spectrum with spin orbit coupling effect will have a doublet structure that display either two far apart signals as in Zn2p (which has a doublet of $Zn2p_{3/2}$ at 1021.6 eV and $Zn2p_{1/2}$ at 1045 eV, with a BE difference of 23.4 eV) or closely separated signals as in Ru3d (doublet of $Ru3d_{5/2}$ at 279.90 eV and $Ru3d_{3/2}$ at 284.07 eV, with a BE difference of 4.17 eV). In the Zn2p (Ru3d), for the p orbital (d orbital), the subscript number 3/2 and 1/2 (5/2 and 3/2) indicate the sum of angular quantum number (1 and 2 for p and d orbitals) and spin orbital number (+1/2 or -1/2). The extrinsic effect like electron shake-up or shake-off take place when energy is transferred from a photoelectron to another electron, resulting into the latter's excitation from the core level. This phenomena gives rise to the satellite structure that is observed in the core level spectra of transition metals like Nickel (Ni2p), Iron (Fe2p) and Cobalt (Co2p). Similarly, plasmon or phonon interaction also leads to the energy transfer that occur between photoelectrons

and delocalized electrons or phonons. As a consequence, the involved photoelectrons could disclose an extra emission at relatively higher binding energies. The involvement of these processes or effects make the quantification of the photoelectron spectra largely complex and challenging.

In general, the various information that could be obtained and its relation to the XPS spectra are detailed as below:

i) Chemical shift - The binding energy of an electron depends on the oxidation state of the atom which is further dependent on the surrounding chemical environment. Hence, any change in chemical environment of the material could be noticed in XPS spectra, through the shift from its typical binding energy value and the reasons behind the shift can be as quite diverse:

   - element with higher oxidation state will have higher binding energy and vice versa.
   - when two materials are brought together, the transfer of electrons is initiated by the one with higher electronegativity or the one with lower work function, leading to change in the oxidation state of the material.

     For example, when there is a loss of valence electrons, oxidation state increases, leading to an increase in binding energy and vice versa.

ii) Full width half maximum (FWHM) - There are several parameters that can affect the FWHM values and they are:

   - lifetime of the core level,
   - instrumental factor or surface charge effects,
   - physical parameters like addition of new component or crystallinity or temperature or deviation from stoichiometry.

     Additionally, broadening or narrowing of the main peak in a spectra occurs, this might indicate oxidation or reduction. But to confirm this effect, its satellite structure should also be accompanied by noticeable changes.

iii) Element quantification - could be done by determining the atomic concentration (C_x)

of any element in the sample by using the following equation:

$$C_x = \frac{I_{ij}/S_i}{\Sigma\, I_i/S_i} \tag{2.2}$$

where I and S represent the intensity and sensitivity factor respectively; i and j are element of sample and core level of the element i respectively.

Moreover, the following aspects should be taken into consideration, for the atomic ratio calculation:

- sensitivity factor values are instrument specific, therefore, should use the values that are found in the instrument manual.
- when the peaks of same material (eg: doublet or multiplet peaks) or of those close to each other, are examined, the above formula could be used with normal sensitivity factor.
- when peaks of elements have very different binding energies one should use a correction factor, in addition to the use of atomic sensitivity factor values, because they involve varying kinetic energies for the excitation of electrons. And the correction factor can be calculated by measuring a sample of known stoichiometry, which can be used further to determine the corrected atomic ratio values.

iv) Core level intensity (of one material) - can increase or decrease, with the removal or addition of another material, respectively. For example, removing contaminants by a heating step, usually increase the core level of a material, whereas, deposition of another material on its top will reduce the intensity.

v) Valence band maximum - could be extracted by extrapolating a line across the binding energy of valence band onset, such that it will intersect the background. These values, along with the core level BE values, helps to designate the band alignment structure of the materials. In addition, when more than one material is used, the shifts in core level or valence band maximum of the substrate will lead to the identification of band bending that occur at the interface of the substrate and contact material.

In this thesis, XPS was used to analyze the chemical state of scaffold (as synthesized, post treated) and heterostructured photocatalysts. Additionally, investigations regarding the band alignment at the interface of the heterostructure photocatalysts and in-situ water (vapour) exposure studies on scaffold and heterostructured photocatalysts were performed using the XPS technique.

All the above mentioned XPS related experiments were performed at the Darmstadt Integrated System for Material research (DAISY-MAT) system (Schematic shown in Figure 2.4. It is a physical electronics PHI 5700 multi technique surface analysis system combined with thin film deposition (sputtering, atomic layer) chambers, enabled with a vacuum transfer system. The XPS measurement chamber is equipped with a monochromatic Al Kα X-Ray source providing photon with hν = 1486.6 eV, operates at 10^{-9} mbar.

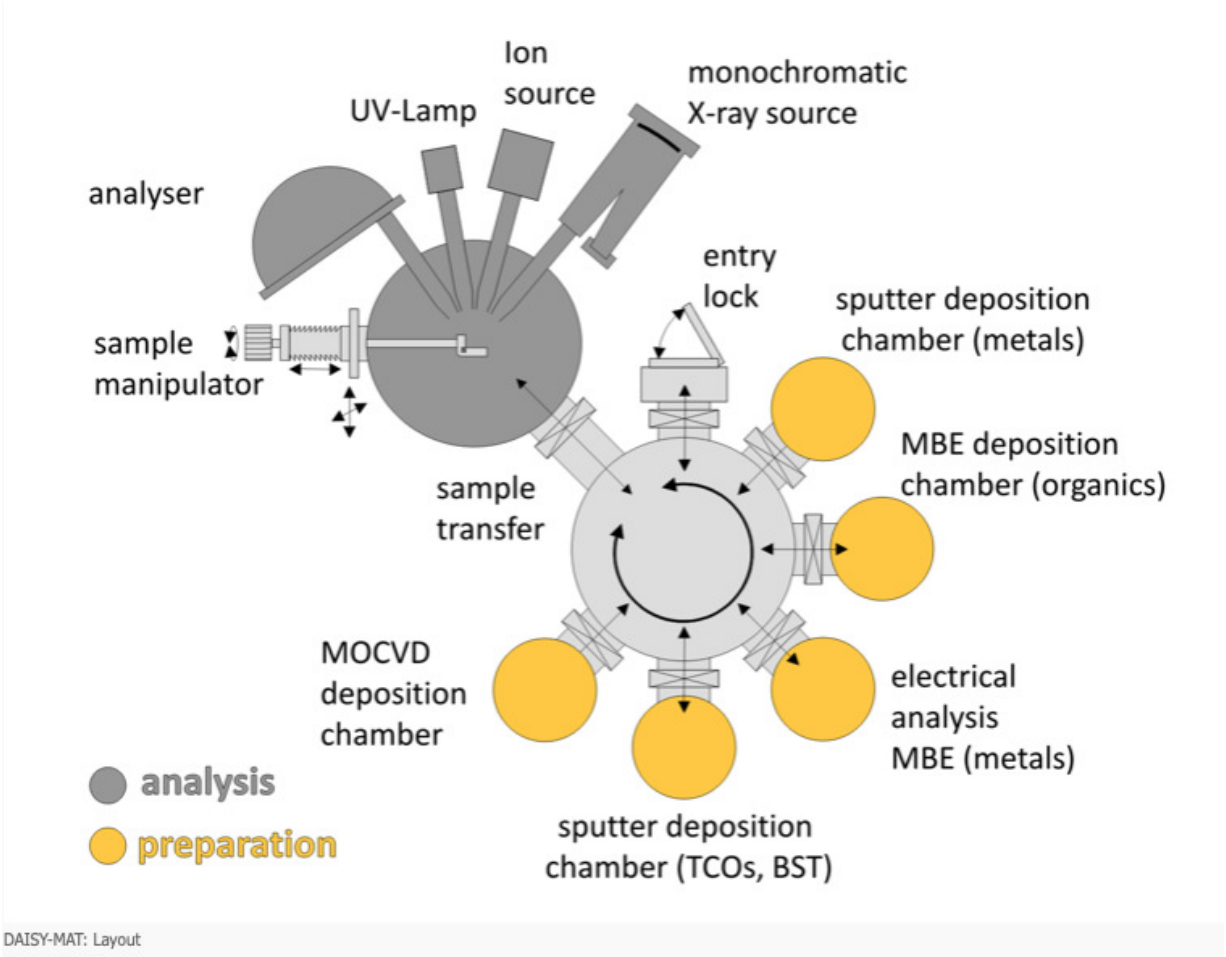

Figure 2.4: Layout of DAISYMAT system.

All spectra were measured at a photoelectron take-off angle of 0 (normal emission) and room temperature. Given that Φ_{sp} is a photoelectron spectrometer specific parameter, any deviation due to instrument factors during the measurement could be corrected by employing the calibration method, where the Fermi level of a cleaned metallic sample is measured and aligned to the binding energy of zero. For the samples studied in this thesis, the binding energies (BE) of respective elements were obtained in reference to the BE calibration that was performed through measuring the Fermi edge of sputter cleaned Silver (Ag) standard.

Ag standard XPS measurement procedure - For this, silver foil mounted on a stainless steel sample holder was used and the following steps were done:

i) argon ion gun sputtering of the Ag standard, for about ten minutes, using the sputtering parameters - kinetic energy of 1 keV and sample current of 0.9 μA for the sputtering area of 4 $\times$ 4 mm

ii) measuring the survey spectrum of Ag and confirming that there is no contamination (carbon or hydroxide) on the surface

iii) measuring the high resolution spectra of core level ($Ag3d_{5/2}$ that occur at 368.26 eV) and Fermi edge

These spectra were then utilised to perform the BE calibration for all the investigated samples.

For all the samples studied by XPS in this thesis, the photoelectron spectra were recorded under two modes: survey mode and high resolution mode. In survey mode, a broad range of binding energy (from - 1 to 1400 eV, that utilizes a pass energy of 187.75 eV, with 0.800 eV/step and 100 ms as energy step size and step duration, respectively) will be swept once, the spectra obtained is called as **survey spectra** (an example of ZnO with and without contaminants is shown in Figure 2.5a). Signals from Auger, valence and core electrons, along with a background (that increase with an increasing BE) could be identified in this survey spectra, which is usually performed to identify the chemical species and observe presence/absence of contaminants on the surface. In a high resolution mode, specific binding energy range that is of interest (core level (Zn2p, Figure 2.5b), auger (Zn LMM,Figure 2.5c) and valence band (of ZnO, Figure 2.5d) regions) will be swept for multiple times, called as high resolution photoelectron spectra. This spectra will give a detailed chemical and electronic information about the material being investigated and this measurement is carried out using a pass energy of 5.85 eV, with 0.050 eV/step and 100 ms as energy step size and step duration, respectively.

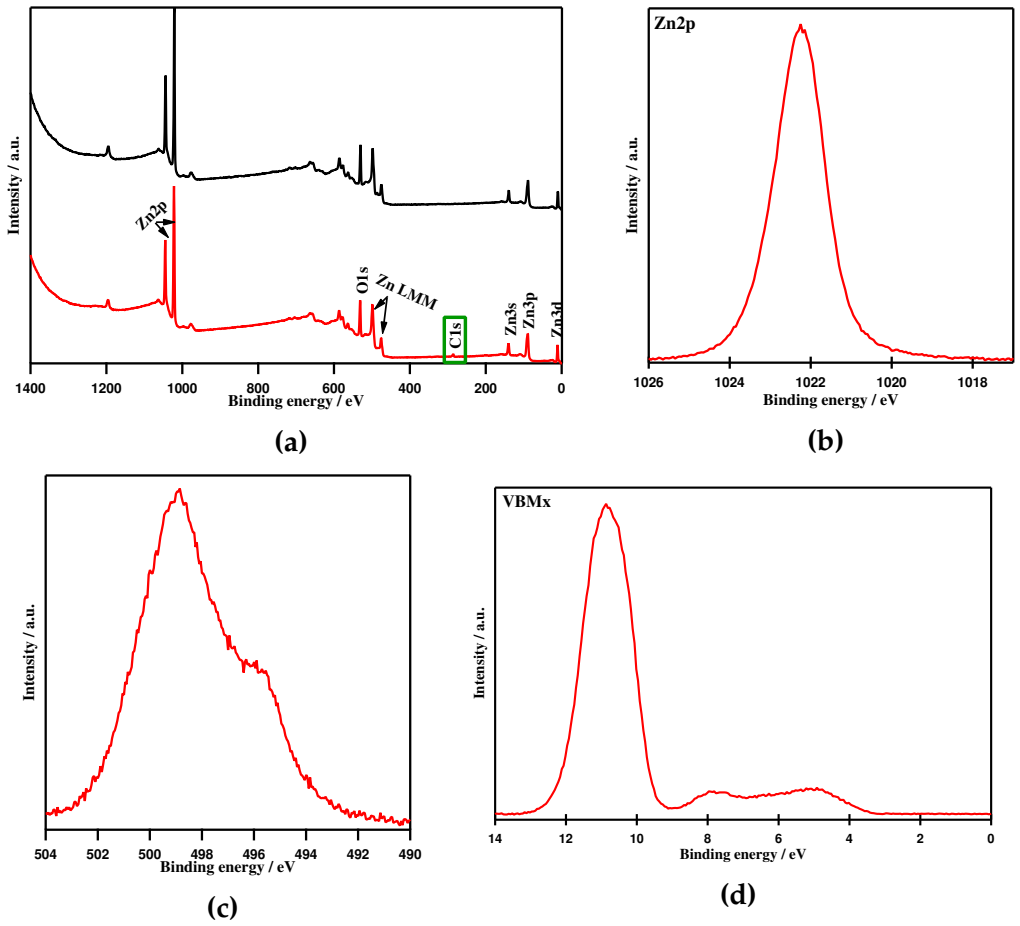

Figure 2.5: Example XPS spectra showing (a) Survey spectra of ZnO with (red line) and without (black line) contaminants displaying the core levels, auger and valence band regions and high resolution spectra showing (b) Zn2p, (c) Zn Auger and (d) valence band maximum spectra of ZnO.

Apart from the previously listed out common information that could be obtained from a typical XPS spectra, when a core level spectrum is identified with a secondary feature like shoulder or extra peak, this would indicate the change in actual chemical composition or the presence of adsorbates. For example, the shoulder peak that accompanies the oxygen (O1s) spectra (as shown in Figure 2.6) is associated to the presence of adsorbates. This kind of information could be used to distinguish the surface before and after an oxidation or reduction treatment. For example, in this thesis, ambience exposed ZnO was heat treated (at 400° C) in presence of oxygen. To confirm the removal of contaminants (apart from confirming the disappearance of carbon (C1s) peak), reduction in the shoulder peak of O1s spectra, along with an increase in its main peak (Figure 2.6) was considered.

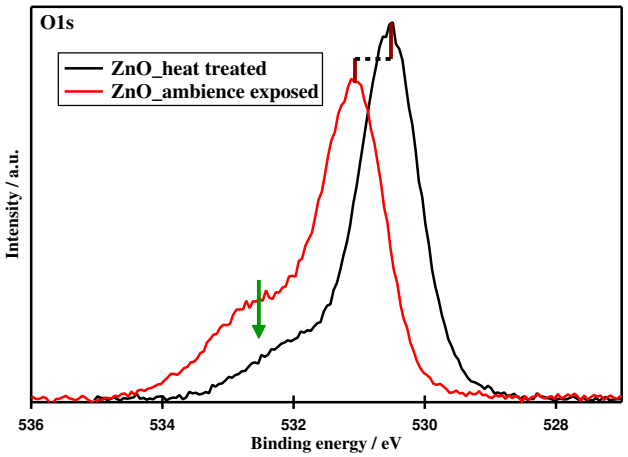

Figure 2.6: Oxygen (O1s) spectra of ZnO, where heat treated surface (black line) is identified with a reduced shoulder peak as compared to that of an ambience exposed surface (red line), along with an increase in intensity of the main line.

For the fitting procedures like difference spectra, intensity area calculation and deconvolution that are utilized in this thesis, background (that occurs as a result of inelastic electron scattering) subtraction have been performed. For this process, generally, Shirley [207] or Tougaard procedure is preferred over the conventional polynomial procedure, in regard to a physical point of view. Hence, in prior to all the fitting procedures involved in XPS spectra (discussed in this thesis), Shirley background correction was carried out.

2.2.1.1. Interface experiment procedures

Investigations regarding the interfaces between solids and between solid and liquid (or vapour) are highly interesting for understanding the function of devices and surface reactivity related to catalysis/photocatalysis processes, respectively. In case of a complete structure (for interface between solids), analysis of chemical and electronic properties of the interfaces are not possible, since photoemission is highly surface sensitive (interface properties in complete structure are buried under successively deposited layers). However, this could be overcome by studying the fundamental properties of interfaces, i.e, by carrying out a step-by-step film deposition and systematic photoemission analysis after each deposition step (The schematic of step-by-step investigation through interface experiment is shown in Figure 2.7).

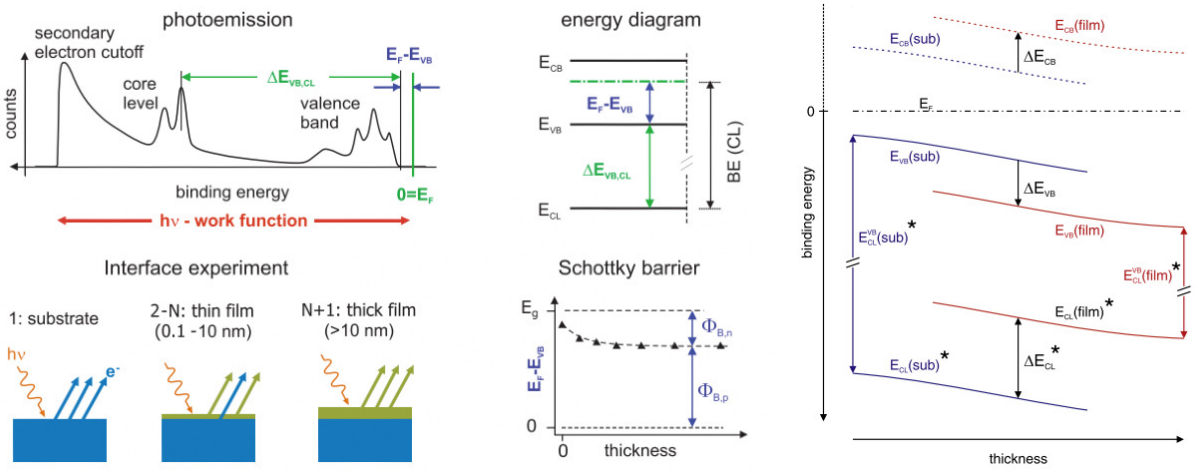

Figure 2.7: A schematic photoemission spectrum (Top left) and its relation to the energy band diagram (Top middle) of a semiconductor. Interface properties are obtained by stepwise depositing a contact material (Bottom left) and evaluating the chemical and electronic information as a function of film thickness (Bottom middle, example of schottky barrier evolution as a function of film thickness). Right side image shows the determination of energy band alignment between two semiconductors by photoelectron spectroscopy (using Kraut method [25]), where experimentally determined quantities are indicated by asterisks. Adapted from refs [26,27]

An interface experiment usually starts with a clean substrate surface, in our case, zinc oxide nanorods, which was introduced through the load lock (Figure 2.4), thereby shifting from ambient pressure to UHV (10^{-7} - 10^{-9} mbar) condition. The contact material (NiO or RuO_2) was deposited in several steps until a complete attenuation of the substrate signal is attained, to investigate the interface properties. Furthermore, as detailed in Section 3.4 and 3.5, ZnO surface without and with surface cleaning was used as the scaffold surface, for investigating the interfacial properties of NiO/ZnO (oxygen partial pressure during NiO deposition was also varied as a parameter) and RuO_2/ZnO.

For this type of layer-by-layer growth of the contact material, usually the targeted film thickness is about 5-10 nm, with respect to the inealstic mean free path requirements (3λ). As a result, for attaining a complete set of interface properties for the two involved materials, several deposition steps starting from the sub-monolayer coverage will be required. For this, XPS spectra of substrate surface was investigated to determine the initial valence band (VB) ($E_{VB,0}$(sub)) position and the binding energy difference between core level and VB ($E^{VB}_{CL,0}$(sub)). Similarly, after the growth of a relatively thick film (such that substrate signal is not seen), final VB ($E_{VB,final}$(film)) position and the binding energy difference between core level and VB ($E^{VB}_{CL,final}$(film)) can extracted (as shown in Figure 2.7). On attaining a thick film, the chemical states of contact film and substrate will not change thereafter and thus the core level to VBMx distance will become a constant, indicating that core level and VBMx

changes are occurring in parallel to the increase in film thickness. In fact, the VBMx position is valid only at the initial and final deposition steps, because, in the intermediate steps there will be an overlap of the valence band spectrum of contact material and the substrate. With all these information, one can gain insights into the growth modes of the deposited films, the chemical interactions at the interface and on the electronic properties (such as Schottky barrier heights, band discontinuities, shift in Fermi level positions and work function), with the help of such a systematic interface experiment.

2.2.1.2. Water exposure experiments

Apart from the solid/solid interface as detailed above, solid/liquid (vapour) interfaces were also investigated for NiO/ZnO, planar NiO and bare ZnO films. These experiments were carried out to understand the chemical changes (XPS interpretations) occurring at the surface of the material investigated, as a result of water adsorption. The step by step procedure for those interface experiments are detailed in Section 5.2. For this interface experiment, initially, the substrate material was inserted through load lock and transferred to the ALD chamber (Figure 2.4), which is typically involved with Al_2O_3 deposition. This chamber is also provided with a closed glass vessel that is filled with distilled water and connected through an ALD valve (a Swagelok 6LVV-ALD3FR4-P-C valve, pneumatically controlled with a MAC 34C-ABA-GDFC-1KT controller), which allows the connection between the vessel (at ambient pressure) and the chamber (UHV). Therefore this chamber was however here used for carrying out the water vapour exposure step. During the water exposure step, the ALD valve will be opened for a brief period of time, letting the flow of water vapour (40° C), thereby allowing it to condense onto the substrate surface. This procedure is repeated for several cycles, each with a wait time that allows vacuum recovering in the chamber (leaving no physisorbed water remains on the substrate/heterostructure surface). In our experiments, this step was performed with water exposure duration of 0.5 s, for 15 cycles, with a wait time or pumping down time of 60 s. And the photoelectron measurements were taken before and water exposure and also after contact material deposition, in case of heterostructure/liquid interface studies.

When the distilled water in the closed vessel reservoir needs to be refilled, the following procedure needs to be carried out with a degassing and for the same reason, the glass vessel was provided with two arms. In order to degas, water stored in one arm needs to be frozen with liquid nitrogen, followed by opening of the ALD valve for a short period of time (few seconds), to create vacuum in the reservoir. Furthermore, the other arm has to be cooled with liquid nitrogen while the arm with frozen water will be heated, to allow condensation and evaporation, respectively. This will be followed by opening of ALD valve

for few seconds and the repetition of the whole procedure for four times, to attain a stable water reservoir.

2.2.2. Photoluminescence (PL)

Photoluminescence is a simple, versatile, and non-destructive technique which is used for probing the electronic structure of the materials.

Principle

When light is directed onto a sample, photons are absorbed and electronic excitation (as a result of excess energy) occurs. This excess energy can be dissipated by the sample through the emission of light, or in other words, luminescence (photoluminescence). Photoexcitation will cause electrons within a material to get excited into their allowed excited states. On relaxation, these electrons will return to their equilibrium (or ground) states, resulting into the release of excess energy in the form of light emission or in the form of vibrations/phonons that result into a radiative or non-radiative process, respectively (Figure 2.8) [28]. The energy of the emitted light (photoluminescence) is typically based on the difference in energy levels between the two electron states (process of transition between the excited state and the equilibrium state).

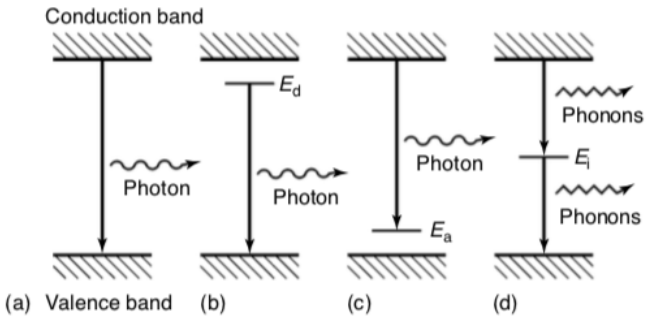

Figure 2.8: Radiative recombination paths: (a) band-to- band; (b) donor to valence band; (c) conduction band to acceptor and (d) Nonradiative recombination via an intermediate state. [28]

Further detailed characterization about the underlying electronic states and bands can be done by applying external parameters like temperature and applied voltage to the samples. In addition to the quantitative information (about amount of light emitted and its relation to the relative contribution of the radiative process), the intensity of the PL signal also provides information regarding the quality of surfaces and interfaces, which is useful when analysing the behaviour of photocatalysts upon light irradiation. Moreover, PL is

claimed to be sensitive to oxygen vacancies (especially for oxides like ZnO) but the peak assignments are still a subject of debate (for ZnO). Despite the controversies, PL analysis has shown interesting revelations about the process of inducing or filling of oxygen vacancies owing to the temperature and atmosphere conditions involved during the post processing treatments. The ordinary RT-PL work has the instrumentation that includes an optical source and an optical power meter or a spectrophotometer (a typical setup is shown in Figure 2.9).

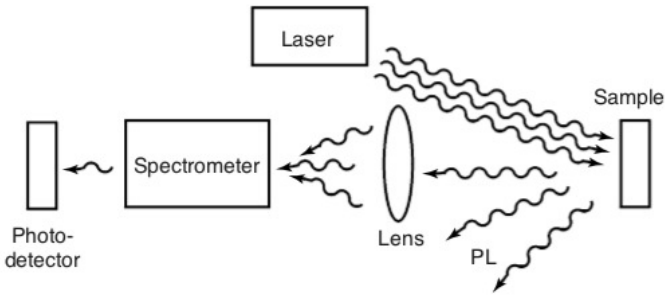

Figure 2.9: Typical experimental set-up for PL measurements. [28]

The information that could be extracted using RT-PL spectra and its relation to the material's optical properties are listed below:

i) Peak shifts - can be red or blue shift depending on whether the shift is towards higher or lower wavelength. In general, red shift is associated to an increase in crystallite size and the reverse for blue shift, commonly identified as the impact from change in quantum confinement effect in the material.

ii) Peak broadening - increase or decrease in the full width half maximum (FWHM) of the peak is often related to the quality of interface when a combination of two materials (like heterostructures) is analysed. Broadening is attributed to the increase in interface fluctuations, while narrowing is related to its decrease (meaning high quality interface) [28].

iii) Intensity - the intensity of the peaks could be used to deduce the ratio between shallow and deep level defects. PL is a dominant tool in identifying the presence of defect levels in the examined material, and the emissions that occur in the range of 300 - 800 nm are categorized into distinctive regions like UV, blue, green, orange and red emissions [17, 157, 208]. Among them the two broadly classified regions are called the near band edge emission (NBE, 380 - 400 nm) and the deep level emission (DLE, 450 - 800 nm). By comparing the ratio of intensity area of these two peaks, one can understand the role played by defects and control their influence by varying the material prepara-

tion parameters.

In this thesis, the intensity ratios were calculated by deconvoluting the spectra into distinctive regions and then obtaining the corresponding area (for NBE [I_{NBE}], DLE [I_{DLE}] and total [I_{Total}] regions of the spectra) below the deconvoluted peaks (using a data analysis software, IgorPro) in PL spectra. An example deconvoluted photoluminescence spectra of NiO/ZnO heterostructure thin film is shown in Figure 2.10.

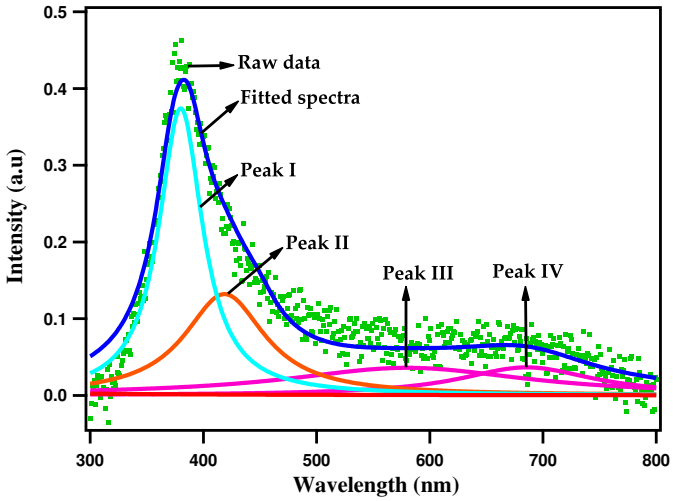

Figure 2.10: Example of deconvolution of the photoluminescence spectra of NiO/ZnO heterostrcuture. Green dotted line represents the raw data, blue line displaying the fit data, black line (Peak I, near band edge emission), magenta lines (Peak II - IV, deep level emission) are the deconvoluted lines.

The DLE peak area is obtained by subtracting the area of NBE peak from the total (fitted) area of the spectrum. Moreover, in order to compare the amount of defect levels present in scaffold films (ZnO) and heterostructures, the ratio calculation was done (for the heterostrcutures) by using the total area of their respective scaffold films (cleaned or uncleaned scaffold).

In our study, PL emission spectra of ZNR, NiO/ZnO and RuO_2/ZnO films (examined area = 2cm $\times$ 2cm) were acquired using a Varian Cary Eclipse, Fluorescence Spectrophotometer equipped with a Xenon flash lamp, which was operated at an excitation wavelength of 325 nm, while emissions were recorded in the range of 300-850 nm. All measurements were done at room temperature.

The other characterization techniques used to analyse the samples of investigation and the Pollutant degradation experiment procedures are detailed in the Appendix.

Chapter 3

Influence of surface cleaning in the interface analysis of NiO/ZnO and RuO_2/ZnO heterostructures

3.1. Experimental strategy

A typical photocatalytic process involves three vital charge kinetics steps as follows: i) charge carrier generation, ii) effective charge separation and transfer and iii) effective charge consumption [58]. They are often considered to be interdependent with each other and compromising any of these steps will result in slower performance in kinetics, thereby affecting the efficiency. These three processes are more effective when heterostructures are used. However, the complexity involved in deciphering the charge transfer mechanism increases (as compared to scaffold), while the comprehension of the charge transfer and separation mechanism is vital. Therefore, one needs to pay closer attention to the overall structure engineering (surface and interface and energy band) of the photocatalyst while designing it [14].

In this chapter, with the aid of step-by-step in-situ XPS analysis, the suitability of NiOand RuO_2 as second material, in building heterostructured with ZnO is investigated. Both NiO and RuO_2 are considered as good co-catalysts due to their excellent electrical and optical properties. NiO is a wide bandgap semiconductor that can act as a hole transport layer and joining it with ZnO will lead to the formation of a p-n heterojunction with an internal electric field developed at the interface [209, 210]. RuO_2 is a transition metal oxide, exhibiting metallic behaviour owing to its partially filled metal-oxygen band and hence,

RuO_2/ZnO leads to a metal/n-type heterojunction [115]. While NiO/ZnO heterostructures were already studied for photocatalytic applications, RuO_2/ZnO were reported only recently [115].

Chemically prepared ZnO is known to have oxygen vacancies, which will alter the interfacial properties significantly [211]. In order to improve the interface with the second material and the charge separation, the ZNR surface was heat treated in presence of oxygen. Such treatments are believed to be helpful in filling the oxygen vacancies and also in removing the adsorbates and impurities [155]. The interface studies in the presence and absence of adsorbates (surface cleaned ZNR) allow exploring the influence of surface states on the achieved band alignment, which was not yet explored before for NiO/ZnO and RuO_2/ZnO.

3.2. Optimization of ZNR scaffold

There are several techniques like vapor-liquid-solid (VLS) growth, vapor-solid (VS) growth, physical vapor deposition (PVD) or chemical vapor deposition (CVD) available for the growth of one dimensional (1D) ZnO nanorods. However, these techniques rely on expensive equipments and high temperature operations (up to 900 °C) leading to high production costs and non-compatibility with certain substrates. The hydrothermal method is known for its mild operating conditions, easy implementation and is considered a good alternative for obtaining aligned nanostructures like ZNR [104]. In order to control the width of the nanorods and their packing density, we have approached three routes, from which the optimized ZNR scaffold was chosen.

a) ZNR - without seed layer

b) ZNR - with seed layer, from 5 mM solution (detailed below, in seeding layer preparation step) exposure

c) ZNR - with seed layer, from 250 mM solution exposure

All the ZNR samples were grown on FTO glass substrates purchased from Dyesol (15Ω/sq.). Before use, the substrates were cleaned for 15 minutes (min) each with acetone and then ethanol, by using an ultrasound bath.

Step 1: Seeding layer preparation: 0.68 g of zinc acetate dihydrate (Sigma Aldrich, ≥99%) and 225 mL of the stabilizing agent, ethanolamine (Sigma Aldrich, ≥99.5%) were added to 15 mL ethanol (VWR, ≥99.8%), to result in 250 mM solution. This mixture was stirred at 60 °C for an hour to attain a homogenenous solution. Stirring was continued

further at room temperature (RT), for 24 hours. Then 500 μL of the homogeneous solution were spin coated on FTO substrates at 3000 rpm, for 20 seconds(s) and the relative humidity (RH) was maintained at 35% during the coating process. This process was repeated 5 times, to ensure complete coverage of the substrate with seeds. Seeded substrates were annealed at 500 °C for 2 hours(h) (ramp = 300 °C/h).

Step 2: Nanorod growth: 0.072 g of zinc nitrate hexahydrate (Sigma Aldrich, ≥99%) and 0.052 g of hexamethylenetetramine (Sigma Aldrich, ≥99.5%) were added to 15 mL of milliQ water and stirred until a homogeneous solution was obtained, which was later transferred to a Teflon lined autoclave. The seeded substrate was immersed in the solution in a tilted position, with the coating facing downward. The hydrothermal process was carried out in an oven at 92 °C, for 1 hour. Afterwards the sample was washed with distilled water, dried in oven at 60 °C for 30 min and finally calcined at 500 °C for 2 h.

The schematic of the proposed routes and the resultant structures are represented in Figure 3.1, based on the observations from SEM images (Figure 3.2). The densely packed ZNR were further used.

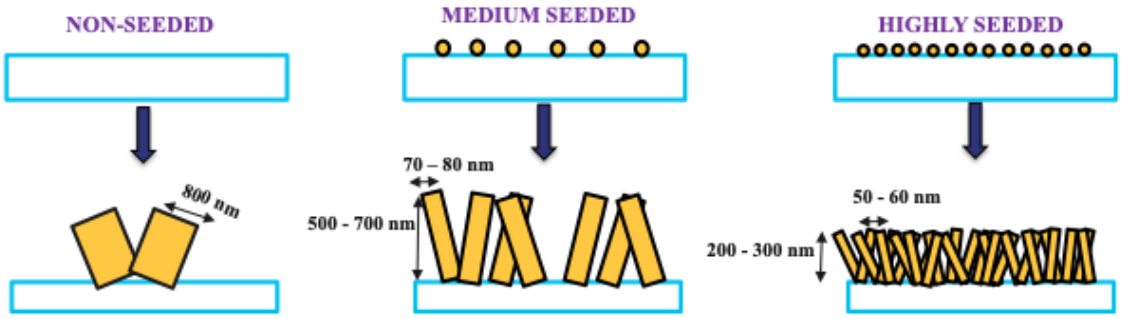

Figure 3.1: Schematic representation of the ZNR film growth optimization.

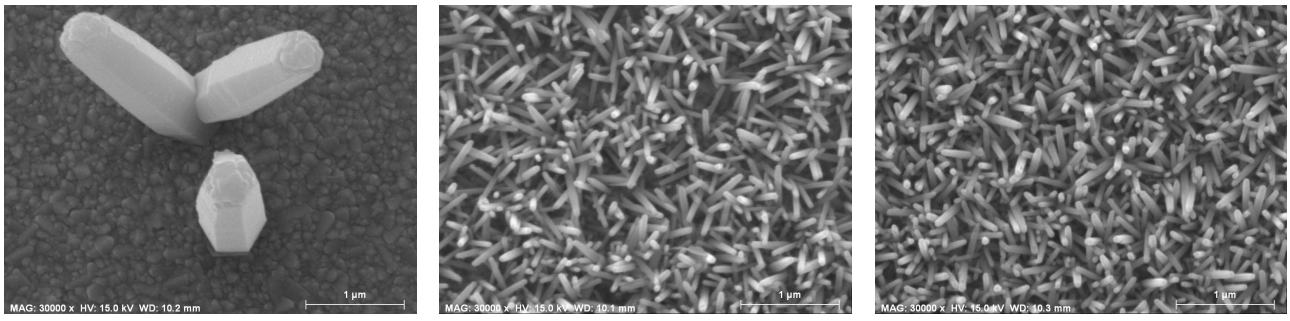

(a) **(b)** **(c)**

Figure 3.2: SEM image of ZNR film (a) without seed layer, (b) with 5 mM seed layer and (c) with 250 mM seed layer.

Very wide nanorods with low packing density (Figure 3.2a), medium packed nanorods (Figure 3.2b) and densely packed aligned nanorods [corresponding to an average aspect ratio of 5] (Figure 3.2c) were hydrothermally grown as function of the seeding layer concentration.

For further optimization of the desired surface to form the heterostructure, a post-processing method like heat treatment was used and both surfaces were compared in all studies reported in this thesis.

The crystallinity and orientation of the hydrothermally grown ZNR were confirmed by X-Ray diffraction (Figure 3.3). The (002) peak corresponding to the wurtzite phase of ZNR (JCPDS card no. 79 - 2205) at $2\Theta = 34.50^{\circ}$ was observed in all the films but with varying intensities based on the concentration of the seeding layer solution, confirming the growth along the c-axis. The intensity of (002) plane was increased with increasing seeding layer precursor concentration and the seed layer made with 250 mM solution showed the highest. This means that in comparison, ZNR prepared from the high concentration achieved more dense and aligned nanostructure than others. And it clearly demonstrates that the growth of ZnO nanorods has taken place along c-axis, confirming the one-dimensional structure growth as desired. Moreover, XRD results are in good agreement with the SEM observations, i.e. when a higher precursor concentration is used, a more densely packed ZNR is obtained.

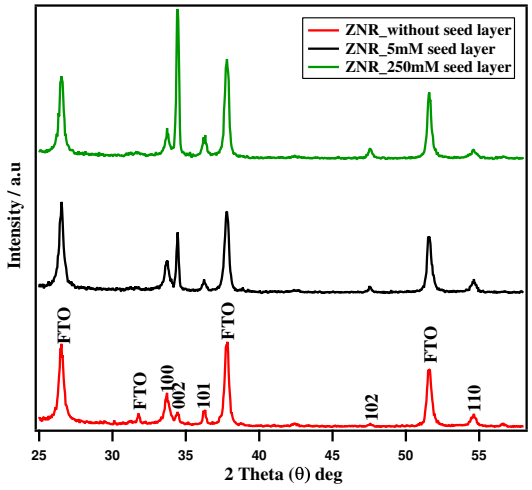

Figure 3.3: XRD spectra of ZNR film.

3.3. Sample description

The ex-situ - ZNR surface, as prepared from hydrothermal growth, is expected to have adsorbates/impurities like hydroxides and carbon due to the exposure to ambient conditions. This surface was named **Z1** throughout the thesis.

In-situ - heat treatment is used as a surface cleaning technique to remove the adsorbates and impurities. The heat treatment was carried out in Ultra High Vacuum (UHV) in the sputtering chamber, in a controlled and static oxygenated atmosphere (Pressure (P_{Tot}) - 0.5 Pa, Oxygen flow - 5 sccm, Temperature (T) - 400° C, Time - 1 h). This cleaned surface is denominated as **Z2**.

Both Z1 and Z2 were used as scaffolds for performing the interface studies with NiO and RuO_2. NiO was deposited step-wise at 40 W power (P) with other parameters as Pressure (P_{Tot}) = 0.5 Pa, Temperature (T) = Room temperature (RT) and substrates to target distance (D_{st}) = 8 cm. The oxygen partial pressure P_{O_2} was varied as 6 and 20% leading to a deposition rate of 15 nm/min and 1.5 nm/min respectively [deposition rates were estimated from thickness observations by profilometer]. And the XPS measurements were done initially on the scaffold and then after each step of NiO deposition. In order to avoid the complete attenuation of scaffold material signal, the number of steps and time of deposition was varied, as a function of the type of scaffold used and P_{O_2} used during the NiO deposition. Based on the parameters employed, the samples were denoted as follows:

a) **Z1N6%** - for P_{O_2} = 6% (O_2 - 1.2 sccm and Ar - 18.8 sccm), Deposition time - 0 to 24 seconds (4 steps)

b) **Z2N6%** - for P_{O_2} = 6% (O_2 - 1.2 sccm and Ar - 18.8 sccm), Deposition time - 0 to 48 seconds (5 steps)

c) **Z2N20%** - for P_{O_2} = 20% (O_2 - 4 sccm and Ar - 16 sccm), Deposition time - 0 to 160 seconds (4 steps)

Concurrently, stepwise deposition of RuO_2 was carried out by DC sputtering under the following parameters:
P_{Tot} = 1 Pa, P = 10 W, D_{st} = 9.4 cm, Deposition rate = 3 nm/min, Argon flow (Ar) = 9.25 sccm, Oxygen flow (O_2) = 0.75 sccm, T = RT and Time = 320 s (Z1), 640 s (Z2).
RuO_2 deposited on Z1 and Z2 are denoted as Z1R and Z2R respectively. Again, XPS measurements were done initially on the scaffolds (Z1 and Z2) and then after each step of RuO_2 deposition (relative to each scaffold). As described in ZnO/NiO deposition, here as well, deposition time is varied based on the variation in the ZNR surfaces, such as to avoid

complete attenuation of the signal from the scaffold material.

3.4. Interface analysis of the NiO/ZnO heterostructure

Figure 3.4 shows the corresponding survey spectra of Z1N6%, Z2N6% and Z2N20%, recorded after each step of the analysis. The survey scan of the scaffolds Z1 and Z2 at the initial step showed the presence of Zn and O, while all the following steps after the NiO deposition confirmed, in addition, the presence of Ni [115, 212, 213]. Any peaks other than those characteristic to ZnO and NiO were not detected, except for Z1, for which C1s was detected. The C1s disappeared after the surface cleaning (Figure 3.4d, sample Z2), confirming that impurities were removed [214].

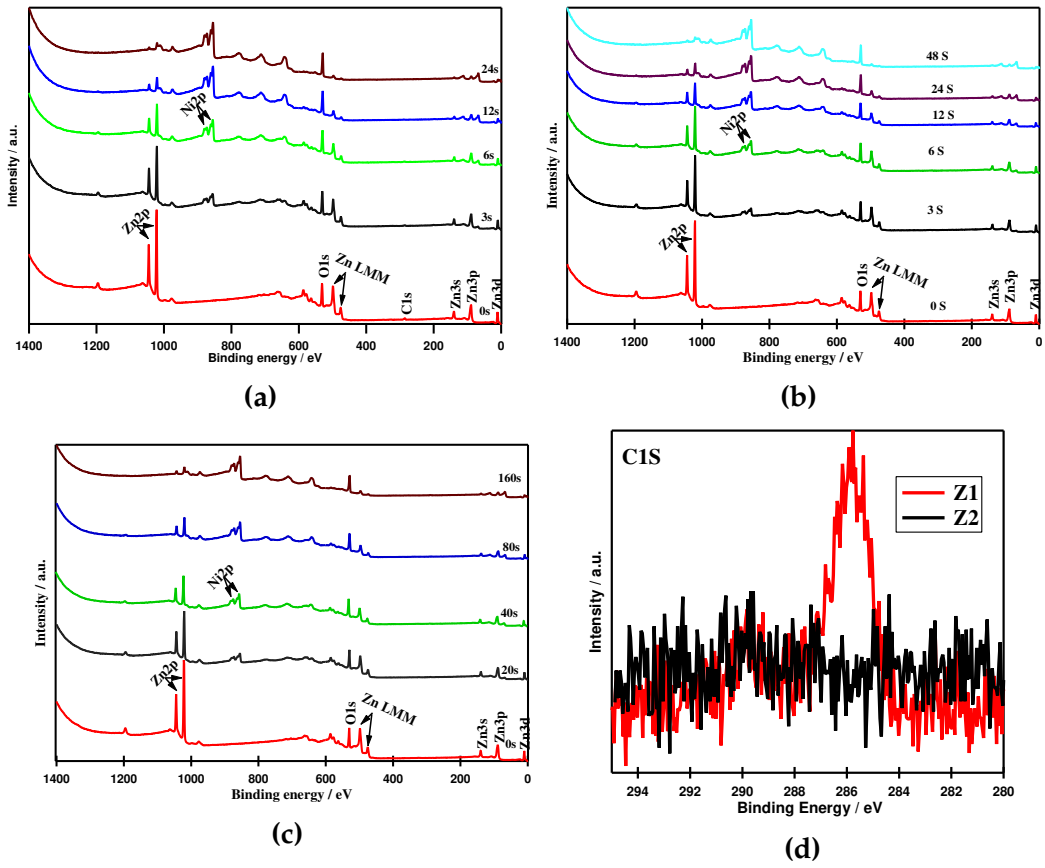

Figure 3.4: Survey spectra of (a) Z1N6%, (b) Z2N6% and (c) Z2N20%. C1s spectra of Z1 and Z2 scaffolds (d).

The Zn2p, Ni2p and O1s core levels are represented as function of deposition time in Figure 3.5. The Zn2p emission line is usually observed as two symmetrical peaks centered at $\simeq$ 1021 eV and $\simeq$ 1044.5 eV, due to the $Zn2p_{3/2}$ and $Zn2p_{1/2}$ core level states of Zinc [115].

Throughout the thesis, the $Zn2p_{3/2}$ alone is taken into consideration (Figures 3.5a, 3.5d and 3.5g).

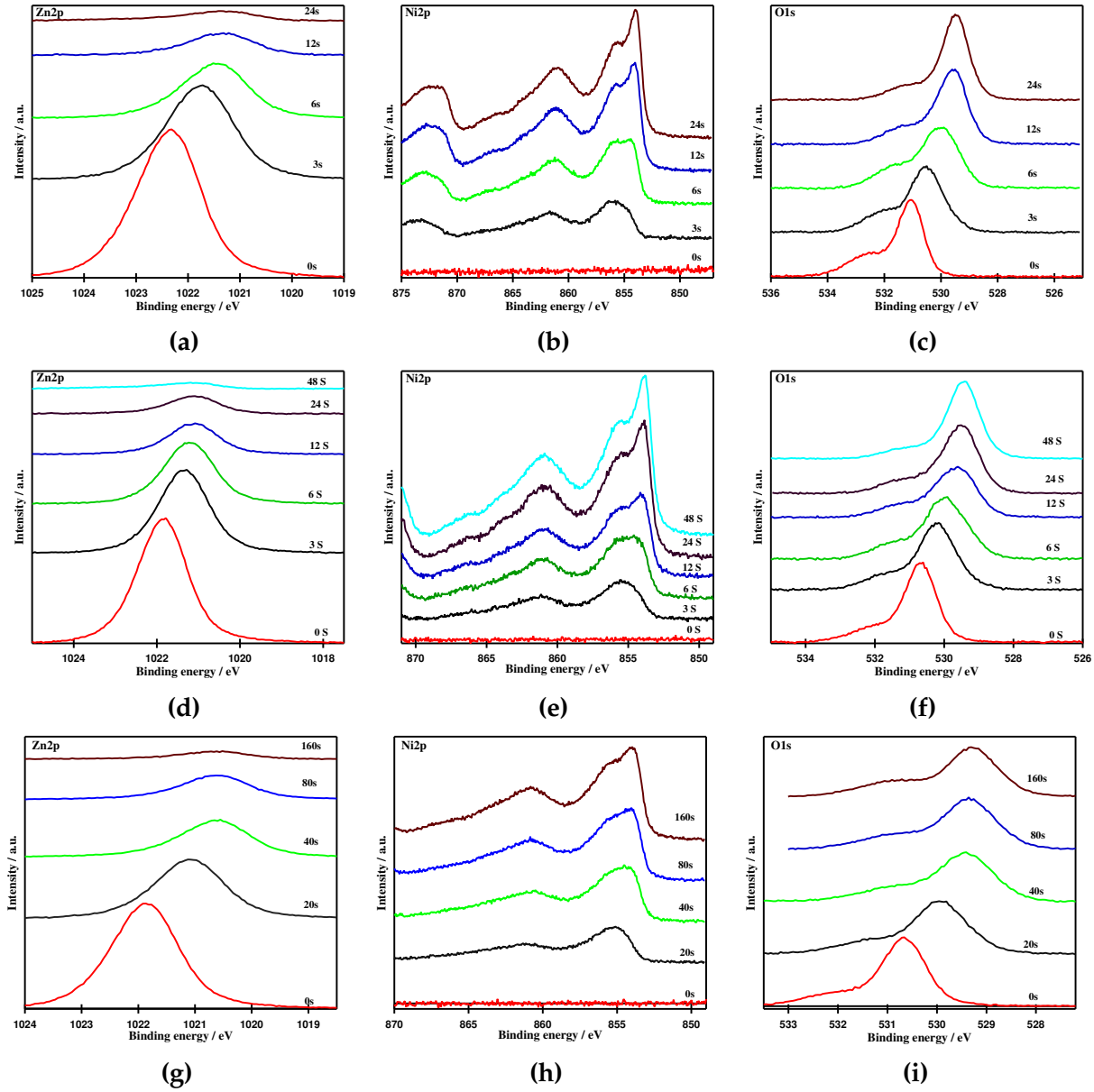

Figure 3.5: Spectra of Zn, Ni and O emission lines for Z1N6% (a-c), Z2N6% (d-f) and Z2N20% (g-i), respectively.

At the initial step, the core level of $Zn2p_{3/2}$ was observed at 1022.33 eV for Z1N6% (Figure 3.5a, Table 3.1) and at 1021.86 eV for Z2N6% (Figure 3.5d, Table 3.1). This shift is attributed to the process of surface cleaning and could be correlated to the disappearance of the C1s peak in Z2 [214]. Figures 3.5a, 3.5d and 3.5g shows that under all conditions, the intensities were reduced with increasing NiO thickness. But no significant changes were observed in their line shape, apart from an inconsistent line width broadening, which might

be due to the interface study conditions involved.

Table 3.1: Zn2p, O1s, $Ni2p_{3/2}$, $Ni2p_{Sat}$ and VBMx binding energies deduced from the XPS spectrum. Subscripts accompanying the sample code represent the NiO deposition time.

Sample Code		Zn2p BE (eV)	O1s Be (eV)	$Ni2p_{3/2}$ BE (eV)	Ni_{Sat} BE (eV)	E_F - VBMx (eV)
Without surface cleaning (Z1)	$Z1N6\%_{0s}$	1022.33	531.05	-	-	3.46
	$Z1N6\%_{3s}$	1021.75	530.53	855.50	861.59	2.88
	$Z1N6\%_{6s}$	1021.45	530.04	854.45	861.27	2.58
	$Z1N6\%_{12s}$	1021.36	529.57	854.14	861.12	2.49
	$Z1N6\%_{24s}$	1021.33	529.47	853.95	861.10	2.46
Surface cleaned (Z2)	$Z2N6\%_{0s}$	1021.86	530.66	-	-	3.06
	$Z2N6\%_{3s}$	1021.32	530.20	855.47	861.16	2.52
	$Z2N6\%_{6s}$	1021.21	529.97	855.15	861.10	2.41
	$Z2N6\%_{12s}$	1021.09	529.63	854.20	861.05	2.29
	$Z2N6\%_{24s}$	1021.05	529.51	853.90	861.02	2.25
	$Z2N6\%_{48s}$	1020.97	529.43	853.86	861.02	2.22
Surface cleaned (Z2)	$Z2N20\%_{0s}$	1021.87	530.65	-	-	3.10
	$Z2N20\%_{20s}$	1021.13	529.95	855.32	861.30	2.44
	$Z2N20\%_{40s}$	1020.70	529.43	854.68	861.20	2.01
	$Z2N20\%_{80s}$	1020.66	529.36	854.23	861.06	1.97
	$Z2N20\%_{160s}$	1020.61	529.26	853.93	861.03	1.92

The multiplet split of the Nip[29,212,213] line was identified with a major peak at $\simeq$ 853.9 eV (Figures 3.5b, 3.5e and 3.5h, Table 3.1), irrespective of the NiO thickness after the final deposition step. This emission line could be attributed to the Ni^{2+} state and the multiplet peak was assisted with a satellite peak centered at $\simeq$ 861.1 eV (Figures 3.5b, 3.5e and 3.5h,

Table 3.1). While the intensities of the Ni2p emission line were seen to be increasing with each step of NiO deposition, its line shape was changing gradually and systematically.

The sample Z1N20%, where the thickness after the final step was $\simeq$ 4 nm (estimation of thickness is based on the deposition rate), exhibited an entangled multiplet (Figure 3.5h). Concurrently, the Ni2p emission lines at the final step for Z1N6% and Z2N6%, whose thickness were $\simeq$ 6 nm and $\simeq$ 12 nm respectively, displayed a well resolved multiplet (Figures 3.5b and 3.5e, respectively). This systematic changes are ascribed to the P_{O_2} involved and also the thickness attained at the final step of analysis.

As shown in Figures 3.5c, 3.5f and 3.5i, the O1s core level lines were observed initially at 531.04 eV for Z1N6% and at 530.6 eV for Z2N6% (Table 3.1), both accompanied by a shoulder that correspond to the surface hydroxyls. The shift towards lower BE of the Z2N6% O1s emission line is the result of two effects, the increasing NiO layer thickness and the surface cleaning.

All the core level lines (Zn2p, Ni2p and O1s, Figure 3.5) and the VBMx (Figure 3.6) were seen to be shifting towards the lower BE, as a function of NiO deposition. This shift indicates the charge transfer between the materials (ZnO and NiO) and thereby the superposition of contact formation and variation in chemical environment [177, 213, 215].

Given that the withdrawal or addition of valence electrons occurs as a result of changes in chemical bonding of the environment, such changes can be observed as chemical shifts in XPS. The BE shifts observed here due to the charge transfer, are due to the space charge layer formation at the interface of NiO/ZnO.

The VBMx at each step was determined by the extrapolation method where the BE of valence band onset intersects the background. The E_F - VBMx difference at initial step was determined to be 3.46 eV for Z1N6% (Figure 3.6a) and 3.06 $\pm$ 0.05 eV for Z2N6% (Figures 3.6b and 3.6c), in Table 3.1, revealing its n-type behaviour. At the same time, E_F - VBMx values of 0.74 eV and 0.61 $\pm$ 0.03 eV were extracted for NiO on the Z1 and Z2 scaffolds respectively, affirming its p-type characteristics. The gradual changes in the E_F - VBMx values of Z1N6%, Z2N6% and Z2N20%, as a function of deposition time (Figures 3.6d and 3.6e) were plotted to emphasize the role of surface states or defects in the interface. The obtained plots evidence that the VBMx position was lowered rapidly with the progress in deposition steps and at higher steps, saturated after 20(40) s for the Z1(Z2)N6% and after 80 s for Z2N20% [211].

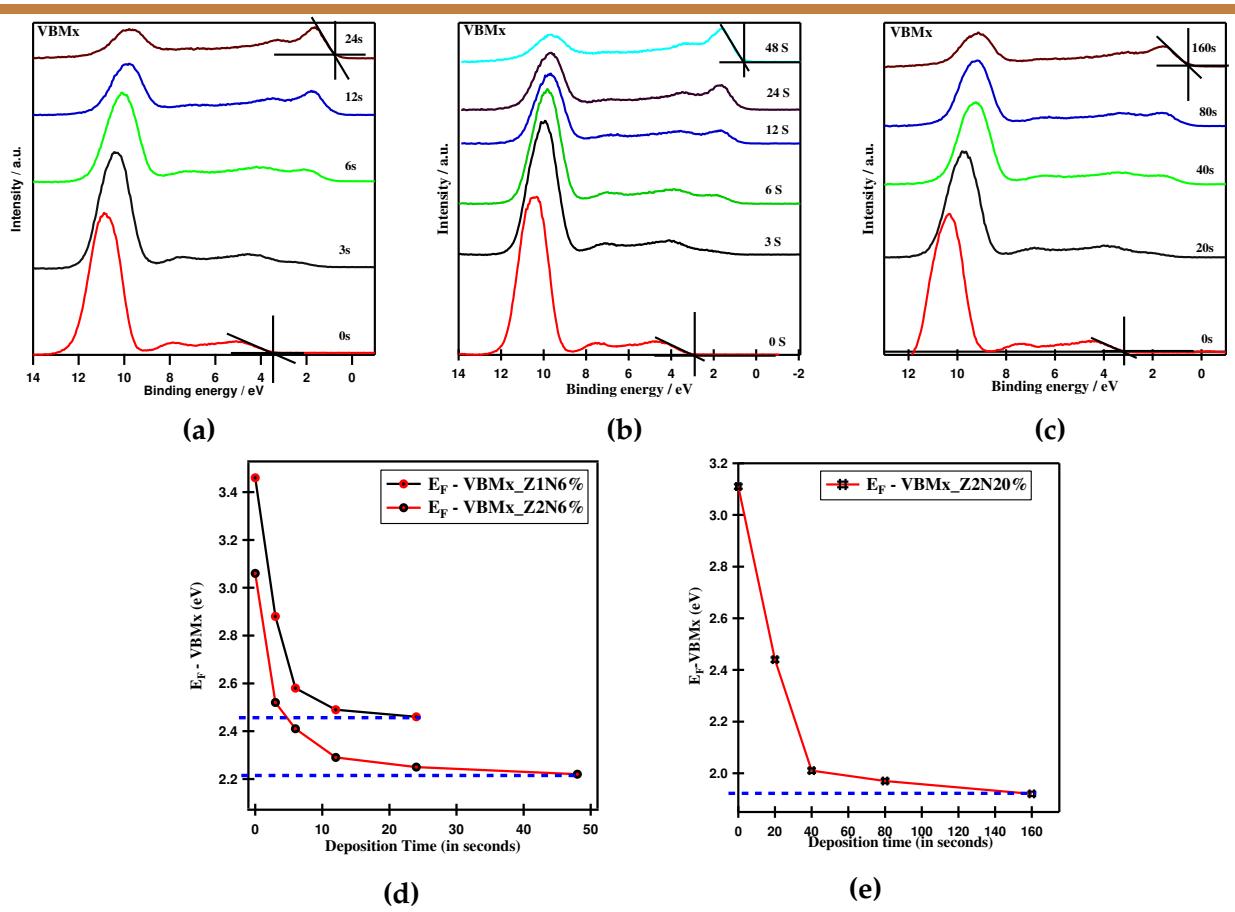

Figure 3.6: Spectra of VBMx for (a) Z1N6%, (b) Z2N6% and (c) Z2N20% and mapping of E_F-VBMx Vs Deposition Time for (d) Z1N6%, Z2N6% and (e) Z2N20%.

To further elucidate the existence of underlying components, the Ni2p and O1s (deconvoluted,Figure 3.7) core level lines were examined. As mentioned earlier, Ni2p exhibited a broader spectrum during the initial steps which evolved into either an entangled multiplet [Z2N20%] or a well characterized multiplet [Z1N6% and Z2N6%] after the final step. Therefore, only the Ni2p spectral line after the final step (Figures 3.5b, 3.5e and 3.5h) was studied in all cases. They revealed the presence of the typical NiO spectra as seen in the spectra of Figures 3.5b and 3.5e at final deposition step (similar to the example presented in Figure 3.7a, from the report of Biesinger et al.[29]) that comprised of three peaks: the main peak at $\simeq$ 853.9 eV attributed to Ni^{2+}, the shoulder peak at higher BE $\simeq$855.5 eV, due to the presence of $Ni(OH)_2$ or NiOOH and the third one situated at $\simeq$ 861.1 eV corresponding to the satellite, (Ni_{Sat}, Figure 3.7b). At lower coverage (in Figures 3.5b, 3.5e and 3.5h) and as seen in the spectrum of Figure 3.7b, there are evidently additional contributions of either $Ni(OH)_2$ or NiOOH, which lead to an increased contribution of the shoulder line at BE $\simeq$855.5 eV.

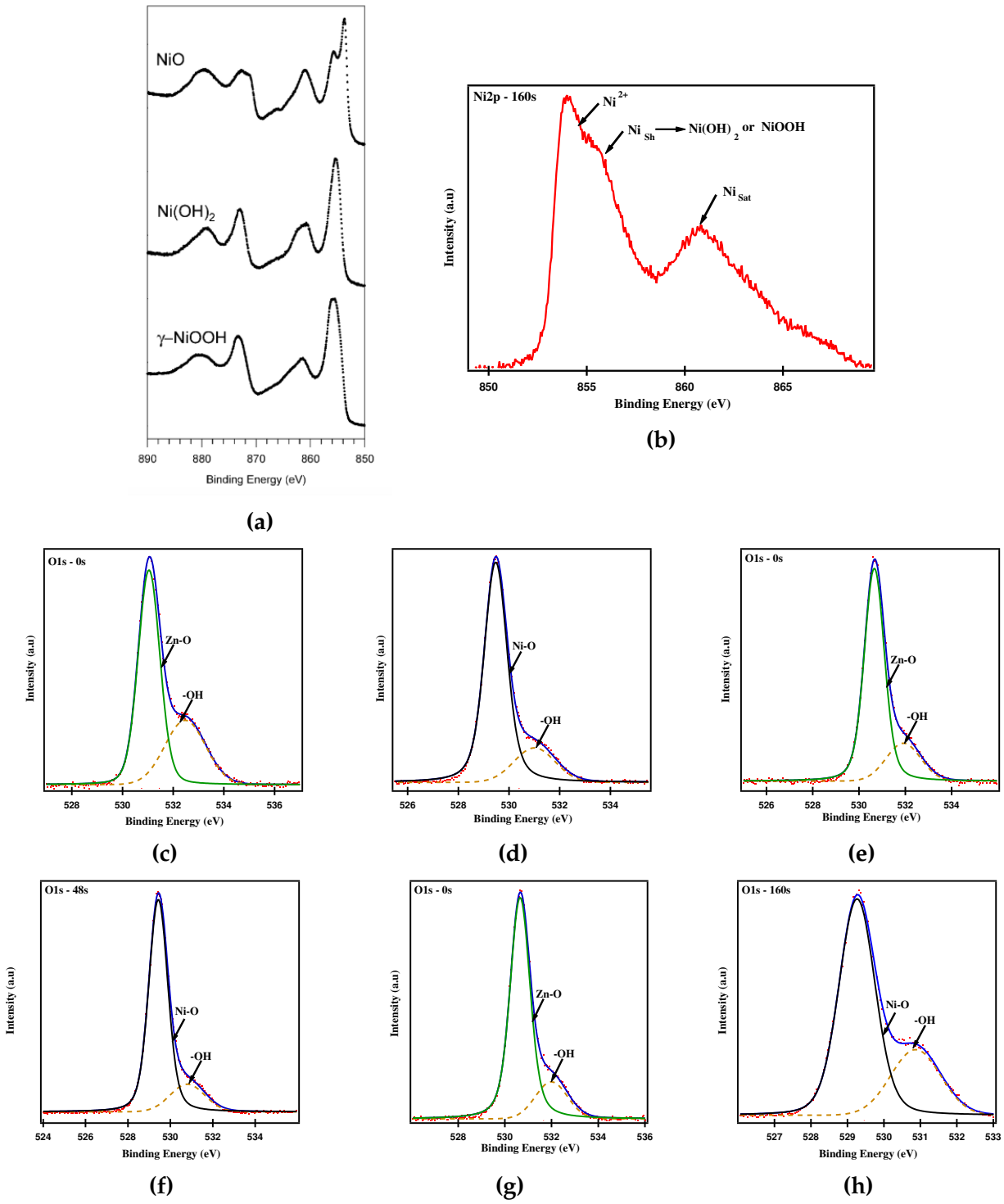

Figure 3.7: Example of Ni2p spectra from Biesinger et al.[29] (a) and the spectra of Ni2p at 160s for Z2N20% (b); Deconvolution spectra of O1s at 0 s and 24 s (c and d), 0 s and 48 s (e and f) and 0 s and 48 s (g and h) deposition time, for Z1N6%, Z2N6% and Z2N20% respectively.

In case of O1s core level lines, the deconvolution was performed at the first and final step, in order to better understand the evolution. In all cases, the deconvolution of O1s at both steps displayed the contribution of two components oxygen in the lattice (O_L) and surface hydroxyls (O_{OH})[115,177]. As a scaffold, for Z1N6%, O_L and O_{OH} were centered at 531.04 eV and 532.47 eV respectively, whereas for Z2N6% and Z2N20%, the corresponding peaks were centered at $\simeq$ 530.6 eV and $\simeq$ 531.9 eV (Figures 3.7c, 3.7e and 3.7g respectively, Table 3.2). And the O_L here is attributed to Zn-O bonding.

Table 3.2: Binding energy values of the deconvoluted O1s (O_L of Zn-O, O_L of Ni-O and O_{OH}) and Ni2p (Ni^{2+} and Ni_{Sat}) peaks for the initial and final steps of analysis and the O_{OH}/O_L ratio at the final step, deduced from XPS spectrum (Deconvolution of the spectra was done using IgroPro software, after Shirley background subtraction). Subscripts accompanying the sample codes represent the NiO deposition time.

Sample Code	O_L of Zn-O / O_L of Ni-O BE (eV)	O_{OH} BE (eV)	O_{OH}/O_L	Ni^{2+} BE (eV)	Ni_{Sat} BE (eV)
$Z1N6\%_{0s}$	531.04 / -	532.47	-	-	-
$Z1N6\%_{24s}$	- / 529.47	531.00	0.20	853.95	861.10
$Z2N6\%_{0s}$	530.66 / -	531.90	-	-	-
$Z2N6\%_{48s}$	- / 529.43	530.80	0.18	853.86	861.02
$Z2N20\%_{0s}$	530.65 / -	531.99	-	-	-
$Z2N20\%_{160s}$	- / 529.26	530.87	0.28	853.93	861.03

At the final step, O_L and O_{OH} were observed in the range of 529.26 - 529.47 eV and 530.8 - 531 eV respectively (Figures 3.7d, 3.7f and 3.7h), where the O_L here is related to Ni-O bonding[177,213,215]. Given that the O_{OH} that occurs after interface formation is situated in the same region as that of O_L corresponding to Zn-O, O_{OH} and O_L of Zn-O are expected to be overlapped.

It is important to note the broadening in the O_L peak of Ni-O (FWHM = 1.2 eV), for Z2N20% than the other counterparts [Z1N6% and Z2N6% - FWHM = 1.07 eV]. This could be due to the lower thickness of the NiO layer and hence the incomplete growth. In addition, the difference noticed in the O_{OH}/O_L ratio ($\simeq$ 0.20 for Z1N6% and Z2N6%; and 0.28 for Z2N20%, Table 3.2) could be correlated to the different P_{O_2} used during the NiO deposition. Also due to the lower NiO thickness ($\simeq$ 4 nm) where the probability of realising O_L from Zn-O is higher for the Z2N20% sample.

Overall, the BE shifts in the Zn2p line for samples Z1N6%, Z2N6% and Z2N20% was accordingly deduced [0.5 eV is added to the BE shifts in Zn2p line of Z2 heterostructures, with respect to the shift of Zn2p peak in Z2 (as a result of heating step) as compared to that of Z1 scaffold, which is a reference material] as 1, 1.39 and 1.76 eV, respectively. This shows that the attained band bending is controlled by the P_{O_2}, but also by the surface cleaning [211]. These shifts were almost consistent with those of the VBMx position.

Band alignment characteristics - NiO/ZnO

All these information extracted from the photoemission spectra were used to derive the band energy profile at the interface of NiO/ZnO. By extracting the values of core level binding energies and distance between fermi level and valence band maximum for each material through the XPS measurements, we were able to determine the band bending in the film and the valence band offset. The band bending (V_{bb}) is given by either the shift in the VBMx of the substrate or the scaffold [here, ZnO], from initial (i) to final (f) step (VBMx(f) - VBMx(i)) or by the shift of the core level line ($\triangle BE_{CL}$(f) - $\triangle BE_{CL}$(i)), as given in equation 3.1 [25, 177, 211], assuming that the energy difference between core level and VBMx is constant.

$$V_{\text{bb}}\ of\ film = \triangle BE_{\text{CL}}(f) - \triangle BE_{\text{CL}}(i) \tag{3.1}$$

The valence band offset $\triangle E_{VB}$ was calculated using equation 3.2 [25, 177, 211], by implementing the values of difference in the core level binding energies of $Zn2p_{3/2}$ and $Ni2p_{3/2}$, $\triangle BE_{CL}$ at the interface and the difference in the core level binding energies of $Zn2p_{3/2}$ and $Ni2p_{3/2}$ in relative to their respective valence band maxima VBMx ($BE_{Zn2p3/2\text{-}VBMx}$ and $BE_{Ni2p3/2\text{-}VBMx}$).

$$\triangle E_{\text{VB}} = BE_{\text{Ni2p3/2-VBMx}} - BE_{\text{Zn2p3/2-VBMx}} + \triangle BE_{\text{CL}} \tag{3.2}$$

For this band alignment, we have chosen the BE difference of ZnO vs NiO after the first deposition steps, assuming that no band bending has been induced at this stage. Furthermore, the conduction band offset $\triangle E_{CB}$ was obtained by using the values of $\triangle E_{VB}$ and the bandgaps of the scaffold (E_g ZnO = 3.37eV) and contact (E_g NiO = 3.7eV) materials, as shown in equation 3.3 [25, 177, 211].

$$\triangle E_{\text{CB}} = E_g NiO + \triangle E_{\text{VB}} - E_g ZnO \tag{3.3}$$

Consequently, the band energy structure before contact and band bending after realising the interface formation were proposed for each interface study conditions, as shown in Figures 3.8 and 3.9. The V_{bb} (calculated according to equation3.1) are noted on the figures. All of them exhibited the type II staggered band alignment. The determined values of valence band offsets were in the range of ≃1.2 - 1.7 eV, while that of conduction band offsets were found to be ≃1.5 - 2 eV. The theoretical estimation of the valence band offset for the NiO/ZnO interface was reported to be 0.94 eV, lower than the experimentally obtained values, 1.47 eV[215]. In comparison to theoretical observations, values from all our studies were higher. And in relation to the previous experimental results, our values were either lower or higher, except for Z2N20%. However, valence band offset values reported by Ma et al.[215] has explained the discrepancies in the valence band offset values through the polarization effect and reported a value of 1.3 eV for polar ZnO. Though this value is close to our observation of 1.21 eV (Figure 3.9d) for Z2N20%, values of Z1N6% (1.72 eV, Figure 3.8b and Z2N6% (1.56 eV, Figure 3.9b) were higher. After the final NiO deposition step, the obtained band bending values were 1.00, 1.39 and 1.76 eV for the Z1N6%, Z2N6% and Z2N20% heterostructures. Our studies reveal that apart from polarization effect, other parameters like surface cleaning and P_{O_2} were influencing the band bending and band discontinuities. Therefore, these discrepancies highlight the importance of studying the role of adsorbates in interface formation and their possible influence on the functional properties.

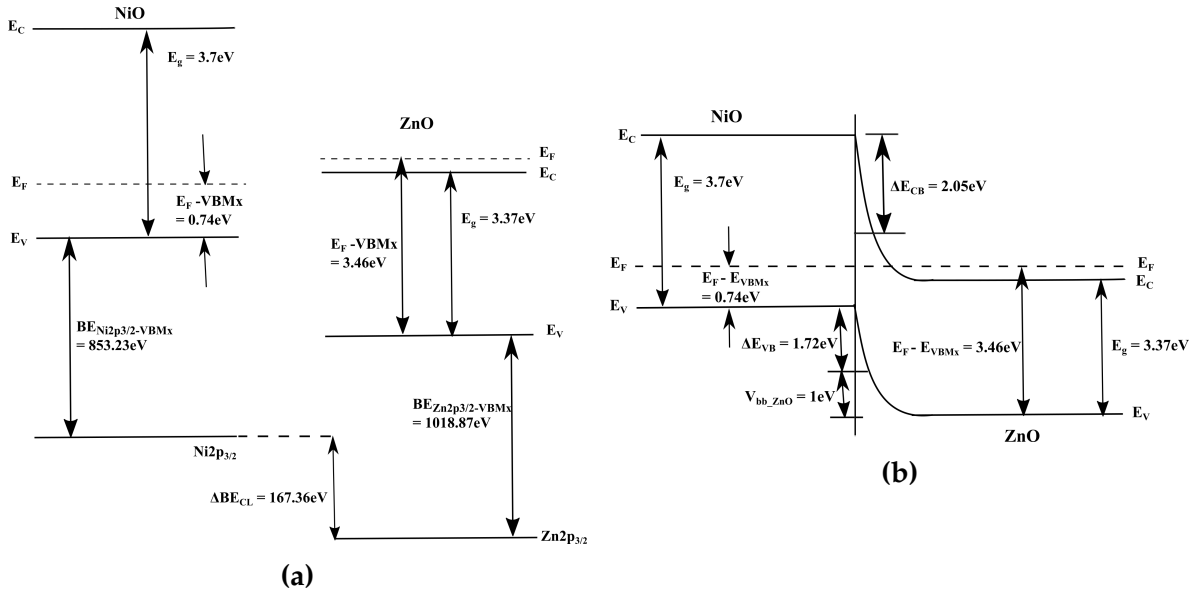

Figure 3.8: Band alignment and band bending at the interface of Z1N6% heterostructure, before (a) and after (b) contact. For details, refer to the text.

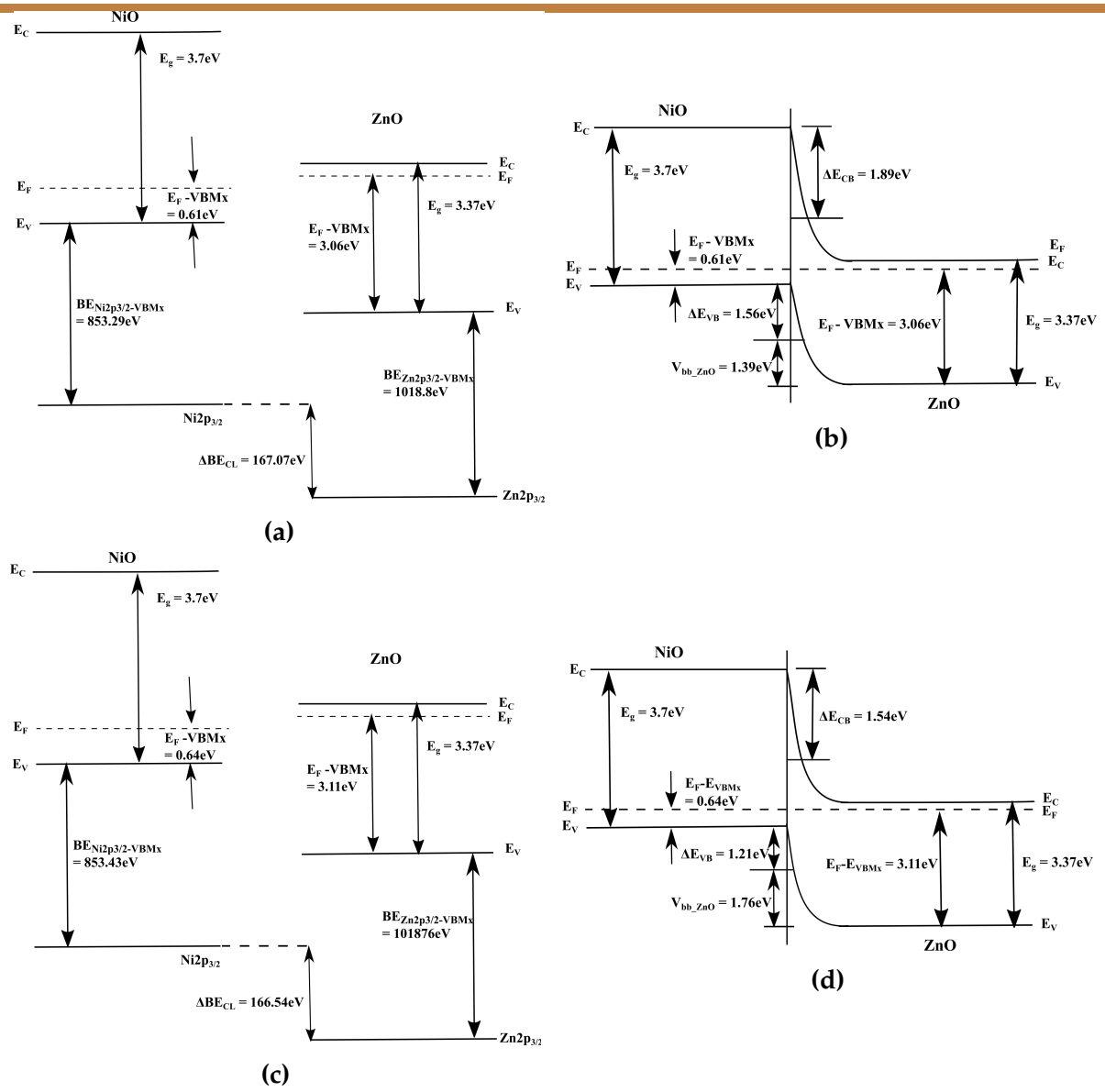

Figure 3.9: Band alignment and band bending at the interface of Z2N6% and Z2N20% heterostructures, before (a and c) and after (b and d) contact. For details, refer to the text.

3.5. Interface analysis of the RuO_2/ZnO heterostructure - Influence of surface cleaning

The elemental and chemical states of scaffold ZNR (Z1 and Z2) and heterostructured ZnO/RuO_2 were analysed using XPS measurements. All the peaks observed in Figure 3.10, could be attributed to Zn, O and Ru in ZnO and RuO_2 [115 216 217], except for Z1 scaffold where a C1s emission was detected owing to its exposure to ambience.

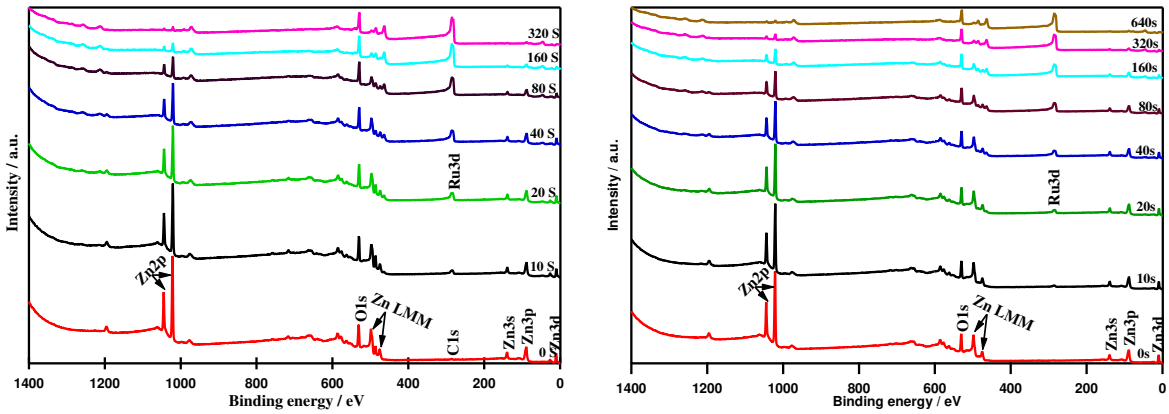

Figure 3.10: Survey spectra of Z1R and Z2R heterostructures.

The step-by-step evolution of individual peaks Zn2p, Ru3d, O1s and VBMx for both Z1R and Z2R after each step of RuO_2 deposition are represented in Figures 3.11 and 3.12. All the core level lines of both Z1R and Z2R shifted towards lower BE with increasing RuO_2 coverage. The intensity of the Zn2p emission decreased while that of Ru3d was increasing, with each step of deposition. Concurrently, the intensity of O1s line was decreasing at the first several steps, but increased at longer deposition time. This could be attributed to the fact that it has a contribution from both ZnO and RuO_2.

The Zn2p emission line was observed at 1022.19 eV for $Z1R_{0s}$ (Figure 3.11a and Table 3.3) and shifted towards lower binding energy [1021.80 eV] ($Z2R_{0s}$, Figure 3.11d and Table 3.3) after surface cleaning. The presence of C1s emission, observed around 284 eV for the Z1R heterostructure, is expected to overlap with the $Ru3d_{3/2}$ core level (and also with its satellite peak at 287.52 eV) situated at $\simeq$ 285.41 eV (Figure 3.11b and Table 3.3) [115]. This makes it difficult to distinguish them from each other. However, the removal of carbon by surface cleaning was confirmed for sample Z2 and this overlap should be avoided in case of Z2R (Figure 3.11e).

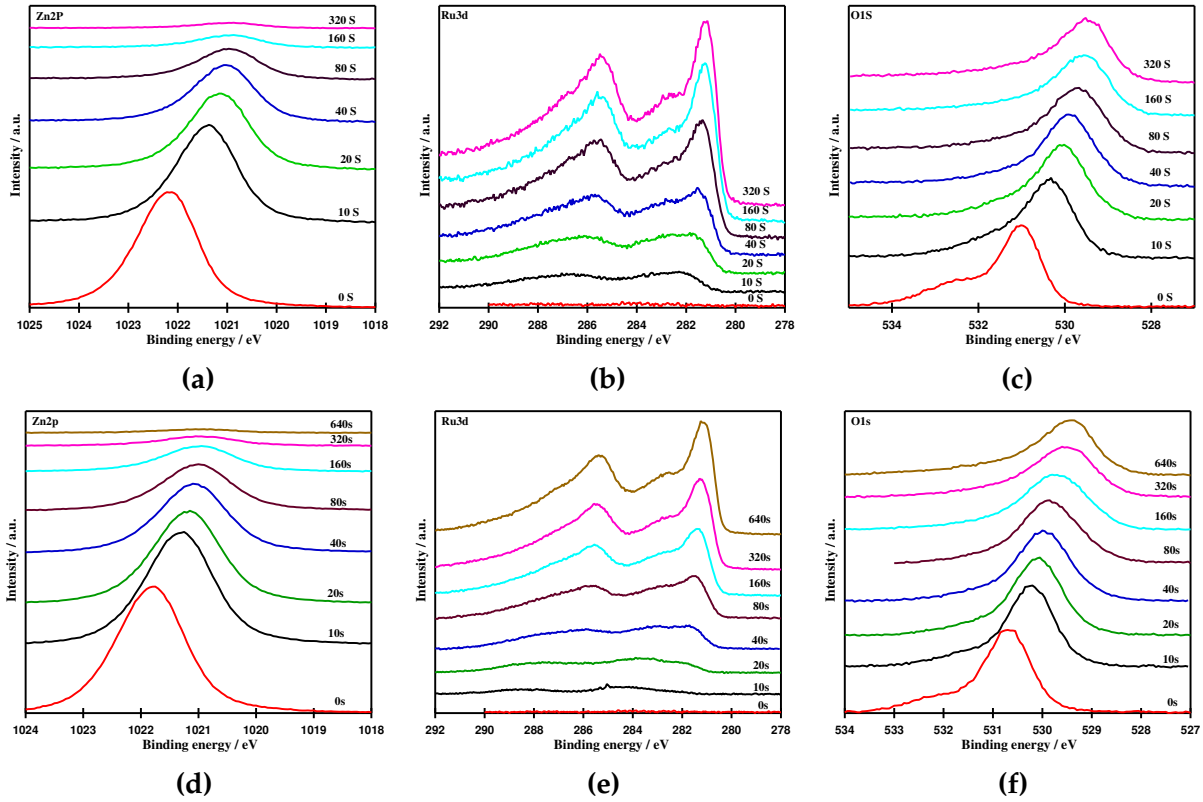

Figure 3.11: Individual spectra of Zn, Ru and O respectively, for Z1R

The evolution of VBMx as a function of deposition time, for samples Z1R and Z2R are illustrated in Figure 3.12a and Figure 3.12b, respectively. The plot of E_F - VBMx values vs deposition time is shown in Figure 3.12c. As observed for NiO/ZnO heterostructure, here as well, the VBMx shift was rapidly decreasing after the initial steps, and saturated after 320 s and 640 s for Z1R and Z2R, respectively. This clearly demonstrates that in case of RuO_2/ZnO interface formation as well, a space charge layer was formed.

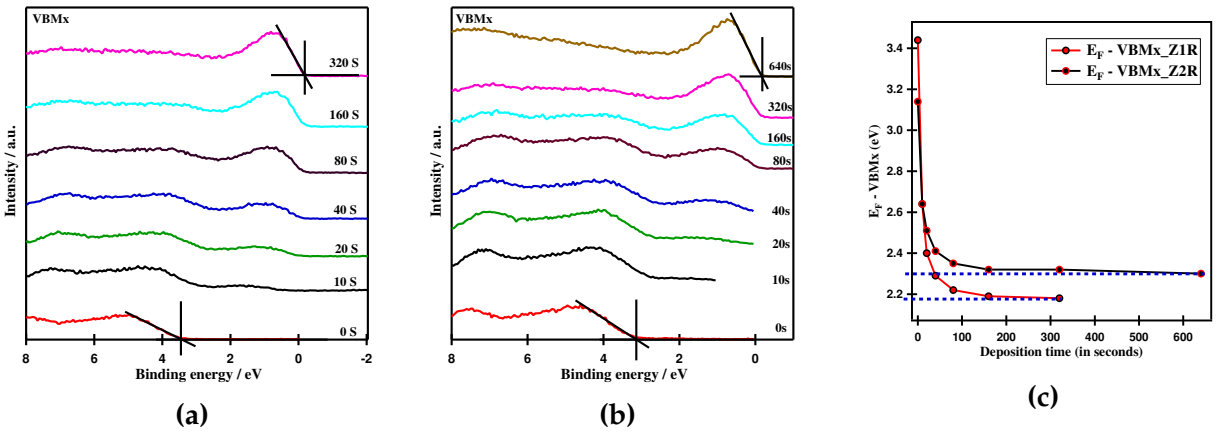

Figure 3.12: Spectra of VBMx (a and b) and E_F-VBMx Vs Deposition Time (c) for Z1R and Z2R.

Table 3.3: Zn2p, O1s and $Ru3d_{5/2}$ binding energies and valence band maximum (VBMx) values as a function of step by step deposition of RuO_2. Subscripts accompanying the sample codes represent the deposition time for RuO_2.

Sample Code		Zn2p BE (eV)	O1s Be (eV)	$Ru3d_{5/2}$ BE (eV)	$Ru3d_{3/2}$ BE (eV)	E_F - VBMx (eV)
Without surface cleaning (Z1)	$Z1R_{0s}$	1022.19	531.02	-	-	3.44
	$Z1R_{10s}$	1021.39	530.35	281.97	-	2.64
	$Z1R_{20s}$	1021.15	530.06	281.77	-	2.40
	$Z1R_{40s}$	1021.04	529.90	281.52	-	2.29
	$Z1R_{80s}$	1020.97	529.68	281.39	-	2.22
	$Z1R_{160s}$	1020.94	529.55	281.30	-	2.19
	$Z1R_{320s}$	1020.93	529.43	281.23	-	2.18
Surface cleaned (Z2)	$Z2R_{0s}$	1021.80	530.68	-	-	3.14
	$Z2R_{10s}$	1021.31	530.23	284.16	-	2.64
	$Z2R_{20s}$	1021.18	530.09	282.97	-	2.51
	$Z2R_{40s}$	1021.08	529.97	281.65	-	2.41
	$Z2R_{80s}$	1021.02	529.84	281.51	-	2.35
	$Z2R_{160s}$	1020.99	529.73	281.39	-	2.32
	$Z2R_{320s}$	1020.99	529.53	281.27	-	2.32
	$Z2R_{640s}$	1020.97	529.38	281.15	-	2.30

Though the line shape of Zn2p was not changing with deposition time, those of Ru3d and O1s were changing gradually. During the initial deposition steps, the Ru3d emission appeared to be a broader spectra at higher BE but changed into a sharp and well resolved spectral line that shifted to lower BE with higher RuO_2 coverage. Similarly, the O1s spectra, the line shape changed with the growth of RuO_2. All these shifts, the change in intensities and line shapes, indicate the evolution and growth of RuO_2 on the ZNR scaffolds Z1 and

Z2.

The Ru3d and O1s core levels were deconvoluted (using IgorPro software), after performing a shirley background subtraction. In case of both $Z1R_{320s}$ and $Z2R_{640s}$ (Figure 3.13), the $Ru3d_{3/2}$ [$\simeq$ 285.3 eV] and $Ru3d_{5/2}$ [$\simeq$ 281.1 eV] contributions were identified, each of them being accompanied by a satellite peak, at +2 eV and +1.35 eV vs. the respective major peaks, respectively [122,217] (Figures 3.13a and 3.14a). These major peaks confirm the formation of RuO_2 and could be assigned to the Ru^{4+} state [122,216,218]. The realisation of satellite peaks for Ru3d are sometimes considered controversial due to the possibility of the occurrence of mixed oxidation states. However, as reported by Kim et al. [216] and Over et al. [219], the satellite peaks could also be attributed to core-hole screening or RuO_2 plasmon, rather than to mixed oxidation state.

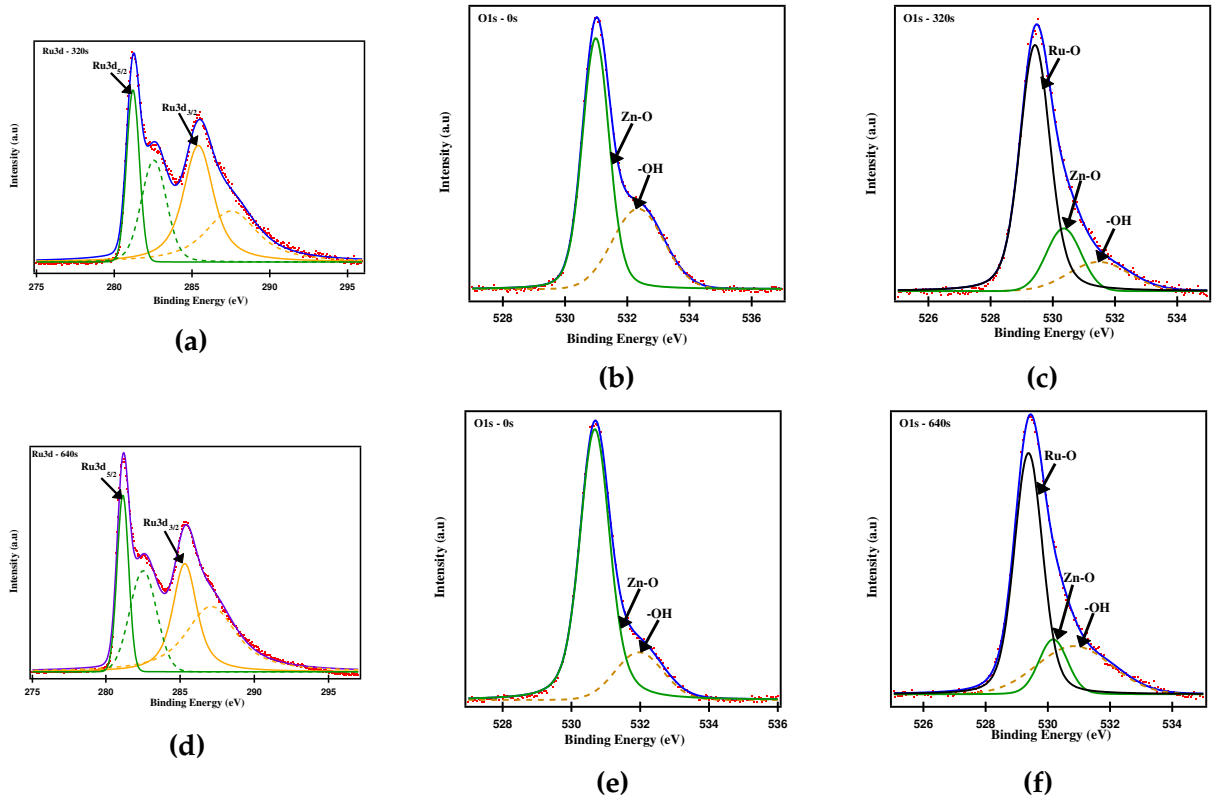

Figure 3.13: Deconvoluted Spectra of Ru3d (at final step (a and d)) and O1s at initial (b and e) and final (c and f) deposition steps, for samples Z1R and Z2R, respectively.

The deconvolution of the O1s peak at first step ($Z1R_{0s}$ and $Z2R_{0s}$), revealed the contribution of two components, the lattice oxygen (O_L) of ZnO (Zn-O centered at 530.99 eV and 530.68 eV, respectively) and surface hydroxyls (O_{OH}) centered at 532.35 eV and 531.96 eV, respectively, as shown in Figures 3.13b and 3.13e. But after the final step of RuO_2 deposition, a third contribution was identified, the O_L of RuO_2 (Ru-O)(Figures 3.13c

and 3.13f). This reaffirms the contribution from both ZnO and RuO_2 in the oxygen peaks at higher deposition times [115].

Band alignment characteristics - RuO_2/ZnO

The shifts in the Zn2p and VBMx lines were used to draw the band alignment structure and evaluate the band bending at the RuO_2/ZnO interface for heterostructures comprising the pristine (Z1) and cleaned (Z2) scaffold (Figures 3.14 and 3.15). The shifts in the Zn2p are calculated according to equation 3.1 in Section 3.4 and correspond to the amount of V_{bb} that has occurred at the interface.

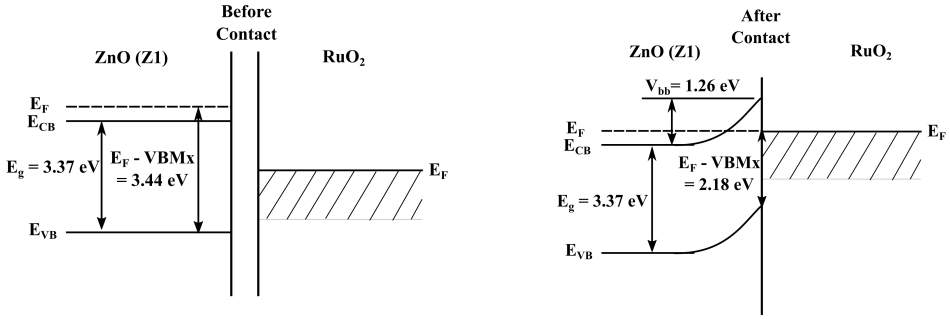

(a) Band alignment - before contact

(b) Band bending - after contact

Figure 3.14: Band alignment and band bending at the interface of Z1R.

The shift in Zn2p from initial to final step of RuO_2 deposition, resulted in a V_{bb} of 1.26 eV for Z1R and 0.83 eV for Z2R. The shift in O1s spectra from initial to the final step was found to be 1.56 eV and 1.3 eV for Z1R and Z2R, respectively. These shifts are higher as compared to the shifts of Zn2p and it might be due to the contribution from both ZnO and RuO_2. This coincides with the previous observations from the change in line shape of O1s and the presence of both Zn-O and Ru-O contributions in the deconvoluted components.

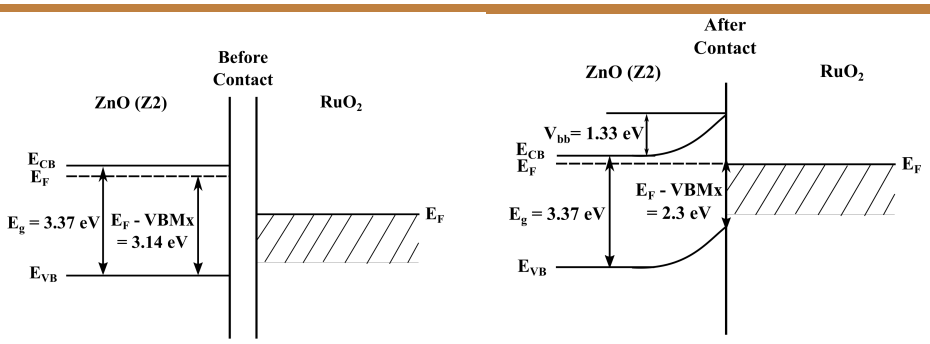

(a) Band alignment - before contact **(b)** Band bending - after contact

Figure 3.15: Band alignment and band bending at interface of Z2R

The shift in values of VBMx, from 3.44 eV (initial step) to 2.18 eV (final step) for Z1R and from 3.14 eV (initial step) to 2.3 eV (final step) for Z2R, suggest that both ex-situ and in-situ ZNR are n-type semiconductor. And the overall shifts, identified as 1.26 eV and 0.84 eV for Z1R and Z2R respectively, were consistent with the shifts observed for Zn2p core levels. Accordingly, the above proposed band diagrams show a a well developed band bending at the RuO_2/ZnO interface, with a higher V_{bb} value for the Z2R heterostructures as a consequence of surface cleaning.

3.6. Conclusion

The interface studies of NiO/ZnO and RuO_2/ZnO were carried out by by step-by-step deposition of the co-catalyst on the pristine (Z1) and cleaned (Z2) scaffolds followed by in-situ XPS analysis. Surface cleaning enabled changes in the doping level of Z1 from n+ to n- for Z2, lowering the relative Fermi level positions from above conduction band (CB) to below CB and this effect was examined for its influence on the interfacial properties. In addition, for the Z2 scaffold the P_{O_2} for the NiO deposition was varied as 6 and 20%. All the core level lines and the VBMx lines shifted towards lower binding energy (BE), from the first step to the final deposition step for both NiO/ZnO and RuO_2/ZnO interfaces, highlighting the change in the chemical environment and the interface formation along with band bending. The line shape of Zn2p did not show any changes in contact with NiO or RuO_2. However, the line shape of O1s was changing only for the RuO_2/ZnO interface, due to the contribution from both Zn-O and Ru-O. In case of NiO/ZnO, O_L of Zn-O was overlapping with the binding region of surface hydroxyls. The Ni2p and Ru3d line shapes were broader and entangled during the first several steps of deposition, but shifted towards lower BE with a well characterized spectra at the final step. This was attributed to the step-

wise growth.

In case of NiO/ZnO, the magnitude of band bending was governed by the involved oxygen partial pressure but also by the presence/absence of adsorbates. The RuO_2/ZnO interface also experienced the same variation as function of surface cleaning. For both types of interfaces, the heterostructures with cleaned ZNR scaffold surface (Z2) attained higher V_{bb} values (Z1N6% - 1 eV, Z2N6% - 1.39 eV and Z1R - 1.26 eV, Z2R - 1.33 eV). Moreover, in case of NiO/ZnO, the interface grown at higher P_{O_2}, attained a higher band bending of 1.76 eV, revealing two competing effects: oxygen vacancy filling or compensation by incoming oxygen and lowering of E_F in NiO. Overall, the interface studies confirmed that both the co-catalyst materials NiO and RuO_2, are suitable for building heterostructures with ZnO, proving a well developed band bending.

Chapter 4

p type-n type NiO/ZnO heterostructured thin films

4.1. Influence of system base pressure during surface cleaning

4.1.1. Experimental strategy

Semiconducting Transition Metal Oxides (STMOs) are of profound interest to material scientists and chemists involved in photocatalysis research, due to their capacity to form electron hole pairs when exposed to light irradiation which increase their surface reactivity [56, 125, 220, 221]. For this reason, comprehensive and complex studies to understand their high reactivity towards the environment are required [58, 222]. Metal oxides can easily accommodate defects or vacancies which are known to influence the electrical and optical properties of the material [149, 223]. Likewise, defects can have both a positive (increasing charge carrier density that would act as donors) and a negative effect (providing trap sites that will act as recombination centres) on the material's performance [167]. Hence, in spite of the complexity involved, it is essential to attain a fine control over the vacancies that drive the functioning of metal oxides [223], evenmore because they affect the interface properties in heterostructures [224].

Over the years, both experimental and computational strategies have been widely investigated to attain the basic understanding in such surface related properties and reactions, especially in relation to photocatalytic materials [225–227]. The aim of this study was to

understand the surface properties of ZNR and the influence of surface in the formation of heterostructure and their corresponding interface properties. Such 1D ZNR grown as thin film is an unique integration of nanostructural and multifunctional properties which are beneficial and desirable for photocatalytic processes [93,228–230]. However, such structures are well known to exhibit n-type conductivity due to the presence of native defects like oxygen vacancies [153,231,232]. Research through several decades has evidenced that oxygen vacancies in metal oxides act as active sites to promote or improve sensing or catalytic processes [16,233], but there were also revelations that they can be detrimental for the process [167]. Therefore, the basic understanding of this material remains inconclusive and challenging. It is crucial to comprehend the reaction mechanism and adsorption of molecules at the surface of such scaffold (base) materials, since their crystallinity and defects like oxygen vacancies limit the probability of acquiring high quality heterostructures.

In this section, we have studied the degree of adsorbates removal by varying the system base pressure used during the heat treatment of the ZNR scaffold cleaning and their influence on the heterostructure formation. The interface properties (band bending, conduction band, valence band and Fermi level position) were studied by XPS and correlated to the photoelectrochemical results (photocurrent, charge transfer resistance). In addition, photoluminescence analysis was carried out on the better performing scaffolds, in order to evaluate the variation in oxygen vacancies in ZNR after the surface cleaning. The highest photocurrent and lowest charge transfer resistance attained by certain films were correlated to the favourable surface and interface properties that were noticed to influence the performance significantly.

4.1.2. Sample description

The scaffold used here were ZNR, whose preparation method and surface cleaning procedure are explained in Section 3.2. The system base pressure (or total pressure, P_{Tot}) was fixed as 5 Pa and 0.5 Pa. The NiO deposition was performed as described in Section 3.2 for the 6% oxygen partial pressure. The deposition time was fixed as 40 s, in order to attain a thickness of $\simeq$ 7-10 nm for all heterostrcutures. In addition, two temperature conditions were tested for the NiO deposition, room temperature (RT) and RT followed by post annealing (PA), in-situ at 250 °C, for 1 h in presence of oxygen (5 sccm). Accordingly, the RT or PA subscripts were added to the sample name. The specific details about the system base pressure used during in surface cleaning, the NiO deposition temperature conditions and their respective sample codes are gathered in Table 4.1. The letter "a" next to the sample code in Z2 and its heterostructures, corresponds to a base pressure of 5 Pa, whereas the letter "b" to 0.5 Pa.

Table 4.1: Sample description. RT - Room temperature, PA - RT followed by post annealing.

Sample Code	Preparation Details	
	Surface Cleaning base pressure (Pa)	NiO deposition (temperature) condition
Z1	-	-
$Z1N_{RT}$	-	RT
$Z1N_{PA}$	-	PA
Z2a	5	-
$Z2aN_{RT}$	5	RT
$Z2aN_{PA}$	5	PA
Z2b	0.5 Pa	-
$Z2bN_{RT}$	0.5 Pa	RT
$Z2bN_{PA}$	0.5 Pa	PA

4.1.3. X-Ray photoelectron spectroscopy - XPS

In this section, the influence of P_{Tot} in removal of adsorbates and further in interfacial properties were examined through XPS measurements. As seen in Chapter 2, here as well, the survey scans were performed and confirmed that the emissions were only from their respective characteristic elements, for all scaffold and NiO/ZnO heterostructure films.

As a result of heating, the Zn2p and O1s core level lines and the valence band maximum of surface cleaned samples (Z2a and Z2b) increased in intensities compared to Z1 (Figures 4.1a to 4.1c), which confirms the removal of adsorbates.

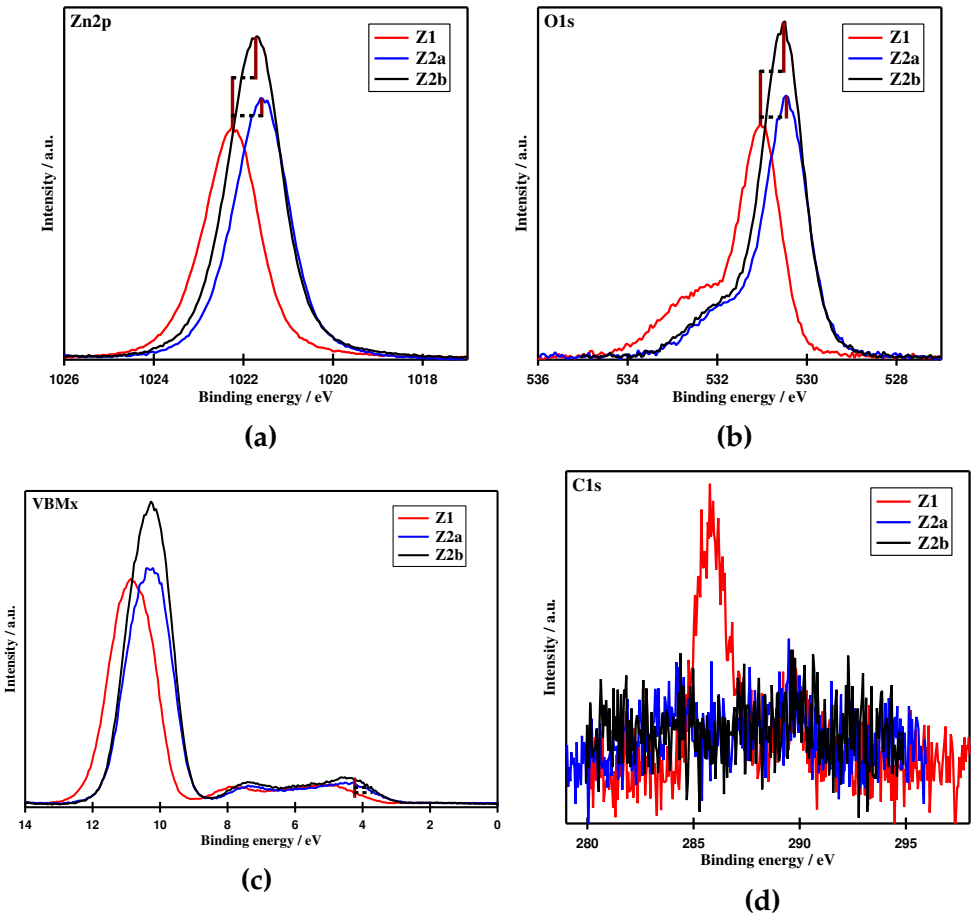

Figure 4.1: XPS spectra showing the (a) Zn2p (b) O1s (c) VBMx and (d) C1s peaks of Z1, Z2a and Z2b scaffold films.

The Zn2p and O1s core level lines shifted towards lower binding energy with surface cleaning (Figures 4.1a and 4.1b, Table 4.2). The Fermi level position to valence band maximum distance (E_F - VBMx) was in the range of 2.85 - 3.47 eV (Figure 4.1c, Table 4.2), indicating the intrinsic n-type character. The Fermi level was lowered after surface cleaning, attaining the lowest value when the 5 Pa system base pressure was used (sample Z2a). The C1s emission was not detected in both Z2a and Z2b (Figure 4.1d), as a consequence of heating. In addition to the observation of shifts, no significant changes were observed in the line shape of Zn2p and O1s emission lines. However, narrowing of the FWHM of the Zn2p (for Z2a and Z2b, with respect to Z1) was noticed, which is correlated to the cleaning process.

Table 4.2: Sample Names and their respective Binding Energies for individual peaks, band bending (w.r.t Z1) in heat treated surfaces (Z2a and Z2b) and the FWHM values of Zn2p and O1s peaks, along with the O/Zn and O_L/O_{OH} ratios for all scaffold films.

	Sample Name		
Characteristics of Individual peaks	Z1	Z2a	Z2b
Zn2p (eV)	1022.33	1021.57	1021.83
O1s (eV)	530.97	530.46	530.67
E_F - VBMx (eV)	3.47	2.85	3.04
V_{bb} (eV)	-	0.76	0.50
$FWHM_{Zn2p}$ (eV)	1.54	1.45	1.40
$FWHM_{O1s}$ (eV)	1.08	1.06	1.08
O/Zn ratio	0.32	0.41	0.43
O_L/O_{OH} ratio	0.73	0.78	0.82

In general, the stoichiometry is not considered to be precisely reliable for ex-situ prepared samples, due to the presence of adsorbates[211]. However, tracking the evolution of O1s and Zn2p peaks for varied annealing conditions is accepted to be considerable for analysing the structure development in the ZnO matrix, as a function of annealing[234]. The O/Zn ratio was deduced (by taking into account only the intensity of the lattice oxygen peak (O_L of Zn-O) and that of the Zn2p peak, in order to identify the changes in stoichiometry that might have occurred as function of the different surface cleaning conditions. For this purpose, O1s spectra of all scaffolds (Z1, Z2a, and Z2b) were deconvoluted (after Shirley background, using IgorPro), as shown in Figures 4.2a to 4.2c. The O1s line of Z2a and Z2b samples showed the existence of two components namely, O_L and surface hydroxyls (-OH, O_{OH}, centered at $\simeq$ 530.5 eV and $\simeq$ 531.8 eV, as opposed to Z1 which had three components [O_L - 530.97 eV, O_{OH} - 532.1 eV and molecular water, O_{H_2O} - 532.78 eV]. The presence of O_{H_2O} in Z1 is typical for an ambience exposed sample.

Furthermore, the atomic ratio of O1s (O_L) and Zn2p peaks for each scaffold surface was calculated using the equation[235,236] below:

$$Atomic \quad ratio(A) = \frac{I_A/F_A}{(I_A/F_A)+(I_B/F_B)} \tag{4.1}$$

where A,B represents O and Zn, I_A, I_B represents intensity area of the O1s peak and Zn2p peak and F_A, F_B represents the atomic sensitivity factor of the respective elements (Zn - 3.354

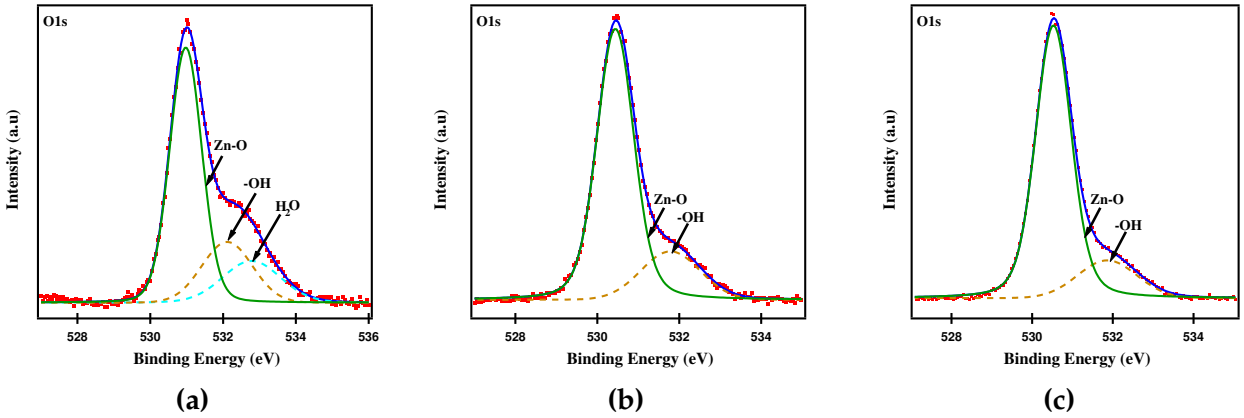

Figure 4.2: Deconvoluted spectra of O1s for (a) Z1, (b) Z2a and (c) Z2b respectively.

and O - 0.711).

Since Zn2p and O1s emission lines have different kinetic energies, a correction term called $Q(E)$ that varies between 0.9 and 1 is generally used to obtain the reasonable ratio. However, usage of this correction term amounts upto only a minor deviation of 1.1% [given that atomic sensitivity factor is used for the calculation], hence the above equation is still considerable [237, 238]. Moreover, to obtain the correction factor, the ratio has to be calculated using a substrate of known stoichiometry, which was not the case here. Therefore, these ratio values were solely used to interpret the variation in ratio before and after the heat treatment, rather than to discuss the absolute values itself.

The O/Zn ratios for Z2a and Z2b were found to increase (0.41 and 0.43 respectively) after surface cleaning as compared to the Z1 (0.31). The same trend was observed for the O_L:O_{OH} ratios (0.73, 0.78 and 0.82 respectively, Table 4.2), reaffirming that there was increase in the oxygen content with increase in the vacuum condition and part of the -OH were desorbed.

As a general rule, in terms of surface-gas system, the resultant layer of adsorption would be based on the balance between adsorption of atoms/molecules from the atmosphere (here, oxygen and H_2O) and the thermal excitation of electrons from the surface of material [239]. Furthermore, oxygen vacancy filling is a process that occurs as a competition between temperature and oxygen partial pressure involved [155]. Our studies reveal that, the system base pressure as well plays a crucial role in the oxygen adsorption/desorption equilibrium. In principle, the treatment in different O_2 atmosphere at high temperature lead to variations in doping as space charge layer is formed. As these effects cannot easily be separated, we assume a homogeneous bulk doping charge for the nanostructured samples.

Under the lower vacuum (5 Pa), oxygen adsorption is favored (it is the P_{O_2} which shifts the equilibrium to the right) with excited electrons being captured by the incoming oxygen (equation 4.2) and resulting into depletion of electrons at the surface and at the same time the oxygen vacancies are filled. Because of the surface coverage by oxygen, further desorption of adsorbates (-OH) is blocked explaining the higher -OH content at the surface.

$$\frac{1}{2}\, O_2\ (gas) + 2e^- + {V_O}^{++} \leftrightarrows {O_0}^x \tag{4.2}$$

At higher vacuum condition (0.5 Pa), the oxygen desorption preferentially occurs and e^- are released leading to a raise in the Fermi level and thus to an increase of electron concentration in the material.

Band energy structure

The shift in the BE values of the Zn2p core level line of after surface cleaning (Z2a and Z2b) with respect to pristine ZNR surface (Z1) gave information about the Fermi level shift and attained band bending at the surface of ZNR and about the extent of depletion that occurred as a consequence of heating. The energy shift of 0.5 eV (Z2b) and 0.76 eV (Z2a) observed in the Zn2p core level lines could be attributed to the band bending developed at the surface of heat treated ZNR, while the change of E_F - VBMx in the bulk is due to redoping. From the impedance measurements (detailed in next subsection, 4.1.6.) we observe a change in the Fermi level position of the bulk. Additionally, from the shift of E_F - VBMx, we could deduce that E_F was above the conduction band for Z1 and shifted inside the conduction band for Z2a and Z2b, once the excess electrons were depleted from the surface. Using these information, the band energy diagrams for the varying scaffold surfaces, were drawn and illustrated in Figure 4.3

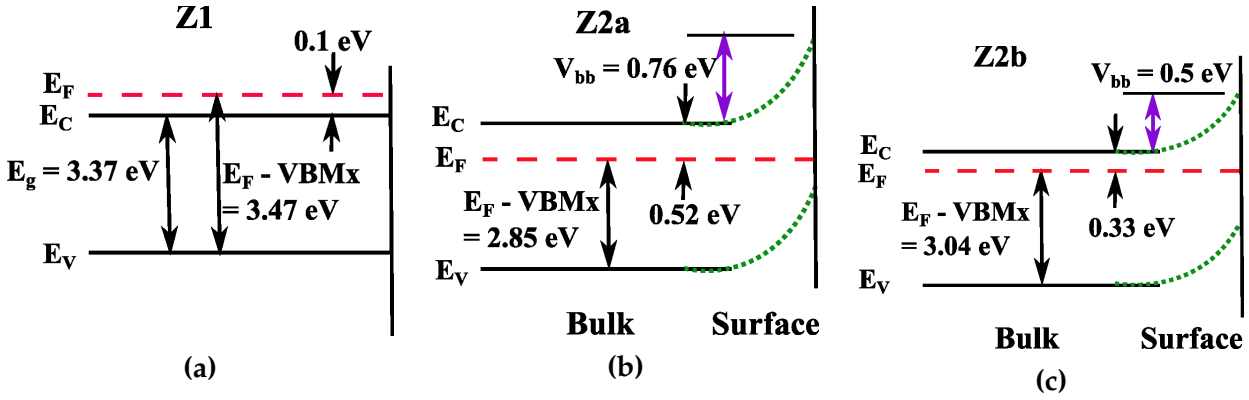

Figure 4.3: Band energy diagram and change of the Fermi level position at different scaffold surfaces (a) Z1, (b) Z2a and (c) Z2b, as an effect of post processing method.

The electron depletion on the surface of Z2a was higher than for Z2b, agreeing well with the trend seen in the O/Zn atomic ratios. However, the scaffold Z2b for which a higher amount of -OH was removed (higher O_L/O_{OH} ratio, Table 4.2) is expected to have improved interfacial properties.

Heterostructured films

Each scaffold film was subjected to NiO deposition conditions as detailed in Section 4.1.2. After NiO deposition, the core level lines of Zn2p, O1s and Ni2p for all heterostructures were shifted towards lower binding energies, with respect to the scaffold (Figure 4.4 and Table 4.3). The Zn2p and the O1s emission lines were identified in the range of 1020.94 - 1021.21 eV and 529.37 - 529.60 eV (Figure 4.4 and Table 4.3), respectively, for all the heterostructures.

Table 4.3: Sample Names and their respective Binding Energies for individual peaks, band bending(w.r.t their scaffold surfaces) in heterostructures and the FWHM values of Zn2p, O1s, Ni^{2+} and Ni_{Sat} peaks for all heterostructured films; all are expressed in units of electron volts(eV). The band bending (V_{bb} due to contact formation of ZnO to NiO was calculated from the shift of the Zn2p core level line; 0.76 and 0.50 eV was added to the V_{bb} values of Z2a and Z2b heterostructures, respectively, with respect to the shift of Zn2p line for the corresponding scaffolds [Z2a and Z2b] in relation to the reference material, Z1 scaffold.

	Sample Code					
Characteristics of Individual peaks	$Z1N_{RT}$	$Z1N_{PA}$	$Z2aN_{RT}$	$Z2aN_{PA}$	$Z2bN_{RT}$	$Z2bN_{PA}$
Zn2p	1021.21	1021.01	1021.45	1020.94	1020.97	1021.00
Ni^{2+}	854.08	853.93	854.04	853.95	853.79	853.82
Ni_{Sat}	861.24	861.09	861.26	861.11	860.94	861.00
O1s	529.60	529.50	529.52	529.48	529.37	529.43
E_F - VBMx	0.67	0.63	0.58	0.56	0.63	0.66
V_{bb}	1.12	1.32	0.88	1.39	1.36	1.33
$FWHM_{Zn2p}$	1.53	1.54	1.51	1.40	1.48	1.62
$FWHM_{O1s}$	1.27	1.08	1.09	1.07	1.20	1.09
$FWHM_{Ni^{2+}}$	1.37	1.26	1.40	1.41	1.18	1.17

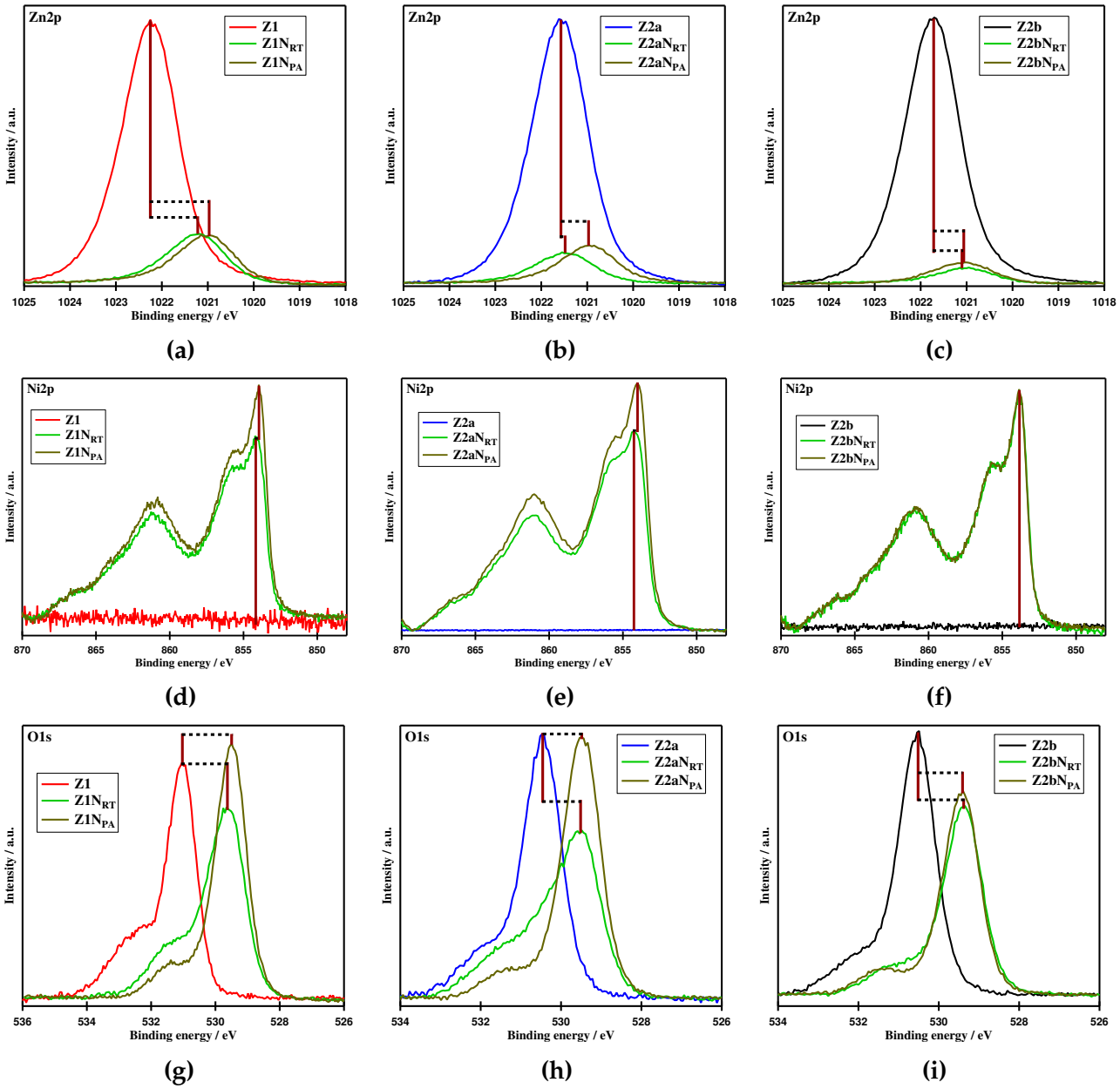

Figure 4.4: Spectra of Zn2p, Ni2p and O1s emission lines (shifts represented in the figure) for Z1 (a, d and g), Z2a (b, e and h) and Z2b (c, f and i) heterostructres along with their corresponding scaffold.

In addition, the Zn2p and Ni2p core levels for the post annealed heterostructure films formed with Z1 and Z2a scaffolds, were further shifted to lower BE in relative to their room temperature counterparts (Figures 4.4a and 4.4b, Table 4.3). But, such a shift was not noticed for the heterostructures formed with the Z2b scaffold (Figure 4.4c, Table 4.3). Concurrently, in all heterostructures, the shift in VBMx was not experiencing any significant changes in their values, as an effect of varying temperature conditions during the preparation (Figure 4.5) The E_F - VBMx difference of heterostructures were occurring in the range of 0.58 - 0.67 eV (Table 4.3), signalling the E_F shift towards the valence band maximum, confirming the

deposition of NiO and thereby its p-type character. Apart from the shifts in BE and intensity variation, another feature of importance in XPS analysis is the peak broadening, which could be related to both intrinsic and extrinsic mechanisms. Extrinsic broadening is usually due to the instrument but is generally avoided with the use of monochromator. Intrinsic broadening is attributed to core-hole lifetime, inhomogenities in the studied material, polar distortions, vibrational/phonon effects etc[240,241]. However, models which correlate the XPS peak broadening with the chemical bonding and the catalytic activity of thin oxide films were proposed only recently[241]. Here, therefore, we are analysing the broadening of the the Zn2p, O1s and Ni^{2+} core level lines, in order understand the effect of surface cleaning on the interface formation and eventually on the catalytic activity of the heterostructured material.

The FWHM of Zn2p and O1s core levels were lying in the range of 1.4 - 1.62 eV and 1.08 - 1.27 eV (Table 4.2 and Table 4.3) respectively, as normally observed for a metal (oxide) and oxygen emission lines. However, there were some noticeable variations in the FWHM values that could be assumed in relation to the nature of chemical bonding between the two materials (ZnO and NiO). The FWHM of O1s peak was around ($\simeq$ 1.08 eV) for almost all films except for $Z1N_{RT}$ and $Z2bN_{RT}$ (1.2 eV) (Table 4.2 and Table 4.3).

The O1s core levels were deconvoluted for all the heterostructures and an example for sample $Z2bN_{RT}$ and $Z2bN_{PA}$ are shown in Figure 4.6. The deconvolution of O1s spectra for all heterostructures revealed two components, O_L and O_{OH}, existing in the range of 529.37 - 529.6 eV and 530.77 - 531.16 eV respectively, Figures 4.6b and 4.6d. As detailed in Section 3.4, here as well, the existence of O_L corresponding to Ni-O and -OH was confirmed, while the contribution of O_L from Zn-O might overlap with the -OH and O_L in Ni-O.

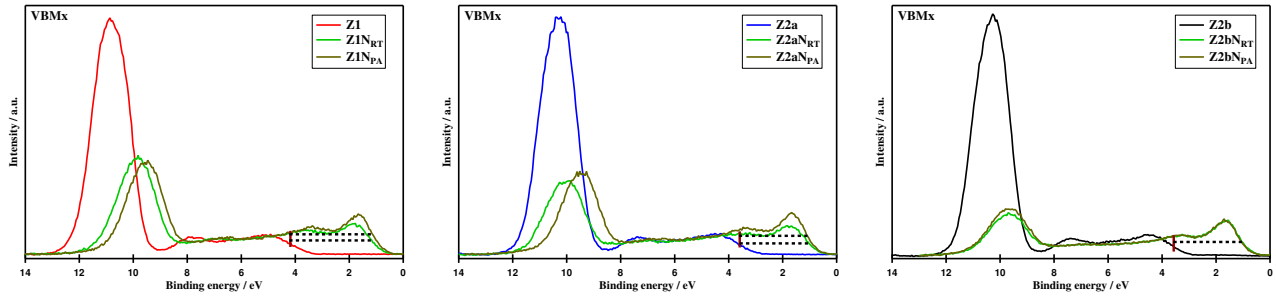

(a) **(b)** **(c)**

Figure 4.5: Spectra of the VBMx of (a) Z1, $Z1N_{RT}$ and $Z1N_{PA}$, (b) Z2a, $Z2aN_{RT}$ and $Z2aN_{PA}$, (c) Z2b, $Z2bN_{RT}$ and $Z2bN_{PA}$.

The Ni^{2+} peak for the heterostructures with Z1 and Z2a, displayed a FWHM of 1.3 - 1.4 eV, and a lower value for the Z2b heterostructures ($\simeq$ 1.17 eV, Table 4.3). This might be due to the fact that the amount of surface hydroxyl was comparatively higher on the

surface of Z1 and Z2a but not on Z2b, which would have induced the change in the nature of bonding of NiO with ZnO[241,242].

The Ni2p spectra of the heterostructures did not show any major change in line shape, as a function of neither scaffold surface cleaning nor the deposition temperature of second material (For example, Figures 4.6a and 4.6c, shows Ni2p spectra of Z2bN$_{RT}$ and Z2bN$_{PA}$, respectively) and thus indicate that mostly NiO was formed on top of the ZnO scaffold. The rather similar value measured for E_F - VBMx (Table 4.3) for the NiO covered surface also indicates the formation of a closely related material.

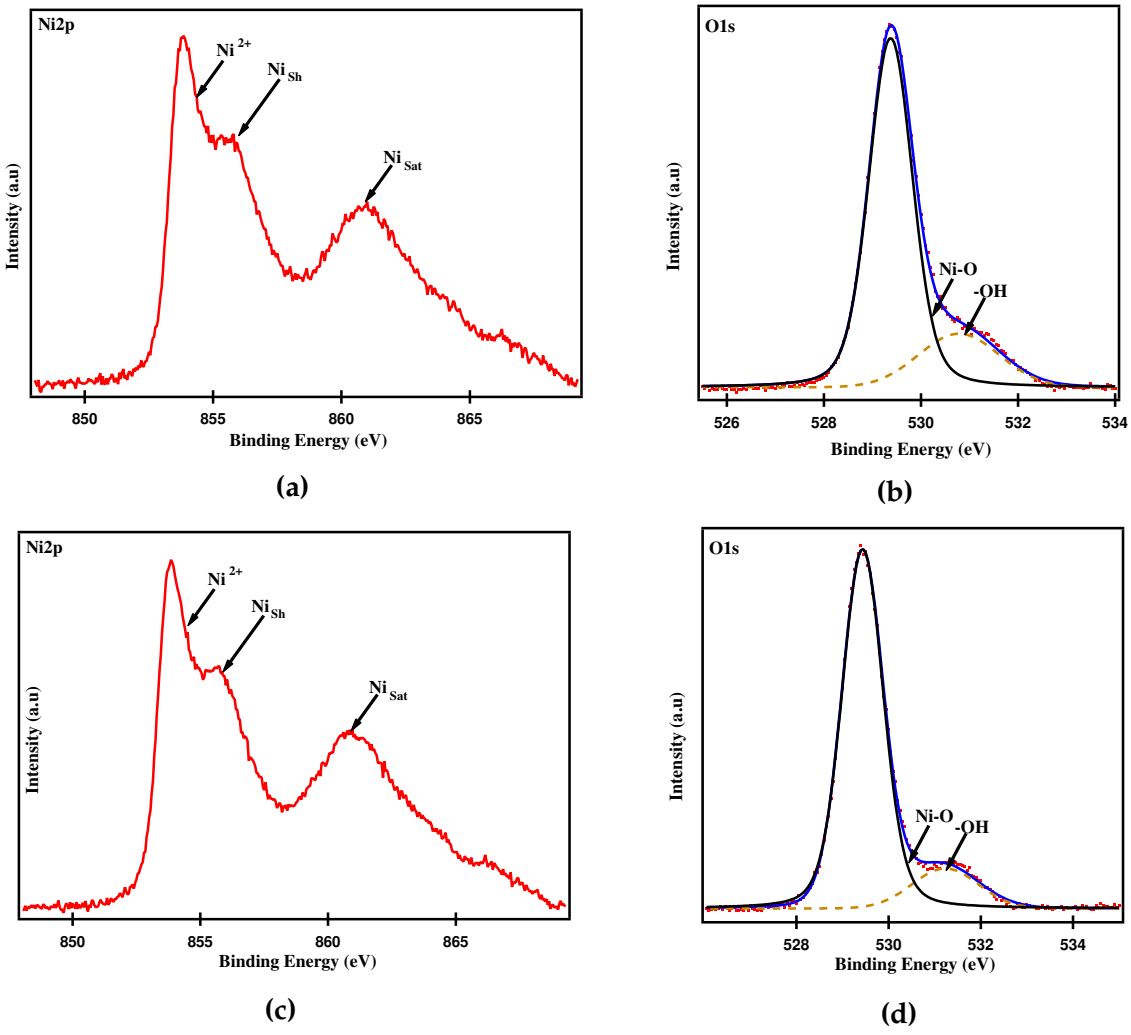

Figure 4.6: As-is spectra of Ni2p and deconvoluted spectra of O1s for Z2bN$_{RT}$ (a and b) and Z2bN$_{PA}$ (c and d) heterostructures, respectively.

Finally, the shifts in BE of Zn2p were used to estimate the attained band bending at the interface of each heterostructure, with the help of equation 2.1 in Section 3.4. The deduced values were ranging between $\simeq$ 0.9 and 1.4 eV, with lowest V_{bb} value for the

heterostructure, Z2aN_{RT} (Table 4.3).

4.1.4. Opto - electronic characterization

Electrochemical Impedance Spectroscopy (EIS) that utilizes a three electrode setup (sample - working electrode, Platinum - counter electrode and Ag/AgCl - reference electrode) was used for performing Linear Sweep Voltammetry (LSV), Impedance analysis and Mott-Schottky (MS) analysis. The Mott - Schottky plots of the scaffold films Z1, Z2a and Z2b were measured in the -0.5 to 0.8 V potential range (30 steps) and the plots are shown in Figure 8.8 (for f=200Hz).

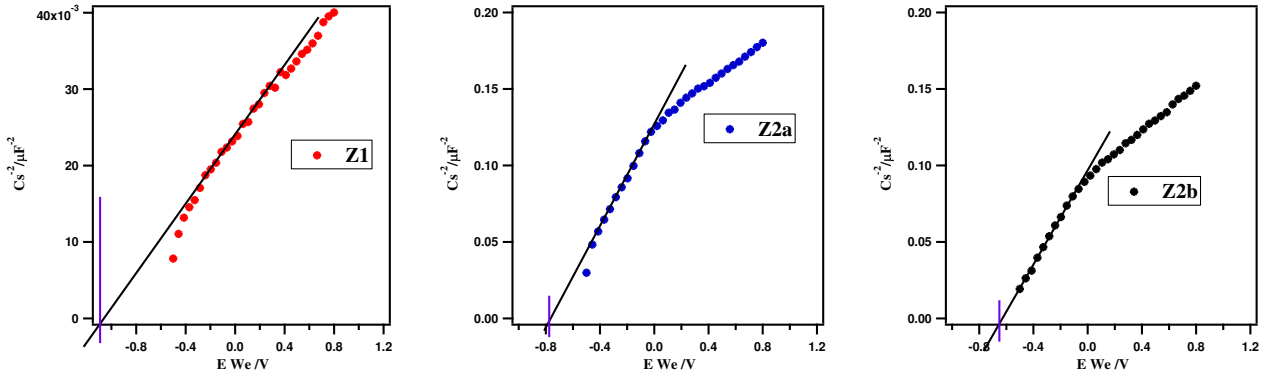

(a) Z1 **(b)** Z2a **(c)** Z2b

Figure 4.7: The Mott-Schottky plots of the scaffold films (a) Z1, (b) Z2a and (c) Z2b, measured in 0.5 M $Na_2SO_4 \cdot 10H_2O$ aqueous solution as electrolyte with Ag/AgCl as reference electrode.

The donor density (N_D) and the flatband potential (E_{FB}) values were extracted from the Mott-Schottky plot as described in Appendix 7.2 (under PhotoElectroChemical measurements) and their values are gathered in Table 4.4.

Table 4.4: The flatband potential and donor density values for the scaffold films, as obtained from MS plots, with Ag/AgCl as reference electrode.

	Sample Name		
Features from MS plots	Z1	Z2a	Z2b
E_{FB} (in V)	-1.02	-0.77	-0.65
N_D (in cm^{-3})	3.4×10^{21}	0.48×10^{21}	0.52×10^{21}

The obtained E_{FB} and N_D of each film clearly indicate that the donor density was reduced after the heat treatment[153], in agreement with the Fermi level lowering below the conduction band. Z2a was noticed to have less carriers than Z2b and in agreement with the wider depletion region.

The current (I) - voltage (V) curves were registered in light for each scaffold and its respective heterostructures are shown in Figures 4.8a to 4.8c. The following features were extracted from the I - V plots: (i) onset potential (V_{OP}) (ii) the photocurrent produced at the water splitting voltage 1.026 V (vs. Ag/AgCl) and (iii) the maximum photocurrent density that can be attained at potentials more anodic than 1.026 V. The determination of onset potential was done by extrapolating the straight line (the linear portion of the I-V was fitted with a line) to the x-axis[243]. The photocurrent noticed at 1.026V and its more anodic potentials were extrapolated on the y-axis and are presented in Table 4.5.

Table 4.5: Representation of onset potential, photocurrent at water splitting voltage and total photo current densities for both scaffold and heterostructured films, with Ag/AgCl as reference electrode.

Sample Name	Onset Potential (V)	Photocurrent at 1.026 V vs. Ag/AgCl (mA/cm^2)	High Current Density (mA/cm^2)
Z1	1.25	0.012	2.70
$Z1N1_{RT}$	1.18	0.060	2.20
$Z1N1_{Pa}$	1.20	0.043	2.70
Z2a	1.40	0.023	1.96
$Z2aN1_{RT}$	1.25	0.013	1.40
$Z2aN1_{PA}$	1.25	0.023	1.15
Z2b	1.28	0.002	0.72
$Z2bN1_{RT}$	1.20	0.084	5.80
$Z2bN1_{PA}$	1.18	0.073	6.60

Theoretically, the E_{FB} is the potential at which photocurrent will arise, but this is never the case because of surface recombination or accumulation of electrons (if p-type) / holes (if n-type) at the surface, due to poor charge transfer kinetics[58]. Therefore, the V_{OP} is always higher than E_{FB}.

Among the scaffold surfaces, Z1 showed lower V_{OP} of 1.25V while Z2a and Z2b showed V_{OP} of 1.4 and 1.28 respectively. The variations in V_{OP} follow the variations in the Fermi level. For the heat treated surfaces, the V_{OP} was directly proportional to the amount of band bending that was observed (in XPS) after heating (i.e, decreasing with increasing vacuum). With higher band bending, the V_{OP} was also higher and so was the barrier that the electrons have to overcome for being transferred to the electrolyte, explaining the lower photocurrent values obtained for the Z2a scaffold and its heterostructures.

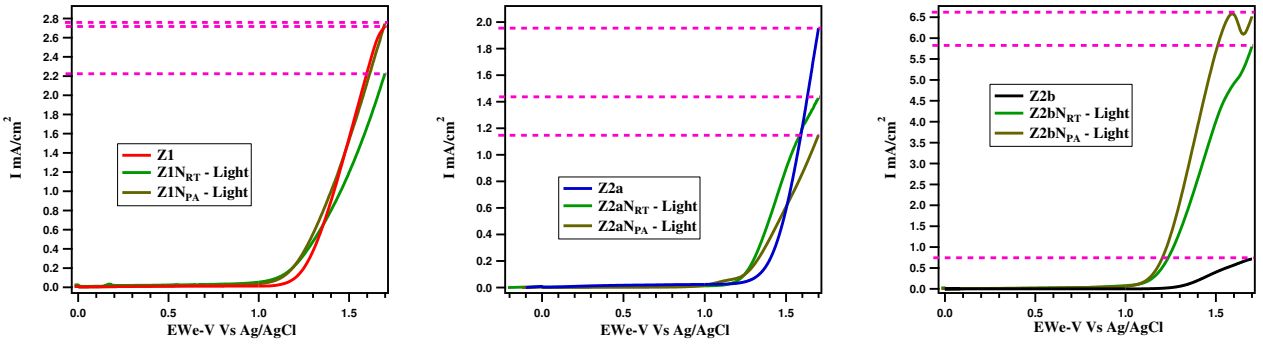

Figure 4.8: Linear Sweep Voltammetry curves for Z1, Z2a and Z2b, and their respective heterostructures (a, b and c respectively), swept in the 0 - 1.7 V voltage range in presence of 0.5 M $Na_2SO_4{\cdot}10H_2O$ aqueous solution as electrolyte.

The pristine Z1 scaffold which exhibited an accumulation of electrons at the surafce would have resulted into a smaller band bending when into contact with the electrolyte and irradiated by light source, leaving photogenerated holes at the surface. This kind of photoresponse is accountable for the slow relaxation of photoinduced electrons, which has enabled higher photocurrent than Z2a counterpart [244]. In case of Z2b, V_{OP} was smaller than that for Z2a counterparts and together with the lower band bending (from XPS) explain the higher photocurrent values obtained.

The onset potential for heterostructures was lower than that of their corresponding scaffold and the photocurrent at 1.026 V (vs. Ag/AgCl) was increased. This demonstrates the enhancement in hole transfer and charge separation. However, the lower maximum photocurrent values of the Z1 and Z2a heterostructures with report to the scaffold suggest that the charge separation process was not so effective. The photoresponse and XPS analysis indicate that surface cleaning under high vacuum (Z2b) leads to improved charge transfer kinetics and reduced surface charge recombination.

4.1.5. Photoluminescence

The study of the photoluminescence response (Figure 4.12) of the pristine (Z1) and cleaned ZNR (Z2b) surface was performed in order to highlight the influence of defects on the photoresponse and estimate their photocatalytic activity.

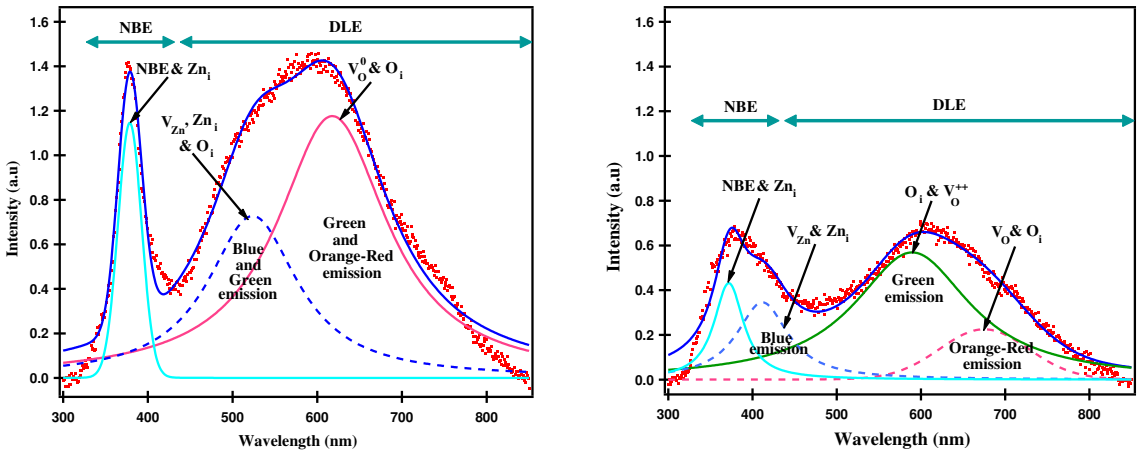

Figure 4.9: Deconvoluted PL spectra of (a) Z1 and (b) Z2, surface cleaned [at 0.5 Pa] and then ambience exposed.

Conventionally, ZnO is capable of giving rise to PL emissions spanning within the range of 300 - 800 nm that are categorized into distinctive regions as UV (375-395 nm), blue (405 - 450 nm), green (500 - 560 nm), orange (600 - 640 nm) and red (650 - 750nm) emissions [17, 157, 208]. These occurrences could be either observed evidently or by the deconvolution process of a broad peak as performed in our studies. The deconvoluted Photo Luminescence (PL) spectra for Z1 and Z2 (after surface cleaning at 0.5 Pa and then ambience exposed) are shown in Figure 4.9a and Figure 4.9b, respectively. Here, the PL spectra of both Z1 and Z2 exhibited two major broad peaks attributed to the Near Bandedge Emission (NBE) and the Deep Level Emission (DLE) (Figures 4.9a and 4.9b), situated in the 387-397 nm and 450-800 nm range, respectively. The former occurs due to the presence of recombination centers at the surface, whereas the latter corresponds to the deep trap levels (vacancies) in ZnO.

After deconvolution, three peaks were identified for the Z1 scaffold PL spectrum that belong to the UV, blue, green and orange-red emissions. This unveiled the presence of shallow and deep level defects like free surface excitons (FX) [158, 175], Zn vacancies (V_{Zn}), Zn intersititals (Zn_i) [158, 162, 245], oxygen vacancies (V_O) and oxygen intersitials (O_i) [162, 245-247]. The narrow NBE peak (UV emission), located at 378nm is the result of free surface excitons

but also due to the shallow level defects like Zn_i. The broad DLE peak included blue, green, orange and red emissions. The transition between Zn_i and V_{Zn} levels led to the blue emission, which overlaps with O_i species that gives the green emission ($\simeq$ 450-550 nm). The peak centered at $\simeq$ 602 nm indicates the presence of excess electrons at the surface as the peak corresponding to neutral oxygen vacancies (V_{O^0})[162,245–247] is mainly observed, in agreement with the XPS studies, which showed that the E_F lies above the conduction band minimum and an electron accumulation layer is formed at the surface.

In case of Z2, all the contributions previously discussed were identified but with shifts and decreased intensity levels. The decline in intensity levels suggest that the surface cleaning in presence of oxygen was effective in reducing the amount of recombination centers. This agrees well with XPS showing a shift of Fermi level position below the CB after heating. The NBE peak of Z2b was blue shifted and broadened (mildly) as an effect of thermal treatment (Figure 4.9b and Table 4.6). In fact, the high value of I_{DLE}/I_{Total} ratio indicates that the contribution of deep level emission was still high, even after the surface cleaning. This could be due to -OH re-adsorption from the ambience during sample transfer to the PL instrument.

Table 4.6: Sample codes and corresponding details from PL spectrum. I_{NBE} and I_{DLE} values were taken by calculating the corresponding area below the deconvoluted peaks (using a data analysis software, IgorPro) in PL spectra.

Sample Code	NBE Peak maximum position (in nm) / Shift	DLE Peak maximum position (in nm) / Shift	FWHM of NBE (in nm)	I_{NBE}/I_{Total}	I_{DLE}/I_{Total}
Z1 - Without surface cleaning	371 / -	602 / -	38	0.18	0.82
Z2 - surface cleaned [at 0.5 Pa] and then ambience exposed	367 / Blue	570 / Blue	40	0.21	0.78

The spectra was noticed to have a broad bridge between NBE and DLE, revealing the contribution of Zn_i and V_{Zn}. The peak corresponding to V_O was also blue shifted with a

reduction in its intensity, a sign that the neutral vacancies were ionized (doubly charged oxygen vacancy, V_O^{++})[17,156,248], through heat treatment under high vacuum and part of them were filled by oxygen as also indicated by the XPS results.

4.1.6. Photo electrochemical impedance studies

PhotoElectrochemical Impedance Studies (PEIS) spectra was recorded for all scaffold and heterostructured films, and the Nyquist plots of the scaffolds and of Z2b and its heterostrcutures are shown in Figures 4.10a and 4.10b (for heterostrcutures with Z1 and Z2a scaffolds, refer to appendix). All scaffold films were fitted with the equivalent circuit composed of five elements [R_s + R_{CT1}||Q1 + R_{CT2}||Q2 - where + and || represents series and parallel connection respectively; model circuit is shown in appendix, Figure 7.10.] whereas all heterostructures (except that of Z2a) were fitted with a circuit comprising of six elements [R_s + R_{CT1}||Q1 + R_{CT2}||Q2 + Q3], due to the observation of diffusion process[249,250]. In the inset of Figure 4.10a, a zoomed image is shown for the high frequency region which illustrates the contribution of R_{CT1}||Q1. The generated fit correlated well with the recorded spectra of all films, as seen in each of their represented spectra.

In these circuits, R_S stands for the contacts and electrolyte resistance, R_{CT1}||Q1 is attributed to the FTO/ZnO/NiO interfaces, whereas the R_{CT2}||Q2 corresponds to the charge transfer resistance and capacity of the double layer formed at the sample/electrolyte interface. In addition, when diffusion was visible Q3 was used to define the diffusion behaviour. The values of R_S, R_{CT1} and R_{CT2} obtained through fitting are gathered in Table 4.7.

Table 4.7: R_s [Contact resistance (FTO/ZnO)], R_{CT1} [Semiconductor or interfacial charge transfer resistance (ZnO-seed/ZNR or ZnO/NiO)] and R_{CT2} [Charge Transfer resistance (Film/Electrolyte)] values for all the scaffold and heterostructured films.

Sample Name	R_s (Ω)	R_{CT1} (Ω)	R_{CT2} (Ω)
Z1	3	38	20527
$Z1N1_{RT}$	160	25	2700
$Z1N1_{PA}$	110	25	63
Z2a	5	30	38639
$Z2aN1_{RT}$	49	28	-
$Z2aN1_{PA}$	161	40	-
Z2b	104	38	40327
$Z2bN1_{RT}$	3	25	334
$Z2bN1_{PA}$	14	28	36

The R_{CT1} values have negligible variation with the type of scaffold or NiO deposition conditions. However the R_{CT2} values of the heterostructures were considerably reduced with report to their corresponding scaffold. Among the scaffold, sample Z1 showed the smallest R_{CT2} value corresponding to the highest maximum photocurrent. The middle frequency contribution could not be detected for the $Z2aN_{RT}$ and $Z2aN_{PA}$ samples indicating a fast charge transfer process. However, the lowest photocurrent values were obtained for these samples. This might be due to the increased surface recombination due to incomplete desorption of adsorbates. The same reasons are behind the poor photocurrent values obtained for Z1 heterostructures. Concurrently, the R_{CT2} values of Z2b heterostrustures were relatively smaller than all other heterostructures, signifying the effective charge transfer and separation at the interface, in agreement with the maximum photocurrent obtained for these heterostructures.

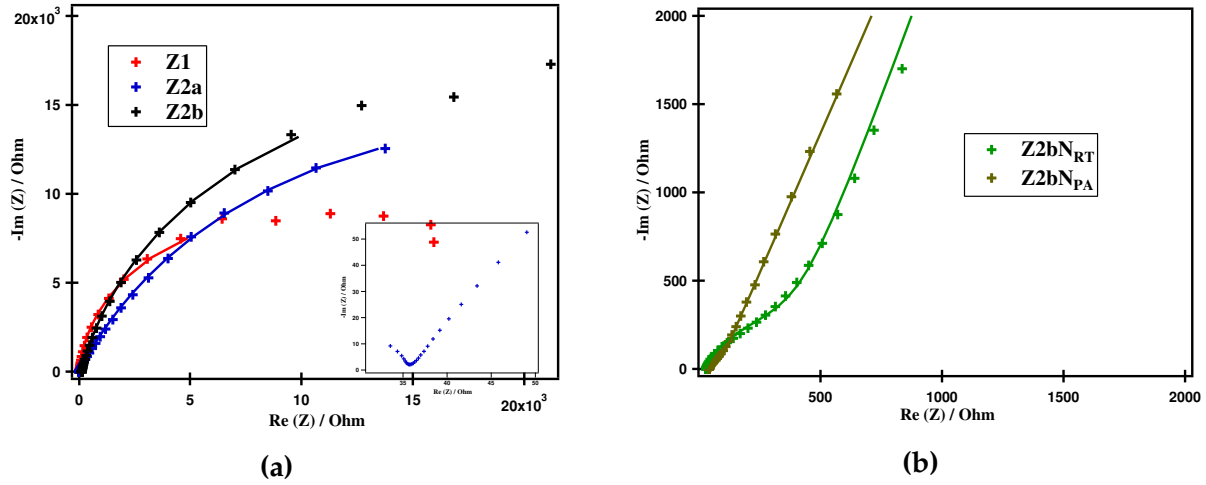

Figure 4.10: Nyquist plot for (a) scaffold (inset showing the first contribution), (b) $Z2bN_{RT}$ and $Z2bN_{PA}$. Symbols and continuous lines in the plots represent the data and the generated fit, respectively.

When comparing the different NiO deposition conditions, the heterostructures with NiO deposited at RT followed by post annealing condition showed lower charge transfer resistance (R_{CT2}), corresponding to higher photocurrent values. The negative influence of remaining adsorbates is clearly noticed for sample $Z1N_{RT}$ for which the photocurrent is lower even if a lower R_{CT2} value compared to Z1 scaffold was obtained. The influence of the NiO deposition temperature on the heterostructure properties is further investigated in the next section.

In conclusion, an enhanced charge separation and faster charge transfer was obtained for the heterostructures with Z2b. This highlights the importance of both surface

and interface properties in enhancing the carrier lifetime and surface reaction kinetics apart from the material response to illumination, which eventually boosts the photocatalytic activity [132,251].

Conclusion

Surface characteristics of ZnO nanorods were successfully modified by varying the system base pressure during heat treatment. The surface of ZNR that was heated at 0.5 Pa was less depleted than the surface that was heated at 5 Pa, indicating that the high vacuum favored the adsorbates and oxygen desorption. The presence of neutral oxygen vacancies (in Z1) and then passivation (ionization, in Z2) was confirmed by PL analysis from the blue shift in the deep level emission The decrease in surface hydroxyl content at the surface was confirmed by XPS. The Mott - Schottky measurement were in agreement with this observation, showing a lower donor density. However, among scaffold, it is the Z1 surface that attained the highest photocurrent due to a pre existent electron accumulation layer that facilitated the holes transfer to the electrolyte.

The XPS studies demonstrated that the band bending at the NiO/ZnO interface was influenced by the scaffold surface pre heating. The heterostructures formed with the ZNR surface treated under high vacuum attained higher band bending and lower charge transfer resistance due to improved interface, eventually leading to the highest photocurrent values. Surface cleaning under high vacuum has enabled an effective charge separation and charge transfer kinetics, and therefore, the Z2b scaffold was used in further studies and denoted as Z2.

As a conclusion, our studies indicate that the system base pressure, the temperature and the oxygen partial pressure should be considered when designing a heterostructure, and proves that, only both the enhancement in charge separation and enrichment in charge transfer will lead to improvement in the photoelectrochemical activity of heterostructures.

4.2. Influence of NiO deposition temperature

4.2.1. Sample description

For this study, we have prepared heterostructures based on ZnO (heat treated at 400 °C in presence of oxygen, under high vacuum as optimized in previous section) and NiO which was deposited at different temperatures, using a partial oxygen pressure (P_{O_2}) of 6% and a deposition time of 40 s (chosen to attain a thickness of 7 - 10 nm), as summarized in Table 4.8. For comparison, the pristine ZNR surface (Z1) was also used to prepare the heterostructures with NiO. The investigations of X-Ray Photoelectron Spectroscopy (XPS) and Photoluminescence (PL) were correlated with the photodegradation activity, allowing the understanding about the role of external factors like ZnO surface cleaning and NiO deposition conditions on the scaffold surface chemistry and consequently on the internal factors (band bending, ratio of shallow level defects vs. deep level defects) on the pollutant degradation response.

Table 4.8: Preparation details and corresponding sample codes

Sample Code	Preparation Details		
	Surface Cleaning (at 0.5 Pa)	Second Material (NiO)	NiO deposition temperature conditions
Z1	No	-	-
$Z1N_{RT}$	No	√	deposited at RT
$Z1N_{PA}$	No	√	deposited at RT and post annealed (at 250 °C, for 1 h in presence of 5 sccm oxygen)
$Z1N_{HT}$	No	√	deposited at high temperature (400 °C)
Z2	Yes	-	-
$Z2N_{RT}$	Yes	√	deposited at RT
$Z2N_{PA}$	Yes	√	deposited at RT and post annealed (at 250 °C, for 1 h in presence of 5 sccm oxygen)
$Z2N_{HT}$	Yes	√	deposited at high temperature (400 °C)

4.2.2. Transmission electron microscopy

The SEM images of the ZNR film after NiO deposition did not show any changes in morphology (as shown in Section 3.2). This is due to the fact that the NiO thickness was very low, below 10 nm. Therefore, the structure of the heterostructures was investigated through TEM.

Figure 4.11a confirms the 1D nanostructure with nanorods being characterized by a smooth surface. After the NiO deposition, the surface of nanorods is uniformly covered by a rough layer (Figures 4.11b and 4.11c) with a thickness in the range of 2-3 nm. We also noticed that the thickness of NiO layer was higher for PA ($\simeq$ 6-7 nm) than that for RT conditions, which might be due to the supplementary post annealing treatment.

The image of the HT film (Figure 4.11d) revealed the formation of cubic nanoparticles of $\simeq$ 5-6 nm (zoomed image in inset of Figure 4.11d), rather than a layer at the surface of nanorods. This indicates that the crystallite size is enhanced due to the slower growth rate. Apart from these features, the lattice spacing of d=0.24 nm that correspond to the (111) lattice planes of cubic NiO was observed, indicating the formation of well crystallized NiO at HT deposition [252] (Images (Figure 8.2) showing the lattice fringes, for each deposition temperature is represented in the Appendix 8.2). The TEM images also demonstrate that the NiO layer was capable of covering the ZNR surface throughout its 200-250 nm length, which could be expected to increase the visible light absorption [174].

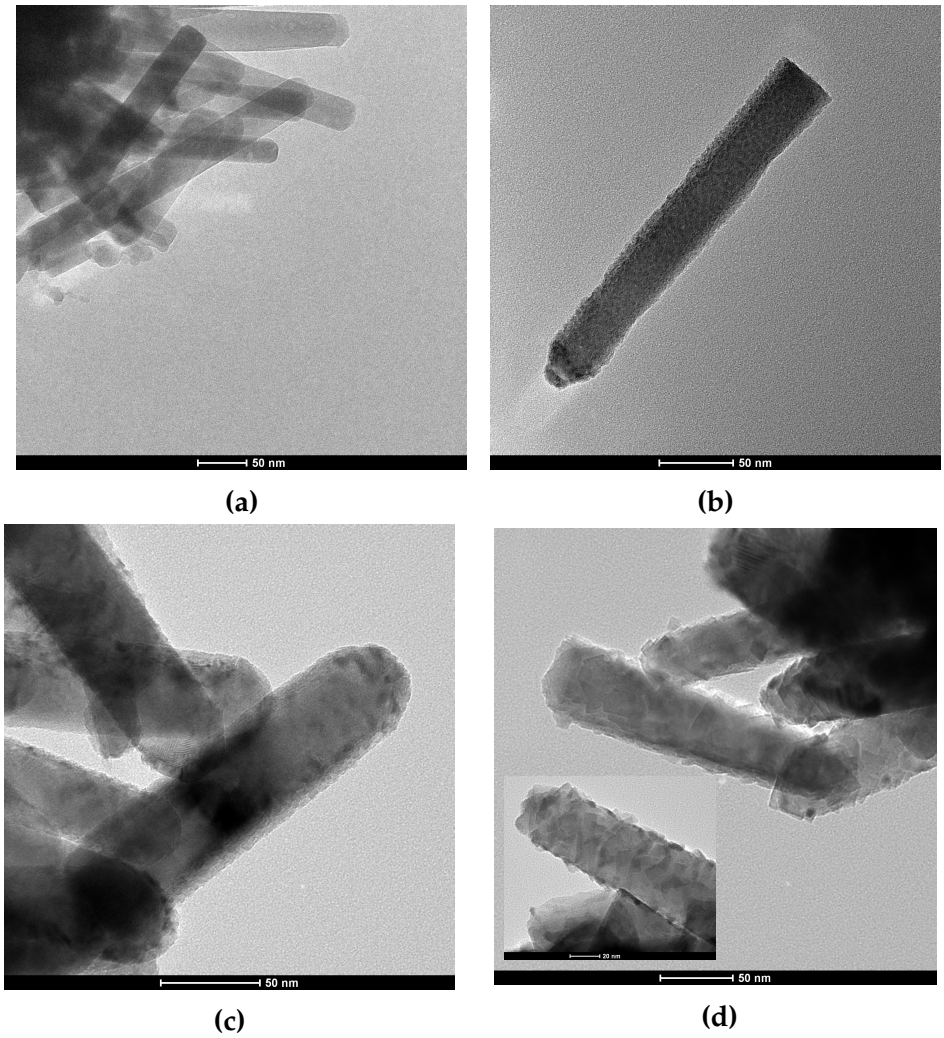

Figure 4.11: TEM image of (a) ZNR, (b) $Z1N_{RT}$, (c) $Z1N_{PA}$ and (d) $Z1N_{HT}$ [zoomed view in the inset]. RT - deposited at Room temperature; PA - deposited at RT and Post Annealed; HT - deposited at High temperature.

4.2.3. Photoluminescence

Furthermore, to gain deep insights into the effect of NiO deposition temperature and surface cleaning on the heterostructure formation, the photoluminesence of Z1 and Z2 scaffold was compared with their respective heterostructures (Figures 4.12a and 4.12b).

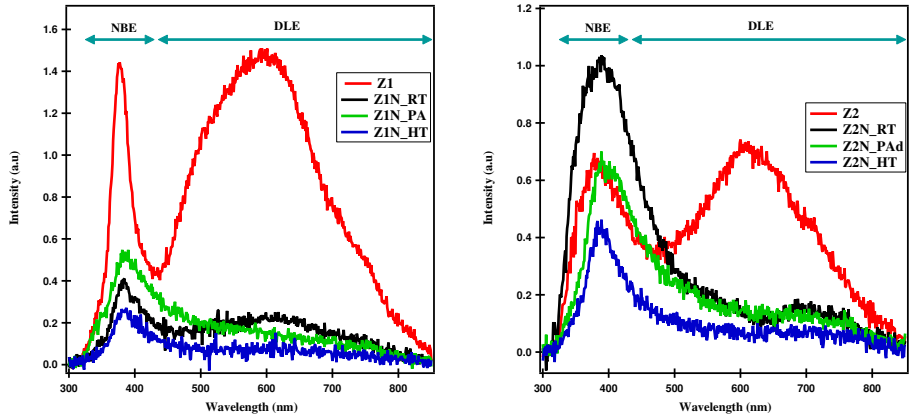

Figure 4.12: Photo Luminescence spectra of (a) Z1 (without surface cleaning) and corresponding heterostructures and (b) Z2 (Surface cleaned) and corresponding heterostructures.

For further understanding the contribution of surface excitons and defects in charge carrier recombination, the intensity ratios I_{NBE}/I_{Total} and I_{DLE}/I_{Total} were determined (after deconvolution) and reported in Table 4.9.

Table 4.9: Sample codes and corresponding information extracted from PL spectrum, determined I_{NBE} and I_{DLE} values were taken by calculating the corresponding area below the deconvoluted peaks (using a data analysis software, IgorPro) in PL spectra.

Sample Code		NBE Peak maximum position (in nm) / Shift	FWHM of NBE (in nm)	I_{NBE}/I_{Total}	I_{DLE}/I_{Total}
Without surface cleaning (Z1)	Z1	371	38	0.18	0.82
	$Z1N_{RT}$	379 / Red	50	0.05	0.11
	$Z1N_{PA}$	381 / Red	61	0.08	0.08
	$Z1N_{HT}$	379 / Red	58	0.04	0.03
Surface cleaned (Z2)	Z2	367 / Red	40	0.21	0.78
	$Z2N_{RT}$	372 / Red	41	0.45	0.34
	$Z2N_{PA}$	381 / Red	48.17	0.08	0.4
	$Z2N_{HT}$	384.1 / Red	41	0.08	0.11

After NiO deposition the intensity of the PL decreased but a matching contribution from both DLE and NBE (Table 4.9) was observed, suggesting that even if charge separation

was enabled (as evidenced through XPS, discussed in the following section), non-radiative recombination across the NiO layer might have occurred. The NBE peaks of almost all heterostructures were red shifted (Table 4.9) signifying an enhancement in the quantum confinement effect[253,254], as a result of nanoscale NiO covering.

In case of sample $Z2N_{RT}$, the red shift accompanied by the increase in intensity of NBE peak might indicate an additional effect, apart from the non-radiative recombination across the NiO layer. Additionally, the broadening as compared to scaffold indicates the presence of fluctuations in interface properties[255,256]. This effect was removed by using a cleaned scaffold and deposition of NiO at HT, as in the case of sample $Z2N_{HT}$.

4.2.4. X-Ray photoelectron spectroscopy

Scaffolds Z1 and Z2, their respective heterostructures, prepared in RT and RT+PA conditions were already compared in Section 4.1.3 (as Z1 and Z2b, their respective heterostructures), however, they are shown here in comparison with their corresponding HT counterparts, in order to understand the influence of NiO deposition temeprature on the interface properties (Figures 4.14a to 4.14d). In addition, the scaffold Z2 was investigated by XPS after exposing Z2 surface to ambience (denoted as Z2 Ex-situ). The emission lines of Z2 Ex-situ [Zn2p (Figure 4.13a), O1s (Figure 4.13b) and C1s (Figure 4.13c), VBMx (Figure 4.13d)] confirmed the existence of Zn and O, but also of carbon and hydroxyl species (increase of the O1s shoulder peak) that were re-adsorbed on the surface of the Z2 sample[177,214,246]. The slight shift of the Zn2p BE of about 0.50 eV (Figure 4.13a and Table 4.10) as well as the E_F - VBMx shift (for Z2, E_F - VBMx = 3.04eV whereas for Z2 Ex-situ, E_F - VBMx = 3.39eV, Table 4.10) were attributed to a change in the doping of the sample from a sample which was n- doped to a sample which is n+ doped, while the reverse was noticed for Z1 and Z2. In principle, we cannot discriminate in these experiments a bulk doping from a surface doping but assume a change of bulk doping because of the small thickness of the nanorods (diameter $\simeq$ 50-60 nm). In addition to the above mentioned changes, there was a decrease in intensity of all peaks and all these confirmed the readsorption of contaminants on the Z2 surface[214].

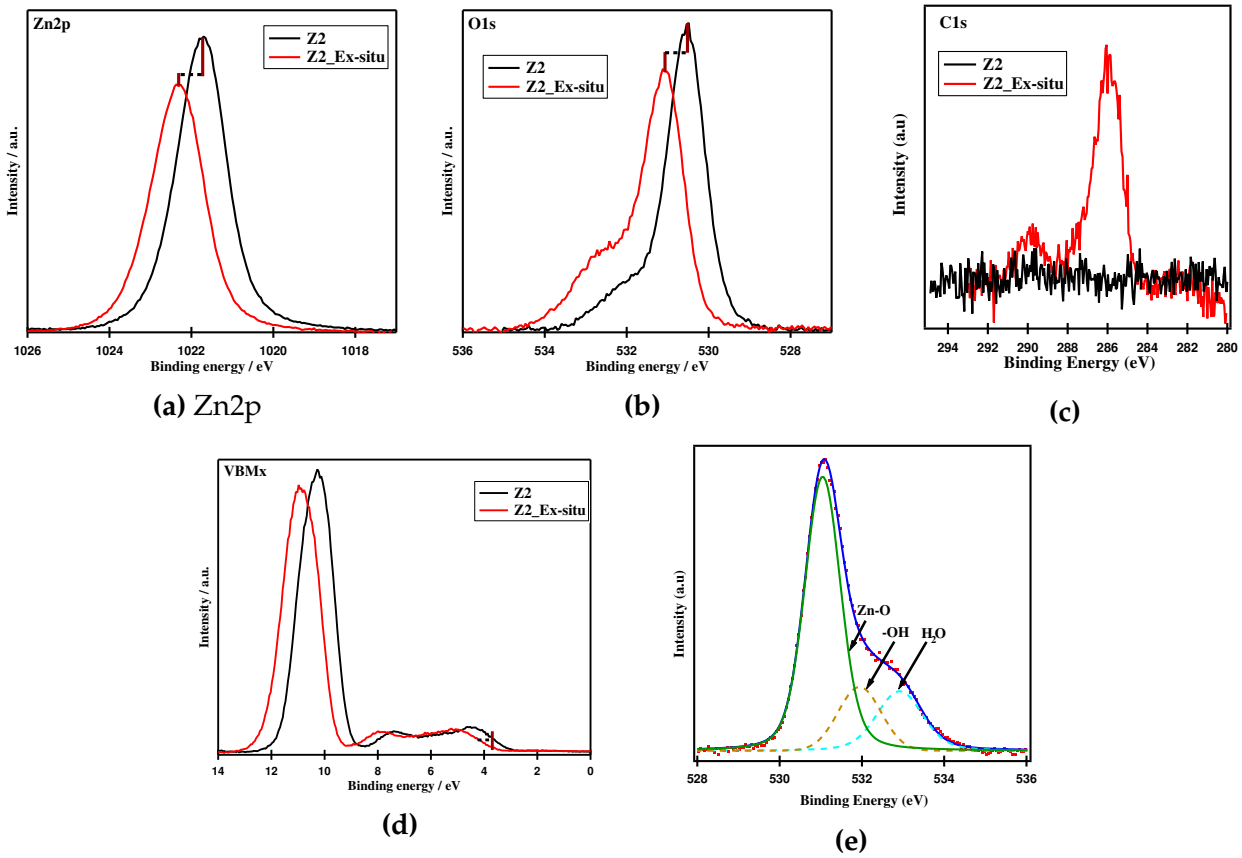

Figure 4.13: Zn2p (a), O1s (b), C1s (c) spectra and VBMx (d) shift for samples Z2 and Z2 Ex-situ (e) O1s peak deconvolution for Z2 ex-situ.

As in case of Z1 (Figure 4.1.2a in Section 4.1), O1s core level line for Z2 Ex-situ was composed of three contributions, lattice oxygen (O_L) - 531.05 eV, hydroxyls (O_{OH}) - 531.94 eV and adsorbed water (O_{H_2O}) - 532.92 eV, Figure 4.13e). In order to identify any changes in the O/Zn ratio, the area under Zn2p and oxygen lattice curves were taken into account for Z2 ex-situ and deduced as 0.41 using equation 4.1 (in Section 4.1). This was similar to the value obtained for Z2 (0.43, in Section 4.1.3), clearly indicating that the chemisorbed oxygen by heat treatment was not affected after exposure to ambience.

With the deposition of NiO, the typical features and satellite structure of Ni^{2+} and O were observed [177] (Figures 4.14b and 4.14c and Figures in appendix). Also, the XPS valence band feature shows the typical spectral signature of NiO (Figure 4.14d and Figure in appendix). However, even for HT conditions, no modification of the satellite peak (from the Ni2p core level) is detected (Figure 4.14b), meaning that the formation of Ni^{3+} is likely unprobable.

Table 4.10: Binding Energy (BE) values of Zn2p, Ni2p, O1s peaks and E_F - VBMx for scaffold surfaces [Z1 (without surface cleaning), Z2 (Surface cleaned) and Z2 Ex-situ] and corresponding heterostructured films of Z1 and Z2 scaffolds. [RT - Room temperature; PA - Post Annealed; HT - High temperature]; 0.50 eV was added to the V_{bb} values of all Z2 heterostructures, with respect to the shift of Zn2p line for Z2 scaffold in relation to the reference material, Z1 scaffold.

Sample Code		XPS Spectra				
		Zn2p (eV)	Ni2p (eV)	O1s (eV)	E_F - VBMx (eV)	V_{bb} (eV)
Without surface cleaning (Z1)	Z1	1022.33	-	531.05	3.47	-
	$Z1N_{RT}$	1021.21	854.16	529.64	0.67	1.12
	$Z1N_{PA}$	1021.01	854.02	529.49	0.63	1.32
	$Z1N_{HT}$	1021.44	854.23	529.89	0.95	0.89
Surface cleaned (Z2)	Z2	1021.83	-	530.67	3.04	0.50
	Z2 Ex-situ	1022.31	-	531.06	3.39	-
	$Z2N_{RT}$	1020.97	853.88	529.37	0.63	1.36
	$Z2N_{PA}$	1021	853.9	529.41	0.66	1.29
	$Z2N_{HT}$	1021.16	854.12	529.63	0.84	1.17

If we compare the observed changes in V_{bb} as well as the changes in relative intensities and position [145 177] of Zn2p, Ni2p and O1s lines (Table 4.10) after NiO deposition (Figures 4.14a to 4.14c and Figures in appendix), a clear trend cannot be extracted that could be related to modification of the growth process of the co-catalyst, neither to changes in the doping of the scaffold. However, some general conclusions can be deduced. The NiO deposition at high temperatures on Z1 and Z2 scaffold shows a larger E_F - VBMx difference (0.84-0.95eV, Table 4.10) compared to RT and PA depositions (0.66eV, Table 4.10), which can be related to a better-defined stoichiometry. The lowering of Fermi level for Z2 and its heterostructures could be attributed to the scaffold surface cleaning treatment which changes the doping level from n+ to a n-. The overall shift in BE that led to band bending is larger for the Z2 heterostructures as compared to the Z1 ones, which can be understood by the removal of adsorbates. Overall, a clearly developed band bending ranging from 1.36 eV to 0.89 eV (Table 4.9) is found after heterostructure formation.

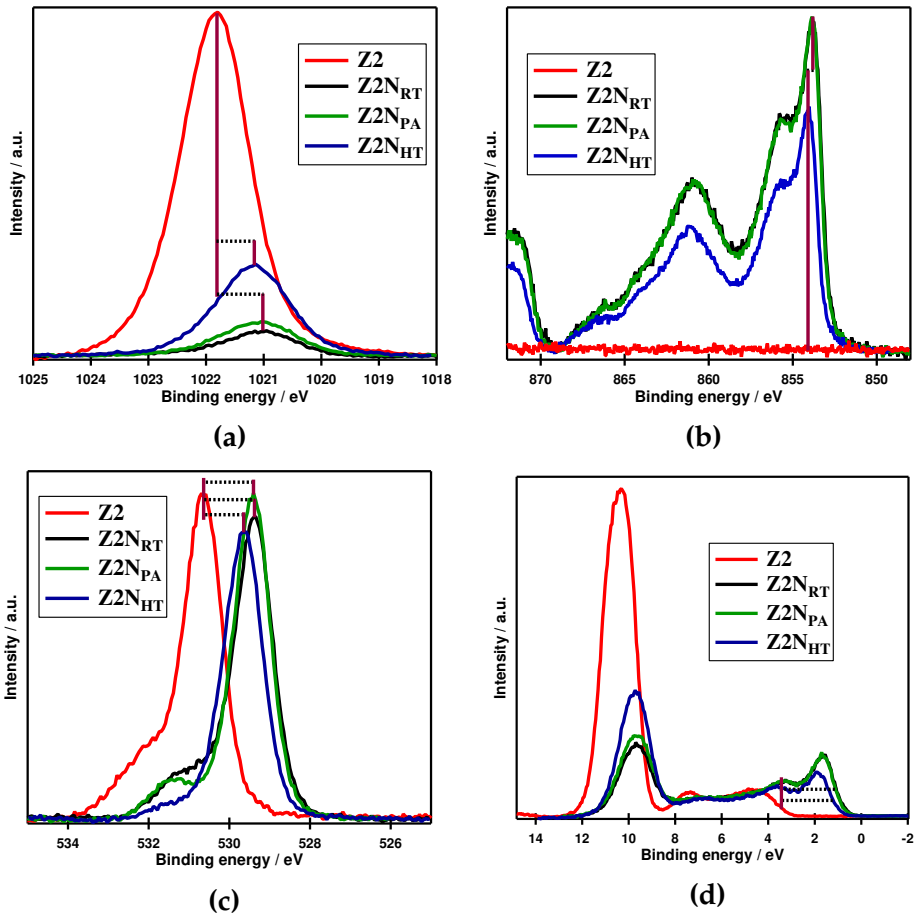

Figure 4.14: Zn2p (a), Ni2p (b), O1s (c) and VBMx (d) spectra of the scaffold Z2 and its heterostructures.

4.2.5. Pollutant degradation

The photodegradation experiments were done as described in Appendix, under section 8.1.4.1. The degradation rate (C_t/C_0 vs. time) for each sample was calculated as according to equation 4.3, plotted in Figure 4.15a and the degradation efficiencies are shown in Figure 4.15b.

$$Efficiency \quad (\eta\%) = \left(1 - \left(\frac{C_t}{C_0}\right)\right) \times 100 \tag{4.3}$$

Where, C_t - Concentration in time; C_0 - Initial concentration.

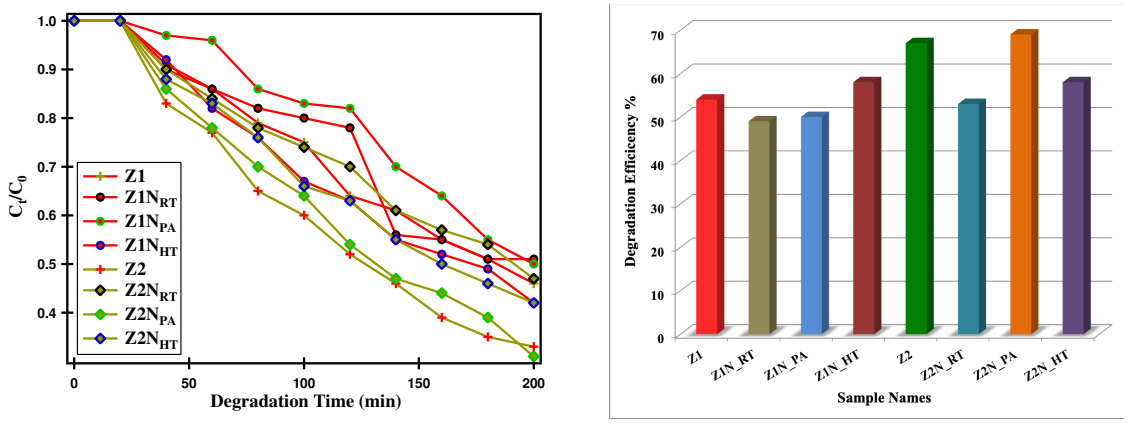

Figure 4.15: (a) C_t/C_0 vs. degradation time for Z1 (without surface cleaning), Z2 (surface cleaned) and their corresponding heterostructures and (b) bar graph plot showing the degradation efficiency. Degradation studies were conducted for 3 replicates of scaffold Z1 (without surface cleaning) and resulted in an error bar of $\pm 2\%$. The Z2 scaffold subjected to degradation study here is practically the surface exposed to ambience after surface cleaning.

Z1 was able to degrade 54% of the pollutant whereas, its heterostructures were found to have lower performance, except for HT whose efficiency was 58%. We believe that four competing mechanisms influence the photodegradation efficiency: (1) the holes photogeneration which is favoured for low NiO thickness, (2) charge recombination which is expected to be enhanced when valence band bending is reduced, (3) ZnO interface charge recombination because of defects and (4) charge recombination across the NiO layer. In case of Z1 heterostructures, the variation of photocatalytic efficiency cannot be explained by a simple combination of these arguments. In case of sample $Z1N_{HT}$ mechanism (1) is prevailing.

Concurrently, the Z2 heterostructures were overall more efficient than their Z1 counterparts, with the highest efficiency for the $Z2N_{PA}$ (69%), however equivalent with the one of the scaffold. From here we conclude that limiting the contribution of mechanism (3) by surface cleaning is mostly influencing the photocatalytic efficiency, and the modest or lack of improvement after NiO deposition might be influenced by mechanism (4), which could be due to a thinner space charge layer.

Recent reports on powder materials have demonstrated that post processing of ZnO or heterostructure formation enhanced the photocatalytic activity due to reduction in surface/bulk defects and improved charge separation [93, 132]. This was also correlated with the photoluminescence response but with inconsistent conclusions; reduction [137, 162, 257] and increase [160, 174, 258] in NBE emission were both related to an enhancement in photocatalytic activity.

Bringing n-type ZnO and p-type NiO material into contact resulted in the formation of a space charge region at the interface and thus band bending (example shown for $Z2N_{RT}$ in Figure 4.16, E_F - VBMx values from Table 4.10). Despite attaining a maximum band bending of $\simeq$1.3 eV in both Z1 and Z2 heterostructures, the pollutant degradation efficiency did not show any improvement (as compared to their respective scaffolds), emphasizing that larger band bending does not generally lead to higher photodegradation efficiency.

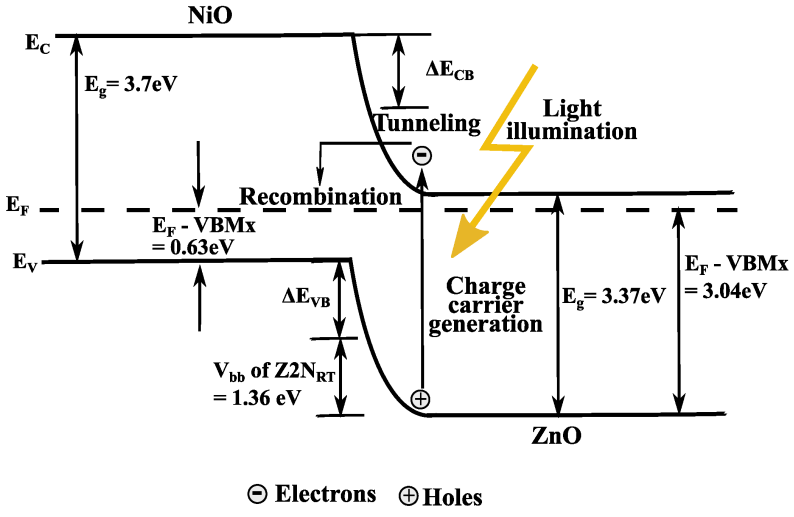

Figure 4.16: Band alignment and band bending for $Z2N_{RT}$ [RT - Room Temperature]. E_F - VBMx values as obtained from the respective XPS spectra; $\triangle E_{CB}$ and $\triangle E_{VB}$ in the figure correspond to conduction band and valence band offsets that could be derived with the systematic interface study as shown in Chapter 3 (Section 3.4).

These results maybe in contrary to previous literature reports where heterostructures were shown to be photocatalytically more active as a consequence of charge separation induced by interfacial band bending [93, 132]. The optimal band bending (height and width of the space charge layer) and its influence on photocatalytic response were not reported in literature previously. Thus, for a detailed discussion of space charge effects in charge carrier separation, all aspects of heterostructure preparation must be taken into consideration. Due to the high doping of the ZnO scaffold, which is an indication of large concentration of bulk/surface defects, the width of the space charge layer shown in Figure 4.16 is very small. As a consequence, charge carriers are not evidently separated due to the contact but instead recombine via the NiO layer by tunnelling through the extremely thin interface barrier. This mechanism can explain the low catalytic efficiencies obtained for Z1 based samples and the slightly improved efficiencies of Z2 samples as here the doping concentration is reduced. Moreover, our XPS and PL studies on the ambience exposed Z2 (same as the scaffold surface used in pollutant degradation), show that the presence of both chemisorbed oxygen with additional -OH and ionized V_O^{++} on the surface of Z2 Ex-situ could have

provided both the necessary active species (superoxide anions and hydroxyls) for pollutant breakdown, resulting into improvement in the degradation rate for the Z2 scaffold than most of its heterostructures itself where recombination through tunnelling are expected to have occurred.

These conclusions are also supported by the PL data, as for all samples we observe a high contribution of defect states as recombination centers. These defect states may also be involved in the electron-hole recombination across the NiO contact layer due to increased rate of electron transfer across the space charge layer. The strong reduction in the overall photoluminescence intensity after NiO deposition, but with an almost equal contribution from deep level and surface defects (Table 4.9), can also be taken as clear argument for the above given hypothesis describing a dominating influence of electron-hole recombination vs. electron-hole separation.

In conclusion, our results indicate that there is a fine balance between the appropriate band bending, a good quality interface and the reduction of charge recombination. Such a balance was only attained for Z2 samples mainly as a consequence of surface cleaning treatment, with little influence from the NiO deposition conditions due to recombination across the NiO layer.

Conclusion

The influence of ZnO surface cleaning (heat treatment in O_2 atmosphere at 400 °C) and NiO (post)deposition temperature on heterostructure formation and final performance in the dye degradation was studied. The XPS study of the bare ZNR revealed that the Fermi level of the ZnO surface without surface cleaning was above the conduction band (CB), which shifted inside the bandgap after surface cleaning treatment with the depletion of excess electrons. This confirms that the doping of ZnO was changed but the XPS results alone cannot discriminate if it has taken place at the surface or in the bulk. By correlating XPS and PL with photodegradation activity we were able to conclude that the improved photocatalytic performance of Z2 samples compared to the Z1 counterparts is mostly the consequence of surface cleaning. Indeed, the modest performance of the heterostroctures compared to the scaffolds indicates that the charge separation after NiO deposition was not as effective as it would have been expected from the band bending values (BB in the range of $\simeq$0.9 to 1.4 eV) because of charge recombination inside the NiO layer (PL results show that DLE and NBE contributions were equally present no matter the deposition conditions). The highest photocatalytic efficiency among Z2 heterostructures is obtained for sample $Z2N_{PA}$ for which the developed NiO layer thickness allowed the mitigation of the tunnelling effect.

Therefore our study demonstrates that the correlation of a high band bending or PL emission quenching/increase with the improved photocatalytic efficiency is not straightforward and other factors must be considered when tuning the band bending such as the materials doping level, the space charge layer thickness, the co-catalyst thickness, etc, in order to achieve effective photocatalytic efficiency.

Given that, Z2 and its heterostructures (with NiO deposited under PA and HT conditions) were showing improvement in the performance, only those NiO deposition conditions were taken for further studied in the next two sections.

4.3. Influence of NiO deposition time

4.3.1. Experimental strategy

The functional properties of heterostructured metal oxide semiconductors widely depend upon the micro/nano structure, grain size and distribution, defect density, surface and interfacial properties, surface to volume ratio and density of active sites, which could be tuned by varying the deposition and post deposition conditions and also the film thickness [259–261]. Thickness of the films of both scaffold and contact material play a critical role in designing the interface of heterostructures; the former as 1D material will influence the depletion layer width along with the thickness of the second material involved [242].

There are some general reports regarding the effect of material thickness that leads to changes in structural growth and surface morphology, which in turn were found to influence the material's optical and electrical properties [259 261]. Furthermore, spontaneous charge transfer to the supported catalyst could be stimulated by tuning the supported film's thickness that could lead to remarkably different chemical and catalytic properties [242].

Though there are a hand full of studies about controlling the aspect ratio of ZnO nanorods [262 263] and the thickness of NiO layer [264–266] individually, as per our knowledge, there are very few studies [174 267] reporting about the thickness effect of NiO on ZNR. Moreover, the previous study was reported based on the sensor or electrical characteristics of the NiO/ZnO heterojunction, thus the NiO thickness effect on the photocatalytic properties of NiO/ZnO heterostructures was not reported so far. In this section, we have investigated the influence of NiO deposition time and thus thickness on the microstructural, optical and electrical properties of the NiO/ZnO heterostructures and correlated them with the performance in the pollutant degradation.

The NiO/ZnO heterostructures were prepared at three varying deposition times, at room temperature followed by post annealing and at high temperature conditions. Transmission Electron Microscopy was used to study the morphology and coverage of NiO over ZNR. And the optical and electronic characteristics were investigated by PL and XPS.

4.3.2. Sample description

The scaffold Z2 was used to deposit NiO (based on the conditions as described for the 6% oxygen partial pressure in Section 3.2), using different deposition time (20 s, 40 s and

60 s at room temperature followed by post annealing (done at 250 °C, for 1 h, in presence of 5 sccm oxygen, noted with "PA" in Table 4.11) and at high temperature (at 400 °C, noted with "HT" in Table 4.11) conditions. The details regarding surface cleaning, the NiO deposition temperature conditions and their respective sample codes are as shown in the Table 4.11.

Table 4.11: Sample code with preparation details, for the samples discussed in this section.

Sample Code	Preparation Details		
	NiO deposition time (s)	NiO deposition temperature conditions	Expected NiO thickness based on deposition rate (nm)
Z2	-	-	-
$Z2N_{PA}$ - 20s	20	PA	3 - 5
$Z2N_{PA}$ - 40s	40	PA	7 - 10
$Z2N_{PA}$ - 60s	60	PA	12 - 15
$Z2N_{HT}$ - 20s	20	HT	3 - 5
$Z2N_{HT}$ - 40s	40	HT	7 - 10
$Z2N_{HT}$ - 60s	60	HT	12 - 15

4.3.3. Transmission electron microscopy

The TEM images corresponding to $Z2N_{PA}$ and $Z2N_{HT}$ at varying deposition times are shown in Figure 4.17. At 20 s of deposition, PA resulted in a very thin layer of $\simeq$ 3 nm (Figure 4.17a) while that of HT condition showed the presence of crystallite patches (Figure 4.17b) covering the surface of ZNR. Though ZnO and NiO cannot be distinguished from the image, the FFT observations indicated the existence of the lattice spacings d=0.24 nm and d=0.25 (and 0.26) nm, that correspond to NiO (111) and ZnO (002) planes, respectively [7, 252, 268].

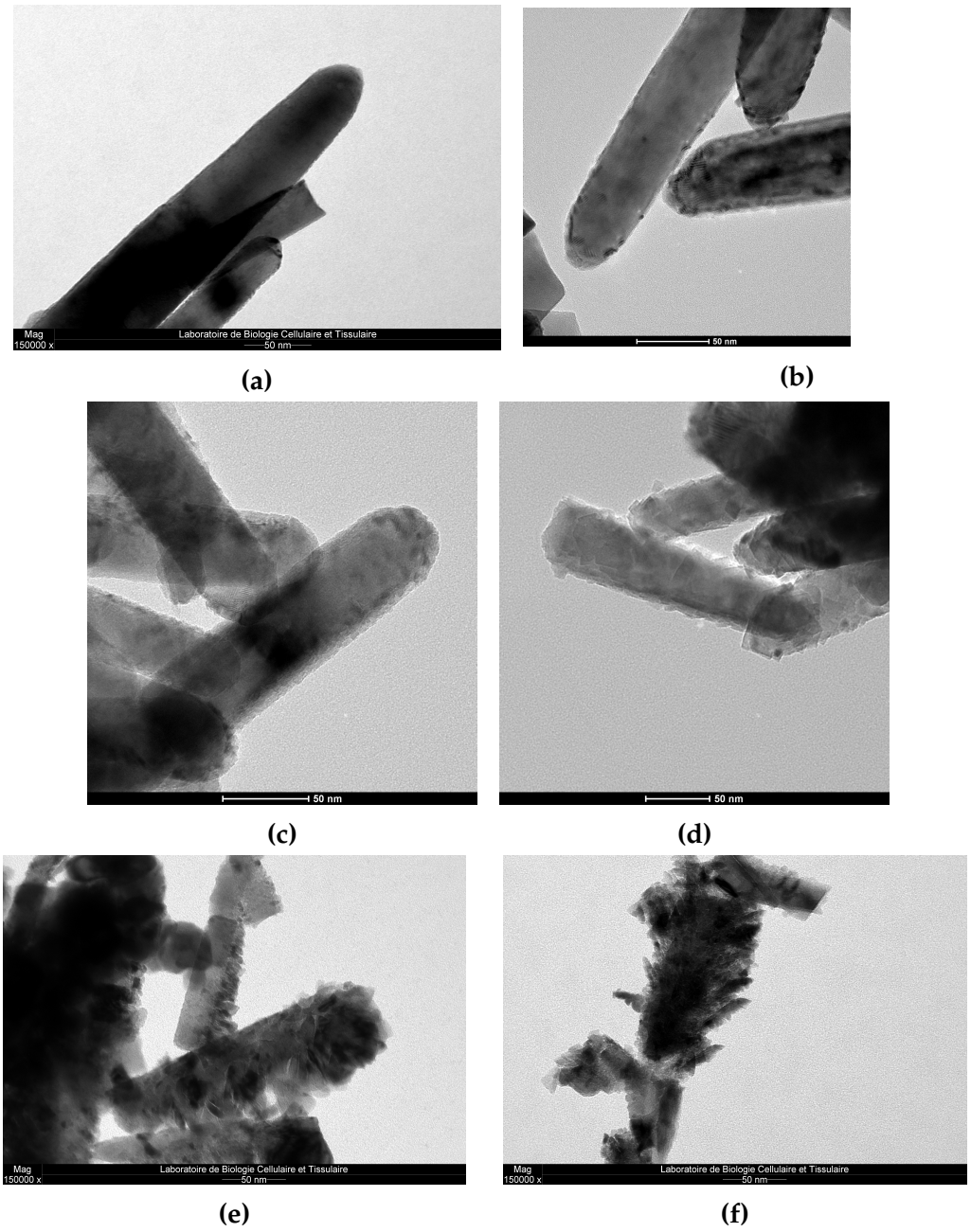

Figure 4.17: TEM image for $Z2N_{PA}$ and $Z2N_{HT}$ at (a and b) 20 s, (c and d) 40 s, (e and f) 60 s respectively. PA = Post Annealing; HT - High temperature.

Deposition at 40 s in PA condition showed a thicker layer of $\simeq$ 6-7 nm (Figure 4.17c) and HT condition showed the NiO coverage with cubic particles, of about 5-6 nm size (Figure 4.17d). The cubic particle formation at HT was also further confirmed by the FFT pattern that displayed a lattice spacing of d=0.24 nm, belonging to the NiO(111) plane [252]. At 60 s of NiO deposition, both PA and HT conditions displayed growth of bigger particles that were branching out from the ZNR surface. In addition, the tip of the nanorods for the 60 s deposition were overcrowded.

4.3.4. Photoluminescence

The PL spectra of $Z2N_{PA}$ and $Z2N_{HT}$ samples at 20, 40 and 60 s NiO deposition times are shown in Figure 4.18, in comparison with the Z2 scaffold. For all the heterostructures, the near band edge peak was identified in the range of 365 - 381 nm, while the deep level emission became weaker. This would mean that the deep level defects were diminished at both PA and HT deposition conditions, irrespective of NiO deposition time.

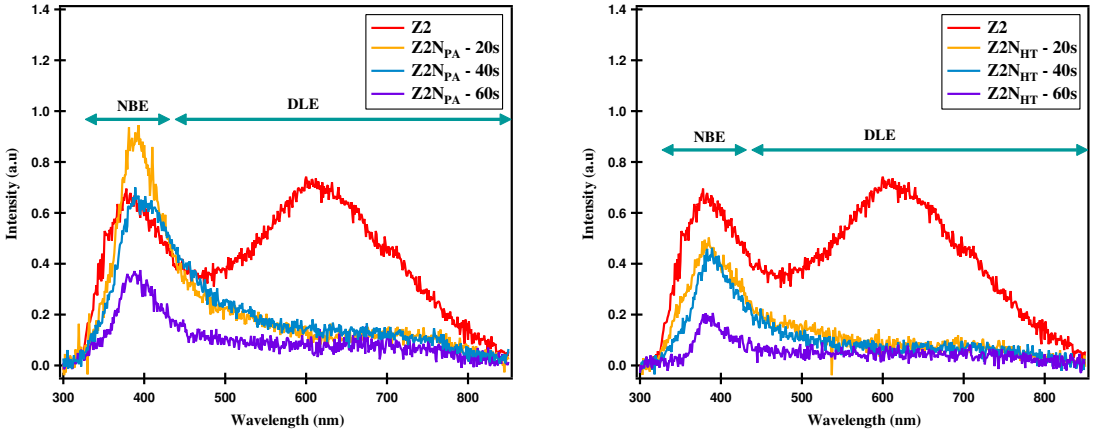

Figure 4.18: PL spectra of $Z2N_{PA}$ and $Z2N_{HT}$ heterostructures for different NiO deposition times.

The near band edge peak position of all heterostructures revealed a red shift, with respect to the position for the Z2 scaffold (Figure 4.18 and Table 4.12). This could be related to the quantum confinement effect that occurs due to change in particle size based on variation in deposition times. And the minimal amount of red shift in $Z2N_{HT}$-20s (compared to other heterostructures) might be due to smaller particle size, not even detectable in TEM [159]. The near band edge intensity in PA films were in the order of 20s>40s>60s, whereas the intensity of $Z2N_{PA}$-20s was higher than that of the Z2 scaffold, due to more surface free excitons [259, 261]. The same trend was observed for the HT series, with the observation that for a 60 s deposition time, the near band edge emission was considerably reduced.

In general, non-radiative recombination centers are ascribed to the presence of surface or interface states which are more probable with decreasing particle size. And the PL intensity is correlated to the particle size i.e, large crystallites (lower surface to volume ratio) will exhibit lower NBE emission [260, 261, 269]. Hence, it is vital to control the density of surface states, but without compromising the near band edge emission efficiency. Furthermore,

Table 4.12: Sample codes and corresponding details from PL spectrum. I_{NBE} and I_{DLE} values were taken by calculating the corresponding area below the deconvoluted peaks (using a data analysis software, IgorPro) in PL spectra. [PA - RT + Post Annealing; HT - High temperature].

Sample Code		NBE Peak maximum position (in nm) / Shift	FWHM of NBE (in nm)	I_{NBE}/I_{Total}	I_{DLE}/I_{Total}
Z2		375.00 / -	40.00	0.21	0.78
$Z2N_{PA}$	20 s	384.23 / Red	34.60	0.14	0.32
	40 s	381.00 / Red	48.17	0.08	0.04
	60 s	383.50 / Red	36.20	0.05	0.13
$Z2N_{HT}$	20 s	380.00 / Red	57.00	0.10	0.20
	40 s	384.10 / Red	40.80	0.08	0.11
	60 s	382.75 / Red	24.20	0.02	0.07

the increase in quantum confinement with a decrease in crystallite sizes are considered to lower the probability of excitonic emission by non-radiative surface recombination [269], thereby increasing the NBE efficiency. Therefore, the highest NBE intensity (Figure 4.18a) was observed for lower deposition times ($Z2N_{PA}$-20s), which showed a very thin layer formation (Figure 4.17a) and the lowest intensity (Figure 4.18b) was observed for the $Z2N_{HT}$-60s which displayed formation of larger particles that branched out from the surface of ZNR (Figures 4.17e and 4.17f).

Furtheron, the I_{NBE}/I_{Total} and I_{DLE}/I_{Total} ratios (Table 4.12) were calculated after deconvolution and values are gathered in Table 4.12. The decrease in surface states from lower to higher deposition time at both PA and HT conditions, is confirmed by the dropping I_{NBE}/I_{Total} values. Additionally, the FWHM broadening of NBE peak, observed in $Z2N_{PA}$-40s and $Z2N_{HT}$-20s as compared to Z2 scaffold indicates the presence of fluctuations in interface properties [255,256]. This effect was not seen in other heterostructures.

4.3.5. X-Ray photoelectron spectroscopy

The recorded XPS survey spectra of Z2 (Zn and O) and their corresponding heterostructures (Zn, Ni and O) revealed the presence of their characteristic peaks (not shown here), without carbon contamination, as a result of suraface cleaning. The evolution of the Zn2p, Ni2p and O1s core levels and valence band maximum emission line as a function of the NiO deposition time are shown in Figure 4.19. The BE of Zn2p, O1s and VBMx were all shifted towards lower values (Figure 4.19 and Table 4.13), due to NiO deposition and the

change in the chemical environment. No clear trend was observed regarding the change in intensities that could be related to the variation in NiO deposition time. However, the BE shifts were used to extract information about the role played by temperature and deposition time on the band bending.

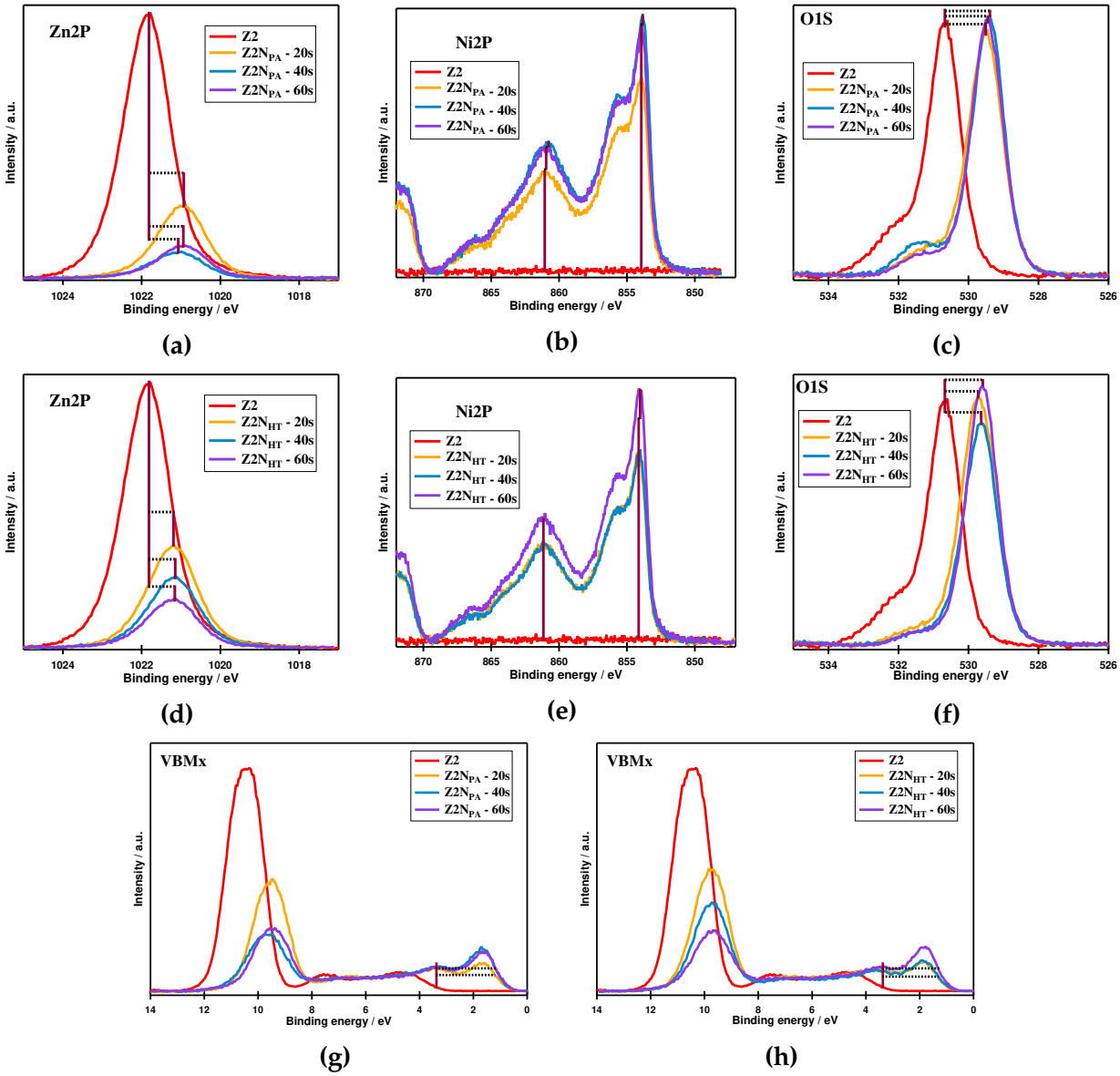

Figure 4.19: Zn2p (a), Ni2p (b), O1s (c) spectra and VBMx (g) shift for $Z2N_{PA}$ at 20, 40 and 60 s; Zn2p (a), Ni2p (b), O1s (c) spectra and VBMx (g) shift for $Z2N_{HT}$ at 20, 40 and 60 s. PA - Post Annealing; HT - High temperature.

The Zn2p emission line was noticed to be centered in the range of 1020.94 - 1021.04 eV for PA films and 1021.16 - 1021.19 eV for HT series (Figures 4.19a and 4.19d), exhibiting only a minimal shift. Similarly, a much lower shift in the Ni2p main, shoulder and Ni_{Sat} peaks were observed for the HT series (Figure 4.19e and Table 4.13).

Moreover, no changes were noticed in the line shape of any of the core level lines due to the temperature or deposition time, except for the O1s and Ni2p core level line of $Z2N_{PA}$-40s. For this sample, an increase in the O1s shoulder indicating more surface hydroxyls (Figure 4.19c) and a mild increase in the Ni2p shoulder line along with a shift in Ni_{Sat} (Figure 4.18b) was noticed, compared to its 20 s and 60 s counterparts. Though the reason behind this occurrence is not clear, it is obvious that the increase in Ni2p shoulder line is correlated with the increase in the O1s shoulder peak.

Table 4.13: Sample Names and their respective binding energies of Zn2p, O1s, Ni^{2+} peaks, band bending and FWHM values of Zn2p and O1s peak, for all heterostructured films; all are expressed in units of electron volts(eV); 0.50 eV was added to the V_{bb} values of all Z2 heterostructures, with respect to the shift of Zn2p line for Z2 scaffold in relation to the reference material, Z1 scaffold.

XPS Spectra (in eV)	Sample Code						
	Z2	$Z2N_{PA}$			$Z2N_{HT}$		
		20 s	40 s	60 s	20 s	40 s	60 s
Zn2p	1021.83	1020.95	1021.04	1020.94	1021.19	1021.16	1021.18
O1s	530.67	529.51	529.43	529.47	529.71	529.64	529.62
Ni^{2+}	-	853.96	853.82	853.91	854.08	854.03	854.02
Ni_{Sat}	-	861.14	861.00	861.12	861.22	861.16	861.19
E_F - VBMx	3.04	0.63	0.66	0.59	0.84	0.84	0.77
V_{bb}	0.50	1.38	1.29	1.39	1.14	1.17	1.15
$FWHM_{Zn2p}$	1.4	1.46	1.62	1.47	1.48	1.43	1.47
$FWHM_{O1s}$	1.08	1.12	1.09	1.06	1.14	1.12	1.06

The broadening of Ni^{2+} peak in $Z2N_{PA}$-20s could be attributed to the change in the nature of bonding due to the post processing step (post annealing) for an incompletely grown NiO[240,241]. Concurrently, the FWHM of O1s were observed to be gradually decreasing from lower to higher deposition times in both PA and HT conditions and this could be ascribed to the growth and bonding of oxygen with the involved metals (Zn and Ni) as a function of time and temperature[270].

As observed in Section 4.2.4, observations here also indicate that NiO deposition at high temperatures shows a larger E_F-VBMx difference (0.77 - 0.84 eV, Table 4.12) compared to post annealed deposition (0.59 - 0.66 eV, Table 4.12), which can be related to a better-

defined stoichiometry. Based on the binding energy shifts of Zn2p, V_{bb} were estimated (using equation 3.1 in Section 3.4) to be ranging from 1.14 eV to 1.39 eV (Table 4.12), with higher values for the $Z2N_{PA}$ samples.

4.3.6. Pollutant degradation

The C_t/C_0 vs. time was plotted and shown in Figure 4.20a, whereas the efficiencies after the final step are shown in Figure 4.20b.

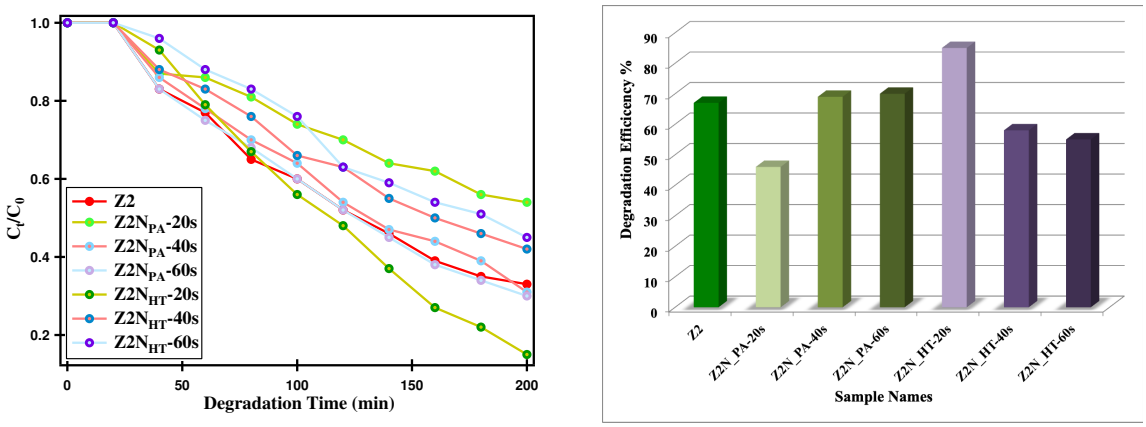

Figure 4.20: (a) C_t/C_0 vs. degradation time for $Z2N_{PA}$ and $Z2N_{HT}$ at varying NiO deposition times (20, 40 and 60 s) in comparison to the Z2 scaffold and (b) bar graph representing the degradation efficiencies for those samples. [PA - Post Annealing; HT - High temperature]

All the heterostructures performed either similar or worst than the Z2 scaffold. This could be attributed to the tunnelling through the thin space charge layer (as concluded previously in Section 4.2.5). When comparing the different NiO deposition conditions, except for the 20 s deposition time, the $Z2N_{PA}$ samples performed better than their $Z2N_{HT}$ counterparts, due to a better charge separation as indicated by the higher band bending values.

Given that all the PA films have attained a minimum band bending of $\simeq$ 0.80 eV (from XPS) suggest they should have similar charge separation capabilities, but the performance was considerably lower for the 20 s as compared to the 40/60 s deposition times. This suggests that the deposition time has influenced the growth of NiO and more specifically the nature of Ni-O bonding as for the 20 s sample (broadening of the Ni2p main peak (Ni^{2+}) was observed).

The attained band bending were smaller for all HT samples with respect to PA

films and hence, they would have been expected to have a lower performance. However, $Z2N_{HT}$-20s gave the highest performance and this could be ascribed to several factors: a better defined stoichiometry, faster charge transfer due to the lower thickness, and increased NBE emission due to the quantum confinement effect. Using longer deposition times will result thicker NiO layers composed of higher crystallites and thus the loss of the quantum confinement effect and increase in carrier diffusion path length, which cannot be compensated by the improved interface (PL analysis shows that sample $Z2N_{HT}$-60s has the lowest FWHM value for NBE peak). These revelations altogether clearly demonstrates the ideology of finding the essential factors that will influence the catalytic activities and their interdependance[242].

Conclusion

The interfacial and photocatalytic activity of the NiO/ZnO heterostructures were tuned by varying the NiO deposition time for two (post)deposition temperature conditions. Observations under TEM showed that the NiO layer thickness/particle size increases with increase in deposition time. For low deposition times a very thin layer was formed, while for longer deposition times (40 s), cubic particles were decorating the ZNR surface. At 60 s deposition time, in both PA and HT films, the NiO particles were branching out of the ZNR surface, with overcrowding at the nanorod tip. At lower deposition times, the near band edge emission was dominating, owing to the higher surface to volume ratio, thereby the increase in quantum confinement effect that amounts to the increase in NBE efficiency. The non-radiative surface recombination increased with longer deposition times, due to increase in particle size and layer thickness. XPS results revealed that a higher band bending could be attained for the post annealed films as compared to high temperature films but the latter exhibited a better defined stoichiometry. However, most of the heterostructures were performing either similar or below the Z2 scaffold, due to the tunnelling effect. The $Z2N_{HT}$-20s achieved highest photocatalytic efficiency by benefiting from several factors: increased photogeneration of holes and reduced tunnelling effect with lower NiO thickness, effective charge separation by faster charge transfer, improved stoichiometry and decreased surface charge recombination due to quantum confinement. Thus a 20s NiO deposition time, at high temperature was further used during the optimization.

4.4. Influence of oxygen partial pressure

4.4.1. Experimental strategy

The impact of sputtering parameters on the Nickel Oxide (NiO) film properties has been studied widely [6,264,271,272] and the influence of oxygen partial pressure (P_{O_2}) is one among the parameters that had been explored [273,274]. The oxygen partial pressure during the DC or RF sputtering of NiO is known to influence the structural, electrical and optical properties of the films [275]. Especially, the surface morphology of NiO was shown to be highly depending on the oxygen partial pressure [274]. Most of the previous reports regarding the effect of oxygen ratio were concerning (doped) NiO [276], for sensor or electrical applications. To our knowledge, the effect of P_{O_2} on the heterostructure formation was not studied for photocatalytic applications.

In this section, we are comparing two oxygen partial pressures (P_{O_2}), 6 and 20%, for the deposition of NiO, in terms of interface properties (XPS), charge recombination effects (XPS and PL) and pollutant degradation performance.

4.4.2. Sample description

Following the previous optimisation, the NiO was deposited at high temperature for 20 seconds for lower P_{O_2} (6%) and for 2 minute at higher P_{O_2} (20%), in order to attain the same layer thickness. The Z2 scaffold (cleaned surface) was used as main photocatalytic material. Correspondingly, the heterostrcutures were denoted as $Z2N_{HT}$-6% and $Z2N_{HT}$-20%

4.4.3. Transmission electron microscopy

Microstructural properties of $Z2N_{HT}$-20% sample was investigated through TEM and shown in Figure 4.21, in comparison with $Z2N_{HT}$-6%.

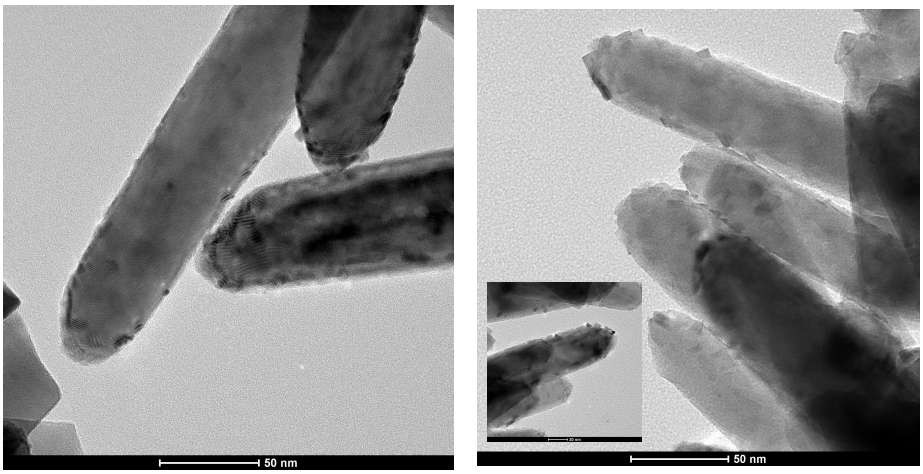

(a) (b)

Figure 4.21: TEM image of (a) $Z2N_{HT}$-6%, (b) $Z2N_{HT}$-20% [zoomed view in the inset]. HT - High temperature.

The TEM image of $Z2N_{HT}$-20% (Figure 4.21b) has shown the formation of cubic particles (5 - 6 nm) that were decorating all over the ZNR surface, in contrary to what was observed for $Z2N_{HT}$-6% (Figure 4.21a, where a thin layer of 3 - 3.5 nm conformal coating was observed, with no specific morphology.

4.4.4. Photoluminescence

The PL spectra of $Z2N_{HT}$-20% is compared with that of $Z2N_{HT}$-6% and Z2 scaffold (Figure 4.22). Similar to previous results, both the NBE and DLE peaks of $Z2N_{HT}$-6% and $Z2N_{HT}$-20% were mitigated after NiO deposition, indicating that charge recombination was reduced. However, as a consequence of larger crystallite formation, $Z2N_{HT}$-20% was exhibiting a red shift and reduction in the NBE efficiency, deep level defects and $FWHM_{NBE}$ (Table 4.14), as opposed to the Z2 scaffold and $Z2N_{HT}$-6% films. This is translated into a lower quantum confinement effect, increase in non-radiative surface recombination centers, with however reduced interface fluctuations, meaning increase in the probability of higher recombination losses.

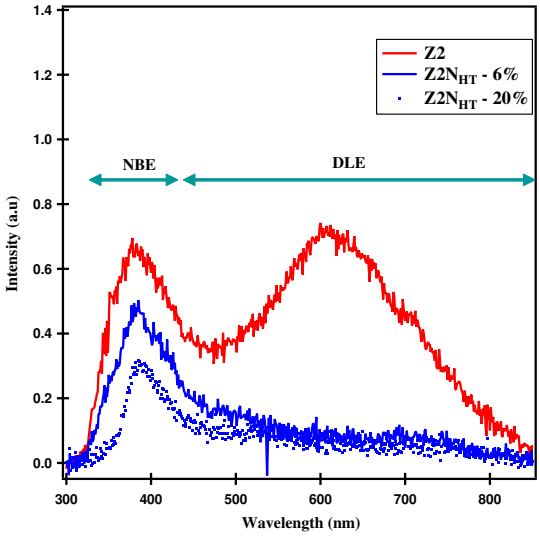

(a)

Figure 4.22: PL spectra of Z2, Z2N$_{HT}$-6% and Z2N$_{HT}$-20%.

Table 4.14: Sample codes and corresponding details from PL spectrum. I_{NBE} and I_{DLE} values were taken by calculating the corresponding area below the deconvoluted peaks (using a data analysis software, IgorPro) in PL spectra. [HT - High temperature].

Sample Code	NBE Peak maximum position (in nm) / Shift	FWHM of NBE (in nm)	I_{NBE}/I_{Total}	I_{DLE}/I_{Total}
Z2	367 / -	40	0.21	0.78
Z2N$_{HT}$-6%	380 / Red	52	0.10	0.20
Z2N$_{HT}$-20%	385 / Red	24	0.03	0.13

The reduction in interface fluctuations (than Z2N$_{HT}$-6%) could be correlated to the fact that oxygen vacancy filling or compensation probability is higher under oxygen rich conditions (Z2N$_{HT}$-20%), thereby avoiding the interface roughness [255, 256].

4.4.5. X-Ray photoelectron spectroscopy

The emission lines of Zn2p, Ni2p, O1s and valence band for all the samples (Z2 scaffold, Z2N$_{HT}$-6% and Z2N$_{HT}$-20%) are shown in Figure 4.23. The intensities of all core level lines and VBMx lines for Z2N$_{HT}$-20% were reduced with respect to Z2 scaffold due to

NiO deposition and shifted towards lower binding energy (Figure 4.23 and Table 4.15).

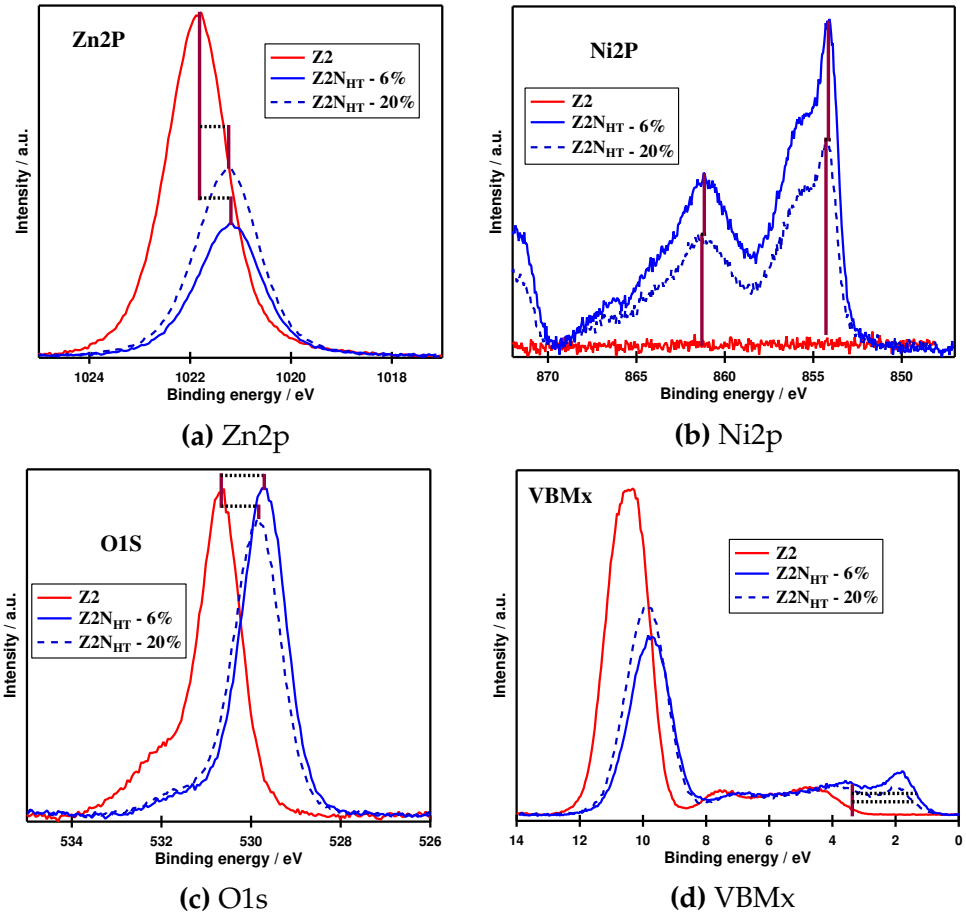

(a) Zn2p **(b)** Ni2p

(c) O1s **(d)** VBMx

Figure 4.23: Zn2p (a), Ni2p (b), O1s (c) spectra and VBMx (d) shift for Z2 scaffold in comparison with Z2N$_{HT}$-6% and Z2N$_{HT}$-20%. HT - High temperature.

All the emission lines of Z2N$_{HT}$-20% were found to be shifted to higher binding energy compared to those of Z2N$_{HT}$-6% (Figure 4.23 and Table 4.15), as a result of increased oxidative process under oxygen rich conditions. Moreover, the shift of Ni$_{Sat}$ to higher binding energy at higher P_{O_2} suggests the formation of Ni^{3+} [274].

The O/Ni ratio were calculated (using equation 4.1 in Section 4.1.3, after Shirley background and peak deconvolution) as 0.80 and 0.84 for Z2N$_{HT}$-6% and Z2N$_{HT}$-20% films respectively, confirming the increase in oxygen incorporation, as expected.

Table 4.15: Sample Names and their respective binding energy and FWHM values of Zn2p, O1s, Ni^{2+} and Ni_{Sat} peaks for all heterostructured films; all are expressed in units of electron volts(eV); 0.50 eV was added to the V_{bb} values of all Z2 heterostructures, with respect to the shift of Zn2p line for Z2 scaffold in relation to the reference material, Z1 scaffold.

XPS Spectra	Sample Code		
	Z2	$Z2N_{HT}$-6%	$Z2_{HT}$-20%
Zn2p (eV)	1021.83	1021.19	1021.24
O1s (eV)	530.67	529.71	529.85
Ni^{2+} (eV)	-	853.08	854.27
Ni_{Sat} (eV)	-	861.22	861.34
E_F - VBMx (eV)	3.04	0.84	0.87
Band bending - V_{bb} (eV)	0.50	1.14	1.09
$FWHM_{Zn2p}$	1.4	1.48	1.48
$FWHM_{O1s}$	1.08	1.14	1.24
$FWHM_{Ni^{2+}}$	-	1.17	1.17

The line shape of Zn2p the core level lines were not exhibiting any changes as a result of increase in P_{O_2}, except for broadening effects in the O1s core level lines (Table 4.15), which might be attributed to the change in stoichiometry [270]. The band bending attained by the $Z2N_{HT}$-20% interface (1.09 eV) was lower than the one attained for $Z2N_{HT}$-6% (1.14 eV, Table 4.15). This leads to the understanding that the charge separation ability in $Z2N_{HT}$-20% has been compromised (in relation to $Z2N_{HT}$-6%).

4.4.6. Pollutant degradation

The degradation efficiency was calculated according to equation 4.3 in Section 4.2.5 and the C_t/C_0 vs. degradation time curves for Z2, $Z2N_{HT}$-20% and $Z2N_{HT}$-6% films are plotted in Figure 4.24.

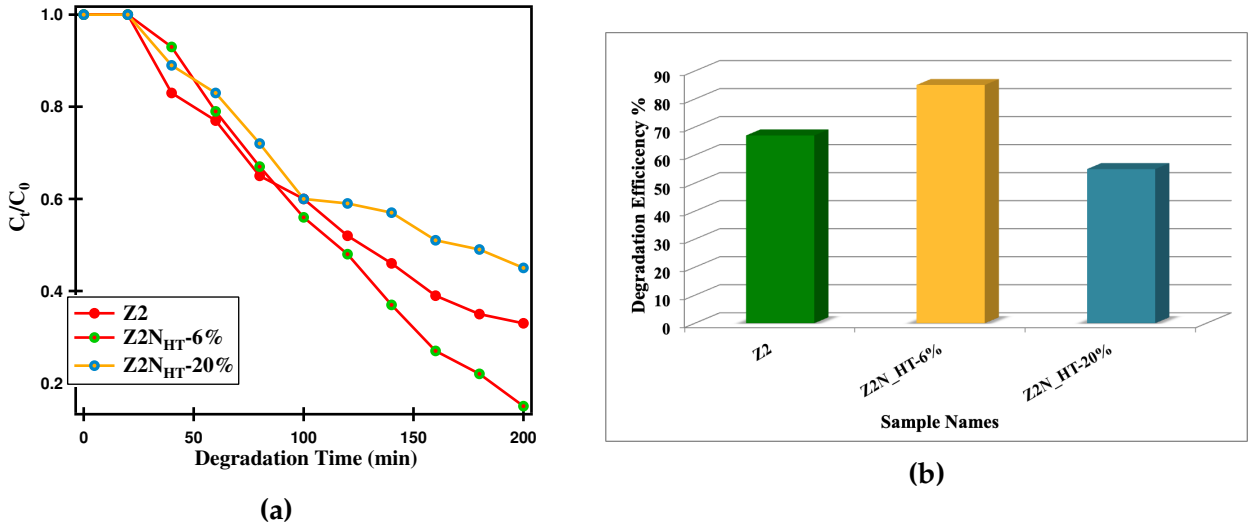

Figure 4.24: (a) C_t/C_0 vs. degradation time and (b) degradation efficiency plots for Z2, Z2N$_{HT}$-20% and Z2N$_{HT}$-6%. [HT - High temperature]

The pollutant degradation rate of Z2N$_{HT}$-20% (55%) was lower than that of Z2 scaffold (67%) and Z2N$_{HT}$-6% (85%). This could be attributed to several factors:

i) though charge separation is enabled by the attained band bending, recombination through tunnelling across the NiO layer (from PL) might have occurred, as noticed in several other heterostructures, including Z2N$_{HT}$-6% (as shown in Section 4.3.6)

ii) irrespective of the formation of active NiO (111) cubic particles, the larger crystallites of 5-6 nm size has led to a decrease in the NBE efficiency due to increased non-radiative surface recombination (from TEM, related to PL)

This explains the reasons behind lack of enhancement in the photocatalytic activity of Z2N$_{HT}$-20%, with an increase in oxygen partial pressure, during the NiO deposition.

Conclusion

NiO was deposited at high temperature, on the cleaned Z2 surface by using two different oxygen partial pressures (6% and 20%). The NiO crytalline nature and size are confirmed by TEM, where higher P_{O_2} has led to higher crystallite sizes. The PL results revealed that deep level defects were reduced but surface recombination was increased, when higher P_{O_2} was used during NiO deposition, owing to the larger crystallite size of the second material (NiO). In addition, the elemental and chemical information from XPS showed that for higher oxygen partial pressure a lower band bending is attained. These

overall optical and electrical aspects were correlated to the lower photocatalytic activity.

4.5. Conclusion

In this chapter, we aimed to optimize the NiO deposition on the ZNR scaffold and to do that we have investigated several parameters, such as the scaffold cleaning treatment, the NiO deposition temperature, the oxygen partial pressure during deposition and the deposition time. For each optimization step, the role of surface and interface properties on the NiO/ZnO heterostructure formation and its influence on pollutant photodegradation was investigated through XPS and PL analysis.

We have proven that heat treating the ZnO nanorods at high temperature (400° C), in presence of oxygen, under high vacuum (0.5 Pa), effectively removes the adsorbates (C, -OH) and favours oxygen desorption, leading finally to a slightly depleted surface and a less n - doped scaffold (Fermi level lowering), as confirmed by XPS and Mott - Schottky measurements. The effect of surface cleaning is readily seen in the drop of the near band edge and deep level emissions (PL) which prove the mitigation of the surface recombination and oxygen vacancy passivation, thus leading to a higher photodegradation efficiency.

Using the cleaned scaffold has improved the interface quality as proven by the higher band bending (XPS analysis) values, the reduced surface recombination and the lower charge transfer resistance obtained for the heterostructures with NiO. Consequently higher photocurrent and photo-degradation efficiency were obtained for these heterostructures. From a first view of XPS results (for 40 s deposition time), post-annealing (PA) the NiO layer has a similar effect with the surface cleaning as both heterostructures with pristine ($Z1N_{PA}$) and cleaned ($Z2N_{PA}$) ZNR scaffold show similar band bending. However, the PL analysis highlights that even if the surface recombination contribution is same in both heterostructures, it is the second one which has less interface fluctuations, thereby allowing the transfer of more charge carriers to ZnO and thus boost the photodegradation activity. When both the bend bending and the near band edge emission diminish a lower photodegradation efficiency is obtained, even if the thinner NiO layer should promote charge carrier photogeneration, as it is the case of the heterostructures with cleaned scaffold and high temperature deposited NiO ($Z2N_{HT}$). The modest boost in the photodegradation efficiency might be due to the non-radiative charge recombination by tunnelling through the thin space charge layer which is related to the high ZnO doping.

With the NiO thickness variation, it was identified that, for deposition times exceeding 20s, the particle size and NiO layer thickness increased leading to the loss of the

quantum confinement effect and increase in the carrier diffusion path, which instead leads to promotion of charge recombination. Furthermore, a thicker NiO layer would block the photogeneration of charge carriers in ZnO.

Even if a lower band bending and near band edge emission (as compared to post annealed sample) is attained when depositing NiO (20 s deposition time) on the cleaned scaffold (0.5 Pa, 400° C) at high temperature (400° C), 6% oxygen partial pressure, these optimized conditions allowed attaining the highest dye degradation efficiency (85%) ever reported for ZnO (1D nanostructured)/NiO heterostructures. In fact, the thinner NiO layer (where NiO particles uniformly decorated the ZnO nanorods) with improved stoichiometry allows the effective photogeneration of charge carriers and charge separation through the quantum confinement effects and the mitigation of the tunnelling effect, while the optimum band bending allows effect charge separation without compromising the charge carrier kinetics.

Chapter 5

In-situ water adsorption studies

5.1. Experimental strategy

Metal oxides, have a high tendency to interact with the exposed environment, which makes them sensitive and thus ideal candidates for catalytic and energy related applications, where surface reactions play a major role[149,179,180]. Therefore, in order to improve the material design for applications such as pollutant degradation and water splitting, one has to understand the influence of surface properties on the interface formation with a second material[277].

Given the complexities (study of interactions at the atomic or molecular level) involved, among several available experimental techniques (listed and discussed in Section 1.8.3), X-ray photoelectron spectroscopy is often used for such investigations. The ability to discriminate betweeen dissociated and molecular water[181], along with the possibility to study the influence of adsorbed water on the heterostructure properties, makes XPS a powerful tool. These studies are useful for optimizing single or heterostructure based materials that participate in processes occurring in water media.

A plethora of earlier reports (both experimental and theoretical investigations) about water interaction with metal oxides were concerning single crystalline materials, however the samples (or surfaces) that are used in technological applications are most often polycrystalline and defect rich. The surfaces rich in adsorbates are ambient sensitive and hence, need to be examined under ultra high vacuum (UHV) conditions. As mentioned earlier in Section 1.8.3, the interaction of water with metal oxides is more complex than with metals, becasue in metal oxides, both the metal cations and oxygen anions can bind

with water, where the latter is usually known to facilitate water dissociation[183]. Among metal oxides or non metallic surfaces, the interaction of water and the corresponding surface reactions were investigated on TiO_2, ZnO, MgO, NiO and Silicon surfaces[181,184].

The basic revelation from all the water interaction reports is that, upon surface water (vapour) exposure, molecules can either be adsorbed or dissociated depending on the strength of water-water or water-surface interactions and the availability of dangling -OH groups.

The ability of zinc oxide nanorod to grow Zn and O atoms alternatively along the c-axis (stacking opposite charged planes and producing a dipole moment in perpendicular to the (0001) plane) makes it a polar surface[154,194,195]. This, along with the high probability (on preparation by chemical route) of having vacancies or impurities influences the ZnO interaction with water. In general, it is agreed that vacancies play a major role in the process of water dissociation[188,197,198]. Heat treatment in the presence of oxygen, of an as prepared ZNR surface, is capable of removing or passivating the impurities/defects forming layer(s) of oxygen adatoms (oxygen atoms adsorbed to the surface on heat treatment in presence of oxygen gas flow). This chemisorbed oxygen is considered to be very reactive in promoting water dissociation[184,199], but is not widely studied. Hu et al[188] demonstrated theoretically (in parallel to experimental studies of Huang et al.[198] and Sun et al.[197]), that in the presence of oxygen vacancies (V_O) water dissociation is promoted.

Being a 1D nanostructure, zinc oxide nanorods (ZNR) are capable of having good charge separation effects[93,200], however, in order to reduce surface charge recombination[55,201] and to enhance the charge transfer characteristics[11,93,202–206], the ZNR scaffold was coated with a thin layer of NiO, targeting photocatalysis and water splitting applications.

In case of Nickel Oxide (NiO), water interaction with (100) and (111) surfaces are widely studied in earlier reviews[181,184]. The major revelations were that, water does not dissociate on the (100) surface, especially under UHV conditions and that NiO (111) is capable of readily dissociating water. It was expected that -OH terminated NiO(100) obtained through growth, could facilitate water dissociation, however, that is not the case[181,184].

Herein, we have studied the interaction of the ZNR scaffold (pristine and surface cleaned) films and their heterostructures with NiO, with water vapour under ultra high vacuum conditions, by using XPS, along with room temperature (RT) photo luminescence (PL). The influence of the presence/absence of adsorbates on the bare ZnO, ZnO/NiO heterostructure surface and interface properties, before and after the water exposure was investigated by step-by-step in-situ XPS. In addition, the planar NiO/ZnO (heterojunction) and NiO (bare) films, were also studied for comparison purposes. In addition, photolu-

minescence investigations were carried out on ZnO scaffold and their heterostructures to elucidate the influence of defect levels (especially deep defects) on band bending.

The interaction of water with metal oxide (semiconductor) polar surfaces and in particular with polycrystalline nano structured ZnO and its heterostructures with NiO are first time investigated here. Such a study finds a direct application in the design and optimization of materials for processes occurring in aqueous media such as photocatalysis or water splitting.

5.2. Sample description

For comparison purposes, ZnO films prepared by both chemical (as explained in Section 3.2, scaffold surfaces made of Zinc Oxide nanorods, Z1 and Z2) and physical (ZnO planar film) methods were used as scaffolds. In addition, NiO deposition was done on bare FTO. The deposition parameters for bare NiO and ZnO by physical method are detailed below:

ZnO planar film growth - a 200 nm film was deposited on 1×1 cm^2 Indium doped Tin Oxide (ITO) substrates by Radio Frequency (RF) sputtering. The deposition rate was 2.8 nm/min for a sample to target distance (D^{st}) of 10 cm in the following conditions: P^{Tot} - 0.5 Pa, Argon/Oxygen mix flow - 3 sccm, Argon flow - 7 sccm, room temperature (RT), deposition time - 72 min, Power (P) = 25 W. These planar ZnO films were denoted as **Z3**.

NiO film growth - a 150 nm film was deposited on FTO substrate by Direct Current (DC) sputtering. The deposition rate was 15 nm/min for D_{st} of 8 cm using the following parameters: P^{Tot} - 0.5 Pa, Oxygen partial pressure (O_2%) - 6%, RT, deposition time - 10 min, P = 40 W. This bare NiO film was denoted as **N**.

Heterostructure preparation

NiO was deposited at room temperature, on all the ZnO surfaces (Z1, Z2, Z3) using the parameters mentioned in NiO film growth (for 6% oxygen partial pressure in Section 3.4), but with different deposition times, as detailed in Table 5.1.

Table 5.1: Sample Code and preparation details, for the scaffolds (Z1, Z2, N) and heterostructures with Z1, Z2 and Z3 scaffolds.

Sample Code	Preparation Details		
	Surface Cleaning (at 0.5 Pa)	NiO deposition time (in s)	Expected NiO thickness (in nm)
Z1 (nanorods, without surface cleaning)	No	-	-
Z2 (nanorods, surface cleaned)	Yes	-	-
N (planar)	No	-	-
Z1N1	No	40	7 - 10
Z2N1	Yes	40	7 - 10
Z2N2	Yes	20	3 - 5
Z3N1 (planar)	No	16	4
Z3N2 (planar)	No	8	2

Water exposure Study

The water exposure study was performed in the UHV chamber which is equipped with a water flow system, in the Atomic Layer Deposition (ALD) set-up of DAISY-MAT (detailed in Section 2.2). During the process of water exposure, water vapour at 40 °C was introduced for 0.5 s for 15 cycles, with a waiting time of 60 s in between each cycle.

The step-by-step XPS analysis sequence was as follows:

1. XPS measurement of the scaffold surface before water exposure
2. XPS measurement after the NiO deposition (step followed only for heterostructured films)
3. XPS measurement after the water (vapour) exposure

5.3. Microstructural properties of the films

The detailed microstructural characterization of the samples can be found in Section 4.1, 4.2 and 4.3. Briefly, Z1 and Z2 samples are formed of 250 nm long and 60 nm wide nanorods with a medium packing density (Figure 5.1a). In case of the Z3 surface and NiO film, rough layers of 200 nm thickness were obtained (Figures 5.1b and 5.1c).

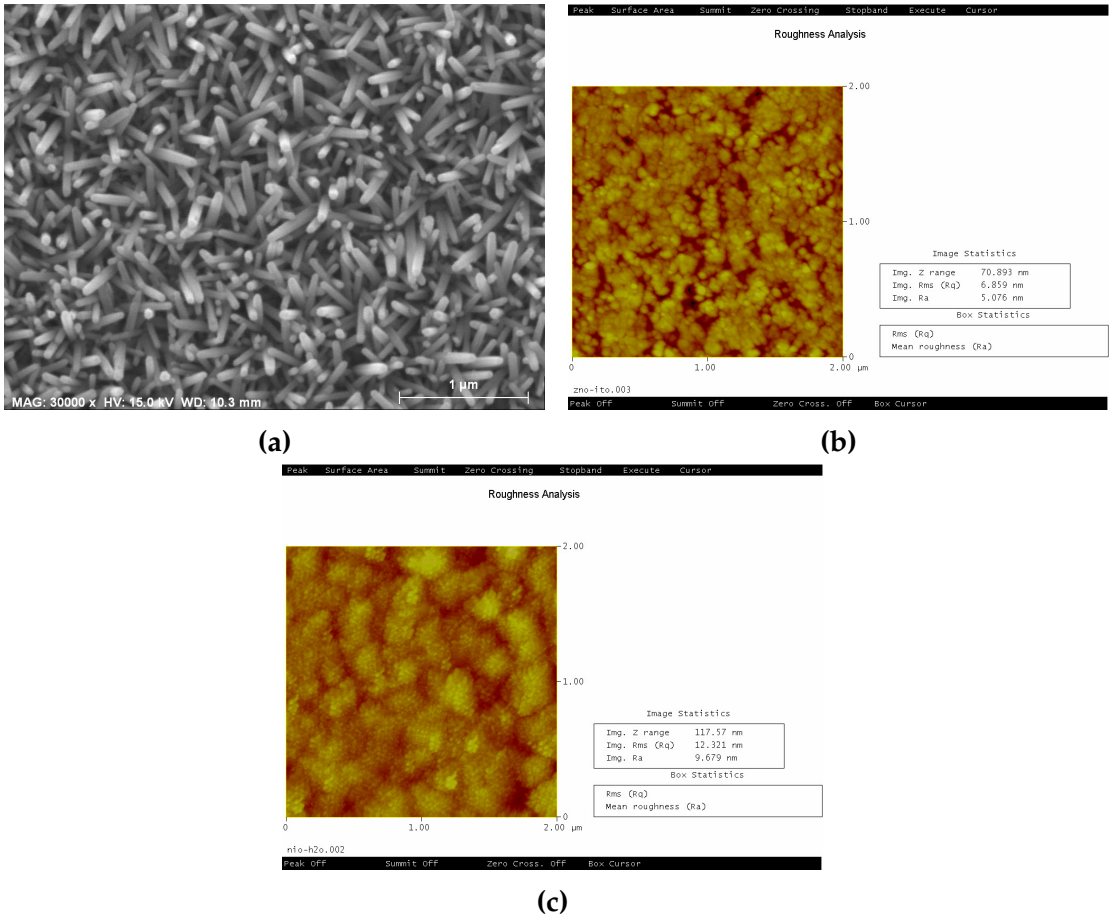

Figure 5.1: SEM image of ZNR (a), AFM images of N and Z3 (b and c) respectively.

5.4. X-Ray photoelectron spectroscopy

The XPS survey spectra of all surfaces were recorded and showed only the presence of characteristic emission lines (Zn, Ni and O) corresponding to ZnO and NiO. The spectra of pristine (Z1) and surface cleaned (Z2) ZnO showed clearly developed Zn2p and O1s lines and a valence band corresponding to ZnO (Figures 5.2a to 5.2f) [177], and in addition Z1 was identified with the presence of C1s peak, due to the film's ambieance exposure. In Section 4.1.3, we have shown that if the surface was cleaned (Z2), the Zn2p and O1s peak intensities increased and the C1s peak disappeared, evidencing the impurities or adsorbates removal [214]. Also with cleaning, a change in the doping of the ZnO layer occurred, as the Fermi level (E_F) situated above the conduction band (CB) minimum for Z1 [190,278] shifted inside the bandgap. This correspond to the shift of the Zn2p peak, upto 0.48 eV towards lower binding energy (BE) (Table 5.2) and a reduction in the Fermi level to valence band maximum (VBMx) distance (E_F - VBMx), from 3.47 eV for Z1 to 3.04 eV for Z2. In the case of planar NiO film, the Ni2p core level (Figure 5.2g) was observed to have three contributions: a main peak at 853.85 eV corresponding to Ni^{2+} in NiO, a shoulder peak (Ni^{Sh} at 855.7 eV and a satellite peak (Ni^{sat}) at 861 eV, where the shoulder peak indicates the presence of $Ni(OH)_2$ or NiOOH species [29,279]. The position of E_F was found to be at 0.52 eV, which is normal for a p-type material.

As a general rule, the BE of Zn2p, O1s, Ni2p and VBMx in all scaffold material (Z1, Z2 and N) shifted towards higher values after water vapour exposure (Table 5.2 and Figure 5.2) with consecutive diminution of their intensity. In particular, the shift of O1s and VBMx lines towards higher BE and the mild reduction in the O1s peak intensity (Table 5.2, the Figures 5.2b, 5.2c, 5.2e, 5.2f, 5.2h and 5.2i), are a proof of surface interaction with the water molecules [190]. Surprisingly and contrastingly, the Zn2p peak (Figure 5.2a) shows both a slight increase in intensity and a shift towards lower BE.

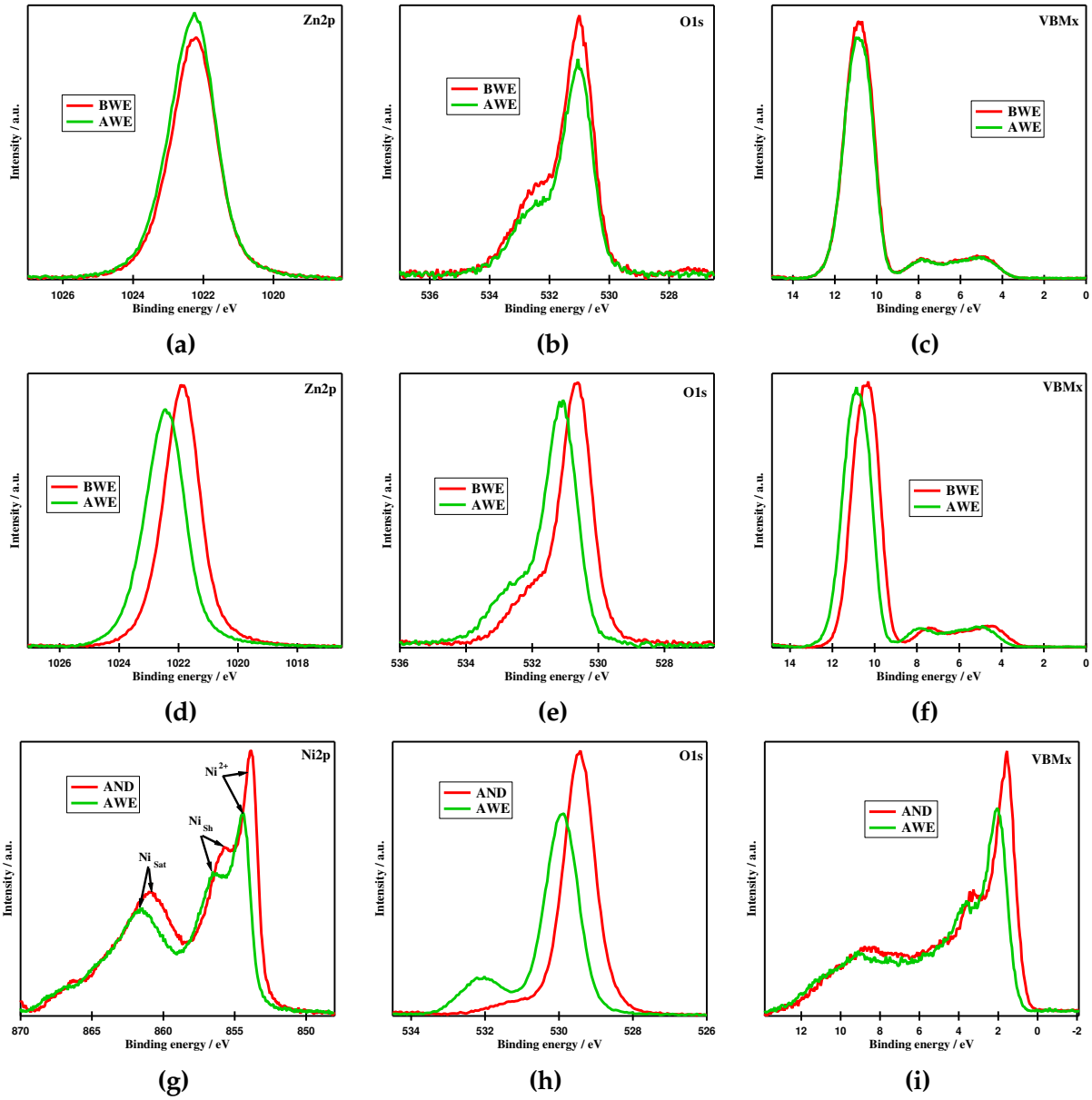

Figure 5.2: Individual spectra of Zn2p, O1s and VBMx, for Z1 (a,b,c), Z2 (d,e,f) and Ni2p, O1s and VBMx for sample N (g,h,i), before (BWE) and after water exposure (AWE), after NiO deposition (AND).

Table 5.2: Binding energy of the Zn2p, Ni^{2+}, Ni^{Sh}, Ni^{sat}, O_L lines and E_F - VBMx peaks before and after water exposure for all the scaffold surfaces and their heterostructures. BWE, AWE and AND stand for before, after water exposure and after NiO deposition.

Sample Code	Steps	Zn2p (eV)	Ni_{2+} (eV)	Ni_{3+} (eV)	Ni_{Sat} (eV)	O1s (eV)	E_F - VBMx (eV)
Without surface cleaning (Z1)	BWE	1022.33	-	-	-	531	3.47
	AWE	1022.25	-	-	-	531.00	3.50
Surface cleaned (Z2)	BWE	1021.85	-	-	-	530.64	3.04
	AWE	1022.41	-	-	-	531.08	3.48
Bare NiO on FTO (N)	BWE	-	853.85	855.70	861.00	529.45	0.52
	AWE	-	854.43	856.33	861.68	529.93	0.92
Z1N1	BWE	1022.20	-	-	-	531.00	3.45
	AND	1021.19	854.06	855.75	861.24	529.60	0.67
	AWE	1021.93	854.72	856.51	861.87	530.26	1.17
Z2N1	BWE	1021.73	-	-	-	530.53	2.95
	AND	1021.00	853.90	855.54	861.04	529.45	0.53
	AWE	1022.00	854.54	856.27	861.82	530.03	1.00
Z2N2	BWE	1021.70	-	-	-	530.43	2.90
	AND	1021.03	854.00	855.61	861.10	529.50	0.51
	AWE	1021.88	854.56	856.32	861.80	530.20	0.95
Z3N3	BWE	1021.62	-	-	-	530.36	2.72
	AND	1020.71	853.94	855.61	861.09	529.45	0.54
	AWE	1021.57	854.45	856.26	861.75	530.00	1.03
Z3N4	BWE	1021.61	-	-	-	530.30	2.70
	AND	1020.91	854.03	855.66	861.15	529.53	0.66
	AWE	1021.56	854.45	856.25	861.66	530.00	0.95

The deconvoluted O1s spectra (before water exposure) of the Z1 sample (Figure 5.3a) shows three contributions: the lattice oxygen (O_L) at 531 eV, bonded hydroxyls (O_{OH}) at 532.1 eV and physisorbed water (O_{H_2O}) at $\simeq$ 533 eV[190,278]. After the water exposure, the O_{OH} (531.6 eV) and O_{H_2O} (532.5 eV) lines were shifted towards lower BE (Figure 5.3b), with a dominant contribution from O_{H_2O}.

As opposed to the Z1 scaffold, only two contributions, O_L at 530.64 eV and O_{OH} at 531.9 eV were identified in the O1s peak of the cleaned ZnO surface (Z2) (Figure 5.3c). Nevertheless, after water exposure (Figure 5.3d), the third contribution, O_{H_2O} ($\simeq$ 533 eV) was also detected, while the former two were shifted to higher BE (Table 5.3).

For the NiO planar film, the O_L (529.45 eV) and O_{OH} (531.03 eV) contributions were identified on the pristine surface (i.e, before water exposure step). Whereas after water exposure, the O_{OH} was completely suppressed and O_{H_2O} peak appeared at 532 eV(Figures 5.3e and 5.3f).

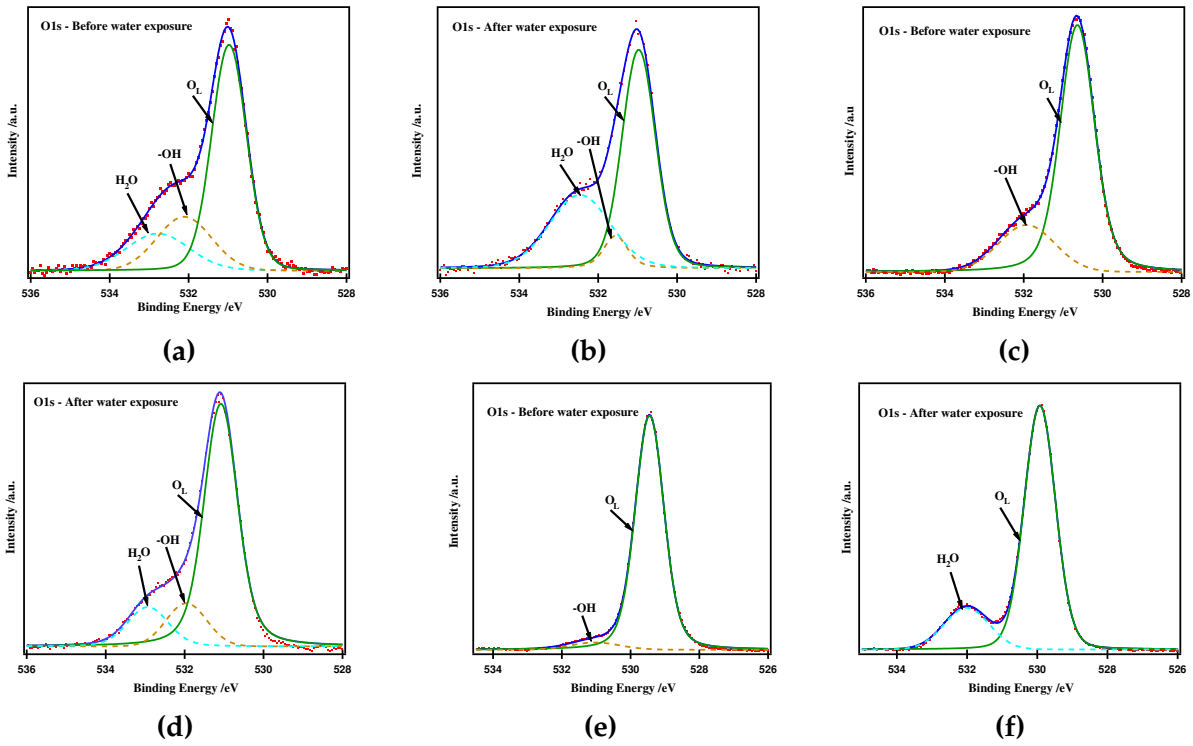

Figure 5.3: Deconvoluted O1s spectra for Z1 - without surface cleaning (a and b), Z2 - surface cleaned (c and d) and N - planar NiO (e and f) film, for before and after water exposure conditions respectively.

After NiO deposition on the Z1 and Z2 scaffolds (sample Z1N1, Z2N1 and Z2N2), the intensity of the Zn2p and O1s peaks diminished (Figures 5.4a, 5.4c, 5.4d and 5.4f and Figures 8.11a and 8.11c in Appendix, respectively) and shifted towards lower BE (Table 5.3), along with the appearance of the Ni2p peak. This confirms the junction formation between ZnO and NiO. After water exposure, the Zn2p, Ni2p and O1s peaks were further reduced in intensity but with a shift towards higher BE (Figures 5.4a to 5.4f , Figures 8.11a to 8.11c in Appendix, respectively and Table 5.3), proving the surface interaction with water.

For the heterostructures with planar scaffold surface (Z3), (Figures 5.4g to 5.4i and Figures 8.11d to 8.11f in Appendix), though the Zn2p, O1s and Ni2p core levels were identified in the same range as in the 1D scaffold and heterostructures, many features and observations were different. After NiO deposition, the intensity of Zn2p was reduced significantly, the Ni2p peak was very intense and sharp for the small thickness (4nm) as compared to the Z1 and Z2 heterostructures and the O1s peak was also intensified. Also, the intensity of Zn2p after the water exposure step was mildly increased as opposed to the other heterostructures. We believe that these particularities in the XPS for samples Z3N3 and Z3N4 are due to the morphology of the scaffold i.e the planar surface was easily and fully covered by the NiO layer, resulting in a higher concentration of NiO.

The E_F position variation after each step, follows the same trend for all the ZnO/NiO heterostructures (with both planar and nanostructured ZnO scaffold) i.e, it lowers after NiO deposition and raises back after water exposure, corresponding to a shift of the VBMx line towards lower BE and then back again toward higher BE, respectively (Table 5.2 and Figure 8.13 in Appendix).

The shifts in the core level BE of Zn2p following the different steps provides information about the amount of band bending (V_{bb}) at the interface. As observed in Table 5.3, after the water exposure, V_{bb} partial band flattening (Z1N1), near flat band (Z3N3 and Z3N4) [232 280], or even accumulation conditions (Z2N1 and Z2N2) were observed [190 232 281]. This is detrimental for processes like photocatalysis, as band flattening will encourage surface recombination.

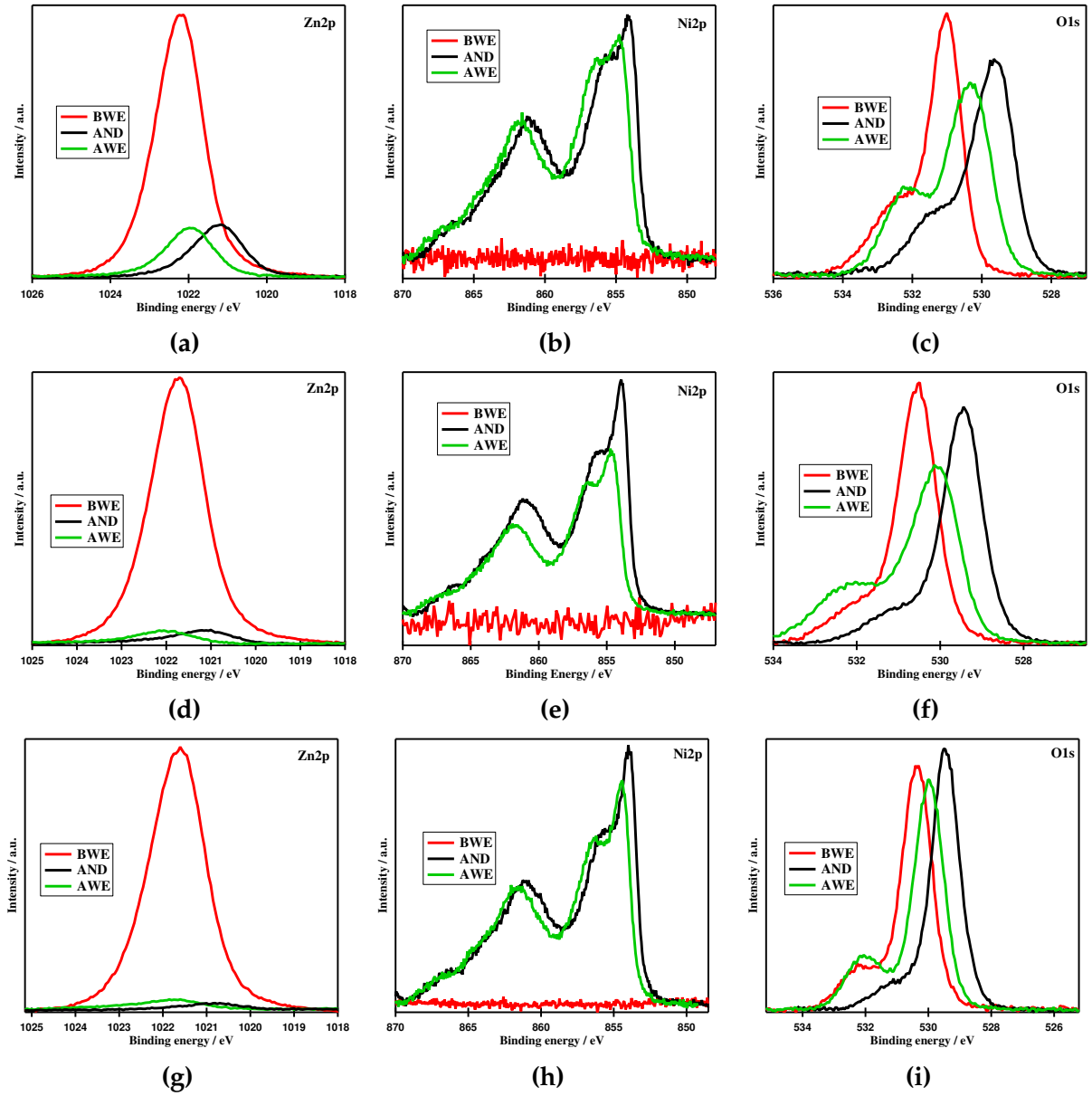

Figure 5.4: Individual spectra of Zn2p, Ni2p and O1s core levels, for Z1N1 (a - c), Z2N1 (d - f) and Z3N3 (g - i). before (BWE) and after water exposure (AWE), after NiO deposition (AND).

Table 5.3: Band bending(V_{bb}), full width half maximum (FWHM) values of Zn2p and O1s emissions and O_{OH}/O_{H_2O} ratio at varying steps - as given for all the samples. before (BWE) and after water exposure (AWE), after NiO deposition (AND). For all heterostructures, the V_{bb} values are represented as xx (yy), where the value without parantheses correspond to estimation from Zn2p BE shift and the value in parantheses correspond to the remaining band bending [value subtracted from V_{bb} attained after heterostructure formation and V_{bb} after water exposure]

Sample Code	Steps	Band Bending (V_{bb}) (eV)	FWHM (eV)		O_{OH}/O_{H_2O} ratio
			Zn2p (in eV)	O_L (in eV)	
Z1 - Without surface cleaning	BWE	-	1.53	1.08	0.55
	AWE	0.02	1.53	1.02	0.16
Z2 - Surface cleaned	BWE	0.48•	1.38	1.07	-
	AWE	0.56 (-0.08)	1.58	1.02	0.51
N - Bare NiO	BWE	-	-	0.99	-
	AWE	0.59	-	1.07	-
Z1N1	BWE	-	1.44	1.00	0.62
	AND	1.01	1.50	1.27	-
	AWE	0.74 (0.27)	1.43	1.31	0.29
Z2N1	BWE	-	1.39	1.06	-
	AND	0.73	1.52	1.07	-
	AWE	1.00 (-0.27)	1.59	1.19	0.36
Z2N2	BWE	-	1.39	1.03	-
	AND	0.67	1.44	1.26	-
	AWE	0.85 (-0.18)	1.45	1.37	0.48
Z3N3	BWE	-	1.48	1.10	-
	AND	0.91	1.60	1.00	-
	AWE	0.86 (0.05)	1.48	1.15	-
Z3N4	BWE	-	1.51	1.09	-
	AND	0.70	1.39	1.12	-
	AWE	0.65 (0.05)	1.46	1.20	-

As for the scaffold, the O1s core levels of the Z1, Z2 and Z3 heterostructures were deconvoluted (Figure 5.5 and Figure 8.12 in Appendix) and the O_{OH}/O_{H_2O} ratios were calculated (Table 5.3) and the following overall conclusions were drawn:

i). The scaffold Z1 and Z2 and their heterostructures Z1N1, Z2N1 and Z2N2 show the presence of the three contributions, after water exposure (O_L - [530.03 - 531.00 eV], O_{OH} - [530.96 - 531.95 eV] and O_{H_2O} - [532.02 - 532.93 eV]), confirming the water dissociation.

ii). The O_{OH} contribution is not detected on the surface of heterostructures Z3N3 and Z3N4 and of the scaffold N, clearly indicating that water dissociation was not favoured on these surfaces.

iii). Surface cleaning leads to a better water dissociation - the O_{OH}/O_{H_2O} ratio is the highest for sample Z2 among all the other samples.

iv). The water dissociation capability of the Z2 heterostructures decreases with increasing NiO thickness.

The full width half maximum of Zn2p and O1s emission lines were obtained for all samples and at all the steps involved, in order to elucidate the change in line width and its relation to the surface reactions on water interaction. Because, the broadening effect (in addition to the binding energy shifts) is associated with the chemical state changes in the surface atoms [282]. Herein, the change in chemical state occurs as a result of water interaction (despite the broadening observed on NiO deposition during the second step of water exposure study, in case of heterostructures) and thus related to the molecular water adsorption or dissociation. The observations discussed below are in agreement with the reports by Xueqiang et al [282–284], where broadening effects in the metal and oxygen emission lines (in the single crystalline surfaces), as a consequence of water interaction was observed.

Among the ZnO scaffolds, Z1 and Z2, the broadening effect was not seen in the lattice oxygen (O_L) line, whereas it was observed for the Zn2p emission (only in Z2, Table 5.3). This indicate that the change in the chemical environment was around the surface of Zn atoms and that the contribution from oxygen is coming from the lower-laying layers. With the planar NiO film, though the FWHM of Ni^{2+} peak was not significantly affected, that of O_L was broadened (Table 5.3) confirming the adsorption of water molecules, in agreement with the deconvolution of O1s emission line which showed the presence of O_{H_2O}.

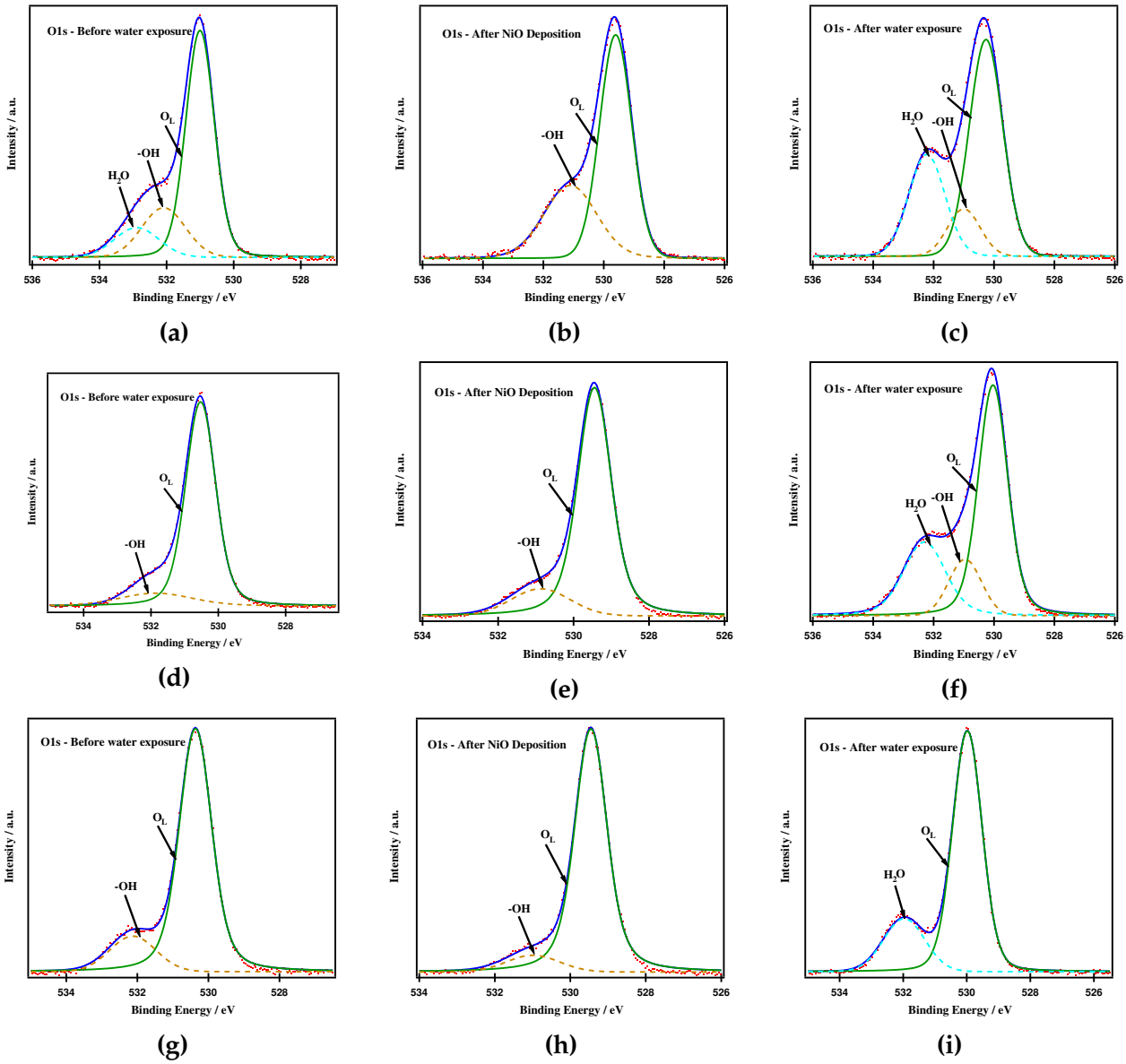

Figure 5.5: Deconvoluted O1s Spectra for Z1N1, Z2N1 and Z3N3. before (BWE) and after water exposure (AWE), after NiO deposition (AND).

In case of ZNR based heterostructures, the broadening effect in Zn2p emission line was either not seen (for Z1N1, scaffold without surface cleaning) or less pronounced (with respect to Z2 scaffold, for Z2N1 and Z2N2, scaffold with surface cleaning), which is because they lay under NiO layer and that their contribution is limited. The FWHM of O_L line was broadened (Table 5.3) in all the above cases but more pronounced in Z2 based heterostructures (Z2N1 and Z2N2). The higher broadening effect for Z2 based heterostructures, is in agreement with the higher O_{OH}/O_{H_2O} ratio, which indicating better water dissociation as compared to all the samples studied. The broadening effect was also noticed in the planar ZnO (Z3) based heterostructures, where the effect was predominant for thicker (Z3N3) NiO

layer, compared to lower one (Z3N4) [Table 5.3] and this could be related to the different morphology of the heterostructure involved. Because, this was in contrary to the broadening effect observed for the Z2 based heterostructures, where the thickness of the NiO layer did not have an influence.

In addition, the chemical changes in the surface of NiO structure as a result of water interaction, were investigated by performing difference spectra (Figure 5.6) between Ni2p emission lines that was obtained after NiO deposition and water exposure steps, for planar NiO and all the NiO/ZnO heterostructure films. As mentioned earlier, the nature of the surrounding atoms will strongly influence the emission line and in case of Ni2p spectra, when the broadening of the main line is accompanied by the broadening of satellite peak and increase in intensity [285, 286], this could be related to the charge transfer from the neighbouring atoms, here oxidation [29].

For planar NiO, as well as for all the heterostructures, the difference spectra displayed broadening of both the main line and the satellite peak, along with a decrease in intensity of the main line, and an increase in the intensity of shoulder and satellite peaks. Both these effects were observed to be influenced by factors like morphology, NiO thickness and scaffold surface (in case of heterostructures). On water interaction, for the ZNR based heterostructures the broadening and intensity variation effects, were determined by whether the scaffold surface was uncleaned (Z1N1, mild effect, Figure 5.6a) or cleaned (Z2 heterostructures, significant effect), in addition to the role played by the NiO thickness (Z2N2 with thin NiO layer had a significant effect compared to Z2N1 with thick NiO layer, Figures 5.6b and 5.6c). This would mean that charge transfer between the NiO layer and adsorbed water molecules was higher for the heterostructures based on clean ZNR scaffold and thinner NiO layer. In contrary, these effects were noticed to be increasing with an increased NiO content, in case of planar (hetero)structures, where Z3N4 with thin NiO layer had a mild effect (Figure 5.6d) while Z3N3 with thick NiO layer and planar (bulk) NiO displayed a noticeable effect (Figures 5.6e and 5.6f). This clearly demonstrates that the water interaction and the resultant change on the surface of NiO are morphology dependent.

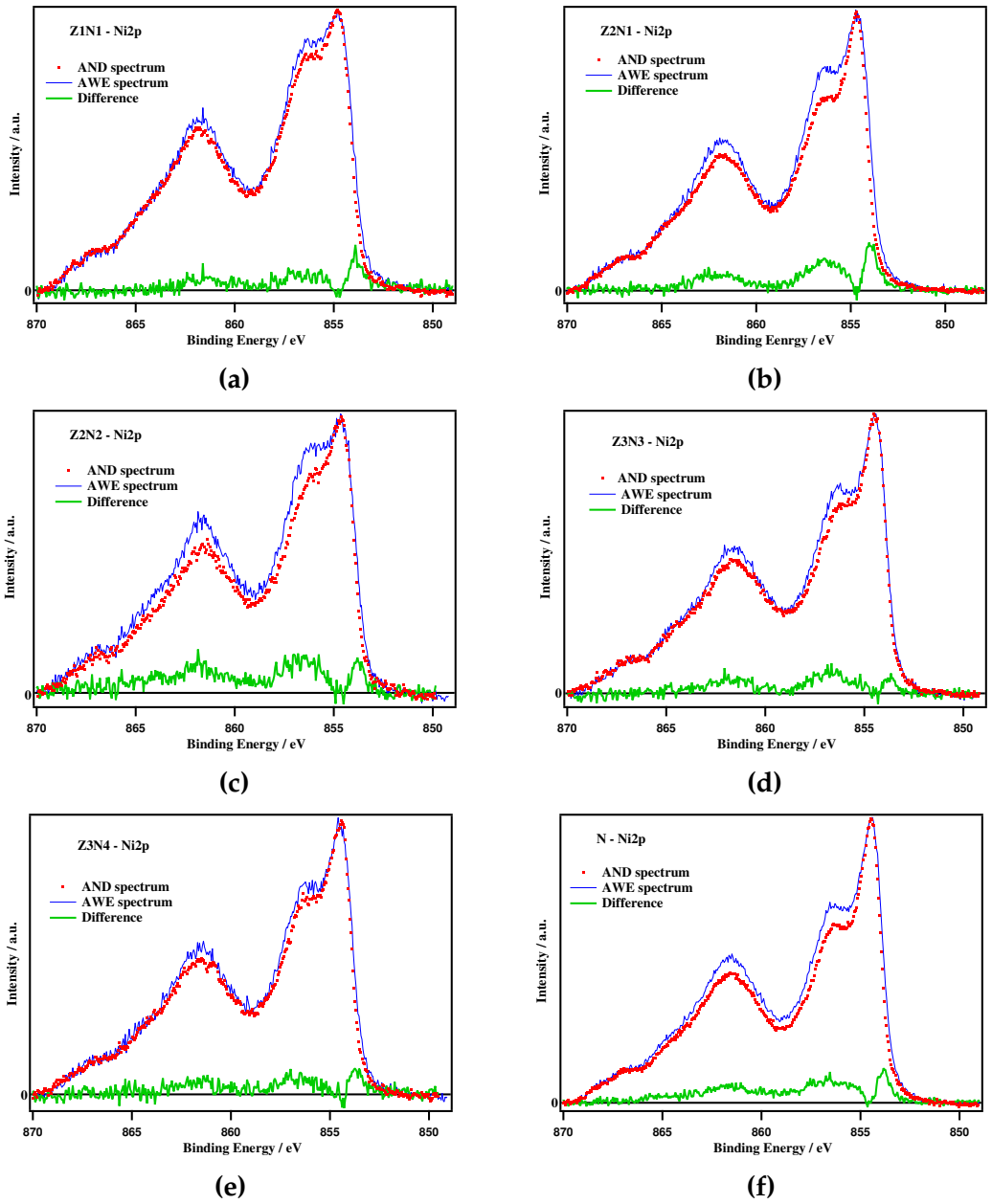

Figure 5.6: Difference spectra of Ni2p between after NiO deposition (AND) and after water exposure (AWE) steps. Shirley background subtraction was done and the spectra was shifted towards same binding energy (of main emission line, Ni^{2+}).

Among all heterostructures, the predominant broadening effect in the Ni2p spectra of Z2N2 revealed an enhanced charge transfer between the neighbouring atoms. This, along with the observed binding energy shifts and the higher O_{OH}/O_{H_2O} ratio indicates effective water dissociation. Whereas, in all other heterostructures, though the broadening effect was noticeable, it could be ascribed to the hydroxides present prior to water exposure or molecularly adsorbed water (after water exposure), since they exhibited only a mild or lack of water dissociation.

5.5. Photoluminescence

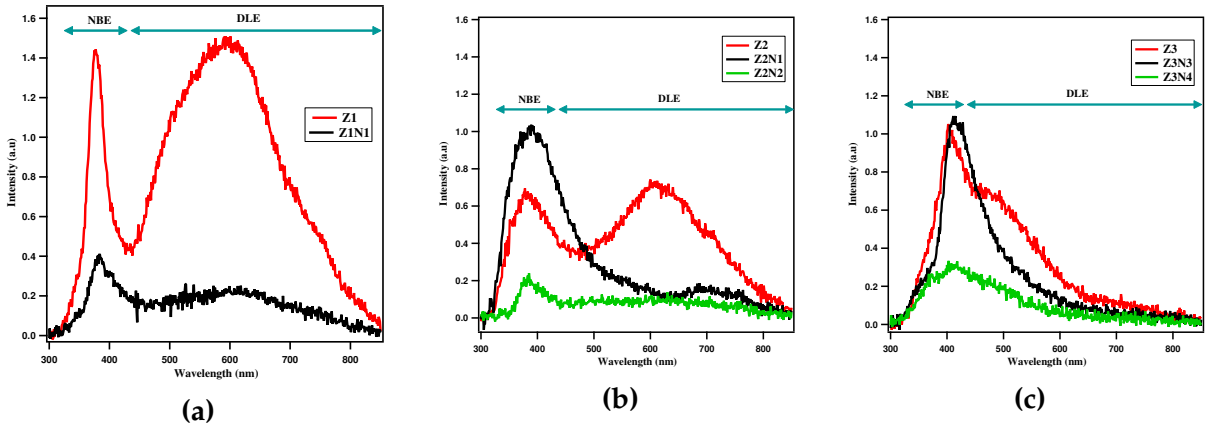

Figure 5.7: PL spectra of the Z1 (a), Z2 (b) and Z3 (c) scaffolds and their respective heterostructures. NBE - Near bandedge emission and DLE - Deep level emission.

The photoluminescence spectra of the ZnO scaffold surfaces (Z1 and Z2) showed the presence of two contributions, a narrow UV emission in the 380-390 nm range and a broad visible emission in the 450-750 nm range [17, 157, 208]. As already presented in Section 4.1.5, the former is termed as near band edge emission and this occurs either due to band-band transitions (photo induced electron in CB recombining with holes in VB) or electron/hole or electron/traps recombination; whereas the latter is termed deep level emission and appears due to recombination with deep level traps or defects. The trap levels closer to CB are zinc vacancies and interstitials (V_{Zn} and Zn_i) and the deep level defects comprise the oxygen vacancies and interstitials (V_O and O_i). Among the films that were investigated here, Z1 and Z2 were found to have both near bandedge and deep level emission regions while the scaffold Z3 was noticed to have stronger near bandedge emission and only a mild contribution from Zn_i, O_i and V_O (Figure 8.14 (a - c) in Appendix). When comparing Z1 and Z2, it is clear that the surface cleaning has removed the surface vacancies and thus reduced the surface and bulk recombination, with both near bandedge and deep level emission peaks being lower in intensity (Figures 8.14a and 8.14b in Appendix). Both ZNR based heterostructures (with scaffold Z1 and Z2) and the planar heterostructure (with scaffold Z3) films had significant reduction in the intensity of near bandedge emission along with the reduction/suppression of the deep level emission region after NiO deposition (Figure 5.7). However, for the in-situ scaffold surfaces (Z2 and Z3), longer NiO deposition times (Z2N1 - $\simeq$ 7 nm and Z3N3 $\simeq$ 4 nm) led to an enhancement in the NBE emission. Moreover, the band distribution of the NBE peak (a shoulder is observed for the Z3 counterparts), indicates that the deep level defects are still present.

It is important to notice that sample Z2N2 which has the lowest vacancy contribution has the best water dissociation properties among the ZNR based heterostructures. However it is still the bare scaffold Z2 which dissociates water better. In fact, the higher surface concentration of V_O in Z2 might be coming from the ambient exposure (during sample transfer to PL instrument), exposure which is avoided for Z2N2 when NiO is deposited. The reduction of deep level emissions in both 1D structured and planar based heterostructures implies that the prevention of bulk recombination due to the deep levels (V_O and O_i) was effective irrespective of material's structure[175].

5.6. Band bending at the interfaces and band alignment on water exposure

The E_F of pristine ZNR (Z1) (at 3.47 eV, Table 5.2) lies above the CB, revealing excess electrons i.e an accumulation layer[190,287] at the surface (Figure 5.8a), with negligible change after the water exposure (Figure 5.8a). Once the surface was cleaned (Z2), the E_F (at 3.04 eV, Table 5.2) was lowered below the CB, leading to electron depletion[287] at the surface(Figure 5.8b). After water exposure, its E_F was again above the CB minimum, revealing the presence of an accumulation layer at the surface (Figure 5.8b).

The E_F of pristine NiO was initially found to be 0.52 eV (Table 5.2) above the VBMx and after water exposure, a depletion layer was formed (as shown in Figure 5.8c).

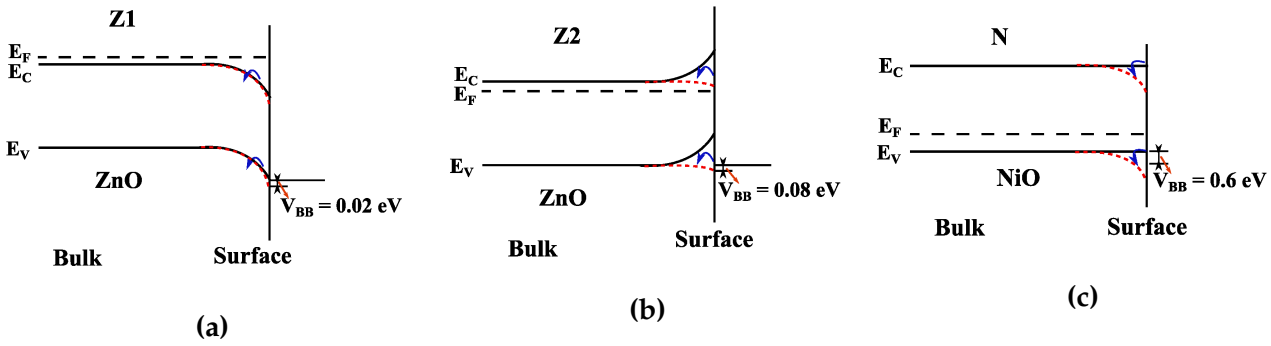

Figure 5.8: Schematic band alignment of the scaffolds (Z1, Z2 and N), before and after water exposure; (a) Z1 surface with initially an accumulation layer, showing increase in accumulation after water exposure (b) Z2 surface with a depletion layer after surface cleaning and then showing accumulation after water exposure and (c) N surface showing depletion after water exposure step. V_{bb} values shown in figures correspond to the red dotted line, that represent the remaining band bending, after water exposure.

As a proof of water interaction, the intensity of all individual peaks from the XPS spectra were diminished and a shift towards higher BE was observed, irrespective of the sample structure or NiO thickness, inversely to what happened after NiO deposition. By tracing the shifts in the Zn2p BE, through all the steps (shown in Figure 5.9) for all the heterostructures, informations on interface parameters could be extracted. To enable better understanding about each case of the samples discussed (in this chapter), in regard to the BE shifts in Zn2p emission lines and also the influence in band bending at each step of the water exposure study, the V_{bb} values of Z2 heterostructures were not determined with respect to the shift of Zn2p line for Z2 scaffold in relation to the reference material, Z1 scaffold (Whereas, in all the previous chapters, V_{bb} values of all Z2 heterostructures were determined in relation to the reference material, Z1 scaffold). This was also because heterostructures based on planar ZnO (Z3) are compared and discussed together with the ZNR based heterostructures.

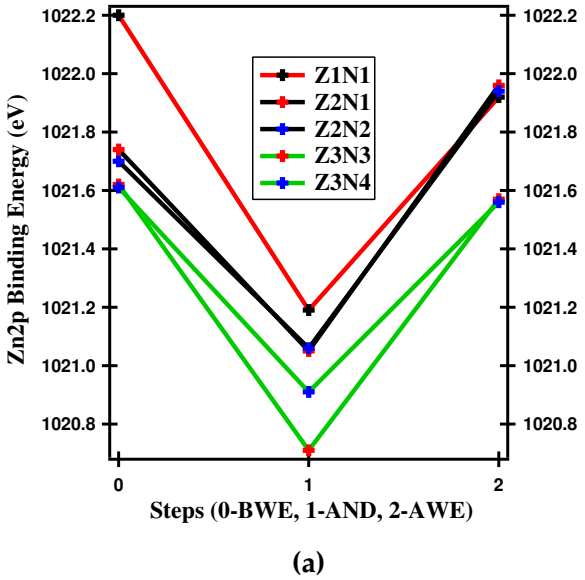

(a)

Figure 5.9: Binding Energy Vs Steps involved water exposure study for heterostructures

Before water exposure, the initial position of Zn2p core level was strongly influenced by whether the surface was not cleaned (Z1, Z1N1, 1022.23 - 1022.33 eV) or surface cleaned (Z2, Z2N1, Z2N2, Z3N3 and Z3N4, 1021.61 - 1021.85 eV). From Figure 5.9 we can see that, heterostructures based on the Z2 and Z3 scaffolds have a similar Zn2p BE, as they were prepared in-situ (values of V_{bb} before water exposure step in Table 5.3). However, in case of the Z3N3 and Z3N4 planar heterostructures a significant difference in the attained band bending is observed, corresponding to a small variation in NiO thickness. In contrast, the ZNR based heterostructures showed significant change in band bending due to the influence of surface cleaning and only minor changes due to the variation in the NiO thickness (the Zn2p BE values of Z2N1 and Z2N2 after NiO deposition almost superimposed, Figure 5.9)

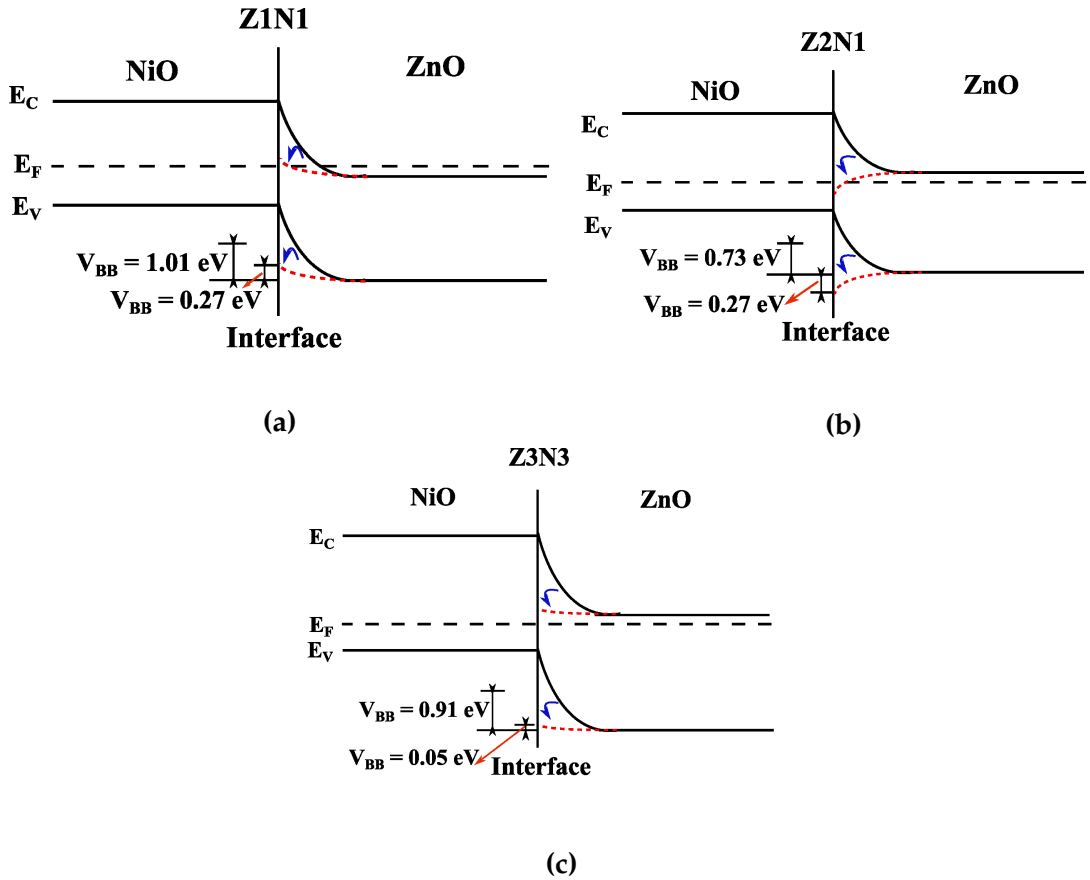

Figure 5.10: Band alignment after NiO deposition, before and after water exposure for (a) Z1N1 (partial band flattening) (b) Z2N1 (accumulation of electrons) and (c) Z3N3 (partial band flattening). V_{bb} values corresponding to the red dotted line represent the remaining band bending, after water exposure.

. After the water exposure step, the Zn2p core level shifted towards higher BE for all the heterostructures. In case of the heterostructures based on ZNR scaffold, V_{bb} of 1.01, 0.73 and 0.67 eV were obtained for Z1N1, Z2N1 and Z2N2 respectively (Table 5.3, Figures 5.10a and 5.10b, Figure 8.15a in Appendix). After the water exposure step, the attained V_{bb} was reversed, leading to a partial band flattening conditions (in case of Z1N1, Table 5.3, Figure 5.10a) or even accumulation (in case of Z2N1 and Z2N2, Table 5.3, Figure 5.10b and Figure 8.15a in Appendix). On comparing the evolution of the band bending and O_{OH}/O_{H_2O} ratios at varying steps, one can clearly see that both the surface and interface properties are influencing the water dissociation process. Among the ZNR based heterostructures, Z2N2 had the highest O_{OH}/O_{H_2O} ratio corresponding to a minimum electron accumulation layer after water exposure, indicating that water dissociation process was favoured.

Concurrently, the planar heterostructures Z3N3 and Z3N4 which showed V_{bb} of

0.91 and 0.7 eV (Table 5.3, Figure 5.10c and Figure 8.15b in Appendix) respectively, exhibited nearly flat band conditions after the water exposure step leaving behind only 0.05 eV, (Table 5.3, Figure 5.10c and Figure 8.15b in Appendix) of band bending from the previously attained values. This along with the absence of O_{OH} component were corroborated with the poor water dissociation properties.

The water dissociation properties observed for Z1 and Z2 are in contrary with the results of Hu et al[188] who demonstrated theoretically (in comparison to experimental studies of Huang et al.[198] and Sun et al.[197]), that the presence of V_O increased the number of binding sites for incoming water molecules. Our studies have revealed that the removal of the V_O (Fermi level shifted inside the bandgap and upward band bending) has enhanced the water dissociation process which is confirmed by the higher O_{OH}/O_{H_2O} ratio after water exposure, on the surface cleaned Z2.

This contradiction was also addressed by John et al.[193] where they were comparing the surface characteristics of ZnO in UHV/DFT and ambient pressure XPS studies. They agree that O_{OH} and O_{H_2O} co-exist on almost all films in UHV conditions but found some discrepancies when comparing with the ambient pressure results, highlighting the importance of experimental conditions.

5.7. Pollutant degradation

The C_t/C_0 vs. degradation time curves for all scaffold and heterostructure films are plotted in Figure 8.14a and the degradation efficiency (calculated according to equation 4.3 in Section 4.2.5) values are plotted in Figure 8.14b. The degradation efficiencies of Z1 [54%] and Z2 [67%] scaffold films were higher than bare NiO [14%] (Figure 5.11), indicating that 1D nanostructure without adsorbates is an effective scaffold surface for performing the photocatalytic degradation, in agreement with water exposure results.

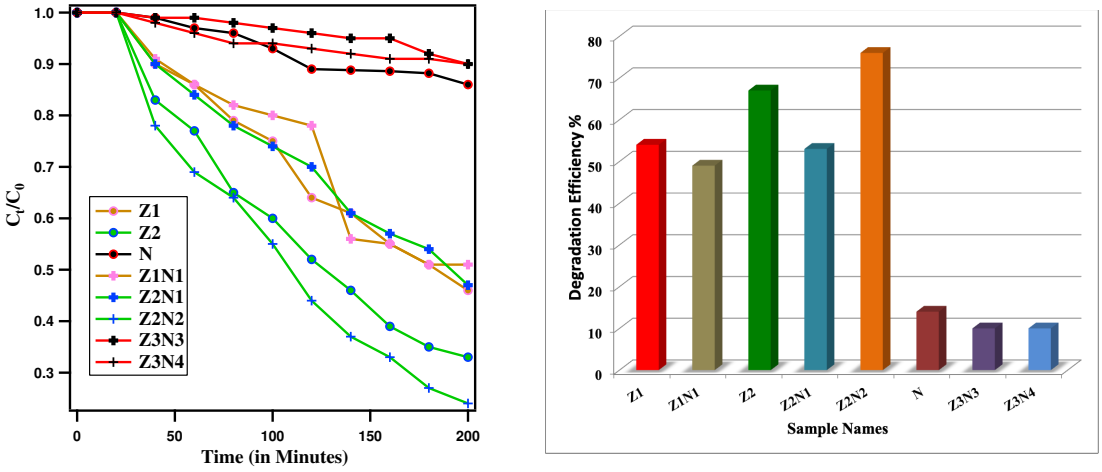

Figure 5.11: C_t/C_0 vs. degradation time curves (a) and degradation efficiencies (b) for Z1 (without surface cleaning), Z2 (surface cleaned), their corresponding heterostructures (Z1N1, Z2N1 and Z2N2), planar NiO (N) and planar NiO/ZnO heterostructures (Z3N3 and Z3N4). Degradation study was conducted for 3 samples of scaffold Z1 (without surface cleaning) and resulted in an error bar of $\pm 2\%$.

The efficiency values (Figure 8.14b) obtained here were found to be, certainly in agreement with what was noticed for each of them after water exposure with respect to their water dissociating capabilities. While all Z1 and Z2 based heterostructures showed less or comparable performance with respect to their scaffolds, the planar NiO (N) and the NiO/ZnO heterostructures based on planar ZnO (Z3) showed poor performance irrespective of the NiO thickness. The poor degradation efficiencies of N, Z3N3 and Z3N4 could be attributed to the lower specific surface (planar scaffold), along with the partial band flattening after water exposure and charge recombination due to deep level defects.

Despite the observations of band bending (meaning, charge separation at the interface) both Z1N1 and Z2N1 were seen to have lower efficiency with respect to their scaffold, no matter the presence or absence of adsorbates on the scaffold surface. This is more contradictory for Z2N1, for which the NBE emission was enhanced. However, its dissociation capabilities was better than Z1N1, explaining the improved degradation efficiency compared to Z1N1. Whereas, for Z2N2, whose NiO layer thickness was $\simeq$ 2.5 nm (based on TEM image, not shown here), both NBE and DLE emissions were significantly reduced (relative to Z2 scaffold and Z2N1) and showed a higher O_{OH}/O_{H_2O} ratio which corresponds to a mild improvement in the degradation efficiency, with respect ot Z2 scaffold. This could be related to the significant reduction in deep level defects. The overall modest improvement in the degradation efficiency after heterostructure formation indicates the probability of recombination across the NiO layer, as detailed in Section 4.2.4. The champion efficiency

obtained for the Z2 scaffold could be attributed to the presence of both adsorbed oxygen and hydroxide layer (after its exposure to ambience, as discussed in Section 4.2.5, which corresponds to the actual surface exposed to pollutant degradation).

The correlation between XPS, PL and pollutant degradation revealed that improving the ability to dissociate water promotes the degradation process (being a hole dependent process).

5.8. Conclusion

The water interaction studies were successfully performed on Zinc Oxide nanorod (ZNR) based scaffold and heterostructures (with NiO). For comparison purposes, the same analysis were performed on the planar NiO and NiO/ZnO heterostructures based on planar ZnO. In case of scaffold films, water exposure resulted into the shift towards higher binding energy, for all the emission lines (Zn2p (ZnO) or Ni2p (NiO), O1s and VBMx), along with a reduction in intensity, all of which serve as a proof for water interaction at their surface. In case of heterostructures based on surface cleaned ZnO (Z2), the effect of adsorbate removal was noticed in the attained band bending (V_{bb}), where NiO deposition (of 10 nm) on ZnO surface without cleaning, Z1 [Z1N1] led to a 1.01 eV of band bending and to a lower value (0.73 eV) when deposited on Z2 [Z2N1]. In terms of NiO layer thickness (Z2N1 vs. Z2N2), the effect was minimal (V_{bb} - 0.73 vs. 0.67 eV). Whereas, when the planar ZnO (Z3) was used as a scaffold, a relatively significant difference (0.21 eV) in band bending was observed, which correspond to a 2 nm variation (between Z3N3 and Z3N4) in the NiO thickness. The photoluminescence spectra of all the heterostructures, revealed the reduction in the deep level emission, indicating the mitigation of the bulk recombination irrespective of material's structure. For Z2N1 and Z3N3, the near band edge emission was found to be increased (than their respective scaffold and relative heterostructures), suggesting that recombination through the NiO layer might be higher in these cases. After the NiO deposition and water exposure, the Zn2p, O1s and Ni2p emission lines diminished and shifted towards lower and higher binding energy, respectively. Interestingly, our study shows that on water exposure, the V_{bb} of the NiO/ZnO heterostructures (with both planar ZnO and ZNR based scaffold) exhibited partial band flattening or (almost)flat-band and even accumulation conditions. Concurrently, the heterostructures which showed near flat band conditions also exhibited a poor water dissociation (hydroxides were not even identified on the surface for bare NiO and planar heterostructures), corresponding to the lowest photodegradation efficiencies. The 1D nanostructured scaffold without adsorbates (Z2) and its heterostructure with a thin NiO layer showed the best water dissociation capabilities along with along with the main-

tained band bending explain the improved photodegradation performance with respect to the Z1 counterparts. Therefore, we have provided experimental evidences that a scaffold surface with less vacancies promote water dissociation and thereby enhances the pollutant degradation.

Chapter 6

Industrial Implementation

6.1. Experimental strategy

The lab scale experiments are not always easy to implement at pilot scale for any new technology in the view of commercialization. For this reason, an upscaling test was further implemented at our industrial partner, Aquatic Science. Aquatic Science, among their other products and services, provide solutions for water filtering or purification for ornamental ponds, swimming pools and fish tanks. Their solutions for water purification include products based on nanomaterials and heterogeneous photocatalysis. Two types of modules were tested, for quality control calibration using the standard nano-TiO_2 that is already part of their commercial product and the other one allowed the comparison of TiO_2 (purchased and coated on steel plates) with ZnO (nanorod based thin films, prepared as optimized in Chapter 3).

6.2. Material description

TiO_2 preparation - The commercially purchased TiO_2 solution and isopropanol were used at 1:1 ratio, to prepare 1.4 mL solution. This was then sprayed from a top nozzle, on the inner walls of the cylinder (Figure 6.3a, in next section), reaching a thickness of 100 nm (which amounts to $\simeq 0.002$ g/cm^3). The cylinder was then dried in an oven at 200° C, for 15 mins.

ZnO preparation - The ZnO nanorod were grown on FTO substrates of 4×4

cm^2 dimensions and used in module 2 (Section 6.4). The ZnO nanorod growth was done following the same protocol as the one used for the smaller dimension substrates (detailed in Section 3.2), except for the seeding layer which was prepared by ultrasonic spray pyrolysis (USP) method. This is because of the substrate size restriction coming available with the spin coating equipment available. The nanorod growth was confirmed through SEM observation (not shown here), with a final layer thickness of 250 nm (amounting to $\simeq 0.007$ g/cm^3).

6.3. Module 1 - UVSynergy 10

Module 1 is based on the industry's commercialized reactor called **UVSynergy 10**. It consists of a steel cylinder (area 7540 cm^2, diameter = 40 cm and height = 40 cm), which is provided with a nozzle at the top (Figure 6.1), that can allow a 360° spraying angle. The structure of this nozzle is extended like a shell, down upto $3/4^{th}$ of the cylinder's height. The cylinder is also provided with two other openings/inlets, one to the top left and the other to the bottom right, to which the tubes were connected, to enable the water flow. Two connecting tubes are attached to the flow regulating motor, that was working at a flow speed of 5300 mL/min.

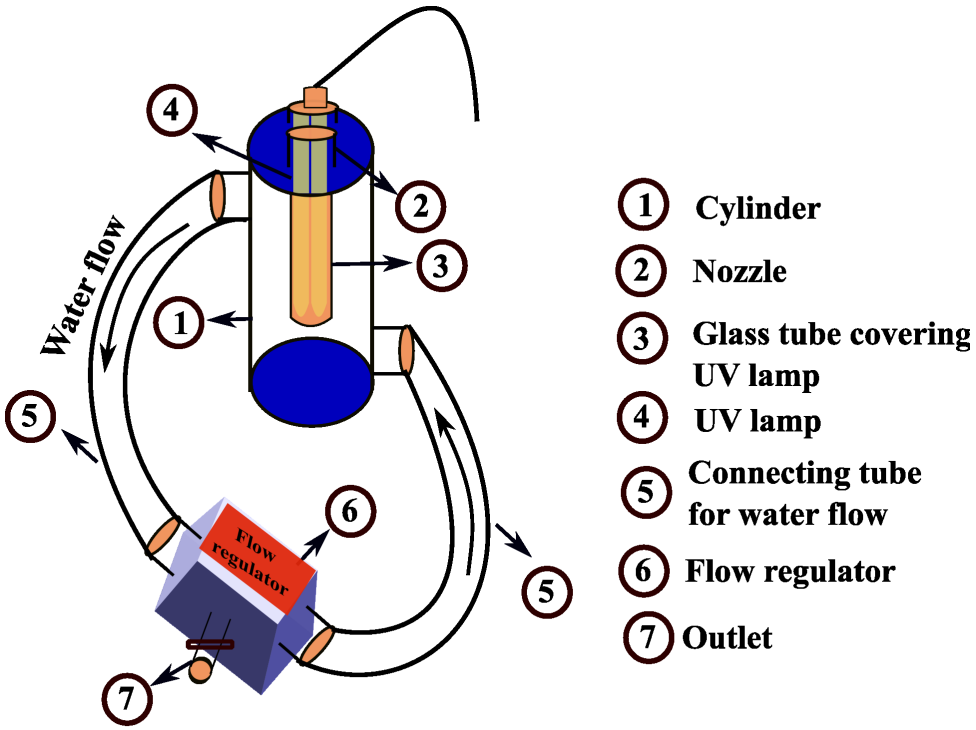

Figure 6.1: Schematic of module 1 - UVSynergy 10, the water flow setup used for RhodamineB degradation.

The UV lamp used was a monochromator (λ_{max} = 365 nm) with $\simeq$ 3-4 mW/cm^2 irradiance and the lamp to photocatalyst (inner wall of the cylinder) distance was $\simeq$ 5 cm. The power of the UV lamp was measured using a solarmeter (model 5.0), which had a spectral response in the wavelength range of 280 - 400 nm (peak response at 370 nm), with an accuracy of $\pm$ 5%. The volume capacity of the cylinder (including the solution necessary to fill the connecting tubes), was measured to be 6430 mL and the same was utilized for all the degradation tests done using module 1. For comparison purposes, cylinder with and without TiO_2 coating were tested. Every 20 minutes, aliquots of dye solution were collected through the outlet (no. 7 in Figure 6.1) and analyzed in UV - VIS spectrophotometer.

6.4. Module 2 - Three compartment based water flow

Module 2 was prepared from one of their older testing product and was based on three compartments (made up of steel), as shown in Figure 6.2. Each compartment was built from square plates (whose inner side was provided with stripes that can be used to fix to the other plate) to form a cubic structure with its top side open. An UV (LED) lamp that operates at a wavelength of 280 nm (obtained from GD Tech) was fixed to the top of the middle compartment, below which a quartz plate was placed as the cover, whereas the bottom of the middle compartment constituted the photocatalyst used for testing. Thereby allowing the UV irradiation to reach the photocatalyst pollutant system, in this setup. The power of UV light used was observed to be 2 - 3 mW/cm^2, determined with the help of solarmeter, as detailed in Section 6.3. And the distance between the lamp surface and the photocatalyst surface was measured as $\simeq$5 cm, similar to that in module 1. The other two compartments were closed with poly vinyl chloride (PVC) plates. Each compartment was separated by a separator (which had several holes to it), thereby enabling the flow of water between the compartments. Each and every piece of the compartment(s) used for building the module were joined together with the help of Silicon paste.

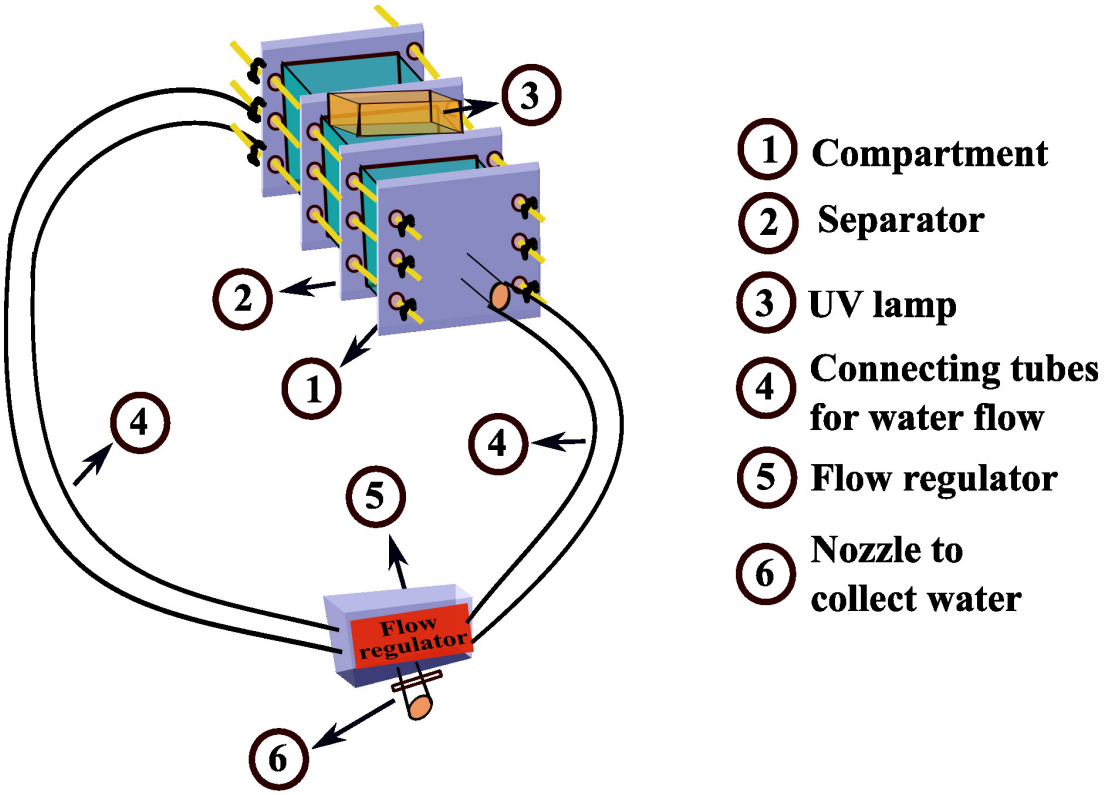

Figure 6.2: Three compartment based water flow setup for RhodamineB degradation.

The outer end plates of the module was provided with nozzles, to which one end of the tubes were connected in order to allow the flow of water. The other end of the connecting tubes were then fixed to a flow regulator that was capable of producing a 750 mL/min flow. However, it should be considered that the compartments are provided with the separators that have holes and this configuration will modify the speed of water flow within the compartments. This module was capable of holding $\simeq$ 1000 mL of the pollutant solution. As mentioned earlier, the plate that constituted the bottom of the middle compartment was used to fix the photocatalyst and the tests were done in three configurations:

1. steel plate, without coating
2. steel plate coated with TiO_2 (using the same coating procedure as used in module 1)
3. ZnO nanorod grown FTO substrates were placed on top of the steel plate (without coating)

The other two compartments were always having the bottom plate which was without any photocatalyst, since no light irradiation is provided in those compartments.

As for module 1, the flow regulator was provided with an outlet nozzle, through which aliquot solutions were collected every 20 minutes during the degradation test and examined with the UV-Visible spectrophotometer.

6.5. Pollutant degradation

The RhodamineB protocol, that was employed in lab-scale experiments (detailed in Section 8.1.4.1. in Appendix) was implemented here as well. Solutions of varying concentration (1.25μM, 2.5μM and 5μM) were prepared from the stock solution (20μM (10 mg/L)), for pollutant degradation tests using both module 1 and module 2. For TiO_2 coating related tests, the pH was adjusted to $\simeq$7, in relation to the point of zero charge for TiO_2. For the same reasons, the pH for ZnO based tests was adjusted to $\simeq$8. The RhB absorbance was monitored using an UV-VIS measurement system, "Spectra max plus 384" (for RhodamineB, the absorbance occurs at 554 nm). These values were further used to calculate the unknown concentration of the solution (as described in Section 8.1.4.1. in Appendix) and also for calculating the degradation efficiencies using equation 4.3 in Section 4.2.5.

For module 1 - The following degradation experiments were carried out (notation in parantheses indicate the sample names with which they are noted in Figure 6.3):

1. with TiO_2 coating
   - RhB solution, 1.25 μM [test was performed on TiO_2 coating that was annealed at 160 $^\circ$ C (T1) and 200 $^\circ$ C (T2), respectively]
   - RhB solution, 2.5 μM (T3)
   - RhB solution, 5 μM (T4)
2. without TiO_2 coating
   - RhB solution, 1.25 μM (T5)
   - RhB solution, 5 μM (T6)

   All cylinders were annealed at 200 $^\circ$ C, except for this, "T1".

The degradation curves and the photodegradation efficiencies (after 160 minutes) obtained for varying testing conditions on module 1 are represented in Figures 6.3a and 6.3b, respectively.

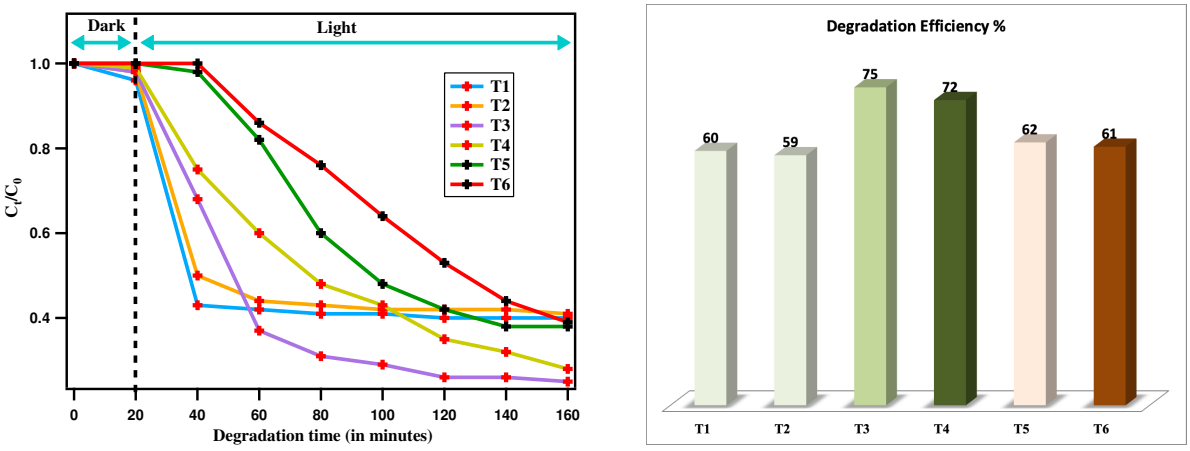

(a) **(b)**

Figure 6.3: (a) C_t/C_0 vs. degradation time for with and without TiO_2 coating, tested using varying RhB concentrations.

1. **For the TiO_2 coating, tested with 1.25 μM (T1 and T2),** the RhB concentration was degraded to almost half, in the first 20 minutes of light irradiation, but saturated after that; no difference in performance was noticed by varying the drying temperature involved in TiO_2 coating process.

2. **T3 -** For the RhB concentration of 2.5 μM, degradation to more than half of the initial concentration occurred in the first 30 - 40 mins of light irradiation, and the highest efficiency of 75% was reached, among all the other concentrations tested.

3. **T4 -** For higher RhB concentration, the solution was degraded to half the initial concentration after 1 hour of light irradiation.

   Module 1 that was tested without photocatalyst coating, for 1.25 (T5) and 5 (T6) μM of RhB concentration - did not show any degradation during dark and under light irradiation for 20 mins. However, after this timeline, there was a slow and gradual reduction in the concentration of RhB, reaching half of the initial concentration and an efficiency of upto $\simeq$ 60% was observed, irrespective of the initial concentration involved.

These observations lead to the assumptions that, in case of cylinder without coating, under continuous exposure, the light source alone was capable of degrading the pollutant. This phenomena is contrary to the observations from lab scale experiments, where no change in concentration was observed after 3 hours of light irradiation. The possible factors that could have led to the degradation of RhB in the absence of photocatalyst in module 1 is, the light to solution distance and the water flow system that would have enabled high probability of light-pollutant interaction.

Moreover, in case of coated cylinders, at all RhB concentration levels, the degradation efficiency was observed to be saturating after the first 20 (1.25 μM solution) or 60 (2.5 and 5 μM solution) minutes of light irradiation. This might be attributed to the temperature building up inside the cylinder with the increasing exposure time. Because, increase in temperature is known to induce charge carrier recombination at the photocatalyst surface, thereby limiting the efficiency that could be attained [51]. This might be probably avoided by introducing a cooling system.

Overall, the coated cylinder attained the highest photodegradation efficiency (75%), when using a 2.5 μM RhB solution, in 20 - 40 min of degradation time.

However, given that the size of the bottom plate that holds the photocatalyst in the compartment is about 7.2 $\times$ 7.2 cm, the ideal amount of solution to be used for treatment should be about 700 - 750 mL. But the volume capacity in module 2 is $\simeq$ 1000 mL, which will increase the amount of pollutant that the photocatalyst will deal with. Therefore, to avoid further complications, a lower RhB concentration, 1.25 μM was used for the tests with module 2.

Tests using module 2 - Degradation experiment was carried out as follows:

1. without photocatalyst, denoted as **without coating**

2. with TiO_2 coating, prepared and annealed under the same conditions as described in module1, denoted as **TiO_2**

3. with ZnO nanorod films, denoted as **ZNR - run 1**, where run 1 to run 3 indicate the number of test runs performed using this sample

   Between each run, the entire module (with samples inside) was washed few times with fresh water and then air blown through the nozzles, to remove remaining water. Furthermore, the module was dried in a hot air oven at 100° C for about an hour.

The degradation curves and the photodegradation efficiencies (after 180 minutes) obtained for varying samples and also the test runs performed with ZnO nanorod films, on module 2 are represented in Figures 6.4a and 6.4b, respectively.

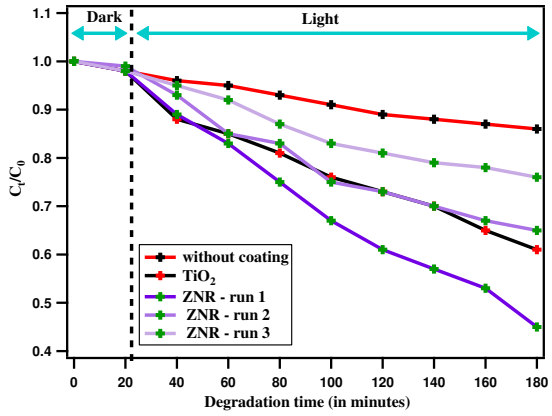

(a)

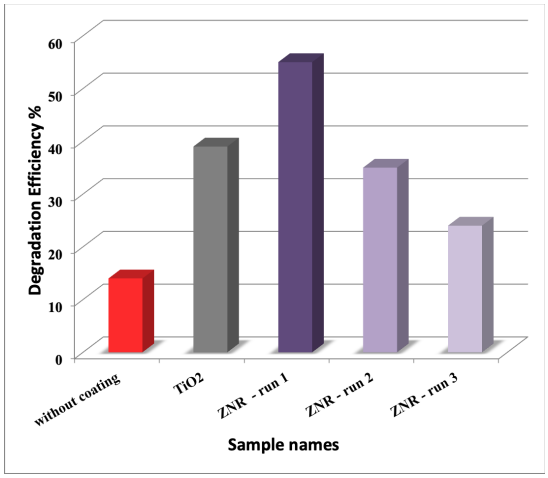

(b)

Figure 6.4: (a) C_t/C_0 vs. degradation time for with and without TiO_2 coating, with ZnO nanorod films for few runs, tested using RhB concentration of 1.25 μM.

First of all, the degradation performance of the runs with and without TiO_2 coating in module 1 are not comparable to that of module 2, due to the fact that the photocatalyst to pollutant ratio and the area of light exposure with respect to the amount of RhB solution used were different. However, as noticed for a module 1, here as well the setup without coating exhibited degradation but at a mild level (significant degradation was seen in module 1). Degradation test with TiO_2 coated steel plate was capable of reaching $\simeq$ 40% of degradation efficiency, at the end of 180 minutes. The use of ZnO nanorod films showed a mild improvement compared to TiO_2 coated plates reaching up to 55% of efficiency in the first run (Figures 6.4a and 6.4b). It is important to mention here that the mass of the active material in case of ZnO nanorod films was 3.5 times higher than the one of TiO_2. This would mean that the RhB degradation performance using ZnO and TiO_2 films was more or less same. Moreover, the successive runs 2 and 3 using ZNR films showed reduction in performance, by reaching an efficiency of 35% and 24%, respectively.

The important take away information from the tests with ZnO nanorods in module 2 are:

- ZnO nanorods were capable of showing a comparable performance in relation that of TiO_2, which might be due to the increased surface area with the use of one dimensional nanostructures.
- in the first run, the efficiency attained matches that of the efficiency observed for ZnO nanorods in lab scale experiments, indicating that the performance is maintained when upscaling.

- significant reduction in performance during the successive runs might be due to the photocorossion which is typical for ZnO as a bare or scaffold material.

In addition, the heat was noticed to be building up in the metallic structure to which the UV LED light was fixed to but was not spreading to the module itself, probably because they are fixed separately. However, in order to understand the role of temperature in the degradation performance, further studies should be done.

6.6. Conclusion

The lab scale protocol for the degradation of the pollutant RhodamineB was tested at pilot scale for the commercialized product (UVSynergy 10) of Aquatic Science. Implementation of the protocol revealed that presence of photocatalyst was evidently enhancing the degradation process but suffers from system heating up. The test using varying concentration of RhB showed that, at lower concentration the charge kinetics was fastest and for medium concentration, the best performance was obtained. The performance was limited by the heating up of the system and saturation was observed after 60 minutes, or even earlier for lower dye concentration.

Concurrently, module 2 setup was used to compare the performance of the standard TiO_2 and ZnO nanorod films. As opposed to the performance in the absence of photocatalyst, both TiO_2 (40%) and ZnO (55%) showed an improved degradation performance. Moreover, ZnO was noticed to have reduction in the performance on successive runs, indicating the probability of photocorossion. This might be avoided with the use of heterostructured photocatalysts. As an important factor, in terms of lab scale to pilot scale implementation, ZnO nanorod films was observed to be capable of maintaining similar performance.

Bibliography

Bibliography

[1] W. Wu, C. Jiang, and V. A. Roy, "Recent progress in magnetic iron oxide-semiconductor composite nanomaterials as promising photocatalysts," *Nanoscale*, vol. 7, no. 1, pp. 38–58, 2015.

[2] Z. Hao, L. Xu, B. Wei, L. Fan, Y. Liu, M. Zhang, and H. Gao, "Nanosize a-Bi2O3 decorated Bi2MoO6 via an alkali etching process for enhanced photocatalytic performance," *RSC Advances*, vol. 5, pp. 12 346–12 353, 2015.

[3] Kai Yu, Shaogui Yang, Huan He, Cheng Sun, Chenggang Gu and Y. J. State, "Visible Light-Driven Photocatalytic Degradation of Rhodamine B over NaBiO3: Pathways and Mechanism," *Journal of Physical Chemistry A*, vol. 113, pp. 10 024–10 032, 2009.

[4] P. Pichat, *Functional Nanostructured Materials and Membranes for Water Treatment Risk Analysis of Water Pollution Photocatalysis Activated Carbon for Water and Wastewater Treatment Biological Wastewater Treatment Ozonation of Water and Waste Water*, 2013.

[5] M. Niskanen, M. Kuisma, O. Cramariuc, V. Golovanov, T. I. Hukka, N. Tkachenko, and T. T. Rantala, "Porphyrin adsorbed on the (1010) surface of the wurtzite structure of ZnO-conformation induced effects on the electron transfer characteristics," *Physical Chemistry Chemical Physics*, vol. 15, no. 40, pp. 17 408–17 418, 2013.

[6] H. L. Chen, Y. M. Lu, and W. S. Hwang, "Characterization of sputtered NiO thin films," *Surface and Coatings Technology*, vol. 198, no. 1-3 SPEC. ISS., pp. 138–142, 2005.

[7] M. Ding, H. Yang, T. Yan, C. Wang, X. Deng, S. Zhang, and J. Huang, "Fabrication of Hierarchical ZnO @ NiO Core âĂŞ Shell Heterostructures for Improved Photocatalytic Performance," *Nanoscale Research Letters*, vol. 13, no. 260, pp. 1–9, 2018.

[8] J. M. González Carballo, E. Finocchio, S. García, S. Rojas, M. Ojeda, G. Busca, and J. L. G. Fierro, "Support effects on the structure and performance of ruthenium catalysts for the Fischer-Tropsch synthesis," *Catalysis Science and Technology*, vol. 1, no. 6, pp. 1013–1023, 2011.

[9] C. Ren, B. Yang, M. Wu, J. Xu, Z. Fu, Y. Lv, T. Guo, Y. Zhao, and C. Zhu, "Synthesis of Ag/ZnO nanorods array with enhanced photocatalytic performance," *Journal of Hazardous Materials*, vol. 182, no. 1-3, pp. 123–129, 2010. [Online]. Available: http://dx.doi.org/10.1016/j.jhazmat.2010.05.141

[10] H. Fan, M. Sun, P. Ma, M. Yin, L. Lu, X. Xue, X. Zhu, D. Li, and J. Ma, "UV photodetectors based on 3D periodic Au-decorated nanocone ZnO films," *Nanotechnology*, vol. 27, no. 36, pp. 1–7, 2016. [Online]. Available: http://dx.doi.org/10.1088/0957-4484/27/36/365303

[11] S. Bai, W. Jiang, Z. Li, and Y. Xiong, "Surface and Interface Engineering in Photocatalysis," *ChemNanoMat*, vol. 1, pp. 223–239, 2015.

[12] J. Zhen Zhang and John T. Yates, "Band Bending in Semiconductors: Chemical and Physical Consequences at Surfaces and Interfaces," *Chemical Reviews*, vol. 112, pp. 5520–5551, 2012.

[13] J. Low, J. Yu, M. Jaroniec, S. Wageh, and A. A. Al-Ghamdi, "Heterojunction Photocatalysts," *Advanced Materials*, vol. 29, no. 20, pp. 1 601 694–1 – 1 601 694–20, 2017.

[14] S. Bai, J. Jiang, Q. Zhang, and Y. Xiong, "Steering charge kinetics in photocatalysis: Intersection of materials syntheses, characterization techniques and theoretical simulations," *Chemical Society Reviews*, vol. 44, pp. 2893–2939, 2015.

[15] L. J. Brillson, *Oxide Semiconductors: Surfaces and Interfaces of Zinc Oxide*, 1st ed. Copyright © 2013 Elsevier Inc. All rights reserved., 2013, vol. 88. [Online]. Available: http://dx.doi.org/10.1016/B978-0-12-396489-2.00004-7

[16] F. Kayaci, S. Vempati, I. Donmez, N. Biyikli, and T. Uyar, "Role of zinc interstitials and oxygen vacancies of ZnO in photocatalysis: A bottom-up approach to control defect density," *Nanoscale*, vol. 6, no. 17, pp. 10 224–10 234, 2014.

[17] S. Vempati, J. Mitra, and P. Dawson, "One-step synthesis of ZnO nanosheets: A blue-white fluorophore," *Nanoscale Research Letters*, vol. 7, no. August, pp. 1–10, 2012.

[18] A. Ramirez-Canon, M. Medina-Llamas, M. Vezzoli, and D. Mattia, "Multiscale design of ZnO nanostructured photocatalysts," *Physical Chemistry Chemical Physics*, vol. 20, no. 9, pp. 6648–6656, 2018.

[19] S. Kenmoe and P. Ulrich Biedermann, "Water aggregation and dissociation on the ZnO(1010) surface," *Physical Chemistry Chemical Physics*, vol. 19, no. 2, pp. 1466–1486, 2017.

[20] W. Zhao, M. Bajdich, S. Carey, A. Vojvodic, J. K. Nørskov, and C. T. Campbell, "Water dissociative adsorption on NiO(111): Energetics and structure of the hydroxylated surface," *ACS Catalysis*, vol. 6, no. 11, pp. 7377–7384, 2016.

[21] A. Verdaguer, G. M. Sacha, H. Bluhm, and M. Salmeron, "Molecular structure of water at interfaces: Wetting at the nanometer scale," *Chemical Reviews*, vol. 106, no. 4, pp. 1478–1510, 2006.

[22] L. Dobrzanski and Szindler, "Sol gel TiO2 antireflection coatings for silicon solar cells," *Journal of Achievements in Materials and Manufacturing Engineering*, vol. 52, no. 1, pp. 7–14, 2012. [Online]. Available: http://www.journalamme.org/index.php?id=226

[23] C. Lohaus, "The Fermi Level in Hematite," Ph.D. dissertation, Technical University of Darmstadt, Germany., 2018.

[24] W. J. Andreas Klein, Thomas Mayer, Andreas Thissen, "Photoelectron Spectroscopy in Materials Science and Physical Chemistry: Analysis of Composition, Chemical Bonding and Electronic Structure of Surfaces and Interfaces," *BUNSEN-MAGAZIN*, vol. 10, no. 4, pp. 124–139, 2008.

[25] E. A. Kraut, R. W. Grant, J. R. Waldrop and S. P. Kowalcyzk, "Precise Determination of the Valence-Band Edge in X-Ray Photoemission Spectra: Application to Measurement of Semiconductor Interface Potentials," *Physical Review Letters*, vol. 44, no. 24, pp. 1620–1623, 1980.

[26] A. Klein, "Transparent conducting oxides: Electronic structure-property relationship from photoelectron spectroscopy with in situ sample preparation," *Journal of the American Ceramic Society*, vol. 96, no. 2, pp. 331–345, 2013.

[27] ——, "Energy band alignment at interfaces of semiconducting oxides: A review of experimental determination using photoelectron spectroscopy and comparison with theoretical predictions by the electron affinity rule, charge neutrality levels, and the common anion," *Thin Solid Films*, vol. 520, no. 10, pp. 3721–3728, 2012. [Online]. Available: http://dx.doi.org/10.1016/j.tsf.2011.10.055

[28] T. H. Gfroerer, "Photoluminescence in Analysis of Surfaces and Interfaces," in *Encyclopedia of Analytical Chemistry*, 2006, pp. 1–23.

[29] M. C. Biesinger, L. W. Lau, A. R. Gerson, and R. S. C. Smart, "The role of the Auger parameter in XPS

studies of nickel metal, halides and oxides," *Physical Chemistry Chemical Physics*, vol. 14, no. 7, pp. 2434–2442, 2012.

[30] A. Chauhan, "Deformation and damage mechanisms of ODS steels under high-temperature cyclic loading," Ph.D. dissertation, 2018. [Online]. Available: https://publikationen.bibliothek.kit.edu/1000080339

[31] K. D. Malviya, H. Dotan, K. R. Yoon, I. D. Kim, and A. Rothschild, "Rigorous substrate cleaning process for reproducible thin film hematite (α-Fe2O3) photoanodes," *Journal of Materials Research*, vol. 31, no. 11, pp. 1565–1573, 2016.

[32] P. D. Nguyen, T. M. Duong, and P. D. Tran, "Current progress and challenges in engineering viable artificial leaf for solar water splitting," *Journal of Science: Advanced Materials and Devices*, vol. 2, no. 4, pp. 399–417, 2017. [Online]. Available: https://doi.org/10.1016/j.jsamd.2017.08.006

[33] C. Andrade, M. Danielly, T. Faulin, V. Hering, and D. S. Parra Abdall, "Biosensors for detection of Low-Density Lipoprotein and its modified forms," *Biosensors for Health, Environment and Biosecurity*, no. July, 2012.

[34] J. F. Rubinson and Y. P. Kayinamura, "Charge transport in conducting polymers: Insights from impedance spectroscopy," *Chemical Society Reviews*, vol. 38, no. 12, pp. 3339–3347, 2009.

[35] G. Crini, "Non-conventional low-cost adsorbents for dye removal: A review," *Bioresource Technology*, vol. 97, no. 9, pp. 1061–1085, 2006.

[36] M. I. Litter and N. Quici, "Advanced Oxidation Processes for Water and Wastewater Treatment Photochemical Advanced Oxidation Processes for Water and Wastewater Treatment," *Recent patents on Engineering*, vol. 4, no. 3, pp. 217 – 241, 2010.

[37] T. Robinson, G. McMullan, R. Marchant, and P. Nigam, "Remediation of dyes in textile effluent: A critical review on current treatment technologies with a proposed alternative," *Bioresource Technology*, vol. 77, no. 3, pp. 247–255, 2001.

[38] N. N. Mahamuni and Y. G. Adewuyi, "Advanced oxidation processes (AOPs) involving ultrasound for waste water treatment: A review with emphasis on cost estimation," *Ultrasonics Sonochemistry*, vol. 17, no. 6, pp. 990–1003, 2010. [Online]. Available: http://dx.doi.org/10.1016/j.ultsonch.2009.09.005

[39] Y. Deng and R. Zhao, "Advanced Oxidation Processes (AOPs) in Wastewater Treatment," *Current Pollution Reports*, vol. 1, no. 3, pp. 167–176, 2015.

[40] O. Ganzenko, D. Huguenot, E. D. van Hullebusch, G. Esposito, and M. A. Oturan, "Electrochemical advanced oxidation and biological processes for wastewater treatment: A review of the combined approaches," *Environmental Science and Pollution Research*, vol. 21, no. 14, pp. 8493–8524, 2014.

[41] A. Ibhadon and P. Fitzpatrick, "Heterogeneous Photocatalysis: Recent Advances and Applications," *Catalysts*, vol. 3, pp. 189–218, 2013.

[42] C. Byrne, G. Subramanian, and S. C. Pillai, "Recent advances in photocatalysis for environmental applications," *Journal of Environmental Chemical Engineering*, vol. 6, no. 3, pp. 3531–3555, 2018. [Online]. Available: https://doi.org/10.1016/j.jece.2017.07.080

[43] William H. Glaze, "Drinking-water treatment with Ozone," *Environmental Science and Technology*, vol. 21, no. 3, pp. 224 – 230, 1987.

[44] A. Turki, H. Kochkar, G. Berhault, and A. Ghorbel, *p-Hydroxybenzoic acid degradation by Fe/Pd-HNT catalysts with in situ generated hydrogen peroxide*. Elsevier Masson SAS, 2010, vol. 175, no. Ii. [Online]. Available: http://dx.doi.org/10.1016/S0167-2991(10)75115-6

[45] W. H. Glaze, J.-w. Kang, and H. Douglas, "Ozone : Science & Engineering The Chemistry of Water

Treatment Processes Involving Ozone , Hydrogen Peroxide and Ultraviolet Radiation," *Ozone Science & Engineering*, no. August 2011, pp. 335–352, 2008.

[46] K. M. Lee, C. W. Lai, K. S. Ngai, and J. C. Juan, "Recent developments of zinc oxide based photocatalyst in water treatment technology: A review," *Water Research*, vol. 88, pp. 428–448, 2016.

[47] S. L.Suib, *New and Future Developments in Catalysis: Solar photocatalysis*, 2013.

[48] K. Maeda, "Photocatalytic water splitting using semiconductor particles: History and recent developments," *Journal of Photochemistry and Photobiology C: Photochemistry Reviews*, vol. 12, no. 4, pp. 237–268, 2011. [Online]. Available: http://dx.doi.org/10.1016/j.jphotochemrev.2011.07.001

[49] K. Fujishima, Akira and Honda, "Electrochemical Photolysis of Water at a Semiconductor Electrode," *Nature*, vol. 238, pp. 37–38, 1972.

[50] S. N. Frank and A. J. Bard, "Heterogeneous Photocatalytic Oxidation of Cyanide Ion in Aqueous Solutions at TiO2 Powder," *Journal of the American Chemical Society*, vol. 99, no. 1, pp. 303–304, 1977.

[51] U. I. Gaya and A. H. Abdullah, "Heterogeneous photocatalytic degradation of organic contaminants over titanium dioxide: A review of fundamentals, progress and problems," *Journal of Photochemistry and Photobiology C: Photochemistry Reviews*, vol. 9, no. 1, pp. 1–12, 2008.

[52] S. B. A. Hamid, S. J. Teh, and C. W. Lai, "Photocatalytic Water Oxidation on ZnO: A Review," *Catalysts*, vol. 7, no. 93, pp. 1–14, 2017.

[53] R. A. Al-Rasheed, "Water Treatment By Heterogeneous Photocatalysis an overview," pp. 1 – 14, 2005.

[54] F. E. Osterloh, "Photocatalysis versus Photosynthesis: A Sensitivity Analysis of Devices for Solar Energy Conversion and Chemical Transformations," *ACS Energy Letters*, vol. 2, pp. 445–453, 2017.

[55] K. S. Meng Ni, Michael K.H. Leung, Dennis Y.C. Leung, "A review and recent developments in photocatalytic water-splitting using TiO2 for hydrogen production," *Renewable and sustainable energy reviews*, vol. 11, pp. 401–425, 2007.

[56] G. G. Bessegato, T. T. Guaraldo, and J. F. D. Brito, "Achievements and Trends in Photoelectrocatalysis : from Environmental to Achievements and Trends in Photoelectrocatalysis : from Environmental to Energy Applications," *Electrocatalysis*, no. June, pp. 1–28, 2015.

[57] S. Pasternak and Y. Paz, "On the Similarity and Dissimilarity between Photocatalytic Water Splitting and Photocatalytic Degradation of Pollutants," *ChemPhysChem*, vol. 14, pp. 2059–2070, 2013.

[58] S. Bai and Y. Xiong, "Some recent developments in surface and interface design for photocatalytic and electrocatalytic hybrid structures," *Chemical Communications*, vol. 51, pp. 10 261–10 271, 2015. [Online]. Available: http://dx.doi.org/10.1039/C5CC02704G

[59] ——, "Precise control over the surface and interface structures of nanocatalysts," *Science Advances Today*, vol. 1, pp. 1–10, 2015.

[60] H. Park, H.-i. Kim, G.-h. Moon, and W. Choi, "Photoinduced charge transfer processes in solar photocatalysis based on modified TiO 2," *Energy Environ. Sci.*, vol. 9, pp. 411–433, 2016.

[61] E. Baldev, D. Mubarakali, A. Ilavarasi, D. Pandiaraj, K. A. S. Syed, and N. Thajuddin, "Colloids and Surfaces B : Biointerfaces Degradation of synthetic dye , Rhodamine B to environmentally non-toxic products using microalgae," *Colloids and Surfaces B: Biointerfaces*, vol. 105, pp. 207–214, 2013. [Online]. Available: http://dx.doi.org/10.1016/j.colsurfb.2013.01.008

[62] Y. Wang, Z. Yan, and X. Wang, "Photocatalytic Degradation of Rhodamine B Dye over Novel Porous TiO 2 -SnO 2 Nanocomposites Prepared by Hydrothermal Method," *International Journal of Photoenergy*, vol. 2014, pp. 928 519–1 – 928 519–7, 2014.

[63] M. Hassanpour, H. Safardoust-hojaghan, and M. Salavati-niasari, "Degradation of methylene blue and Rhodamine B as water pollutants via green synthesized Co 3 O 4 / ZnO nanocomposite," *Journal of*

Molecular Liquids, vol. 229, pp. 293–299, 2017. [Online]. Available: http://dx.doi.org/10.1016/j.molliq.2016.12.090

[64] E. R. Nestmann, G. R. Douglas, T. I. Matula, C. E. Grant, and D. J. Kowbel, "Mutagenic Activity of Rhodamine Dyes and Their Impurities as Detected by Mutation Induction in Salmonella and DMA Damage in Chinese Hamster Ovary Cells," *Cancer Research*, vol. 39, no. November, pp. 4412 – 4417, 1979.

[65] S. Lin, W.-l.-j. Hasi, X. Lin, S.-q.-g.-w. Han, X.-t. Lou, F. Yang, D.-y. Lin, and Z.-w. Lu, "Analytical Methods Rapid and sensitive SERS method for determination substrates," *Analytical Methods*, vol. 7, no. June, pp. 5289–5294, 2015. [Online]. Available: http://dx.doi.org/10.1039/C5AY00028A

[66] Oliver Merka, Viktor Yarovyi, Detlef W. Bahnemann and M. Wark, "pH-Control of the Photocatalytic Degradation Mechanism of Rhodamine B over Pb3Nb4O13," *The Journal of Physical Chemistry C*, vol. 115, pp. 8014–8023, 2011.

[67] Jiandong Zhuang, Wenxin Dai, Qinfen Tian, Zhaohui Li, Liyan Xie, Jixin Wang and P. Liu, "Photocatalytic Degradation of RhB over TiO2 Bilayer Films: Effect of Defects and Their Location," *Langmuir*, vol. 26, no. 12, pp. 9686–9694, 2010.

[68] J. He, J. Zhao, T. Shen, H. Hidaka, and N. Serpone, "Photosensitization of Colloidal Titania Particles by Electron Injection from an Excited Organic DyeâĹŠAntennae Function," *The Journal of Physical Chemistry B*, vol. 101, no. 44, pp. 9027–9034, 2002.

[69] D. Gumy, A. G. Rincon, R. Hajdu, and C. Pulgarin, "Solar photocatalysis for detoxification and disinfection of water: Different types of suspended and fixed TiO2 catalysts study," *Solar Energy*, vol. 80, no. 10, pp. 1376–1381, 2006.

[70] Y. Wang, Y. Z. Zheng, S. Lu, X. Tao, Y. Che, and J. F. Chen, "Visible-light-responsive TiO2-coated ZnO:I nanorod array films with enhanced photoelectrochemical and photocatalytic performance," *ACS Applied Materials and Interfaces*, vol. 7, no. 11, pp. 6093–6101, 2015.

[71] S. SUBRAMANIAN, J. S. NOH and J. A. SCHWARZ, "Determination of the point of zero charge of composite oxides," *Journal of Catalysis*, vol. 114, pp. 433–439, 1988.

[72] X. Shen, *Molecularly Imprinted Photocatalysts*. Elsevier Inc., 2015. [Online]. Available: http://dx.doi.org/10.1016/B978-0-12-801301-4.00010-4

[73] S. Mohamed El, S. Fawzy, and S. Mohamed Ha, "Preparation of Modified Nanoparticles of Zinc Oxide for Removal of Organic and Inorganic Pollutant," *Trends in Applied Sciences Research*, vol. 12, no. 1, pp. 1–9, 2017.

[74] M. N. Zafar, Q. Dar, F. Nawaz, M. N. Zafar, M. Iqbal, and M. F. Nazar, "Effective adsorptive removal of azo dyes over spherical ZnO nanoparticles," *Journal of Materials Research and Technology*, no. x x, pp. 1–13, 2018. [Online]. Available: https://doi.org/10.1016/j.jmrt.2018.06.002

[75] L. V. Trandafilović, D. J. Jovanović, X. Zhang, S. Ptasińska, and M. D. Dramićanin, "Enhanced photocatalytic degradation of methylene blue and methyl orange by ZnO:Eu nanoparticles," *Applied Catalysis B: Environmental*, vol. 203, pp. 740–752, 2017.

[76] T. Mahmood, M. T. Saddique, A. Naeem, P. Westerhoff, S. Mustafa, and A. Alum, "Comparison of different methods for the point of zero charge determination of NiO," *Industrial and Engineering Chemistry Research*, vol. 50, no. 17, pp. 10 017–10 023, 2011.

[77] H. Chen, S. Wageh, A. A. Al-Ghamdi, H. Wang, J. Yu, and C. Jiang, "Hierarchical C/NiO-ZnO nanocomposite fibers with enhanced adsorption capacity for Congo red," *Journal of Colloid and Interface Science*, vol. 537, pp. 736–745, 2019. [Online]. Available: https://doi.org/10.1016/j.jcis.2018.11.045

[78] T. M. Elmorsi, M. H. Elsayed, and M. F. Bakr, "Na doped ZnO Nanoparticles Assisted Photocatalytic

Degradation of Congo Red Dye using Solar Light," *American Journal of Chemistry*, vol. 7, no. 2, pp. 48–57, 2017.

[79] M. Anpo, M. Takeuchi, Y. Horiuchi, M. Matsuoka, J. Zhang, J. Schneider, and D. W. Bahnemann, "Understanding TiO 2 Photocatalysis: Mechanisms and Materials," *Chemical Reviews*, vol. 114, no. 19, pp. 9919–9986, 2014.

[80] A. Shafaei, M. Nikazar, and M. Arami, "Photocatalytic degradation of terephthalic acid using titania and zinc oxide photocatalysts: Comparative study," *Desalination*, vol. 252, no. 1-3, pp. 8–16, 2010. [Online]. Available: http://dx.doi.org/10.1016/j.desal.2009.11.008

[81] N. Daneshvar, M. H. Rasoulifard, A. R. Khataee, and F. Hosseinzadeh, "Removal of C.I. Acid Orange 7 from aqueous solution by UV irradiation in the presence of ZnO nanopowder," *Journal of Hazardous Materials*, vol. 143, no. 1-2, pp. 95–101, 2007.

[82] P. Zhang, D. Wu, J. Xu, Y. Cao, Y. Cao, W. Li, Y. Yu, and J. Yuan, "Investigation on a novel ZnO/TiO2âĂŞB photocatalyst with enhanced visible photocatalytic activity," *Physica E: Low-dimensional Systems and Nanostructures*, vol. 58, pp. 118–123, 2013.

[83] T. Y. Ma, Z. Y. Yuan, and Q. J. L. Cao, "Hydrangea-like meso-macroporous ZnO-CeO2 binary oxide materials: synthesis, photocatalysis and CO oxidation," *European Journal of Inorganic Chemistry*, no. 5, pp. 716–724, 2010.

[84] X. Hou, "Nonaqueous fabrication of ZnO/Au nanohybrids with enhanced photocatalytic activity," *Materials Letters*, vol. 137, pp. 319–322, 2014. [Online]. Available: http://dx.doi.org/10.1016/j.matlet.2014.09.024

[85] R. Comparelli, E. Fanizza, M. L. Curri, P. D. Cozzoli, G. Mascolo, and A. Agostiano, "UV-induced photocatalytic degradation of azo dyes by organic-capped ZnO nanocrystals immobilized onto substrates," *Applied Catalysis B: Environmental*, vol. 60, no. 1-2, pp. 1–11, 2005.

[86] T. Pauporté and J. Rathouský, "Electrodeposited mesoporous ZnO thin films as efficient photocatalysts for the degradation of dye pollutants," *Journal of Physical Chemistry C*, vol. 111, pp. 7639–7644, 2007.

[87] A. I. H. Yang and Peidong, "Semiconductor Nanowires for Energy Conversion Allon," *Chemical Reviews*, vol. 110, pp. 527 – 546, 2010.

[88] R. C. Pawar and C. S. Lee, *Heterogeneous Nanocomposite-Photocatalysis for Water Purification*, 2015. [Online]. Available: https://linkinghub.elsevier.com/retrieve/pii/C20140026500

[89] W.-N. Su, B.-J. Hwang, A. G. Tamirat, J. Rick, and A. A. Dubale, "Using hematite for photoelectrochemical water splitting: a review of current progress and challenges," *Nanoscale Horizons*, vol. 1, no. 4, pp. 243–267, 2016.

[90] E. G. Yang and Peidong, "Light Trapping in Silicon Nanowire Solar Cells," *Nano Letters*, vol. 10, pp. 1082 – 1087, 2010.

[91] G. Liu, X. F. Zhang, H. Peng, R. A. Huggins, Y. Cui, K. McIlwrath, and C. K. Chan, "High-performance lithium battery anodes using silicon nanowires," *Nature Nanotechnology*, vol. 3, no. 1, pp. 31–35, 2007.

[92] N. P. Dasgupta and P. Yang, "Semiconductor nanowires for photovoltaic and photoelectrochemical energy conversion," *Frontiers of Physics*, vol. 9, no. 3, pp. 289–302, 2014.

[93] S. Liu, C. Han, Z.-R. Tang, and Y.-J. Xu, "Heterostructured semiconductor nanowire arrays for artificial photosynthesis," *Materials Horizons*, vol. 3, no. 4, pp. 259–364, 2016.

[94] R. K. Joshi and J. J. Schneider, "Assembly of one dimensional inorganic nanostructures into functional 2D and 3D architectures. Synthesis, arrangement and functionality," *Chemical Society Reviews*, vol. 41, no. 15, pp. 5285–5312, 2012.

[95] J. J. Wu and C. H. Tseng, "Photocatalytic properties of nc-Au/ZnO nanorod composites," *Applied Catalysis B: Environmental*, vol. 66, no. 1-2, pp. 51–57, 2006.

[96] D. Adler and B. B. Schwartz, *Disordered Semiconductors*, 1987.

[97] S. Lany, "Semiconducting transition metal oxides," *Journal of Physics Condensed Matter*, vol. 27, no. 28, pp. 283 203, 1–18, 2015.

[98] X. Gu, C. Li, S. Yuan, M. Ma, Y. Qiang, and J. Zhu, "ZnO based heterojunctions and their application in environmental photocatalysis," *Nanotechnology*, vol. 27, no. 40, pp. 1–21, 2016. [Online]. Available: http://dx.doi.org/10.1088/0957-4484/27/40/402001

[99] S. G. Kumar and K. S. Rao, "Zinc oxide based photocatalysis: Tailoring surface-bulk structure and related interfacial charge carrier dynamics for better environmental applications," *RSC Advances*, vol. 5, pp. 3306–3351, 2015.

[100] H. Wang, Q. Ma, H. Niu, X. Mao, L. Wan, J. Xu, and S. Miao, "Hydrothermal Growth of Aligned ZnO Nanorods along the Seeds Prepared by Magnetron Sputtering and its Applications in Quantum Dots," *Journal of Nanomaterials & Molecular Nanotechnology*, vol. 2, no. 1, pp. 1–5, 2013.

[101] S. Xu and Z. L. Wang, "One-dimensional ZnO nanostructures: Solution growth and functional properties," *Nano Research*, vol. 4, no. 11, pp. 1013–1098, 2011.

[102] N. Arai, T. D. Dao, T. Nabatame, C. V. Hoang, T. Nagao, G. Han, Y. Wada, and M. Aono, "Plasmon-mediated photocatalytic activity of wet-chemically prepared ZnO nanowire arrays," *Physical Chemistry Chemical Physics*, vol. 17, no. 11, pp. 7395–7403, 2015. [Online]. Available: http://dx.doi.org/10.1039/C4CP05843G

[103] C.-C. W. Yuan-Chang Liang, Ya-Ru Lo, N.-C. Xu, and Institute, "Shell Layer Thickness-Dependent Photocatalytic Activity of Sputtering Synthesized Hexagonally Structured ZnO-ZnS Composite Nanorods," *Materials*, vol. 11, no. 87, pp. 1 – 11, 2018.

[104] P. Colson, A. Schrijnemakers, B. Vertruyen, C. Henrist, and R. Cloots, "Nanosphere lithography and hydrothermal growth: How to increase the surface area and control reversible wetting properties of ZnO nanowire arrays?" *Journal of Materials Chemistry*, vol. 22, no. 33, pp. 17 086–17 093, 2012.

[105] C. J. Chang, M. H. Hsu, Y. C. Weng, C. Y. Tsay, and C. K. Lin, "Hierarchical ZnO nanorod-array films with enhanced photocatalytic performance," *Thin Solid Films*, vol. 528, pp. 167–174, 2013. [Online]. Available: http://dx.doi.org/10.1016/j.tsf.2012.09.083

[106] H. K. D. Cappus, C. Xu, D. Ehrlich, B. Dillmann, C. A. Ventnce Jr., K. Al Shamery and H.-J. Freund, "Hydroxyl groups on oxide surfaces : NiO (100), NiO (lll)," *Chemical Physics*, vol. 177, pp. 533–546, 1993.

[107] C. Zhang, H. Zhao, H. Yang, B. Liu, S. Liu, A. Wei, and L. Ning, "Superior photocatalytic activities of NiO octahedrons with loaded AgCl particles and charge separation between polar NiO {111} surfaces," *Applied Catalysis B: Environmental*, vol. 172-173, pp. 165–173, 2015. [Online]. Available: http://dx.doi.org/10.1016/j.apcatb.2015.02.007

[108] N. Kitakatsu, V. Maurice, C. Hinnen, and P. Marcus, "Surface hydroxylation and local structure of NiO thin films formed on Ni(111)," *Surface Science*, vol. 407, no. 1-3, pp. 36–58, 1998.

[109] F. Zhang, Y. Wang, W. Zhang, G. Li, and L. Wei, "Facet-dependent photocatalytic performance of NiO oriented thin films prepared by pulsed laser deposition," *Physica B: Condensed Matter*, vol. 457, pp. 194–197, 2014. [Online]. Available: http://dx.doi.org/10.1016/j.physb.2014.10.014

[110] K. M. Domen and Kazunari, "Photocatalytic Water Splitting: Recent Progress and Future Challenges," *The Journal of Physical Chemistry Letters Letters*, vol. 1, pp. 2655 – 2661, 2010.

[111] A. Kudo and Y. Miseki, "Heterogeneous photocatalyst materials for water splitting," *Chemical Society Reviews*, vol. 38, no. 1, pp. 253–278, 2009.

[112] K. Pirkanniemi and M. Sillanpää, "Heterogeneous water phase catalysis as an environmental application: A review," *Chemosphere*, vol. 48, no. 10, pp. 1047–1060, 2002.

[113] B. Sun, G. Zhou, T. Gao, H. Zhang, and H. Yu, "NiO nanosheet/TiO2nanorod-constructed p-n heterostructures for improved photocatalytic activity," *Applied Surface Science*, vol. 364, pp. 322–331, 2016. [Online]. Available: http://dx.doi.org/10.1016/j.apsusc.2015.12.158

[114] Y. Liu, G. Li, R. Mi, C. Deng, and P. Gao, "An environment-benign method for the synthesis of p-NiO/n-ZnO heterostructure with excellent performance for gas sensing and photocatalysis," *Sensors and Actuators, B: Chemical*, vol. 191, pp. 537–544, 2014.

[115] M. T. Uddin, Y. Nicolas, C. Olivier, L. Servant, T. Toupance, S. Li, A. Klein, and W. Jaegermann, "Improved photocatalytic activity in RuO2-ZnO nanoparticulate heterostructures due to inhomogeneous space charge effects," *Physical Chemistry Chemical Physics*, vol. 17, no. 7, pp. 5090–5102, 2015. [Online]. Available: http://dx.doi.org/10.1039/C4CP04780J

[116] D. Amaranatha Reddy, R. Ma, and T. K. Kim, "Efficient photocatalytic degradation of methylene blue by heterostructured ZnO-RGO/RuO2 nanocomposite under the simulated sunlight irradiation," *Ceramics International*, vol. 41, no. 5, pp. 6999–7009, 2015. [Online]. Available: http://dx.doi.org/10.1016/j.ceramint.2015.01.155

[117] S. Bang, S. Lee, T. Park, Y. Ko, S. Shin, S. Y. Yim, H. Seo, and H. Jeon, "Dual optical functionality of local surface plasmon resonance for RuO2nanoparticle-ZnO nanorod hybrids grown by atomic layer deposition," *Journal of Materials Chemistry*, vol. 22, no. 28, pp. 14 141–14 148, 2012.

[118] A. Alshammari, A. Bagabas, and M. Assulami, "Photodegradation of rhodamine B over semiconductor supported gold nanoparticles: The effect of semiconductor support identity," *Arabian Journal of Chemistry*, 2014. [Online]. Available: http://dx.doi.org/10.1016/j.arabjc.2014.11.013

[119] Y. Su, X. Zhao, Y. Bi, and X. Han, "ZnO/AgâĂŞAg2O microstructures for high-performance photocatalytic degradation of organic pollutants," *Clean Technologies and Environmental Policy*, vol. 21, no. 2, pp. 367–378, 2018. [Online]. Available: https://doi.org/10.1007/s10098-018-1641-0

[120] K. J. Kim, P. B. Kreider, C. H. Chang, C. M. Park, and H. G. Ahn, "Visible-light-sensitive nanoscale Au-ZnO photocatalysts," *Journal of Nanoparticle Research*, vol. 15, no. 5, 2013.

[121] T. Sakata, K. Hashimoto and T. Kawai, "Catalytic Properties of Ruthenium Oxide on n-Type Semiconductors under Illumination," *Journal of Physical Chemistry*, vol. 88, no. 22, pp. 5214 – 5221, 1984.

[122] D. J. Morgan, "Resolving ruthenium: XPS studies of common ruthernium materials," *Surface and Interface Analysis*, vol. 47, pp. 1072–1079, 2015.

[123] Y. Lin, S. Zhou, D. Wang, G. Yuan, R. Liu, and S. W. Sheehan, "Semiconductor nanostructure-based photoelectrochemical water splitting: A brief review," *Chemical Physics Letters*, vol. 507, no. 4-6, pp. 209–215, 2011. [Online]. Available: http://dx.doi.org/10.1016/j.cplett.2011.03.074

[124] J. Joy, J. Mathew, and S. C. George, "Nanomaterials for photoelectrochemical water splitting âĂŞ review," *International Journal of Hydrogen Energy*, vol. 43, no. 10, pp. 4804–4817, 2018. [Online]. Available: https://doi.org/10.1016/j.ijhydene.2018.01.099

[125] A. K. Arora, V. S. Jaswal, K. Singh, and R. Singh, "Applications of Metal/Mixed Metal Oxides as Photo catalyst: A Review." *Orient. J. Chem*, vol. 32, pp. 2035–2042, 2016.

[126] S. Dong, J. Feng, M. Fan, Y. Pi, L. Hu, X. Han, M. Liu, J. Sun, and J. Sun, "Recent developments in heterogeneous photocatalytic water treatment using visible light-responsive

photocatalysts: A review," *RSC Advances*, vol. 5, no. 19, pp. 14 610–14 630, 2015. [Online]. Available: http://dx.doi.org/10.1039/C4RA13734E

[127] T. Gao, Z. Chen, Q. Huang, F. Niu, X. Huang, L. Qin, and Y. Huang, "A review: Preparation of bismuth ferrite nanoparticles and its applications in visible-light induced photocatalyses," *Reviews on Advanced Materials Science*, vol. 40, no. 2, pp. 97–109, 2015.

[128] M. Mishra and D.-M. Chun, "α-Fe 2 O 3 as a photocatalytic material: A review," *Applied Catalysis A: General*, vol. 498, pp. 126–141, 2015. [Online]. Available: http://dx.doi.org/10.1016/j.apcata.2015.03.023

[129] Sagadevan Suresh, "Semiconductor Nanomaterials, Methods and Applications: A Review," *Nanoscience and Nanotechnology*, vol. 3, no. 3, pp. 62–74, 2013. [Online]. Available: http://article.sapub.org/10.5923.j.nn.20130303.06.html

[130] S. Kundu and A. Patra, "Nanoscale strategies for light harvesting," *Chemical Reviews*, vol. 117, no. 2, pp. 712–757, 2017.

[131] N. Savage and M. S. Diallo, "Nanomaterials and water purification: Opportunities and challenges," *Journal of Nanoparticle Research*, vol. 7, no. 4-5, pp. 331–342, 2005.

[132] J. L. Huanli Wang, Lisha Zhang, Zhigang Chen, Junqing Hu, Shijie Li, Zhaohui Wang and X. Wang, "Semiconductor heterojunction photocatalysts: design, construction, and photocatalytic performances," *Chemical Society Reviews*, vol. 43, pp. 5234 – 5244, 2014.

[133] S. Hernández, D. Hidalgo, A. Sacco, A. Chiodoni, A. Lamberti, V. Cauda, E. Tresso, and G. Saracco, "Comparison of photocatalytic and transport properties of TiO 2 and ZnO nanostructures for solar-driven water splitting," *Phys. Chem. Chem. Phys.*, vol. 17, pp. 7775–7786, 2015.

[134] S. Choudhary, S. Upadhyay, P. Kumar, N. Singh, V. R. Satsangi, R. Shrivastav, and S. Dass, "Nanostructured bilayered thin films in photoelectrochemical water splitting - A review," *International Journal of Hydrogen Energy*, vol. 37, pp. 18 713–18 730, 2012.

[135] C. Klingshirn, "ZnO: From basics towards applications," *Physica Status Solidi (B) Basic Research*, vol. 244, no. 9, pp. 3027–3073, 2007.

[136] M. A. Mohd Adnan, N. M. Julkapli, and S. B. Abd Hamid, "Review on ZnO hybrid photocatalyst: Impact on photocatalytic activities of water pollutant degradation," *Reviews in Inorganic Chemistry*, vol. 36, no. 2, pp. 77–104, 2016.

[137] K. Qi, B. Cheng, J. Yu, and W. Ho, "Review on the improvement of the photocatalytic and antibacterial activities of ZnO," *Journal of Alloys and Compounds*, vol. 727, pp. 792–820, 2017. [Online]. Available: https://doi.org/10.1016/j.jallcom.2017.08.142

[138] S. Shen, C. Kronawitter, and G. Kiriakidis, "An overview of photocatalytic materials," *Journal of Materiomics*, vol. 3, pp. 1–2, 2017.

[139] S. Bai, W. Yin, L. Wang, Z. Li, and Y. Xiong, "Surface and interface design in cocatalysts for photocatalytic water splitting and CO 2 reduction," *RSC Adv.*, vol. 6, pp. 57 446–57 463, 2016.

[140] A. W. Bott, "Electrochemistry of Semiconductors," *Current Sepaartions*, vol. 3, pp. 87–91, 1998.

[141] M. Quintana, T. Edvinsson, A. Hagfeldt, and G. Boschloo, "Comparison of dye-sensitized ZnO and TiO2 solar cells: Studies of charge transport and carrier lifetime," *Journal of Physical Chemistry C*, vol. 111, no. 2, pp. 1035–1041, 2007.

[142] R. Ahmad, N. Tripathy, M. S. Ahn, K. S. Bhat, T. Mahmoudi, Y. Wang, J. Y. Yoo, D. W. Kwon, H. Y. Yang, and Y. B. Hahn, "Highly Efficient Non-Enzymatic Glucose Sensor Based on CuO Modified Vertically-Grown ZnO Nanorods on Electrode," *Scientific Reports*, vol. 7, pp. 1–10, 2017.

[143] S. Ma, R. Li, C. Lv, W. Xu, and X. Gou, "Facile synthesis of ZnO nanorod arrays and hierarchical

nanostructures for photocatalysis and gas sensor applications," *Journal of Hazardous Materials*, vol. 192, pp. 730–740, 2011.

[144] D. Ju, H. Xu, Z. Qiu, J. Guo, J. Zhang, and B. Cao, "Highly sensitive and selective triethylamine-sensing properties of nanosheets directly grown on ceramic tube by forming NiO/ZnO PN heterojunction," *Sensors and Actuators, B: Chemical*, vol. 200, pp. 288–296, 2014.

[145] H. Tian, H. Fan, G. Dong, L. Ma, and J. Ma, "NiO/ZnO p-n heterostructures and their gas sensing properties for reduced operating temperature," *RSC Advances*, vol. 6, pp. 109 091–109 098, 2016.

[146] Y. G. Habba, M. Capochichi-Gnambodoe, L. Serairi, and Y. Leprince-Wang, "Enhanced photocatalytic activity of ZnO nanostructure for water purification," *Physica Status Solidi (B) Basic Research*, vol. 253, no. 8, pp. 1480–1484, 2016.

[147] J. Xu, Y. Cui, Y. Han, M. Hao, and X. Zhang, "ZnOâĂŞgraphene composites with high photocatalytic activities under visible light," *RSC Adv.*, vol. 6, pp. 96 778–96 784, 2016.

[148] M. T. Qamar, M. Aslam, I. M. Ismail, N. Salah, and A. Hameed, "Synthesis, characterization, and sunlight mediated photocatalytic activity of CuO coated ZnO for the removal of nitrophenols," *ACS Applied Materials and Interfaces*, vol. 7, no. 8757-8769, 2015.

[149] U. Diebold, S.-C. Li, and M. Schmid, "Oxide Surface Science," *Annual Review of Physical Chemistry*, vol. 61, no. 1, pp. 129–148, 2010. [Online]. Available: http://www.annualreviews.org/doi/10.1146/annurev.physchem.012809.103254

[150] L. J. Brillson and Y. Lu, "ZnO Schottky barriers and Ohmic contacts," *Journal of Applied Physics*, vol. 109, pp. 121 301–121 333, 2011.

[151] J. Rodrigues, T. Holz, R. F. Allah, D. Gonzalez, T. Ben, M. R. Correia, T. Monteiro, and F. M. Costa, "Effect of N<inf>2</inf> and H<inf>2</inf> plasma treatments on band edge emission of ZnO microrods," *Scientific Reports*, vol. 5, pp. 1–9, 2015. [Online]. Available: http://dx.doi.org/10.1038/srep10783

[152] C. Wöll, "The chemistry and physics of zinc oxide surfaces," *Progress in Surface Science*, vol. 82, pp. 55–120, 2007.

[153] Y. Tu, S. Chen, X. Li, J. Gorbaciova, W. P. Gillin, S. Krause, and J. Briscoe, "Control of oxygen vacancies in ZnO nanorods by annealing and their influence on ZnO/PEDOT:PSS diode behaviour," *Journal of Materials Chemistry C*, vol. 6, no. 7, pp. 1815–1821, 2018.

[154] T. Cossuet, F. Donatini, A. M. Lord, E. Appert, J. Pernot, and V. Consonni, "Polarity-Dependent High Electrical Conductivity of ZnO Nanorods and Its Relation to Hydrogen," *Journal of Physical Chemistry C*, vol. 122, no. 39, pp. 22 767–22 775, 2018.

[155] D. B.-B. Charlotte Drouilly, Jean-Marc Krafft, FreÌĄdeÌĄric Averseng, Sandra Casale, CeÌĄline Chizallet, Vincent Lecocq, HerveÌĄ Vezin, HeÌĄleÌĂne Lauron-Pernot, and G. Costentin, "ZnO oxygen vacancies formation and filling followed by in situ PL and in situ EPR.pdf," pp. 21 297–21 307, 2012.

[156] A. R. Gheisi, C. Neygandhi, A. K. Sternig, E. Carrasco, H. Marbach, D. Thomele, and O. Diwald, "O 2 adsorption dependent photoluminescence emission from metal oxide nanoparticles," *Phys. Chem. Chem. Phys.*, vol. 16, pp. 23 922–23 929, 2014.

[157] C. Chevalier-César, M. Capochichi-Gnambodoe, F. Lin, D. Yu, and Y. Leprince-Wang, "Effect of growth time and annealing on the structural defect concentration of hydrothermally grown ZnO nanowires," *AIMS Materials Science*, vol. 3, no. 2, pp. 562–572, 2016. [Online]. Available: http://www.aimspress.com/article/10.3934/matersci.2016.2.562

[158] B. Ha, H. Ham, and C. J. Lee, "Photoluminescence of ZnO nanowires dependent on O2 and Ar annealing," *Journal of Physics and Chemistry of Solids*, vol. 69, pp. 2453–2456, 2008.

[159] Y. G. Wang, S. P. Lau, X. H. Zhang, H. H. Hng, H. W. Lee, S. F. Yu, and B. K. Tay, "Enhancement of near-band-edge photoluminescence from ZnO films by face-to-face annealing," *Journal of Crystal Growth*, vol. 259, no. 4, pp. 335–342, 2003.

[160] J. P. Richters, T. Voss, D. S. Kim, R. Scholz, and M. Zacharias, "Enhanced surface-excitonic emission in ZnO/Al2O3 core-shell nanowires," *Nanotechnology*, vol. 19, no. 305202, pp. 1–4, 2008.

[161] M. E. Manríquez, L. E. Noreña, J. A. Wang, L. Chen, J. Salmones, J. González-garcía, C. Reza, F. Tzompantzi, J. G. H. Cortez, L. Ye, and H. Xie, "One-Pot Synthesis of Ru-Doped ZnO Oxides for Photodegradation of 4-Chlorophenol," *International Journal of Photoenergy*, pp. 7 605 306–1 – 7 605 306–12, 2018.

[162] B. Sarma, S. K. Deb, and B. K. Sarma, "Photoluminescence and photocatalytic activities of Ag/ZnO metal-semiconductor heterostructure," *Journal of Physics: Conference Series*, vol. 765, no. 1, 2016.

[163] P. Pradhan, J. C. Alonso, and M. Bizarro, "Photocatalytic performance of ZnO: Al films under different light sources," *International Journal of Photoenergy*, vol. 2012, 2012.

[164] X. Fu, J. Wang, X. Wang, W. Han, Z. Li, and P. Liu, "Relationship between Oxygen Defects and the Photocatalytic Property of ZnO Nanocrystals in Nafion Membranes," *Langmuir*, vol. 25, no. 2, pp. 1218–1223, 2008.

[165] G. R. Li, T. Hu, G. L. Pan, T. Y. Yan, X. P. Gao, and H. Y. Zhu, "Morphology-function relationship of ZnO: Polar planes, oxygen vacancies, and activity," *Journal of Physical Chemistry C*, vol. 112, no. 31, pp. 11 859–11 864, 2008.

[166] F. Kayaci, S. Vempati, C. Ozgit-akgun, and N. Biyikli, "Environmental Enhanced photocatalytic activity of homoassembled ZnO nanostructures on electrospun polymeric nanofibers : A combination of atomic layer deposition and hydrothermal growth," *Applied Catalysis B: Environmental*, vol. 156-157, pp. 173–183, 2014. [Online]. Available: http://dx.doi.org/10.1016/j.apcatb.2014.03.004

[167] J. H. Kim, Y. J. Jang, J. H. Kim, J.-W. Jang, S. H. Choi, and J. S. Lee, "Defective ZnFe ₂ O ₄ nanorods with oxygen vacancy for photoelectrochemical water splitting," *Nanoscale*, vol. 7, no. 45, pp. 19 144–19 151, 2015. [Online]. Available: http://xlink.rsc.org/?DOI=C5NR05812K

[168] Y. Yang, W. Que, X. Zhang, Y. Xing, X. Yin, and Y. Du, "Facile synthesis of ZnO/CuInS2nanorod arrays for photocatalytic pollutants degradation," *Journal of Hazardous Materials*, vol. 317, pp. 430–439, 2016. [Online]. Available: http://dx.doi.org/10.1016/j.jhazmat.2016.05.080

[169] A. Di Mauro, M. E. Fragalà, V. Privitera, and G. Impellizzeri, "ZnO for application in photocatalysis: From thin films to nanostructures," *Materials Science in Semiconductor Processing*, vol. 69, pp. 44–51, 2017.

[170] N. Kaneva, I. Stambolova, V. Blaskov, Y. Dimitriev, S. Vassilev, and C. Dushkin, "Photocatalytic activity of nanostructured ZnO films prepared by two different methods for the photoinitiated decolorization of malachite green," *Journal of Alloys and Compounds*, vol. 500, pp. 252–258, 2010.

[171] E. Rokhsat and O. Akhavan, "Improving the photocatalytic activity of graphene oxide/ZnO nanorod films by UV irradiation," *Applied Surface Science*, vol. 371, pp. 590–595, 2016. [Online]. Available: http://dx.doi.org/10.1016/j.apsusc.2016.02.222

[172] Z. Zhang, L. Sun, D. Zhao, B. Li, C. Shan, Z. Song, and D. Shen, "Gold nanoparticles modified ZnO nanorods with improved photocatalytic activity," *Journal of Colloid and Interface Science*, vol. 363, no. 1, pp. 175–181, 2011. [Online]. Available: http://dx.doi.org/10.1016/j.jcis.2011.07.005

[173] S. Xiao, L. Zhao, X. Leng, X. Lang, and J. Lian, "Synthesis of amorphous TiO2 modified ZnO nanorod film with enhanced photocatalytic properties," *Applied Surface Science*, vol. 299, pp. 97–104, 2014. [Online]. Available: http://dx.doi.org/10.1016/j.apsusc.2014.01.192

[174] J. Li, F. Zhao, L. Zhang, M. Zhang, H. Jiang, S. Li, and J. Li, "Electrospun hollow ZnO/NiO heterostructures with enhanced photocatalytic activity," *RSC Advances*, vol. 5, pp. 67 610–67 616, 2015.

[175] A. Echresh, C. O. Chey, M. Zargar Shoushtari, V. Khranovskyy, O. Nur, and M. Willander, "UV photodetector based on p-NiO thin film/n-ZnO nanorods heterojunction prepared by a simple process," *Journal of Alloys and Compounds*, vol. 632, pp. 165–171, 2015.

[176] G. Vijayaprasath, P. Sakthivel, R. Murugan, T. Mahalingam, and G. Ravi, "Deposition and characterization of ZnO/NiO thin films," in *AIP Conference Proceedings*, 2016, pp. 080 033–1 – 080 033–3.

[177] R. Deng, B. Yao, Y. F. Li, Y. M. Zhao, B. H. Li, C. X. Shan, Z. Z. Zhang, D. X. Zhao, J. Y. Zhang, D. Z. Shen, and X. W. Fan, "X-ray photoelectron spectroscopy measurement of n-ZnO/p-NiO heterostructure valence-band offset," *Applied Physics Letters*, vol. 94, no. 2, pp. 022 108–1 – 022 108–3, 2009.

[178] F. Tian and Y. Liu, "Synthesis of p-type NiO/n-type ZnO heterostructure and its enhanced photocatalytic activity," *Scripta Materialia*, vol. 69, no. 5, pp. 417–419, 2013. [Online]. Available: http://dx.doi.org/10.1016/j.scriptamat.2013.05.040

[179] Editorial, "Surface Chemistry of Oxides," *Chemical Reviews*, pp. 3859–3862, 2013.

[180] J. Chakhalian, A. J. Millis, and J. Rondinelli, "Whither the oxide interface," *Nature Materials*, vol. 11, no. 2, pp. 92–94, 2012. [Online]. Available: http://www.nature.com/doifinder/10.1038/nmat3225

[181] M. A. Henderson, "The Interaction of Water with Solid Surfaces: Fundamental Aspects Revisited," *ChemInform*, vol. 46, pp. 1 – 308, 2002.

[182] H. Bluhm, "Photoelectron spectroscopy of surfaces under humid conditions," *Journal of Electron Spectroscopy and Related Phenomena*, vol. 177, no. 2-3, pp. 71–84, 2010. [Online]. Available: http://dx.doi.org/10.1016/j.elspec.2009.08.006

[183] J. Guo, K. Bian, Z. Lin, and Y. Jiang, "Perspective: Structure and dynamics of water at surfaces probed by scanning tunneling microscopy and spectroscopy," *Journal of Chemical Physics*, vol. 145, no. 16, 2016.

[184] P. a. Thiel, T. E. Madey, and A. P. Sloan, "THE INTERACT ION OF WATER WITH SOLID SURFACES : FUNDAMENTAL ASPECTS," *Surface Science Reports*, vol. 7, no. 1987, pp. 211–385, 1987. [Online]. Available: http://www.sciencedirect.com/science/article/pii/016757298790001X

[185] A. Michaelides, "Density functional theory simulations of water-metal interfaces: Waltzing waters, a novel 2D ice phase, and more," *Applied Physics A: Materials Science and Processing*, vol. 85, no. 4, pp. 415–425, 2006.

[186] A. Hodgson and S. Haq, "Water adsorption and the wetting of metal surfaces," *Surface Science Reports*, vol. 64, no. 9, pp. 381–451, 2009. [Online]. Available: http://dx.doi.org/10.1016/j.surfrep.2009.07.001

[187] J. W. Olle BjoĬĹrneholm, Martin H. Hansen, Andrew Hodgson, Li-Min Liu, David T. Limmer, Angelos Michaelides, Philipp Pedevilla, Jan Rossmeisl, Huaze Shen, Gabriele Tocci, Eric Tyrode Marie-Madeleine Walz and H. Bluhm, "Water at Interfaces," *Chemical Reviews*, vol. 116, pp. 7698 – 7726, 2016.

[188] H. Hu, H.-f. Ji, and Y. Sun, "The effect of oxygen vacancies on water wettability of a ZnO surface," *Phys. Chem. Chem. Phys.*, vol. 15, no. Md, pp. 16 557–16 565, 2013.

[189] J. Rentao Mu, Zhi-jian Zhao, Zdenek DohnaÂť'lek and Gong, "Structural motifs of water on metal oxide surfaces," *Chemical Society Reviews*, vol. 46, no. 7, pp. 1785–1806, 2017.

[190] R. Heinhold, G. T. Williams, S. P. Cooil, D. A. Evans and M. W. Allen, "Influence of polarity and hydroxyl termination on the band bending at ZnO surfaces_Vbb and elec acc.pdf," *Physical Review B*, vol. 88, pp. 235 315–1 – 235 315–9, 2013.

[191] A. Felmy, J. M. Zachara, M. I. McCarthy, V. E. Henrich, C. Eggleston, G. E. Brown, K. H. Nealson, W. H. Casey, D. A. Sverjensky, D. W. Goodman, M. F. Toney, G. Maciel, D. L. Clark, and M. Grätzel, "Metal

Oxide Surfaces and Their Interactions with Aqueous Solutions and Microbial Organisms," pp. 77–174, 2002.

[192] M. Fingerle, S. Tengeler, W. Calvet, T. Mayer, and W. Jaegermann, "Water Interaction with Sputter-Deposited Nickel Oxide on n-Si Photoanode : Cryo Photoelectron Spectroscopy on Adsorbed Water in the Frozen Electrolyte Approach," *Journal of The Electrochemical Society*, vol. 165, no. 4, pp. 3148–3153, 2018.

[193] J. T. Newberg, C. Goodwin, C. Arble, Y. Khalifa, J. A. Boscoboinik, and S. Rani, "ZnO(1010) Surface Hydroxylation under Ambient Water Vapor," pp. 472–478, 2018.

[194] T. Cossuet, E. Appert, J. L. Thomassin, and V. Consonni, "Polarity-Dependent Growth Rates of Selective Area Grown ZnO Nanorods by Chemical Bath Deposition," *Langmuir*, vol. 33, no. 25, pp. 6269–6279, 2017.

[195] A. Pimentel, A. Samouco, D. Nunes, A. Araújo, R. Martins, and E. Fortunato, "Ultra-fast microwave synthesis of ZnO nanorods on cellulose substrates for UV sensor applications," *Materials*, vol. 10, no. 11, pp. 4–10, 2017.

[196] Y. Chen, H. Zhao, B. Liu, and H. Yang, "Charge separation between wurtzite ZnO polar {001} surfaces and their enhanced photocatalytic activity," *Applied Catalysis B: Environmental*, vol. 163, pp. 189–197, 2015. [Online]. Available: http://dx.doi.org/10.1016/j.apcatb.2014.07.044

[197] Ren-De Sun, Akira Nakajima, Akira Fujishima, Toshiya Watanabe and K. Hashimoto, "Photoinduced Surface Wettability Conversion of ZnO and TiO2 Thin Films," *Journal of Physical Chemistry B*, vol. 105, pp. 1984 – 1990, 2001.

[198] L. Huang, S. P. Lau, H. Y. Yang, E. S. P. Leong, and S. F. Yu, "Stable Superhydrophobic Surface via Carbon Nanotubes Coated with a ZnO Thin Film," *Journal of Physical Chemistry B*, vol. 109, pp. 7746–7748, 2010.

[199] A. F. Carley and S. Rassias, "The Specificity of Surface Oxygen in the Activation," *Surface Science*, vol. 135, pp. 35–51, 1983.

[200] C. Sci, F. L. Formal, T. Nicolas, M. Cornuz, T. Moehl, M. Gr, and K. Sivula, "Passivating surface states on water splitting hematite photoanodes with," *Chemical Science*, vol. 2, pp. 737–743, 2011.

[201] C. Jiang, S. J. Moniz, M. Khraisheh, and J. Tang, "Earth-abundant oxygen evolution catalysts coupled onto ZnO nanowire arrays for efficient photoelectrochemical water cleavage," *Chemistry - A European Journal*, vol. 20, no. 40, pp. 12 954–12 961, 2014.

[202] X. Li, J. Yu, and M. Jaroniec, "Hierarchical photocatalysts," *Chemical Society Reviews*, vol. 45, pp. 2603–2636, 2016.

[203] X. Li, J. Yu, J. Low, Y. Fang, J. Xiao, and X. Chen, "Engineering heterogeneous semiconductors for solar water splitting," *Journal of Materials Chemistry A*, vol. 3, no. 6, pp. 2485–2534, 2015.

[204] N. Nasiri, R. Bo, L. Fu, and A. Tricoli, "Three-dimensional nano-heterojunction networks: A highly performing structure for fast visible-blind UV photodetectors," *Nanoscale*, vol. 9, no. 5, pp. 2059–2067, 2017.

[205] N. Guijarro, M. S. Prévot, and K. Sivula, "Surface modification of semiconductor photoelectrodes," *Physical Chemistry Chemical Physics*, vol. 17, no. 24, pp. 15 655–15 674, 2015.

[206] S. Wang, J.-h. Yun, B. Luo, T. Butburee, P. Peerakiatkhajohn, S. Thaweesak, M. Xiao, and L. Wang, "Recent Progress on Visible Light Responsive Heterojunctions for Photocatalytic Applications," *Journal of Materials Science & Technology*, vol. 33, no. 1, pp. 1–22, 2017. [Online]. Available: http://dx.doi.org/10.1016/j.jmst.2016.11.017

[207] C. Fadley and D. Shirley, "Electronic densities of states from x-ray photoelectron spectroscopy," *Journal*

of Research of the National Bureau of Standards Section A: Physics and Chemistry, vol. 74A, no. 4, p. 543, 1970. [Online]. Available: http://nvlpubs.nist.gov/nistpubs/jres/74A/jresv74An4p543{_}A1b.pdf

[208] A. B. Djurišić, Y. H. Leung, K. H. Tam, L. Ding, W. K. Ge, H. Y. Chen, and S. Gwo, "Green, yellow, and orange defect emission from ZnO nanostructures: Influence of excitation wavelength," *Applied Physics Letters*, vol. 88, no. 10, pp. 103 107–1 – 103 107–3, 2006.

[209] M. D. Irwin, D. B. Buchholz, A. W. Hains, R. P. H. Chang, and T. J. Marks, "p-Type semiconducting nickel oxide as an efficiency-enhancing anode interfacial layer in polymer bulk-heterojunction solar cells," *Proceedings of the National Academy of Sciences*, vol. 105, no. 8, pp. 2783–2787, 2008.

[210] L. Li, P. A. Salvador, and G. S. Rohrer, "Photocatalysts with internal electric fields," *Nanoscale*, vol. 6, pp. 24–42, 2014.

[211] S. Siol, J. C. Hellmann, S. D. Tilley, M. Graetzel, J. Morasch, J. Deuermeier, W. Jaegermann, and A. Klein, "Band Alignment Engineering at Cu2O/ZnO Heterointerfaces," *ACS Applied Materials and Interfaces*, 2016.

[212] Q. H. Ren, Y. Zhang, H. L. Lu, Y. P. Wang, W. J. Liu, X. M. Ji, A. Devi, A. Q. Jiang, and D. W. Zhang, "Atomic Layer Deposition of Nickel on ZnO Nanowire Arrays for High-Performance Supercapacitors," *ACS Applied Materials and Interfaces*, vol. 10, no. 1, pp. 468–476, 2018.

[213] M. T. Uddin, Y. Nicolas, C. Olivier, W. Jaegermann, N. Rockstroh, H. Junge, and T. Toupance, "Band alignment investigations of heterostructure NiO/TiO2nanomaterials used as efficient heterojunction earth-abundant metal oxide photocatalysts for hydrogen production," *Physical Chemistry Chemical Physics*, vol. 19, no. 29, pp. 19 279–19 288, 2017. [Online]. Available: http://dx.doi.org/10.1039/c7cp01300k

[214] Q. Cheng, M. K. Benipal, Q. Liu, X. Wang, P. A. Crozier, C. K. Chan, and R. J. Nemanich, "Al2O3and SiO2Atomic Layer Deposition Layers on ZnO Photoanodes and Degradation Mechanisms," *ACS Applied Materials and Interfaces*, vol. 9, no. 19, pp. 16 138–16 147, 2017.

[215] M. J. Ma, B. Lu, T. T. Zhou, Z. Z. Ye, J. G. Lu, and X. H. Pan, "Orientation dependent band alignment for p-NiO/n-ZnO heterojunctions," *Journal of Applied Physics*, vol. 113, no. 16, 2013.

[216] Y. J. Kim, Y. Gao, and S. A. Chambers, "Core-level X-ray photoelectron spectra and X-ray photoelectron diffraction of RuO2(110) grown by molecular beam epitaxy on TiO2(110)," *Applied Surface Science*, vol. 120, no. 3-4, pp. 250–260, 1997.

[217] A. Ananth, M. S. Gandhi, and Y. S. Mok, "A dielectric barrier discharge (DBD) plasma reactor: An efficient tool to prepare novel RuO2nanorods," *Journal of Physics D: Applied Physics*, vol. 46, no. 15, 2013.

[218] A. M. C. Evoy and W. Gissler, "ESCA spectra and electronic properties of some Ruthernium Compunds," *Physica Status Solidi (A) Applications and Materials Science*, vol. 69, pp. K91 – K96, 1982.

[219] M. S. H. Over, A.P. Seitsonen, E. Lundgren and J. Andersen, "On the origin of the Ru-3d5=2 satellite feature from RuO2(110)," *Surface Science*, vol. 504, pp. L196 – L200, 2002.

[220] M. Vittoriadiamanti and M. P. Pedeferri, "Concrete, mortar and plaster using titanium dioxide nanoparticles: Applications in pollution control, self-cleaning and photo sterilization," *Nanotechnology in Eco-Efficient Construction: Materials, Processes and Applications*, pp. 299–326, 2013.

[221] W. Gao and Z. Li, "Nanostructured transition metal oxides and their applications in composites," *Physical Properties and Applications of Polymer Nanocomposites*, pp. 723–742, 2010.

[222] Y. Ning, M. Wei, L. Yu, F. Yang, R. Chang, Z. Liu, Q. Fu, and X. Bao, "Nature of Interface Confinement Effect in Oxide / Metal Catalysts," *The Journal of Physical Chemistry C*, vol. 119, pp. 27 556–27 561, 2015.

[223] R. Dittmann, *Epitaxial Growth of Complex Metal Oxides*, 2015. [Online]. Available: http://linkinghub.elsevier.com/retrieve/pii/B9781782422457000099

[224] N. M. Gupta, "Factors affecting the efficiency of a water splitting photocatalyst: A perspective," *Renewable and Sustainable Energy Reviews*, vol. 71, no. November 2016, pp. 585–601, 2017.

[225] P. Gorai, E. G. Seebauer, and E. Ertekin, "Mechanism and energetics of O and O2 adsorption on polar and non-polar ZnO surfaces," *Journal of Chemical Physics*, vol. 144, no. 18, pp. 184 708, 1–11, 2016.

[226] P. Gorai, E. Ertekin, and E. G. Seebauer, "Surface-assisted defect engineering of point defects in ZnO," *Applied Physics Letters*, vol. 108, no. 24, pp. 241 603, 1–5, 2016.

[227] L. Lin, J. Liu, J. Lv, S. Shen, X. Wu, D. Wu, Y. Qu, W. Zheng, and F. Lai, "Correlation between native defects and morphological, structural and optical properties of ZnO nanostructures," *Journal of Alloys and Compounds*, vol. 695, pp. 1523–1527, 2017. [Online]. Available: http://dx.doi.org/10.1016/j.jallcom.2016.10.292

[228] J. S. Park, I. Mahmud, H. J. Shin, M. K. Park, A. Ranjkesh, D. K. Lee, and H. R. Kim, "Effect of surface energy and seed layer annealing temperature on ZnO seed layer formation and ZnO nanowire growth," *Applied Surface Science*, vol. 362, pp. 132–139, 2016. [Online]. Available: http://dx.doi.org/10.1016/j.apsusc.2015.11.193

[229] M. T. Man, J. H. Kim, M. S. Jeong, A. T. T. Do, and H. S. Lee, "Oriented ZnO nanostructures and their application in photocatalysis," *Journal of Luminescence*, vol. 185, pp. 17–22, 2017. [Online]. Available: http://dx.doi.org/10.1016/j.jlumin.2016.12.046

[230] X. Wang, J. Song, C. J. Summers, J. H. Ryou, P. Li, R. D. Dupuis, and Z. L. Wang, "Density-controlled growth of aligned ZnO nanowires sharing a common contact: A simple, low-cost, and mask-free technique for large-scale applications," *Journal of Physical Chemistry B*, vol. 110, no. 15, pp. 7720–7724, 2006.

[231] C. Mrabet, N. Mahdhi, A. Boukhachem, M. Amlouk, and T. Manoubi, "Effects of surface oxygen vacancies content on wettability of zinc oxide nanorods doped with lanthanum," *Journal of Alloys and Compounds*, vol. 688, pp. 122–132, 2016. [Online]. Available: http://dx.doi.org/10.1016/j.jallcom.2016.06.286

[232] J. C. Moore and C. V. Thompson, "A Phenomenological Model for the Photocurrent Transient Relaxation Observed in ZnO-Based Photodetector Devices," *Sensors*, vol. 13, pp. 9921–9940, 2013.

[233] D. R. Miller, S. A. Akbar, and P. A. Morris, "Nanoscale metal oxide-based heterojunctions for gas sensing: A review," *Sensors and Actuators, B: Chemical*, vol. 204, pp. 250–272, 2014. [Online]. Available: http://dx.doi.org/10.1016/j.snb.2014.07.074

[234] S. B. Feng-Ming Chang, Zhong-Zhe Wu, Jing-Heng Huang, Wei-Ting Chen and K. Y. Lo, "Migration Energy Barriers for the Surface and Bulk of Self-Assembly ZnO Nanorods," *Nanomaterials*, vol. 8, no. 811, pp. 1 – 12, 2018.

[235] G. Zorn, S. R. Dave, X. Gao, and D. G. Castner, "Method for determining the elemental composition and distribution in semiconductor core-shell quantum dots," *Analytical Chemistry*, vol. 83, no. 3, pp. 866–873, 2011.

[236] P. Beccat, P. Da Silva, Y. Huiban, and S. Kasztelan, "Quantitative Surface Analysis by XPS: Application to Hydrotreating Catalysts," *Oil and Gas Science and Technology*, vol. 54, no. 4, pp. 487–496, 1999.

[237] M. P. Seah and I. S. Gilmore, "Quantitative AES. VIII: analysis of auger electron intensities from elemental data in a digital auger database," *Surface and Interface Analysis*, vol. 26, no. 12, pp. 908–929, 1998.

[238] M. P. Seah, I. S. Gilmore, and S. S.J., "Quantitative XPS I. Analysis of X-ray photoelectron intensities from elemental data in a digital photoelectron database," *Journal of Electron Spectroscopy and Related Phenomena*, vol. 120, pp. 93–111, 2001.

[239] P. C. Smith, B. Hu, D. N. Ruzic, P. C. Smith, B. Hu, and D. N. Ruzic, "Low energy ion induced electron emission from gas covered surfaces," *Journal of Vacuum Science & Technology A*, no. 12, pp. 2692–2700, 1994.

[240] P. S. Bagus, E. S. Ilton, and C. J. Nelin, "The interpretation of XPS spectra: Insights into materials properties," *Surface Science Reports*, vol. 68, no. 2, pp. 273–304, 2013. [Online]. Available: http://dx.doi.org/10.1016/j.surfrep.2013.03.001

[241] C. J. Nelin, P. S. Bagus, M. A. Brown, M. Sterrer, and H. J. Freund, "Analysis of the broadening of x-ray photoelectron spectroscopy peaks for ionic crystals," *Angewandte Chemie - International Edition*, vol. 50, no. 43, pp. 10 174–10 177, 2011.

[242] H. J. Freund and G. Pacchioni, "Oxide ultra-thin films on metals: New materials for the design of supported metal catalysts," *Chemical Society Reviews*, vol. 37, no. 10, pp. 2224–2242, 2008.

[243] D. K. Bora and A. Braun, "Solution processed transparent nanoparticulate ZnO thin fi lm electrode for photoelectrochemical water oxidation," *RSC Advances*, vol. 4, pp. 23 562–23 570, 2014.

[244] Z.-m. Liao, K.-j. Liu, J.-m. Zhang, J. Xu, and D.-p. Yu, "Effect of surface states on electron transport in individual ZnO nanowires," *Physics Letters A*, vol. 367, pp. 207–210, 2007.

[245] M. Kakazey, M. Vlasova, E. A. Juarez-Arellano, T. Torchynska, and V. A. Basiuk, "Defect states and morphological evolution in mechanically processed ZnO +: X C nanosystems as studied by EPR and photoluminescence spectroscopy," *RSC Advances*, vol. 6, pp. 58 709–58 722, 2016.

[246] H. B. Lee, R. T. Ginting, S. T. Tan, C. H. Tan, A. Alshanableh, H. F. Oleiwi, C. C. Yap, M. H. H. Jumali, and M. Yahaya, "Controlled Defects of Fluorine-incorporated ZnO Nanorods for Photovoltaic Enhancement," *Scientific Reports*, vol. 6, pp. 1–11, 2016.

[247] Q. Zhu, C. Xie, H. Li, C. Yang, S. Zhang, and D. Zeng, "Selectively enhanced UV and NIR photoluminescence from a degenerate ZnO nanorod array film," *Journal of Materials Chemistry C*, 2014.

[248] B. Chen, H. Zhang, N. Du, D. Li, X. Ma, and D. Yang, "Hybrid nanostructures of Au nanocrystals and ZnO nanorods: Layer-by-layer assembly and tunable blue-shift band gap emission," *Materials Research Bulletin*, vol. 44, no. 4, pp. 889–892, 2009.

[249] M. O. T. Huayang Zhang, Wenjie Tian, Yunguo Li, Hongqi Sun and S. Wang, "A comparative study of metal (Ni, Co, or Mn)-borate catalysts and their photodeposition on rGO/ZnO nanoarrays for photoelectrochemical water splitting," *Journal of Materials Chemistry A*, 2018.

[250] Hao-Lin Feng, Wu-Qiang Wu, Hua-Shang Rao, Quan Wan, Long-Bin Li, Dai-Bin Kuang and C.-Y. Su, "Three-Dimensional TiO2:ZnO Hybrid Array as a Heterostructured Anode for Efficient Quantum-Dot-Sensitized Solar Cells_Charge transfer resistance," *Applied Materials and Interfaces*, vol. 7, pp. 5199–5205, 2015.

[251] Zhengxin Li, Meng Jia, Baxter Abraham, Jolie C. Blake, Daniel Bodine, John T. Newberg and L. Gundlach, "Synthesis and Characterization of ZnO/CuO Vertically Aligned Hierarchical Tree-like Nanostructure," *Langmuir*, vol. 34, pp. 961–969, 2018.

[252] J. Gangwar, K. K. Dey, S. K. Tripathi, M. Wan, R. R. Yadav, R. K. Singh, and A. K. Srivastava, "NiO-based nanostructures with efficient optical and electrochemical properties for high-performance nanofluids," *Nanotechnology*, vol. 24, no. 41, 2013.

[253] A. Echresh, C. O. Chey, M. Z. Shoushtari, O. Nur, and M. Willander, "Tuning the emission of ZnO nanorods based light emitting diodes using Ag doping," *Journal of Applied Physics*, vol. 116, pp. 193 104–1 – 193 104–8, 2014.

[254] Y.-M. Lee, H.-W. Yang, and C.-M. Huang, "Effect of rapid thermal annealing on the structural and

electrical properties of solid ZnO/NiO heterojunctions prepared by a chemical solution process," *Journal of Physics D: Applied Physics*, vol. 45, pp. 225 302–1 – 225 302–7, 2012.

[255] M. A. Reshchikov, G. C. Yi, and B. W. Wessels, "Behavior of 2.8- and 3.2-eV photoluminescence bands in Mg-doped GaN at different temperatures and excitation densities," *Physical Review B - Condensed Matter and Materials Physics*, 1999.

[256] J. M. Li, J. J. Wu, and X. X. Han, "Theory of interface roughness scattering in quantum wells," *Semicond. Sci. Technol*, vol. 13, pp. 709–713, 1998.

[257] L. Shi, F. Wang, Y. Wang, D. Wang, B. Zhao, L. Zhang, D. Zhao, and D. Shen, "Photoluminescence and photocatalytic properties of rhombohedral CuGaO2 nanoplates," *Scientific Reports*, vol. 6, no. January, pp. 1–10, 2016. [Online]. Available: http://dx.doi.org/10.1038/srep21135

[258] W.-c. Sun, Y.-c. Yeh, C.-t. Ko, J.-h. He, and M.-j. Chen, "Improved characteristics of near-band-edge and deep-level emissions from ZnO nanorod arrays by atomic-layer-deposited Al 2 O 3 and ZnO shell layers," *Nanoscale Research Letters*, vol. 6, no. 556, pp. 1–9, 2011.

[259] M. C. Nihan Akin, Yunus Ozen, H. Ibrahim Efkere and S. Ozcelik, "Surface structure and photoluminescence properties of AZO thin films on polymer substrates," *Surface and Interface Analysis*, vol. 47, pp. 93 – 98, 2014.

[260] W. Chen, Z. Wang, Z. Lin, and L. Lin, "Thermoluminescence of ZnS nanoparticles," *Applied Physics Letters*, vol. 70, no. 11, pp. 1465–1467, 1997.

[261] P. Prathap, N. Revathi, Y. P. Venkata Subbaiah, and K. T. Ramakrishna Reddy, "Thickness effect on the microstructure, morphology and optoelectronic properties of ZnS films," *Journal of Physics: Condensed Matter*, vol. 20, no. 3, p. 035205, 2007.

[262] N. J. Ridha, F. K. M. Alosfur, M. Hafizuddin, H. Jumali, and S. Radiman, "Dimensional effect of ZnO nanorods on gas-sensing performance," *Journal of Physics D: Applied Physics*, 2018. [Online]. Available: http://iopscience.iop.org/0022-3727/51/43/435101

[263] Q. Zhu, C. Xie, H. Li, and Q. Yang, "Comparative study of ZnO nanorod array and nanoparticle film in photoelectric response and charge storage," *Journal of Alloys and Compounds*, vol. 585, pp. 267–276, 2014. [Online]. Available: http://dx.doi.org/10.1016/j.jallcom.2013.09.157

[264] A. Mallikarjuna Reddy, A. Sivasankar Reddy, and P. Sreedhara Reddy, "Thickness dependent properties of nickel oxide thin films deposited by dc reactive magnetron sputtering," *Vacuum*, vol. 85, no. 10, pp. 949–954, 2011. [Online]. Available: http://dx.doi.org/10.1016/j.vacuum.2011.02.002

[265] S. Schinzer, M. Biehl, and W. Kinzel, "XPS/HREELS study of NiO films grown on Ni(111)," *Physical Review B - Condensed Matter and Materials Physics*, vol. 60, no. 4, pp. 2900–2907, 1999.

[266] C. S. Garoufalis, A. Barnasas, A. Stamatelatos, V. Karoutsos, S. Grammatikopoulos, P. Poulopoulos, and S. Baskoutas, "A study of quantum confinement effects in ultrathin NiO films performed by experiment and theory," *Materials*, vol. 11, no. 6, pp. 1–10, 2018.

[267] A. Echresh, M. Ali Abbasi, M. Zargar Shoushtari, M. Farbod, O. Nur, and M. Willander, "Optimization and characterization of NiO thin film and the influence of thickness on the electrical properties of n-ZnO nanorods/p-NiO heterojunction," *Semiconductor Science and Technology*, vol. 29, no. 11, 2014.

[268] Q. Su, Z. Dong, J. Zhang, G. Du, and B. Xu, "Visualizing the electrochemical reaction of ZnO nanoparticles with lithium by in situ TEM: Two reaction modes are revealed," *Nanotechnology*, vol. 24, no. 25, 2013.

[269] A. C. Gandhi, C.-H. Liao, W.-L. Yeh, and Y.-L. Huang, "Non-monotonous size-dependent photoluminescence and excitonic relaxations in nanostructured ZnO thin films," *RSC Advances*, vol. 9, no. 4, pp. 2180–2188, 2019. [Online]. Available: http://xlink.rsc.org/?DOI=C8RA09370A

[270] G. M. Bancroft, H. W. Nesbitt, R. Ho, D. M. Shaw, J. S. Tse, and M. C. Biesinger, "Toward a comprehensive understanding of solid-state core-level XPS linewidths: Experimental and theoretical studies on the Si2p and O1s linewidths in silicates," *Physical Review B - Condensed Matter and Materials Physics*, vol. 80, no. 7, pp. 1–13, 2009.

[271] W. Brückner, R. Kaltofen, J. Thomas, M. Hecker, M. Uhlemann, S. Oswald, D. Elefant, and C. M. Schneider, "Stress development in sputtered NiO thin films during heat treatment," *Journal of Applied Physics*, vol. 94, no. 8, pp. 4853–4858, 2003.

[272] O. Kohmoto, H. Nakagawa, Y. Isagawa, and A. Chayahara, "Effect of heat treatment on the oxygen content and resistivity in sputtered NiO films," *Journal of Magnetism and Magnetic Materials*, vol. 226-230, no. PART II, pp. 1629–1630, 2001.

[273] M. Wang, Y. Thimont, L. Presmanes, X. Diao, and A. Barnabé, "The effect of the oxygen ratio control of DC reactive magnetron sputtering on as-deposited non stoichiometric NiO thin films," *Applied Surface Science*, vol. 419, pp. 795–801, 2017. [Online]. Available: http://dx.doi.org/10.1016/j.apsusc.2017.05.095

[274] E. Turgut, Ö. Çoban, S. SarÄśtaÅ§, S. Tüzemen, M. YÄśldÄśrÄśm, and E. Gür, "Oxygen partial pressure effects on the RF sputtered p-type NiO hydrogen gas sensors," *Applied Surface Science*, vol. 435, no. 2, pp. 880–885, 2018.

[275] A. M. Reddy, A. S. Reddy, K. S. Lee, and P. S. Reddy, "Effect of oxygen partial pressure on the structural, optical and electrical properties of sputtered NiO films," *Ceramics International*, vol. 37, no. 7, pp. 2837–2843, 2011. [Online]. Available: http://dx.doi.org/10.1016/j.ceramint.2011.04.121

[276] Y. Ashok Kumar Reddy, A. Sivasankar Reddy, and P. Sreedhara Reddy, "Effect of oxygen partial pressure on the properties of NiO-Ag composite films grown by DC reactive magnetron sputtering," *Journal of Alloys and Compounds*, vol. 583, pp. 396–403, 2014. [Online]. Available: http://dx.doi.org/10.1016/j.jallcom.2013.08.180

[277] H. Y. Hwang, Y. Iwasa, M. Kawasaki, B. Keimer, N. Nagaosa, and Y. Tokura, "Emergent phenomena at oxide interfaces," *Nature Materials*, vol. 11, no. 2, pp. 103–113, 2012. [Online]. Available: http://dx.doi.org/10.1038/nmat3223

[278] M. J. Al-saadi, S. H. Al-harthi, H. H. Kyaw, M. T. Z. Myint, T. Bora, and K. Laxman, "Influence of Atomic Hydrogen , Band Bending , and Defects in the Top Few Nanometers of Hydrothermally Prepared Zinc Oxide Nanorods," *Nanoscale Research Letters*, pp. 1–11, 2017. [Online]. Available: http://dx.doi.org/10.1186/s11671-016-1800-3

[279] A. Gerson, M. C. Biesinger, R. S. C. Smart, B. P. Payne, and L. W. M. Lau, "X-ray photoelectron spectroscopic chemical state quantification of mixed nickel metal, oxide and hydroxide systems," *Surface and Interface Analysis*, vol. 41, no. 4, pp. 324–332, 2009.

[280] J. M. Lantz, "Electrostatic field measurements and band bending at single crystal TiO2 semiconductor electrodes by electric field-induced optical second harmonic generation," pp. 4899–4905, 1994.

[281] R. Gurwitz, R. Cohen, and I. Shalish, "Interaction of light with the ZnO surface : Photon induced oxygen âĂIJ breathing ‚âĂİ oxygen vacancies , persistent photoconductivity , and persistent photovoltage," *Journal of Applied Physics*, vol. 033701, no. 115, pp. 1–9, 2014.

[282] Xueqiang Zhang and Sylwia Ptasinska, "Dissociative Adsorption of Water on an H2O/GaAs(100) Interface: In Situ Near-Ambient Pressure XPS Studies," *The Journal of Physical Chemistry C*, vol. 118, pp. 4259–4266, 2014.

[283] X. Zhang and S. Ptasinska, "Distinct and dramatic water dissociation on GaP(111) tracked by near-ambient pressure X-ray photoelectron spectroscopy," *Physical Chemistry Chemical Physics*, vol. 17, no. 5, pp. 3909–3918, 2015.

[284] ——, "Electronic and chemical structure of the H2O/GaN(0001) interface under ambient conditions," *Scientific Reports*, vol. 6, no. December 2015, pp. 2–7, 2016. [Online]. Available: http://dx.doi.org/10.1038/srep24848

[285] M. A. v. V. Sawatzky and G. A., "Nonlocal Screening Effects in 2p X-Ray Photoemission Spectroscopy Core-Level Line Shapes of Transition Metal Compounds," *Physical Review Letters*, vol. 70, no. 16, pp. 2459–2462, 1993.

[286] M. C. Biesinger, B. P. Payne, A. P. Grosvenor, L. W. Lau, A. R. Gerson, and R. S. C. Smart, "Resolving surface chemical states in XPS analysis of first row transition metals, oxides and hydroxides: Cr, Mn, Fe, Co and Ni," *Applied Surface Science*, vol. 257, no. 7, pp. 2717–2730, 2011. [Online]. Available: http://dx.doi.org/10.1016/j.apsusc.2010.07.086

[287] M. Li, G. Xing, L. F. N. Ah Qune, G. Xing, T. Wu, C. H. A. Huan, X. Zhang, and T. C. Sum, "Tailoring the charge carrier dynamics in ZnO nanowires: The role of surface hole/electron traps," *Physical Chemistry Chemical Physics*, vol. 14, pp. 3075–3082, 2012.

[288] L. M. Manceriu, P. Colson, A. Maho, G. Eppe, N. D. Nguyen, C. Labrugere, A. Rougier, R. Cloots, and C. Henrist, "Straightforward prediction of the Ni 1-x O layers stoichiometry by using optical and electrochemical measurements," *Journal of Physics D: Applied Physics*, vol. 50, no. 22, p. aa6e71, 2017. [Online]. Available: https://doi.org/10.1088/1361-6463/aa6e71

[289] C. F. Windisch, G. J. Exarhos, C. F. Windisch, and G. J. Exarhos, "Mott âĂŞ Schottky analysis of thin ZnO films," *Journal of Vacuum Science & Technology A*, no. 18, pp. 1677–1680, 2000.

[290] L. G. Arriaga and A. M. Fernã, "Determination of at band potential and photocurrent response in (Cd , Zn) S used in photoelectrolysis process," *International Journal of Hydrogen Energy*, vol. 27, pp. 27–31, 2002.

[291] Ya Yang, Wen Guo, Xueqiang Wang, Zengze Wang, Junjie Qi and Y. Zhang, "Size dependence of dielectric constant in ZnO nanowire.pdf," *Nano Letters*, vol. 12, no. March, pp. 1919–1922, 2012.

Chapter 7

Conclusion and Outlook

7.1. Conclusions

Heterogeneous photocatalysis is an environmentally benign and low cost process occurring at normal pressure and temperature which has the ability to tackle some of the 21st century environment problems including CO_2 reduction, pollutant degradation in water and formation of alternative energy sources. In this context, the aim of this project was to develop, characterize and test the photodegradation performance of novel, one dimensional ZnO based heterostructured films.

Previous literature reports indicated that n-type ZnO films should either be coupled to a p-type semiconductor to form a staggered type heterostructures or to a metal to form a Schottky type junction in order to have effective charge transfer and consumption. Based on this NiO and RuO_2 were selected, owing to the favourable band energy alignment and examined for their interfacial properties, thereby exploring their potential to act as co-catalysts.

The literature data on ZnO based thin films (more specifically on ZnO nanorod films) coupled to metals or other semiconducting metal oxides (the NiO/ZnO heterostructures was never reported) indicated that:

- the NiO/ZnO heterostructures as we fabricated them (hydrothermal growth of the ZnO nanorods followed by NiO deposition by sputtering) were never reported for the photocatalytic degradation of pollutants in water.
- in most cases, an improvement in performance is realized after longer exposure times

than the ones used in our study.

- record pollutant degradation efficiencies of 99% are attained only when ZnO is coupled to a metal.
- the enhanced efficiency is attributed to efficient charge transfer without studying the interface properties.

Literature review highlighted that there are no comprehensive systematic studies correlating the internal parameters (band bending, Fermi level, defect type and level) with the external parameters (scaffold surface chemistry and morphology, second material morphology and structure) and further on with the photocatalytic response in case of thin film heterostructures and more particularly for NiO/ZnO thin films.

1. The step-by-step XPS interface studies performed on both NiO/ZnO and RuO_2/ZnO thin films based on both pristine and cleaned ZNR scaffold allowed us to conclude that both NiO and RuO_2 can lead to a well-developed band bending when combined with ZnO and are a good choice as co-catalysts.
2. Optimum surface cleaning was obtained at high vacuum (0.5 Pa) at 400 °C since desorption of adsorbents and oxygen was enabled.
   - ▶ surface cleaning led to a change in the doping level of the ZnO surface changing from excess electron accumulation to electron depletion.
   - ▶ also, this preliminary study showed that the band bending can be maximized by cleaning the scaffold.
   - ▶ adsorbed hydroxyl and C removal was confirmed by XPS, whereas the change in doping level was highlighted by photoluminescence, valence band maximum position shift (XPS) and electrochemical (Mott-Schottky) analysis.
3. The NiO deposition conditions (temperature, oxygen partial pressure and deposition time) were optimized to be: deposition at high temperature (400 °C), P_{O_2} = 6% and 20 s deposition time, ZNR scaffold cleaning (as mentioned at point 2) prior to deposition.
   - ▶ even if a lower band bending and near band edge emission (compared to heterostructures involving other parameters) are attained, these optimized conditions allowed to attain the highest dye degradation efficiency (85%) ever reported for NiO/ZnO(1D nanostructured) heterostructures.
   - ▶ shorter NiO deposition times (thinner layer) are preferred to ensure shorter charge

diffusion paths and to maintain an optimum band bending and not compromise the photoactivity of ZnO scaffold.

- using higher oxygen partial pressure during the deposition has enhanced the growth rate leading to larger NiO particles (TEM), higher interface fluctuations and charge recombination (PL).

4. The heterostructures with cleaned ZNR and optimized NiO show a modest improvement in Rhodamine B photodegradation. Though a good band bending was achieved (TEM showed that the ZnO rods were conformally coated with nanometer scale NiO particles) and interface fluctuations were limited (near band edge emission peak narrowing, PL), recombination through the NiO layer (equal contribution from shallow and deep level defect was shown by PL analysis) due to the thin space charge layer reduced the performance of these materials.

5. In this thesis, for the first time in this thesis in-situ water exposure studies were carried out under UHV conditions on the bare ZnO (nanorods and planar layer) and its heterostructures with NiO to understand how water dissociation is influenced by the presence of adsorbates, also how it impacts the interfacial properties and consequently the photo degradation performance.

6. The studies showed that scaffold cleaning leads to improved water dissociation and thus enhanced photodegradation efficiency due to surface passivation with chemisorbed oxygen.

7. Water exposure reduces the band bending of single cleaned scaffold and its heterostructures, i.e the band bending was flattened or even reversed (accumulation layer).

8. The heterostructures that showed near flat-band conditions, exhibited poor water dissociation capabilities and this was correlated to their lower photodegradation efficiency.

9. The NiO/ZnO heterostructures optimized at point 3 maintained a suitable band bending allowing effective water dissociation, spontaneous charge transfer and thus, improved photodegradation efficiency.

10. The complex correlation of XPS, PL and photodegradation performance is one of the original points of this thesis and allowed concluding that in order to maximize the efficiency of our system, charge separation should be effective (attaining band bending), the deep level charge recombination should be reduced (minimized deep level emission) and non-radiative recombination as well (leading to increased near band

edge emission), the doping level of the scaffold should be optimum.

11. Testing at industrial pilot scale was realized at Aquatic Science and performances comparable to the one obtained in the lab scale test were attained. Even more those test revealed an improvement of photocatalytic performance when using the ZnO nanorod film instead of a TiO_2 reference layer.

The samples showing champion efficiencies are summarized in the table below:

Table 7.1: List of samples that showed better photocatalytic response, along with their preparation, electrical/optical property and water dissociation details; Details of as-is ZNR (Z1) is shown, for comparison purposes and 0.50 eV was added to the V_{bb} values of Z2 (surface cleaned) and its heterostructures, with respect to the shift of Zn2p line (from XPS) for Z2 scaffold in relation to the reference material, Z1 scaffold.

Sample Code	Preparation conditions	Contact material thickness (nm)	V_{bb} (eV)	O_{OH}/O_{H_2O} ratio [after in-situ water exposure]	Degradation efficiency (η%)
Z1	Seed layer + Hydrothermal growth + calcination at 500°C	-	-	0.16	54
Z2	surface cleaning of Z1 at 400°C in presence of oxygen	-	0.50	0.51	67
$Z2N_{RT}$	NiO deposited using P_{O_2} = 6% , deposition time = 20 s at RT, on Z2 scaffold	$\simeq$3.5	1.17	0.48	74
$Z2N_{HT}$	NiO deposited using P_{O_2} = 6% , deposition time = 20 s, at HT, on Z2 scaffold	$\simeq$3	1.14	-	85

The overall studies performed during this doctoral work has evidenced that enhancement could be attained by playing around with the parameters that will give better control over band bending (optimizing the layer thickness of second material) and deep level defects (adjusting the oxygen partial pressure during the deposition) that will enable the attainment of better charge separation as well as charge kinetics in the system.

7.2. Outlook

Studies performed in this doctoral work have shown few areas of exploration that could be taken further and are listed below:

1. Given that the system ZnO 1D (hydrothermal growth)/NiO (sputtering) was first studied in this thesis, with the NiO layer conformally covering the ZnO rods, other heterostructures configurations that would allow spatial separation of the two materials forming the junction (ex: side-wise deposition of contact material on the ZnO nanorods, varying the thickness of the ZnO rods) should be explored.

2. The optimization of the NiO deposition conditions has not been exhaustive, and in particular the influence of the oxygen partial pressure on the growth rate and doping level and its influence on the interface properties should be further studied.

3. Photoluminescence analysis has shown that recombination through the NiO layer occurs and we believe that this might be due to the thin space charge layer owing to the high doping level of ZnO. In future the influence of ZnO doping level on the space charge layer width should be carried on.

4. The Rhodamine B (cationic dye) degradation tests were carried at pH = 8 in order to encourage the dye adsorption on the surface of the photocatalysts (at a pH > point of zero charge the heterostructures surface is charged negatively). However within the limit of stability of the two materials, higher pH values (8.5, 9 and 9.5) should also be tested to maximize the efficiency.

5. The ability of the heterostructures (prepared during this work) to degrade other type of dye pollutants and pharmaceuticals and personal care products (PPCPs), would also be interesting.

6. Interface studies on the RuO_2/ZnO (n+ and n- doped) were for the first time in this work and proved that a band bending is attained when coupling these two materials and constitutes the base for further development and optimization of this system for photocatalytic photodegradation.

7. The in-situ water adsorption studies have revealed for the first time the correlation of the water dissociation capability and band bending rearrangement with the photodegradation performance and proven the importance of carrying such studies on any system functioning in water media. Hence, the NiO/ZnO heterostructures prepared at varying temperature conditions or RuO_2/ZnO heterostructures or any other

heterostructures that are interesting for aqueous media involving applications would be of interest to explore further in detail.

8. Furthermore, the synthesis of such heterostructures by using a large scale deposition method (spray, sputtering) and their reusability (reconditioning) should be envisaged, to confirm their compatibility with an industrial scale usage.

Chapter 8

Appendix

8.1. Characterization Techniques

8.1.1. X-Ray Diffractometer (XRD)

X-Ray Diffractometer is one of the primary non-destructive techniques used to characterize a wide range of materials including powder samples (minerals, metals, semiconductors), polymers, thin films etc. It provides an unique XRD pattern that gives information about the crystalline phase, purity of the samples, the degree of crystallinity, stress and strain (to identify the possible amount of deviation from pure samples' structure in case of doped/sensitized samples), crystallite size and lattice parameters.

XRD diffraction follows the principle of Bragg's law, which relates the wavelength, the angle of diffraction and the interplanar distance. The working is as follows: when the X-ray source with a wavelength λ interacts with the sample, it will produce a constructive interference when the Bragg's law is satisfied (Equation 8.1).

$$n\,\lambda \;=\; 2\,d\,sin\,\theta \tag{8.1}$$

where, d = lattice spacing in the crystal and θ = angle of incidence.

In general there are components like Kα1,Kα2,Kβ, but the commonly used radiation is CuKα radiation (λ=1.5418A$\bar{\circ}$) and the angle of rotation can vary between 20° - 80° and sometimes 2° - 20° (based on the sample requirements). The occurrence of constructive interference and peak intensity will be produced as a signal, which is then processed and

converted into a pattern of 2θ Vs Counts.

In our study, the X-ray diffraction (XRD) measurement was carried out for ZNR film using Bruker, D8 Diffractometer equipped with a Cu kα radiation source in the grazing incidence mode (incidence angle 1 $^\circ$) in the 2Θ = 20 - 70 $^\circ$ range in a 2° min^{-1} scan rate. Thin film samples of 2 $\times$ 2 cm^2 were loaded onto a customized sample holder for measuring XRD.

8.1.2. Scanning Electron Microscopy (SEM)

Scanning Electron Microscope is a powerful, efficient and non-destructive method which enables imaging of the samples with a resolution down to nanometer scale. It is capable of producing images by scanning the surface of the sample with focussed beam of high energy electrons. It is used to:

1. determine sample morphology and structure by scanning the surface or cross section of the sample

2. analyse the chemical composition of the sample (using EDS-Energy Dispersive X-Ray Spectroscopy)

3. determine the crystal structure and preferential orientation (using EBSD-Electron Back Scatter Diffraction)

Principle

In principle, a high energy electron beam is generated and focussed onto the specimen which penetrates upto 1 μm depending on the used acceleration voltage, working distance and spot size. On interaction, a variety of particles or waves or signals like secondary electrons, backscattered electrons, Auger electrons, X-rays and Photons are produced (Figure 8.1). Among them, the secondary and backscattered electrons are used for imaging the sample while other particles are generally used for Energy-Dispersive X- ray Spectroscopy (EDX). The secondary electrons that occur due to inelastic scattering are produced from the surface of the sample and the backscattered electrons which are the result of elastic scattering are produced by deeper interaction. Finally, the images are produced by the electron beam which performs a raster scan over the surface of the sample.

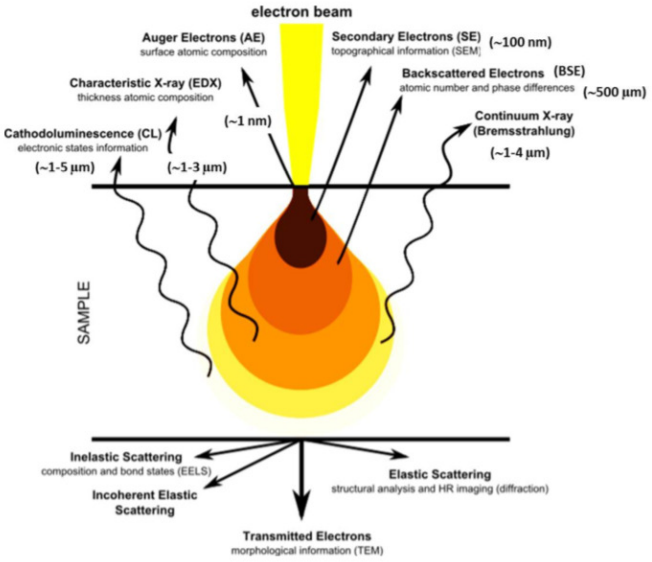

Figure 8.1: Electron-matter interaction volume and the different types of signals which are generated. [30]

Among its advantages we can enunciate:

i) the variety of information like imaging, chemical composition analysis and crystal structure determination.

ii) powerful, non-destructive and efficient technique.

iii) easy to operate.

iv) minimal sample preparation.

v) can be used for conductive as well as non-conductive samples.

In our study, SEM images of ZNR samples were acquired using a FEG-SEM (XL 30, FEI) operated at 15kV, using a spot size of 4 and at a stage to sample distance of 10 mm. All the samples were gold sputtered, to avoid sample charging.

8.1.3. Transmission Electron Microscopy (TEM)

Transmission electron microscopy (TEM) is also a powerful microscopic technique that can be utilized to obtain high (atomic) resolution images of materials (chemical or biological).

TEM transmits a focused, high-energy electron beam through the sample (grid).

The electrons interact with the nuclei of atoms in the sample and scatters off which are then projected onto a fluorescent screen. This process allows the collection of atomic scale images. In addition, the orientation of crystallographic planes can be analyzed with the help of a selected area electron diffraction (SAED) pattern that can be obtained from single nanostructures. The combination of the information gained from atomic scale imaging and diffraction patterns will lead to identification of the surface crystallographic planes of a material.

Similar to SEM, here as well, the elemental composition of a sample can be obtained through EDX. This technique involves ionization of the sample from the X-rays of the microscope and the ionization events are then analyzed with a solid-state energy dispersive detector. Each element provides a unique pattern of X-ray lines from the K, L, and M shells allowing straightforward analysis. This technique is also used for constructing elemental maps to characterize the microstructural composition and elemental distribution (very useful when multiple components are involved on the nanometer scale).

In this study, TEM images were obtained by employing a TECNAI G2 TWIN (FEI) operating at 200kV.

Sample Preparation

The photocatalysts were scratched from the FTO substrates and then dispersed in ethanol (99.8%, Sigma-Aldrich Co.) using an ultrasonic bath and few droplets of the suspension were placed (drop by drop, allowing the time to dry) on the carbon (C) grid.

8.1.4. Ultra Violet-Visible Spectrophotometer (UV-VIS)

There are several spectroscopy techniques that makes use of the Ultra Violet and Visible light ranges and Ultra Violet Visible Spectroscopy is one among them, used for the determination of concentrations and analyses of the dissolved substances. It is well known that UV and visible region correspond to 190 - 400 nm and 400 - 800 nm of the light spectrum. UV-VIS can be used to measure the absorbance of UV or visible light by a sample, which could be done at a (desired) single wavelength or performing a scan over a range of the available spectrum.

Principle and Working

UV spectroscopy is capable of measuring the ratio of the transmitted light with respect to the incident light in the wavelength of UV-VIS range. The light source is typically

based on deuterium and tungsten lamps which will provide the UV-VIS irradiation that covers the range of 200 - 800 nm. Generally, light absorption leads to the excitation of electrons from lower to higher energy levels (i.e, ground to excited state). As the energy levels are quantized, only photons that possess required energy and can cause transitions from one level to another, will be absorbed. The amount of light absorbed could be related to the concentration of the substance, the liquid layer thickness, and the absorption co-efficient at a particular wavelength, as described by the Beer-Lambert law (equation 8.2).

$$A = \varepsilon\, c\, l \tag{8.2}$$

where, A = Absorbance, ε = absorption co-efficient (constant for each material), c = solution concentration and optical path length (1 cm).

This law is obeyed when the absorbance varies linearly with the concentration. A calibration curve (Figure 8.1.2b in Appendix), is used to determine the concentration of unknown samples subjected to pollutant degradation experiment.

The higher the optical density of the sample, the higher will be the absorption and hence, the optical density is usually followed to be as pathlength of 1 cm. The liquid sample is usually kept in an optically flat, transparent container (made of regular glass or quartz), called a cell or cuvette. Two cells will be utilized, one for the reference solution (typically distilled water, called as blank) and the other for sample to be studied.

The outcome photons from light source will be splitted by the diffraction grating, providing two equal beams, one passing through the reference or standard (called as reference beam) and the other through the sample (called as sample beam). The intensities from both the beams are measured by the detectors, denoted as I_0 and I_T, respectively and this could be related to the following equation:

$$A = log_{10} \frac{I_0}{I_T} \tag{8.3}$$

where, A = Absorbance, I_0 = light intensity from reference cell and I_T = light intensity from sample cell.

In this dissertation, the Shimadzu UV3600 Plus spectrophotometer was utilized for investigating the RhodamineB concentration before and after photodegradation by measuring the absorption spectrum.

8.1.4.1. Degradation experiment using RhodmaineB

All degradation experiments were carried out with 20 mL ($1.3\ 10^{-6}$ M, i.e 13 μg) of Rhodamine B - RhB (Sigma Aldrich, $\geq$95%). The prepared substrates were cut into 1cm $\times$ 1cm that supported around 0.13 mg of ZnO and used in the degradation studies. The ratio between photocatalyst and pollutant used here is 10:1, where the ratio usually used for powder photocatalysts is 50:1. Initially, the film was kept under dark for 20 min, with mild stirring, in order to ensure adsorption of pollutants on the surface. It was then exposed to the light source for 180 min. Then, 1 mL of aliquot sample was taken at time 0 and then every 20 min and analyzed by UV-Visible spectrophotometry. This enabled monitoring the pollutant degradation over time and comparing the degradation capabilities of each sample.

Degradation study experiments were performed under a 5 mW/cm^2 UV light source (maximum wavelength 365 nm), with the sample placed at 18 cm distance from the UV source. RhodamineB (RhB) was used as the model pollutant for investigation. A stock solution of 10 mg/L was prepared and stored in dark. Solution of 1.25 mM were prepared from the stock (pH adjusted to 8), to be used during the degradation tests with $1cm^2$ films . Initially the sample was stirred in dark for 20 min to achieve equilibrium and then exposed to UV light for 3 hours. Absorption spectra of RhB were registered every 20 min.

Furthermore, the unknown concentration of a solution could be identified with the help of a systematic calibration experiment. For this, the RhB solution of known concentrations (from higher to lower) were prepared and their absorbance curves (Figure 8.2a) were measured using UV-Vis spectrophotometer. These absorbance values were plotted against the concentration values from solution preparation, to obtain the calibration curve, shown in Figure 8.2b. And this calibration curve was used to identify the concentration of the solution at each step of the degradation experiments that was carried out in presence of the photocatalyst and light irradiation. Moreover, in order to make sure that degradation of RhB does not occur in the absence of photocatalyst material, RhB solution was exposed to light source without the photocatalyst and the absorbance were measured before and after the light exposure and shown in Figure 8.2c (concentration of RhB solution and exposure time employed here was same as those used in degradation experiments with photocatalyst). This confirmed that no degradation was taking place in the absence of a photocatalyst.

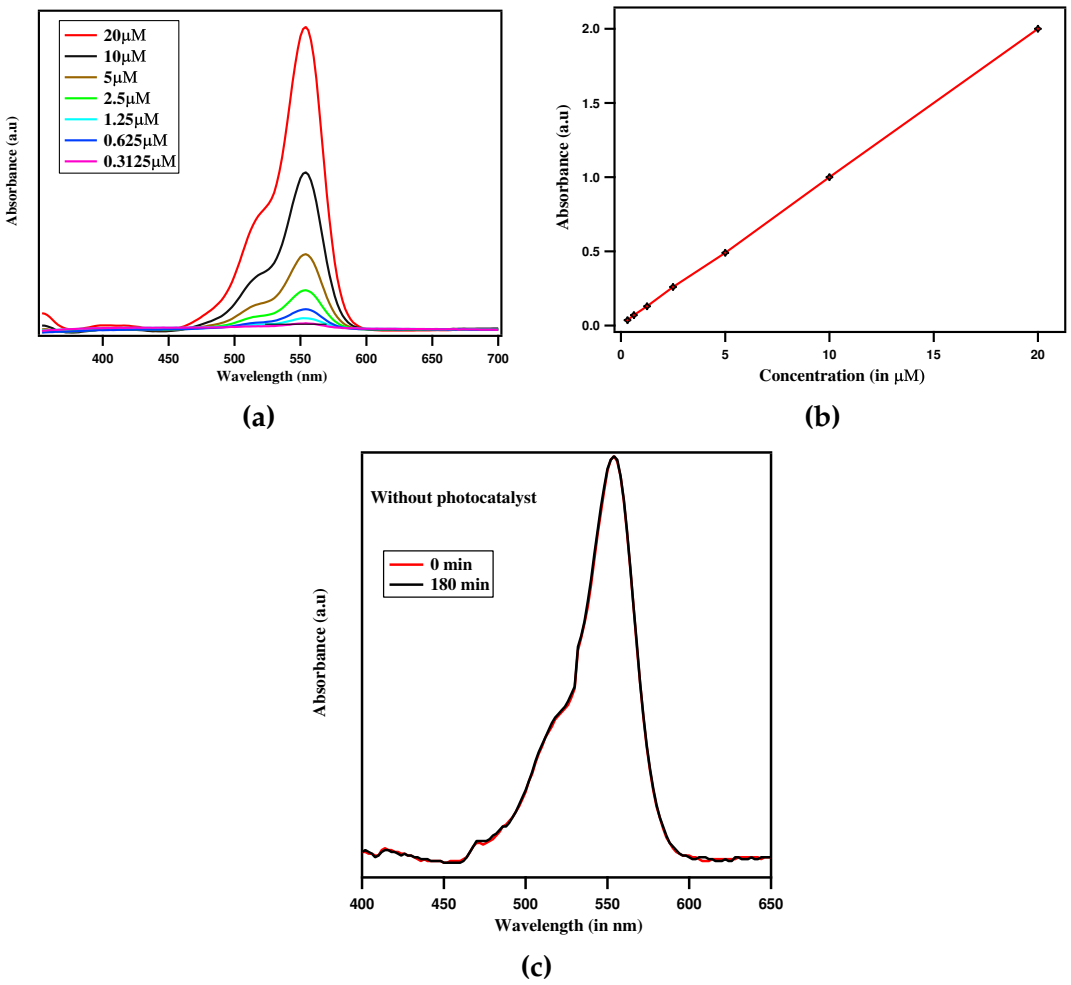

Figure 8.2: (a) Absorbance curves from higher to lower concentration of RhodamineB aqueous solution and (b) Calibration curve representing concentration vs. absorbance and (c) UV-Vis spectra of RhB before and after exposure to light irradiation for 180 min, without the presence of photocatalyst.

8.1.5. Photo-electrochemical measurements

The photo electro chemical measurements for all the samples were carried out in the order: Electrochemical impedance (EiS,at 0 bias), Mott-Schottky (MS) and I - V measurements. This order was followed, in order to avoid changing the nature of the sample, before the MS analysis. This was confirmed by checking that the open circuit potential did not change after the charge transfer resistance measurements by EiS.

In this thesis, Linear sweep voltammetry (LSV) and Electro chemical Impedance Spectroscopy (EIS) were carried out in dark and light conditions, whereas the Mott-Schottky (MS) analysis was done (only for scaffold films) in dark.

Working electrode preparation

In case of both scaffold and heterostructured photocatalysts, samples of 1×1 cm^2 dimensions were used as the working electrodes. The corner of the sample was carefully rubbed with the scratch paper to have access to the FTO.

Photo electro chemical system works with a potentiostat and a 3-electrode setup (using a home-made cappucino cell, as shown in Figure 8.3) that consists of a counter electrode (typically a Platinum wire), reference electrode (in our case, Ag/AgCl, whose electrode potential [E°] against standard hydrogen electrode [SHE] is, 0.204 V) and working electrode (sample to be studied). These electrodes are immersed into the suitable electrolyte, which can provide constant ionic strength, little or no concentration gradient near the electrode and a stable pH, thereby facilitating the electrochemical process at the surface of working electrode in the presence of an applied potential that is delivered by the potentiostat.

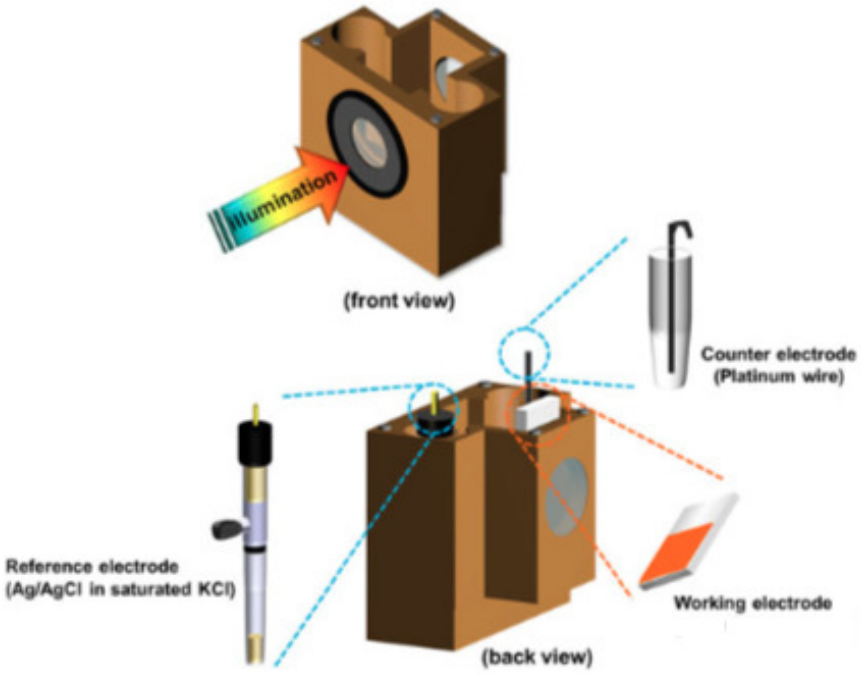

Figure 8.3: Schematic illustration of the cappuccino cell. [31]

In general, photoelectrochemical measurements could be used to identify the performance of a material in the water splitting reactions and their charge transfer characteristics. Photocatalytic water splitting involves water oxidation and reduction reactions and these processes require a thermodynamic potential difference of 1.23 V vs. SHE or RHE [reversible hydrogen electrode]. However, a semiconductor with a bandgap of $\geqslant$ 1.8 - 2.2 V is usually considered suitable for water splitting, in order to compensate the losses

incurred by recombination and/or kinetics. The water oxidation/reduction reaction and the corresponding thermodynamic potential difference are:

$$4\,H_2O + 4\,e^- \rightarrow 2\,H_2 + 4\,OH^- \quad (HER) \quad E^\circ = 0.0\,V\ vs\ RHE \tag{8.4}$$

$$4\,OH^- + 4\,e^- \rightarrow O_2 + 4\,e^- + 4\,H_2O \quad (OER) \quad E^\circ = 1.23\,V\ vs\ RHE \tag{8.5}$$

where, HER is hydrogen evolution reaction and OER is oxygen evolution reaction.

The evolution of these reactions could be observed in the current (I) - voltage (V) characteristics, as shown in Figure 8.4. Therefore, the performance of a photoelectrode could be investigated by sweeping the potential in a desired window, which will display the amount of photocurrent that could be attained by the material.

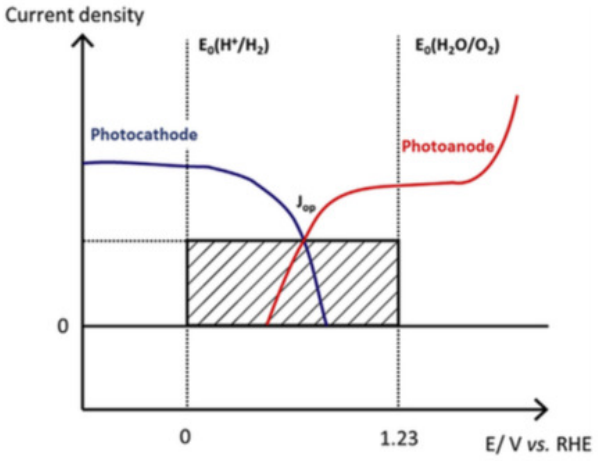

Figure 8.4: Overlaid I - V curves of a p-type photocathode and an n-type photoanode representing the HER and OER through photo driven water splitting. [32]

The procedure to obtain such a graph is called **Linear sweep voltammetry** (**LSV**), where the voltage is swept linearly, with a fixed scan rate, in a given potential range and the resulting current (I) will be monitored. This experiment will cause the occurrence of electrochemical oxidation and reduction of the species at the electrode surface, which is being induced by the change in concentration of electroactive species (based on the applied potential). Therefore, in presence of light irradiation, the photocurrent will be produced and current - voltage (I - V) curves are obtained, from which one can obtain the following three information:

1. the onset potential - the potential at which the photocurrent is 0 mA

2. the photocurrent at water splitting voltage (1.23 V vs. SHE and 1.026 V vs. Ag/AgCl) - This will display the amount of photocurrent that could be attained above the corresponding thermodynamic potential difference or at that water splitting voltage

3. the maximum photocurrent - implies the maximum value attained in the scanned potential range

The voltage at which maximum photocurrent is obtained (could be determined by drawing a linear line from the maximum photocurrent value to the x - axis, the potential applied) reveals the amount of overpotential that will be required to achieve higher photocurrent efficiency.

EIS measurements:

Impedance spectroscopy helps in studying the charge transfer (or electrical) resistance characteristics of a system, where the surface phenomena and changes in bulk properties occur. Impedance (Z) is usually measured by perturbing the system under a small time varying potential ($\simeq$20 mV) which can be described by the wave form, $x = x_0 \sin(\omega t)$, where x_0 is the amplitude and ω is the radial frequency ($\omega = 2\Pi\nu$). In a linear system, the resulting output signal [based on the function, $y = y_0 \sin(\omega + \varphi)t$, where φ is phase angle] is dephased and thus has a different amplitude. This impedance (Z) can be represented as either Bode plot [$\log|Z|vs.\varphi$] or Nyquist plot [Z_{im} vs. Z_r, where 'im' is imaginary and 'r' is real].

In case of the Nyquist plot, | Z | is usually represented as a vector and, the angle between the vector and the x-axis of the plot is generally called as the phase angle φ. An example Nyquist plot showing these parameters is illustrated in Figure 8.5.

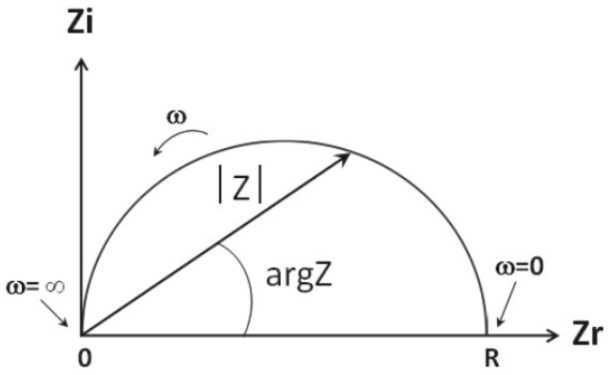

Figure 8.5: Nyquist plot with impedance vector. [33]

The conductive behaviour [resistive/capacitive] of the system, at a particular frequency range, will influence the Z_r, Z_{im} and φ. For example, when a material is exhibiting ideal resistive behaviour, there will be no imaginary contribution with a phase angle of 0°; whereas, an ideal capacitive behaviour will induce the lack of contribution from the real part with φ of - 90°.

Therefore, the electrochemical behaviour of a system that is observed through the impedance spectrum could be translated into an equivalent circuit with the help of single or multiple sub - circuit elements like resistor (R), capacitor (C) and inductor (I), as illustrated in Figure 8.6.

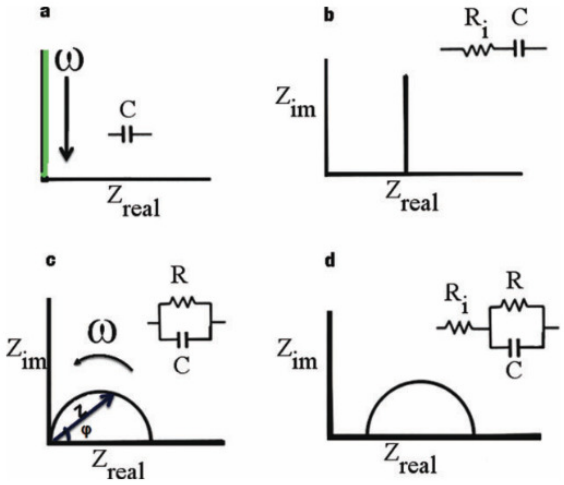

Figure 8.6: Nyquist plots for (a) an ideal capacitor, (b) an ideal capacitor in series with a resistor, (c) a capacitor in parallel with a resistor, and (d) a resistor in series with a parallel RC-circuit.[34]

Based on all the above discussed parameters, the circuit used to fit the photoelectrochemical impedance measurements for the samples studied in Section 3.1 was observed to be consisting of either 5 or 6 elements, as illustrated in Figure 8.7.

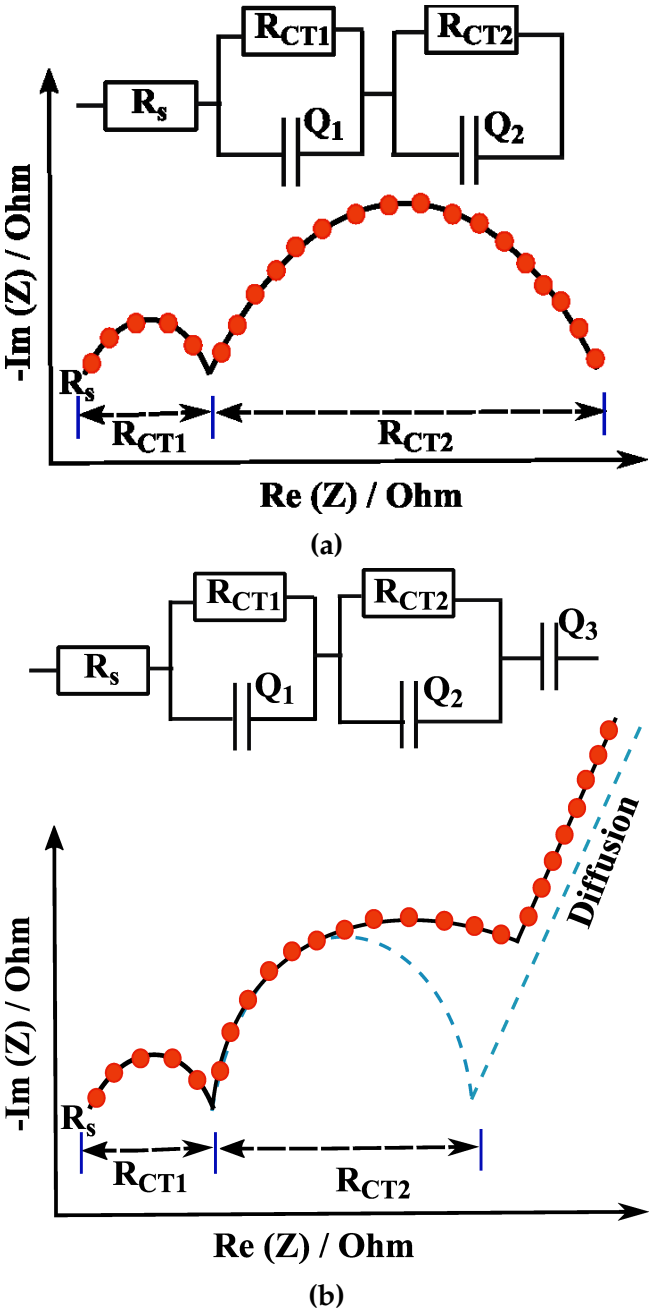

Figure 8.7: The illustration of the EIS spectra fit in the absence (a) and in the presence of diffusion (b). The first semicircle in the high frequency range corresponds to the FTO/ZnO/NiO interface (R_{CT1} and Q1), whereas the second semicircle is attributed to the charge transfer resistance at the film/electrolyte interface (R_{CT2} and Q2) and R_S stands for the contacts and electrolyte resistance.

In principle, MS analysis is performed by analysing the system responsive to the sinusoidal signal for each frequency in a given range, as function of the applied bias. The range of the applied bias is chosen as to comprise the open circuit potential and in order to make evident the accumulation or depletion regimes. An example of plots displaying the

electron rich (accumulation) and depleted regions are shown below, in Figure 8.8.

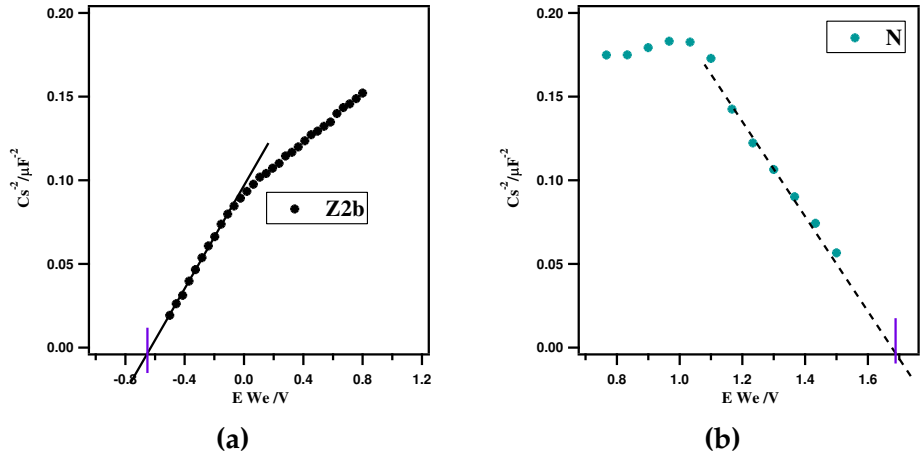

Figure 8.8: Mott-Schottky plots showing the typical curve for accumlation and depletion regimes, in bare (a) ZnO and (b) NiO films, respectively. The linear slope intersecting the x-axis represent the flatband potential (E_{FB}) value for the respective material.

When a photocatalyst film is immersed into the electrolyte, migration of charge carriers occur until the equilibration of the Fermi levels are attained. As a consequence, the space charge layer will be formed at both the ends, i.e, at semiconductor surface (negative, forming depletion layer) and in the electrolyte (positive, called as Helmholtz layer) with the development of band bending at the interface. This charge separation could be observed by measuring the total capacitance (C) (in the suitable frequency range), which comprises the the semiconductor space charge layer (C_{SC}) and the Helmholtz layer in electrolyte (C_H), as expressed in the equation below:

$$\frac{1}{C_C} = \frac{1}{C_{SC}} + \frac{1}{C_H} \tag{8.6}$$

However, the chosen electrolyte needs to be prepared at sufficient concentration asto provide constant ionic strength, such that no concentration gradient occurs next to the sample and pH is stable. Under this condition, the contribution of the Helmholtz layer becomes negligible because its thickness is lower than that of the space charge layer[288]. Hence, the overall measured capacitance will be dominated by the space charge capacitance and its perturbation with the applied potential is described by the Mott-Schottky equation[289,290]:

$$\frac{1}{{C_{SC}}^2} = \left(\frac{2}{e\varepsilon_0\varepsilon_r N_D A_2}\right)\left(E - E_{FB} - \frac{KT}{e}\right) \tag{8.7}$$

Where, C_{SC} - is the capacitance of the space-charge region of the film at potential E, E_{FB} is the flatband potential, N_D is the free carrier concentration of the semiconductor, and A is

the area ($\sim$ 0.8 cm^2); e is the charge of the electron, ε_0 is the permittivity of free space, ε_r is the relative dielectric constant of ZnO nanorod (2.7[291], as per diameter of the nanorod which is around 80 nm in our nanorods), k is the Boltzmann constant, and T is the absolute temperature.

Further on, the slope of the linear part could be used to determine the charge carrier concentration (N_D) using the equation below:

$$N_D = \frac{2}{e\varepsilon_0\varepsilon_r A^2(slope)} \tag{8.8}$$

The intersection of the linear part with the x-axis (extrapolating the graph with C^2 = 0), gives the flatband potential (E_{FB})[140].

Photoelectrochemical (PEC) properties of each film in Chapter 3.1 was studied using the CHI electrochemical workstation, by employing a three-electrode cell (home-made) with quartz glass window for assisting the illumination on photocatalyst surface (1$\times$1 cm^2). The illumination was done with a Xenon lamp (Arc Lamp Source, 450 W Xe Ozone Free, F/1 from Newport), coupled with KG3 filter (Edmund optics), illuminated at the intensity 1 sun. The 3-electrode cell comprised Platinum (Pt) wire and Ag/AgCl electrode as counter and reference electrode respectively, while the surfaces of scaffold and heterostrcutured were playing the role of working electrode. All the measurements were done with 0.5M $Na_2SO_4.10H_2O$ aqueous solution ($\simeq$ pH-6.6) as electrolyte. Linear Sweep Voltammetry (LSV) was carried out in the 0.3 - 1.7 V potential window for scaffold and 0 - 1.6 V for heterostructures under both dark and light conditions, at 20 mV/Sec scan rate. Mott-Schottky (MS) was performed in the -0.8 to 0.5 V potential range and in the 100 mHz - 200 KHz frequency range (comprising 52 steps), whereas the photoelectrochemical impedance studies (PEIS) were done in the 800kHz - 200mHz frequency range. For LSV, the potential was applied versus reference, whereas for PEIS and MS curves, the potential was applied with respect to open circuit potential, using a $\pm$ 15 mV amplitude signal and all the experiments were carried out at room temperature conditions.

8.2. Chapter 3 - supplementary information

8.2.1. TEM images - as function of NiO deposition temperature

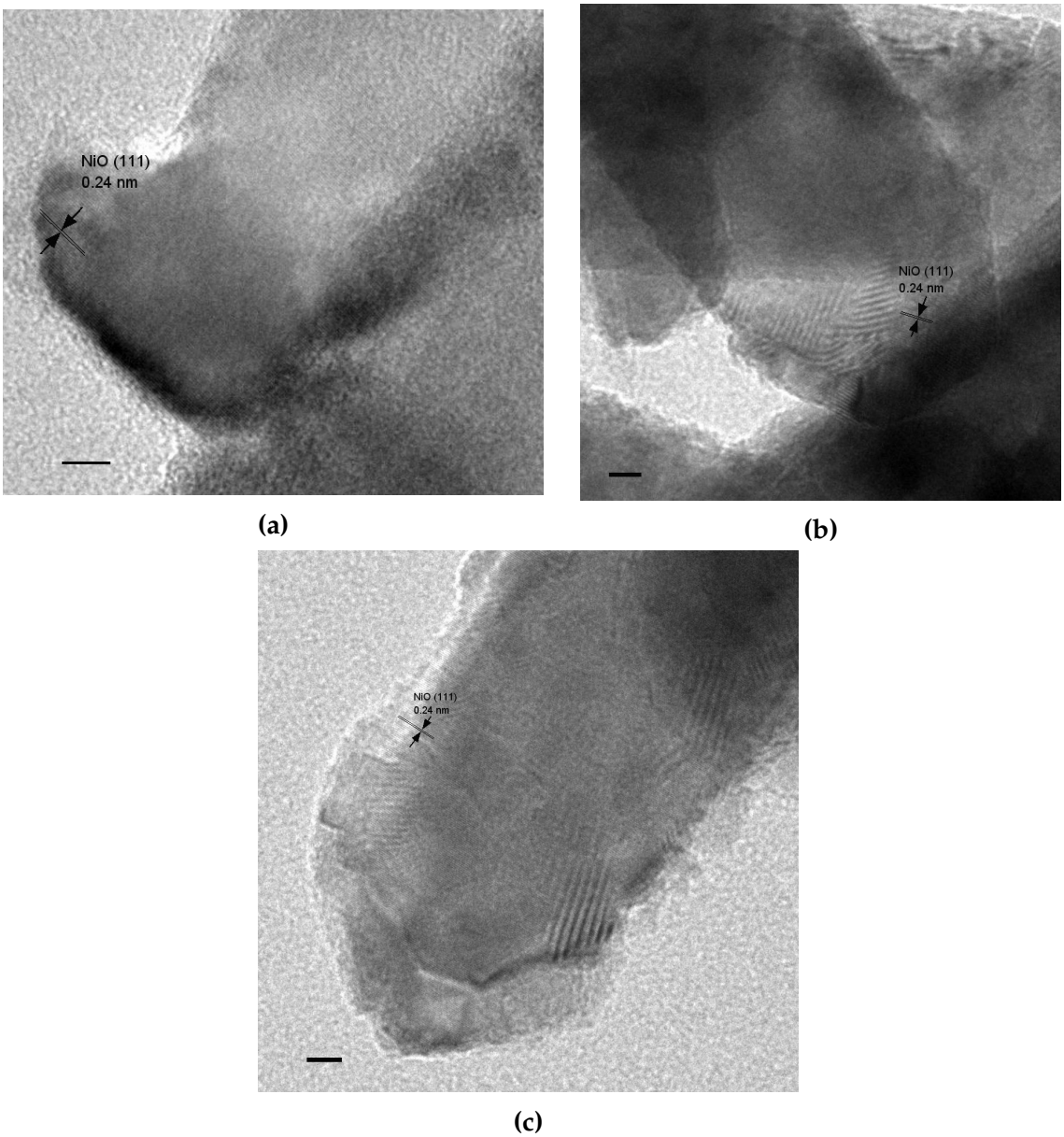

Figure 8.9: TEM images showing the lattice fringes corresponding to NiO (111) plane for (a) $Z1N_{RT}$, (b) $Z1N_{PA}$ and (c) $Z1N_{HT}$.

8.3. Chapter 5 - supplementary information

8.3.1. X-Ray photoelectron spectroscopy

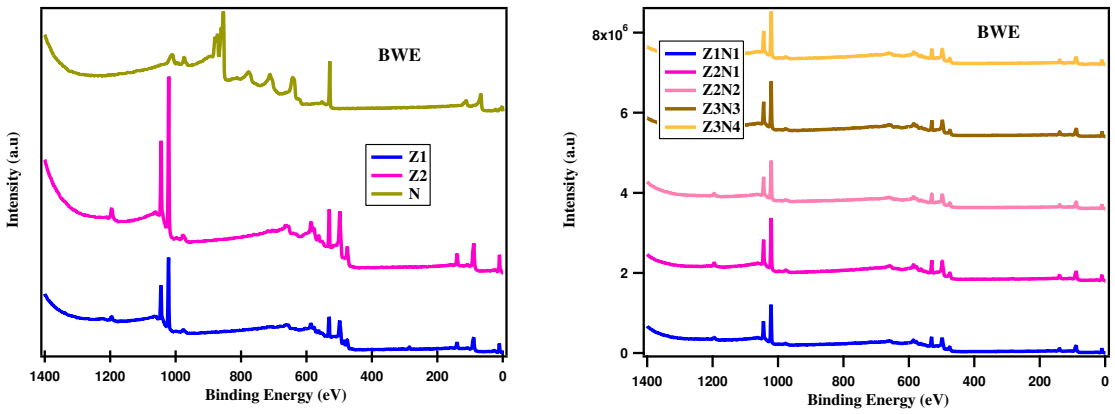

Figure 8.10: Survey spectra for all scaffold (a) and heterostructure (b) films, discussed in Chapter 5.

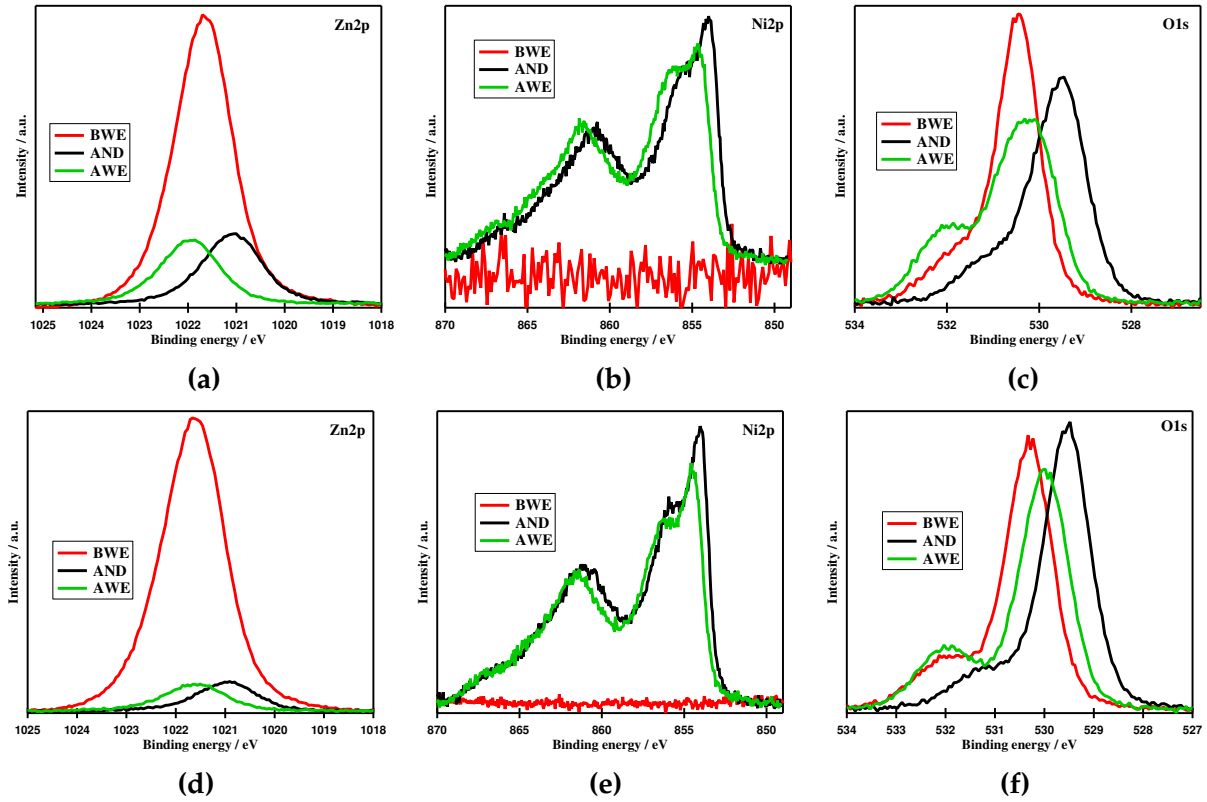

Figure 8.11: Individual spectra of Zn, Ni and O, for Z2N2 (a-c, respectively) and Z3N4 (d-f, respectively). Before Water Exposure (BWE), After NiO Deposition (AND) and After Water Exposure (AWE).

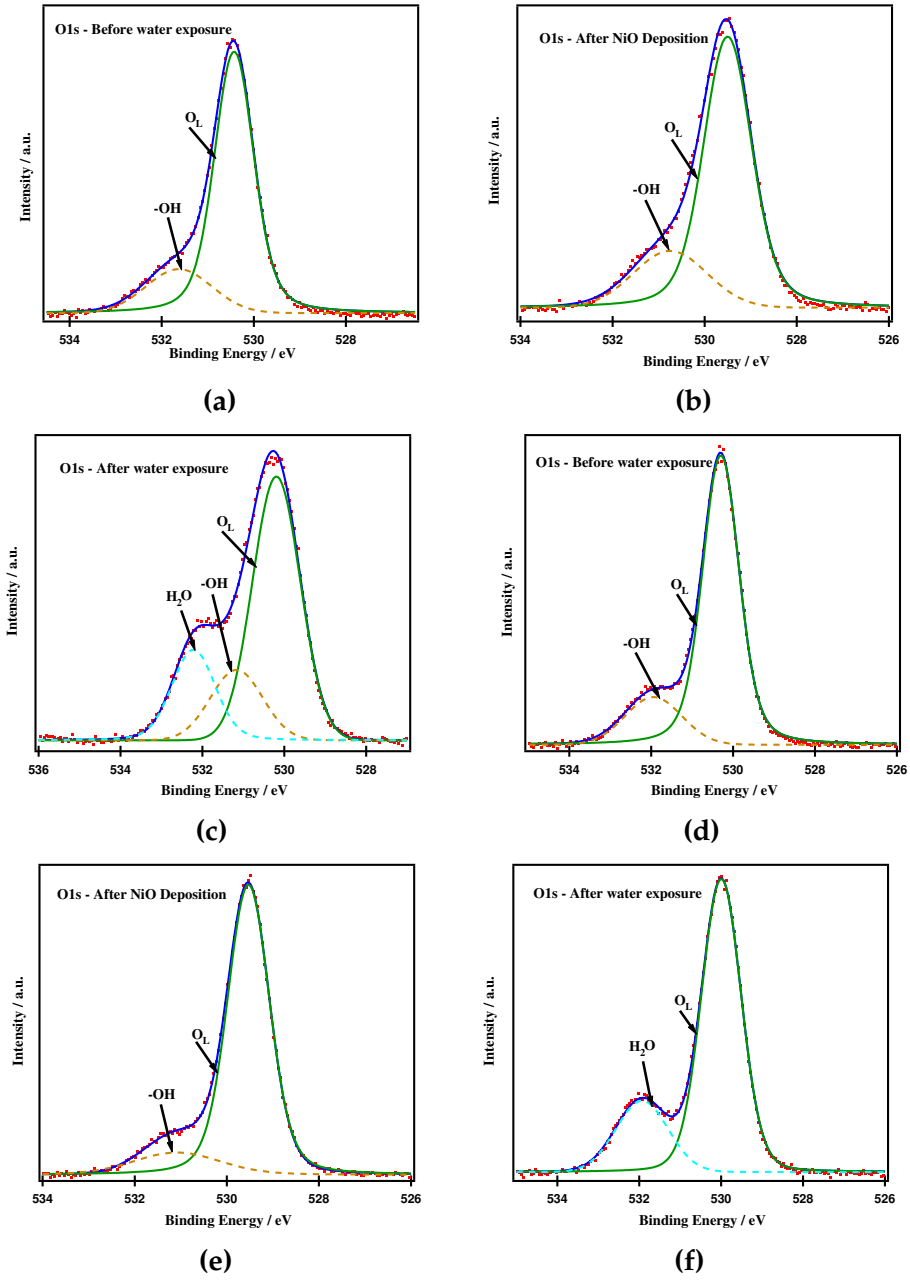

Figure 8.12: Deconvoluted O1s Spectra of Z2N2 and Z3N4, for before(a and d) and after Water Exposure (c and f), after NiO deposition conditions (b and e), respectively.

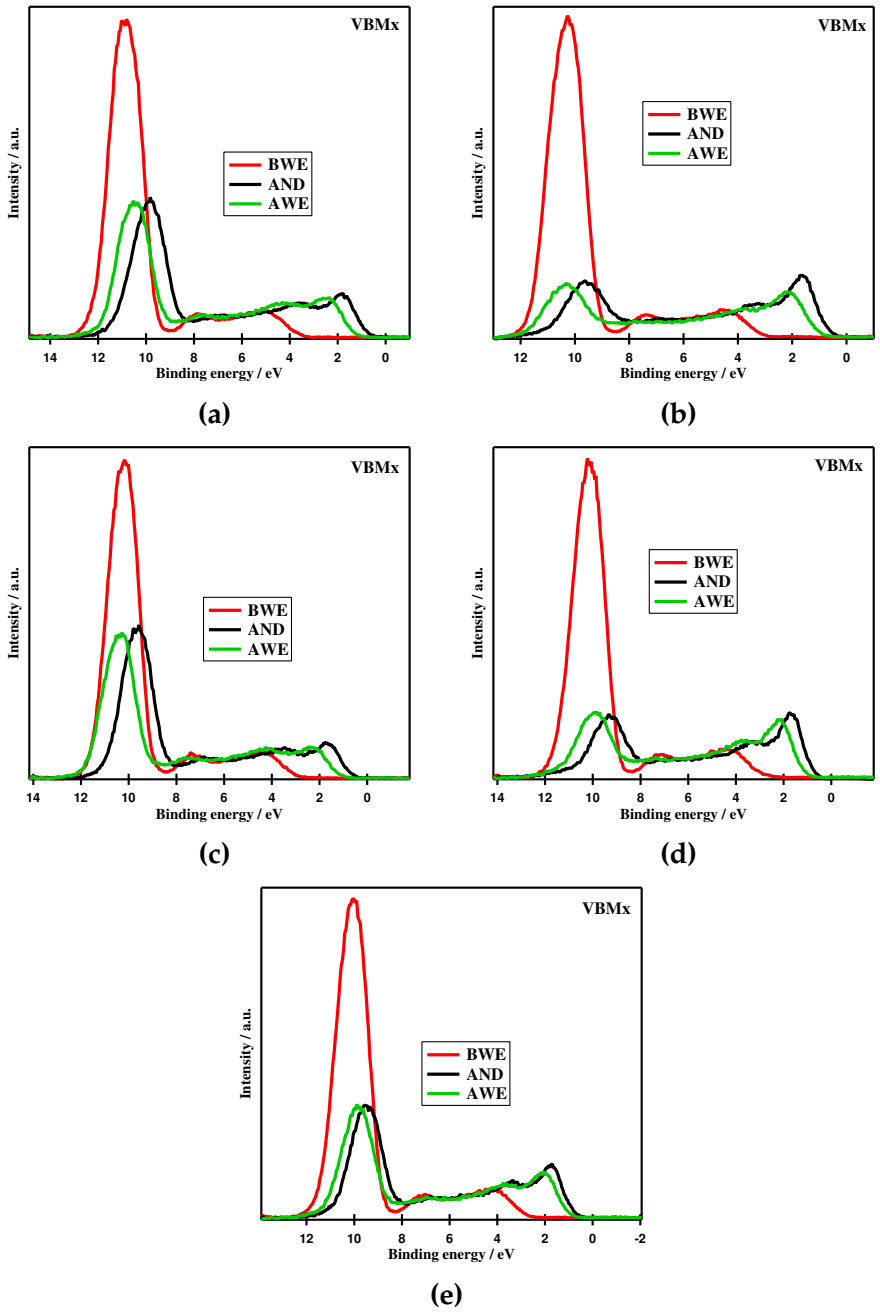

Figure 8.13: Spectra of VBMx for Z1N1 (a), Z2N1 (b), Z2N2 (c), Z3N3 (d) and Z3N4 (e) respectively. Before Water Exposure (BWE), After NiO Deposition (AND) and After Water Exposure (AWE).

8.3.2. Photoluminescence

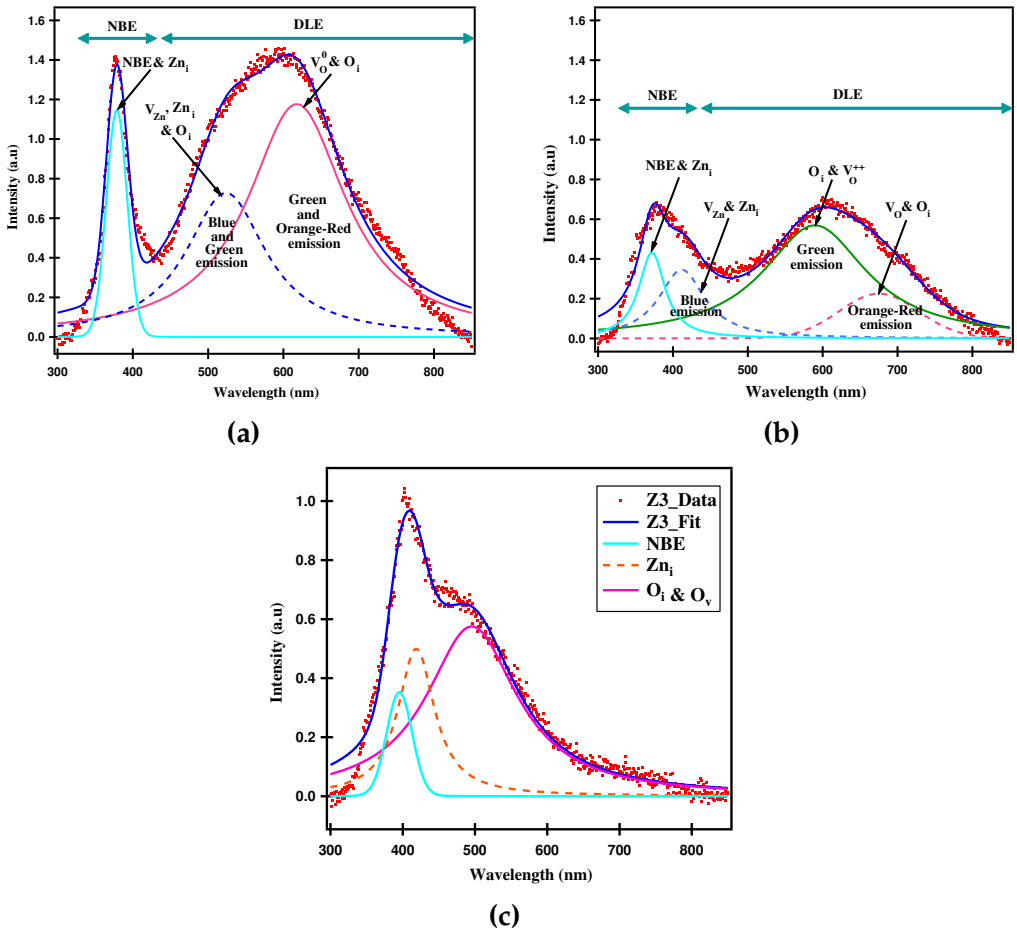

Figure 8.14: Deconvolution of scaffold films for photoluminescence (a)Z1, (b)Z2 and (c)Z3.

8.3.3. Band alignment

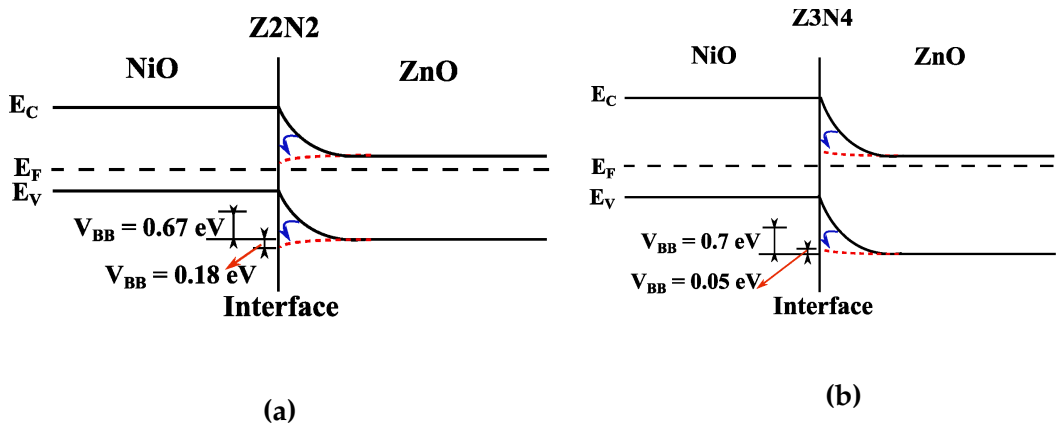

Figure 8.15: Band Alignment after NiO deposition, before and after water exposure; (a) Z2N2 (accumulation of electrons) (b) Z3N4 (partial band flattening). Description in parantheses represent the resultant band bending at NiO/ZnO interface, after water exposure. V_{bb} values shown in figures correspond to the red dotted line, that represent the remaining band bending, after water exposure.